

# **From Nuclei to Compact Stars**



# Contents

<b>1</b>	<b>Topics</b>	<b>1275</b>
<b>2</b>	<b>Participants</b>	<b>1279</b>
2.1	ICRANet . . . . .	1279
2.2	External on going collaborations . . . . .	1279
2.3	Postdocs . . . . .	1280
2.4	Graduate Students . . . . .	1281
<b>3</b>	<b>Publications 2015</b>	<b>1283</b>
3.1	Refereed Journals . . . . .	1283
3.1.1	Printed . . . . .	1283
3.1.2	Accepted for publication or in press . . . . .	1288
3.1.3	Submitted . . . . .	1289
3.1.4	To be submitted . . . . .	1290
3.2	Conference Proceedings . . . . .	1291



# 1 Topics

The study of compact objects such as white dwarfs, neutron stars and black holes requires the interplay between nuclear and atomic physics together with relativistic field theories, e.g., general relativity, quantum electrodynamics, quantum chromodynamics, as well as particle physics. In addition to the theoretical physics aspects, the study of astrophysical scenarios characterized by the presence of a compact object has also started to be focus of extensive research within our group. The research which has been done and is currently being developed within our group can be divided into the following topics:

- **Nuclear and Atomic Astrophysics.** Within this subject of research we study the properties and processes occurring in compact stars in which nuclear and atomic physics have to be necessarily applied. We focus on the properties of nuclear matter under extreme conditions of density and pressure found in these objects. The equation of state of the matter in compact star interiors is studied in detail taking into account all the interactions between the constituents within a full relativistic framework.
- **White Dwarfs Physics and Structure.** The aim of this part of our research is to construct the structure of white dwarfs within a self-consistent description of the equation of state of the interior together with the solution of the hydrostatic equilibrium equations in general relativity. Both unmagnetized and magnetized white dwarfs are studied.
- **White Dwarfs Astrophysics.** We are within this topic interested in the astrophysics of white dwarfs both isolated and in binaries systems. Magnetized white dwarfs, soft gamma repeaters, anomalous X-ray pulsars, white dwarf pulsars, cataclysmic variables, binary white dwarf mergers, and type Ia supernovae are studied. The role of a realistic white dwarf interior structure is particularly emphasized.

- **Neutron Stars Physics and Structure.** We calculate the properties of the interior structure of neutron stars using realistic models of the nuclear matter equation of state within the general relativistic equations of equilibrium. Strong, weak, electromagnetic and gravitational interactions have to be jointly taken into due account within a self-consistent fully relativistic framework. Both unmagnetized and magnetized neutron stars are studied.
- **Neutron Stars Astrophysics.** We study astrophysical systems harboring neutron stars such as isolated and binary pulsars, low and intermediate X-ray binaries, inspiraling and merging double neutron stars. Most extreme cataclysmic events involving neutron stars and their role in the explanation of extraordinarily energetic astrophysical events such as gamma-ray bursts are analyzed in detail.
- **Radiation Mechanisms of White Dwarfs and Neutron Stars.** We here study the possible emission mechanisms of white dwarfs and neutron stars. We are thus interested in both electromagnetic and gravitational radiation at work in astrophysical systems such as compact star magnetospheres, inspiraling and merging relativistic double neutron stars, neutron star-white dwarfs, and neutron star-black hole binaries represent some examples.
- **Exact Solutions of the Einstein and Einstein-Maxwell Equations in Astrophysics.** We analyze the ability of analytic exact solutions of the Einstein and Einstein-Maxwell equations to describe the exterior spacetime of compact stars such as white dwarfs and neutron stars. The problem of matching between interior and exterior spacetimes is addressed in detail. The effect of the quadrupole moment on the properties of the spacetime is also investigated. Particular attention is given to the application of exact solutions in astrophysics, e.g. the dynamics of particles around compact stars and its relevance in astrophysical systems such as X-ray binaries.
- **Critical Fields and Non-linear Electrodynamics Effects in Astrophysics.** We study the conditions under which ultrastrong electromagnetic fields can develop in astrophysical systems such as neutron stars and in the process of gravitational collapse to a black hole. The effects of non-linear electrodynamics minimally coupled to gravity are investigated.

---

New analytic and numeric solutions to the Einstein-Maxwell equations representing black holes or the exterior field of a compact star are obtained and analyzed. The consequences on extreme astrophysical systems, for instance gamma-ray bursts, is studied.



## 2 Participants

### 2.1 ICRAANet

- D. Arnett (Steward Observatory, University of Arizona, USA)
- D. Bini (Istituto Nazionale per l'Applicazione del Calcolo, Italy)
- L. Izzo (ICRAANet, University of Rome, Italy)
- H. Kleinert (Free University of Berlin , Germany)
- V. Popov (ITEP, Moscow, Russia)
- J. A. Rueda (ICRAANet, University of Rome, Italy)
- R. Ruffini (ICRAANet, University of Rome, Italy)
- G. Vereschagin (ICRAANet, University of Rome, Italy)
- S.-S. Xue (ICRAANet, University of Rome, Italy)

### 2.2 External on going collaborations

- K. Boshkayev (Al-Farabi Kazakh National University, Kazakhstan)
- C. Cherubini (Università Campus Biomedico, Rome, Italy)
- S. Chiapparini (Universidade do Estado do Rio de Janeiro, Brazil)
- S. B. Duarte (Centro Brasileiro de Pesquisas Físicas, Brazil)
- S. Filippi (Università Campus Biomedico, Rome, Italy)
- C. L. Fryer (University of Arizona, Los Alamos National Laboratory, USA)

- E. Gacía-Berro (Universitat Politècnica de Catalunya, Spain)
- P. LorénAguilar (University of Exeter, United Kingdom)
- S. O. Kepler (Universidade Federal do Rio Grande do Sul, Brazil)
- B. Külebi (Institut de Ciències de l'Espai, Spain)
- M. Malheiro (Instituto Tecnológico de Aeronáutica, Brazil)
- R. M. Jr. Marinho (Instituto Tecnológico de Aeronáutica, Brazil)
- G. Mathews (University of Notre Dame, USA)
- D. P. Menezes (Universidade Federal de Santa Catarina, Brazil)
- H. Mosquera-Cuesta (Instituto Federal de Educacao, Ciência e Tecnologia do Ceará, Brazil)
- R. Negreiros (Universidade Federal de Fluminense, Brazil)
- L. Pachón (Universidad de Antioquia, Colombia)
- H. Quevedo (Universidad Nacional Autónoma de México, Mexico)
- C. Valenzuela (Universidad del Valle, Colombia)
- C. A. Z. Vasconcellos (Universidade Federal do Rio Grande do Sul, Brazil)

### 2.3 Postdocs

- R. Belvedere (ICRANet-Rio, Universidade Federal Fluminense)
- R. Camargo (ICRANet, University of Rome, Italy)
- J. G. Coelho (ICRANet, University of Rome, Italy)
- S. M. de Carvalho (ICRANet-Rio, Universidade Federal Fluminense)
- M. Muccino (ICRANet, University of Rome, Italy)

## 2.4 Graduate Students

- L. Becerra (ICRANet, University of Rome, Italy)
- D. L. Cáceres (ICRANet, University of Rome, Italy)
- F. Cipolletta (ICRANet, University of Rome, Italy)
- F. G. Oliveira (ICRANet, University of Rome, Italy and Université de Nice Sophia-Antipolis, France)
- J. P. Pereira (ICRANet, University of Rome, Italy and Université de Nice Sophia-Antipolis, France)
- J. F. Rpdriquez (ICRANet, University of Rome, Italy)
- M. L. Warren (University of Notre Dame, USA)
- Y. Wu (ICRANet, University of Rome, Italy and Université de Nice Sophia-Antipolis, France)



## 3 Publications 2015

### 3.1 Refereed Journals

#### 3.1.1 Printed

1. A. Mesquita, M. Razeira, R. Ruffini, J. A. Rueda, D. Hadjimichef, R. O. Gomes, and C. A. Z. Vasconcellos, *An effective field theory for neutron stars with many-body forces, strong  $\Sigma^-$  repulsion, and  $K^-$  and  $\bar{K}^0$  condensation*, *Astronomische Nachrichten* 336, 880 (2015).

The role of many-body correlations (many-body forces) and  $K^-$ - $\bar{K}^0$  condensation in  $\beta$ -equilibrated hyperonic matter is investigated in order to shed some light in the hyperonization puzzle, ie that neutron star mass of  $2M_\odot$  cannot be obtained in the presence of exotic degree of freedoms. In this investigation, we use an effective relativistic QHD-model with parameterized couplings which represents an extended compilation of other effective models found in the literature. Our theoretical approach exhausts the whole fundamental baryon octet ( $n, p, \Sigma^-, \Sigma^0, \Sigma^+, \Lambda, \Xi^-, \Xi^0$ ) and simulates n-order corrections to the minimal Yukawa couplings by considering many-body nonlinear self-couplings and meson-meson interaction terms involving scalar-isoscalar, vector-isoscalar, vector-isovector, and scalar-isovector sectors. Following recent experimental results, we consider in our calculations the extreme case where the  $\Sigma^-$  experiences such a strong repulsion that its influence in the nuclear structure of a neutron star is excluded at all. We study the effects of this exclusion on the phase transition of conventional exotic hadronic matter to hadronic matter containing a condensate of kaons and anti-kaons. As a novelty in the treatment of kaon and anti-kaon condensation in high density nuclear matter, we consider a Lagrangian formulation which describes, in addition to the interaction involving baryons and mesons and the contribution of kaons and anti-kaons in free propagation, the presence of many-body forces involving kaon, anti-kaon and meson fields. To im-

plement the corresponding phase transition we considered the Gibbs conditions combined with the mean-field approximation, giving rise to a mixed phase of coexistence between baryon matter and the condensed of kaons and anti-kaons. Our investigation show that even with kaon condensation, the nuclear equation of state satisfies both the maximum mass and the allowed ranges of mass and radius of neutron stars.

2. L. Becerra, F. Cipolletta, C. L. Fryer, J. A. Rueda, and R. Ruffini, *Angular Momentum Role in the Hypercritical Accretion of Binary-driven-Hypernovae*, *ApJ* 812, 100 (2015).

The induced gravitational collapse paradigm explains a class of energetic,  $E_{iso} \sim 10^{52}$  erg, long-duration gamma-ray bursts (GRBs) associated with Ic supernovae, recently named binary-driven hypernovae. The progenitor is a tight binary system formed of a carbon-oxygen (CO) core and a neutron star (NS) companion. The supernova ejecta of the exploding CO core trigger a hypercritical accretion process onto the NS, which reaches the critical mass in a few seconds, and gravitationally collapses to a black hole, emitting a GRB. In our previous simulations of this process, we adopted a spherically symmetric approximation to compute the features of the hypercritical accretion process. We here present the first estimates of the angular momentum transported by the supernova ejecta,  $L_{acc}$ , and perform numerical simulations of the angular momentum transfer to the NS during the hyperaccretion process in full general relativity. We show that the NS (1) reaches either the mass-shedding limit or the secular axisymmetric instability in a few seconds depending on its initial mass, (2) reaches a maximum dimensionless angular momentum value,  $[(cJ)/(GM^2)]_{max} \sim 0.7$ , and (3) can support less angular momentum than the one transported by supernova ejecta,  $L_{acc} > J_{NS,max}$ , hence there is an angular momentum excess that necessarily leads to jetted emission.

3. R. Ruffini, M. Muccino, M. Kovacevic, F. G. Oliveira, J. A. Rueda, C. L. Bianco, M. Enderli, A. V. Penacchioni, G. B. Pisani, Y. Wang, and E. Zaninoni, *GRB 140619B: a short GRB from a binary neutron star merger leading to black hole formation*, *ApJ* 808, 190 (2015).

We show the existence of two families of short gamma-ray bursts (GRBs), both originating from the merger of binary neutron stars (NSs): family-1 with  $E_{iso} \lesssim 10^{52}$  erg, leading to a massive NS as the merged core,

and family-2 with  $E_{iso} \gtrsim 10^{52}$  erg, leading to a black hole (BH). Following the identification of the prototype GRB 090227B, we present the details of a new example of family-2 short burst: GRB 140619B. From the spectral analysis of the early 0.2 s, we infer an observed temperature  $kT = 324 \pm 33$  keV of the  $e^+e^-$  plasma at transparency (P-GRB), a theoretically derived redshift  $z = 2.67 \pm 0.37$ , a total burst energy  $E_{e^+e^-}^{tot} = (6.03 \pm 0.79) \times 10^{52}$  erg, a rest-frame peak energy  $E_{p,i} = 4.7$  MeV, and a baryon load  $B = (5.52 \pm 0.73) \times 10^{-5}$ . We also estimate the corresponding emission of gravitational waves. Two additional examples of family-2 short bursts are identified: GRB 081024B and GRB 090510, remarkable for its well determined cosmological distance. We show that marked differences exist in the nature of the afterglows of these two families of short bursts: family-2 bursts, leading to BH formation, consistently exhibit high energy emission following the proper-GRB emission; family-1 bursts, leading to the formation of a massive NS, should never exhibit high energy emission. We also show that both the families fulfill an  $E_{p,i} - E_{iso}$  relation with slope  $\gamma = 0.59 \pm 0.07$  and a normalization constant incompatible with the one for long GRBs. The observed rate of such family-2 events is  $\rho_0 = (2.1_{-1.4}^{+2.8}) \times 10^{-4} \text{ Gpc}^{-3} \text{ yr}^{-1}$ .

4. F. Cipolletta, C. Cherubini, S. Filippi, J. A. Rueda, and R. Ruffini, *Fast rotating neutron stars with realistic nuclear matter equation of state*, Phys. Rev. D 92, 023007 (2015).

We construct equilibrium configurations of uniformly rotating neutron stars for selected relativistic mean-field nuclear matter equations of state (EOS). We compute, in particular, the gravitational mass ( $M$ ), equatorial ( $R_{eq}$ ) and polar ( $R_{pol}$ ) radii, eccentricity, angular momentum ( $J$ ), moment of inertia ( $I$ ) and quadrupole moment ( $M_2$ ) of neutron stars stable against mass shedding and secular axisymmetric instability. By constructing the constant frequency sequence  $f = 716$  Hz of the fastest observed pulsar, PSR J1748-2446ad, and constraining it to be within the stability region, we obtain a lower mass bound for the pulsar,  $M_{min} = [1.2-1.4] M_{\odot}$ , for the EOS employed. Moreover, we give a fitting formula relating the baryonic mass ( $M_b$ ) and gravitational mass of nonrotating neutron stars,  $M_b/M = M/M_{\odot} + (13/200)(M/M_{\odot})^2$  [or  $M/M_{\odot} = M_b/M_{\odot} - (1/20)(M_b/M_{\odot})^2$ ], which is independent of the EOS. We also obtain a fitting formula, although not EOS independent, relating

the gravitational mass and the angular momentum of neutron stars along the secular axisymmetric instability line for each EOS. We compute the maximum value of the dimensionless angular momentum,  $a/M = cJ/(GM^2)$  (or “Kerr parameter”),  $(a/M)_{\max} \approx 0.7$ , found to be also independent of the EOS. We then compare and contrast the quadrupole moment of rotating neutron stars with the one predicted by the Kerr exterior solution for the same values of mass and angular momentum. Finally, we show that, although the mass quadrupole moment of realistic neutron stars never reaches the Kerr value, the latter is closely approached from above at the maximum mass value, as physically expected from the no-hair theorem. In particular, the stiffer the EOS, the closer the mass quadrupole moment approaches the value of the Kerr solution.

5. K. Boshkayev, J. A. Rueda, and M. Muccino, *Extracting multipole moments of neutron stars from quasi-periodic oscillations in low mass X-ray binaries*, *Astronomy Reports* 59, 441 (2015).

We consider the kilohertz quasi-periodic oscillations of low-mass X-ray binaries within the Hartle-Thorne spacetime. We show that the interpretation of the epicyclic frequencies of this spacetime with the observed kilohertz quasi-periodic oscillations, within the Relativistic Precession Model, allows us to extract the total mass  $M$ , angular momentum  $J$ , and quadrupole moment  $Q$  of the compact object in a low-mass X-ray binary. We exemplify this fact by analyzing the data of the Z-source GX 5-1. We show that the extracted multipole structure of the compact component of this source deviates from the one expected from a Kerr black hole and instead it points to a neutron star explanation.

6. J. P. Pereira and J. A. Rueda, *Energy decomposition within Einstein-Born-Infeld black holes*, *Phys. Rev. D* 91, 064048 (2015).

We analyze the consequences of the recently found generalization of the Christodoulou-Ruffini black hole mass decomposition for Einstein-Born-Infeld black holes [characterized by the parameters  $(Q, M, b)$ , where  $M = M(M_{\text{irr}}, Q, b)$ ,  $b$  is the scale of the field,  $Q$  the charge,  $M_{\text{irr}}$  the “irreducible mass”, physically meaning the energy of a black hole when its charge is null] and their interactions. We show in this context that their description is largely simplified and can basically be split into two families depending upon the parameter  $b|Q|$ . If  $b|Q| = 1/2$ , then black holes

could have even zero irreducible masses and they always exhibit single nondegenerate horizons. If  $b|Q| > 1/2$ , then an associated black hole must have a minimum irreducible mass (related to its minimum energy) and has two horizons up to a transitional irreducible mass. For larger irreducible masses, single horizon structures raise again. By assuming that black holes emit thermal uncharged scalar particles, we further show in light of the black hole mass decomposition that one satisfying  $b|Q| > 1/2$  takes an infinite amount of time to reach the zero temperature, settling down exactly at its minimum energy. Finally, we argue that depending on the fundamental parameter  $b$ , the radiation (electromagnetic and gravitational) coming from Einstein-Born-Infeld black holes could differ significantly from Einstein-Maxwell ones. Hence, it could be used to assess such a parameter.

7. J. P. Pereira and J. A. Rueda, *Radial Stability in Stratified Stars*, ApJ 801, 19 (2015).

We formulate within a generalized distributional approach the treatment of the stability against radial perturbations for both neutral and charged stratified stars in Newtonian and Einstein's gravity. We obtain from this approach the boundary conditions connecting any two phases within a star and underline its relevance for realistic models of compact stars with phase transitions, owing to the modification of the star's set of eigenmodes with respect to the continuous case.

8. R. Belvedere, J. A. Rueda, and R. Ruffini, *On the Magnetic Field of Pulsars with Realistic Neutron Star Configurations*, ApJ 799, 23 (2015).

We have recently developed a neutron star model fulfilling global and not local charge neutrality, both in the static and in the uniformly rotating cases. The model is described by the coupled Einstein-Maxwell-Thomas-Fermi equations, in which all fundamental interactions are accounted for in the framework of general relativity and relativistic mean field theory. Uniform rotation is introduced following Hartle's formalism. We show that the use of realistic parameters of rotating neutron stars, obtained from numerical integration of the self-consistent axisymmetric general relativistic equations of equilibrium, leads to values of the magnetic field and radiation efficiency of pulsars that are very different from estimates based on fiducial parameters that assume a neutron star mass  $M = 1.4M_{\odot}$ , radius  $R = 10$  km, and moment of inertia

$I = 10^{45}$  g cm<sup>2</sup>. In addition, we compare and contrast the magnetic field inferred from the traditional Newtonian rotating magnetic dipole model with respect to the one obtained from its general relativistic analog, which takes into account the effect of the finite size of the source. We apply these considerations to the specific high-magnetic field pulsar class and show that, indeed, all of these sources can be described as canonical pulsars driven by the rotational energy of the neutron star, and have magnetic fields lower than the quantum critical field for any value of the neutron star mass.

### 3.1.2 Accepted for publication or in press

1. C. L. Fryer, F. G. Oliveira, J. A. Rueda, R. Ruffini, *On the Neutron Star-Black Hole Binaries Produced by Binary-driven-Hypernovae*, to appear in Phys. Rev. Lett.

Binary-driven-hypernovae (BdHNe) within the induced gravitational collapse (IGC) paradigm have been introduced to explain energetic ( $E_{\text{iso}} \gtrsim 10^{52}$  erg), long gamma-ray bursts (GRBs) associated with type Ic supernovae (SNe). The progenitor is a tight binary composed of a carbon-oxygen (CO) core and a neutron star (NS) companion, a subclass of the newly proposed "ultra-stripped" binaries. The CO-NS short-period orbit causes the NS to accrete appreciable matter from the SN ejecta when the CO core collapses, ultimately causing it to collapse to a black hole (BH) and producing a GRB. These tight binaries evolve through the SN explosion very differently than compact binaries studied in population synthesis calculations. First, the hypercritical accretion onto the NS companion alters both the mass and momentum of the binary. Second, because the explosion timescale is on par with the orbital period, the mass ejection can not be assumed to be instantaneous. This dramatically affects the post-SN fate of the binary. Finally, the bow shock created as the accreting NS plows through the SN ejecta transfers angular momentum, braking the orbit. These systems remain bound even if a large fraction of the binary mass is lost in the explosion (well above the canonical 50% limit), and even large kicks are unlikely to unbind the system. Indeed, BdHNe produce a new family of NS-BH binaries unaccounted for in current population synthesis analyses and, although they may be rare, the fact that nearly 100% remain bound implies they

may play an important role in the compact merger rate, important for gravitational waves (GWs) that, in turn, can produce a new class of ultrashort GRBs.

### 3.1.3 Submitted

1. Jaziel G. Coelho, R. C. R. de Lima, D. L. Caceres, M. Malheiro, J. A. Rueda, R. Ruffini, *On the rotation-power nature of SGRs and AXPs*, submitted to ApJ.

We show that nine of the twenty three soft gamma repeaters (SGRs) and anomalous X-ray pulsars (AXPs), namely the 40% of the entire observed population of sources, can be described as canonical pulsars driven by the rotational energy of a neutron star (NS), for which we give the possible range of masses. We also show that if the blackbody component in soft X-rays is due to the surface temperature of the NS, then two more sources become explainable as rotation-powered NSs, leading to a 50% of the population explainable as ordinary pulsars. We show that, within these sources, we find the SGRs/AXPs with observed radio emission as well as the ones possibly associated with supernova remnants, reinforcing a natural explanation for these sources as ordinary pulsars. Assuming on the other hand an alternative model in which SGR/AXPs are rotation-powered white dwarfs (WDs), we show that the entire population can be explained within this scenario. We give tight bounds for the masses, radii, and magnetic field of the WD by requesting the gravitational and rotational stability of the star.

2. J. A. Rueda, R. Ruffini, Y. Wu, S.-S. Xue, *Surface tension of heavy atoms*, submitted to Phys. Rev. C.

Based on the relativistic mean field theory and the Thomas-Fermi approximation, we study the surface properties of heavy atoms in which some of the electrons have penetrated into nuclear cores. Taking into account the strong, weak, and electromagnetic interactions, we numerically study the structure of heavy atoms and calculate the surface tension and Coulomb energy. We analyze the influence of the electron component on the structure of heavy atoms and the surface tension to compare and contrast with known phenomenological results in nuclear physics and the results of the core-crust interface of neutron stars with

global charge neutrality. Based on these results we study the instability against Bohr-Wheeler surface deformations in the case of heavy atoms. The results in this article provide the evidence of strong effects of the electromagnetic interaction and electrons on structure of heavy atoms.

3. R. Belvedere, Jorge A. Rueda, R. Ruffini, *On the Keplerian frequency and moment of inertia of neutron stars*, submitted to Phys. Rev. C.

In our previous treatments of static and rotating neutron stars, we have developed a neutron star model fulfilling global, but not local, charge neutrality. The model is described by what we have called the Einstein-Maxwell-Thomas-Fermi (EMTF) equations, which take into account the strong, weak, electromagnetic, and gravitational interactions within general relativity. Uniform rotation is introduced via the Hartle formalism. We compare and contrast here the moment of inertia and the sequence of maximally rotating (Keplerian) neutron stars obtained from the solution of the EMTF equations, with the claimed universal analytic formulas 1) for the Keplerian sequence by Lattimer & Prakash (2004), and 2) for the moment of inertia as a function of the compactness by Ravenhall & Pethick (1994) and by Lattimer & Schutz (2005). We show that those simple universal analytic formulas cannot properly describe the above properties of neutron stars, irrespective of the condition of charge neutrality applied, namely local or global, leading to inaccurate qualitative and quantitative results.

### 3.1.4 To be submitted

1. K. Boshkayev, J. A. Rueda, *Induced compression by angular momentum loss in super-Chandrasekhar white dwarfs*.
2. R. C. R. de Lima, J. A. Rueda, R. Ruffini, C. A. Z. Vasconcellos, *Rapidly rotating neutron stars with strong sigma-hyperon repulsion*.
3. R. C. R. de Lima, J. A. Rueda, R. Ruffini, C. A. Z. Vasconcellos, *The effects of hyperons on the structure of rapidly rotating neutron stars*.
4. R. Belvedere, S. Chiapparini, S. B. Duarte, J. A. Rueda, R. Ruffini, *Rapidly rotating neutron stars with extended hadronic nuclear models with  $\Delta$ -resonances*.

5. R. Negreiros, Brett Vern Carlson, S. M de Carvalho, *Using cooling for probing proton-superconductivity in the interior of neutron stars.*
6. S. M. Carvalho, R. Negreiros, J. A. Rueda, *Strange stars versus globally neutral neutron stars: structure and cooling.*
7. D. L. Cáceres, S. M. Carvalho, J. G. Coelho, R. C. R. de Lima, J. A. Rueda, *Thermal X-ray emission of massive, fast rotating, highly magnetized white dwarfs.*

### 3.2 Conference Proceedings

1. S. M. de Carvalho, J. A. Rueda, and R. Ruffini, *On the Relativistic Feynman-Metropolis Equation of State at Finite Temperatures*, in Thirteenth Marcel Grossmann Meeting: On Recent Developments in Theoretical and Experimental General Relativity, Astrophysics and Relativistic Field Theories (K. Rosquist, ed.), pp. 2481-2483, Jan. 2015.
2. K. Boshkayev, J. A. Rueda, R. Ruffini, and I. Siutsou, *General Relativistic and Newtonian White Dwarfs*, in Thirteenth Marcel Grossmann Meeting: On Recent Developments in Theoretical and Experimental General Relativity, Astrophysics and Relativistic Field Theories (K. Rosquist, ed.), pp. 2468-2474, Jan. 2015.
3. K. Boshkayev, J. A. Rueda, and R. Ruffini, *SGRs and AXPs as Massive Fast Rotating Highly Magnetized White Dwarfs: the Case of SGR 0418+5729*, in Thirteenth Marcel Grossmann Meeting: On Recent Developments in Theoretical and Experimental General Relativity, Astrophysics and Relativistic Field Theories (K. Rosquist, ed.), pp. 2295-2300, Jan. 2015.
4. J. A. Rueda and R. Ruffini, *Strong, Weak, Electromagnetic, and Gravitational Interactions in Neutron Stars*, in Thirteenth Marcel Grossmann Meeting: On Recent Developments in Theoretical and Experimental General Relativity, Astrophysics and Relativistic Field Theories (K. Rosquist, ed.), pp. 191-209, Jan. 2015.
5. F. G. Oliveira, J. A. Rueda, and R. Ruffini, *X, Gamma-Rays, and Gravitational Waves Emission in a Short Gamma-Ray Burst*, *Astrophysics and Space Science Proceedings*, vol. 40, p. 43, 2015.

# On the Neutron Star-Black Hole Binaries Produced by Binary-driven-Hypernovae

Chris L. Fryer,<sup>1</sup> F. G. Oliveira,<sup>2,3,4</sup> J. A. Rueda,<sup>2,3,4,5</sup> R. Ruffini<sup>2,3,4,5</sup>

<sup>1</sup>*CCS-2, Los Alamos National Laboratory, Los Alamos, NM 87545*

<sup>2</sup>*Dipartimento di Fisica and ICRA, Sapienza Università di Roma, P.le Aldo Moro 5, I-00185 Rome, Italy*

<sup>3</sup>*ICRANet, Piazza della Repubblica 10, I-65122 Pescara, Italy*

<sup>4</sup>*Université de Nice - Sophia Antipolis Cedex 2, Grand Château Parc Valrose, Nice, France and*

<sup>5</sup>*ICRANet-Rio, Centro Brasileiro de Pesquisas Físicas,*

*Rua Dr. Xavier Sigaud 150, Rio de Janeiro, RJ, 22290-180, Brazil*

(Dated: November 12, 2015)

Binary-driven-hypernovae (BdHNe) within the induced gravitational collapse (IGC) paradigm have been introduced to explain energetic ( $E_{\text{iso}} \gtrsim 10^{52}$  erg), long gamma-ray bursts (GRBs) associated with type Ic supernovae (SNe). The progenitor is a tight binary composed of a carbon-oxygen (CO) core and a neutron star (NS) companion, a subclass of the newly proposed “ultra-stripped” binaries. The CO-NS short-period orbit causes the NS to accrete appreciable matter from the SN ejecta when the CO core collapses, ultimately causing it to collapse to a black hole (BH) and producing a GRB. These tight binaries evolve through the SN explosion very differently than compact binaries studied in population synthesis calculations. First, the hypercritical accretion onto the NS companion alters both the mass and momentum of the binary. Second, because the explosion timescale is on par with the orbital period, the mass ejection can not be assumed to be instantaneous. This dramatically affects the post-SN fate of the binary. Finally, the bow shock created as the accreting NS plows through the SN ejecta transfers angular momentum, braking the orbit. These systems remain bound even if a large fraction of the binary mass is lost in the explosion (well above the canonical 50% limit), and even large kicks are unlikely to unbind the system. Indeed, BdHNe produce a new family of NS-BH binaries unaccounted for in current population synthesis analyses and, although they may be rare, the fact that nearly 100% remain bound implies they may play an important role in the compact merger rate, important for gravitational waves (GWs) that, in turn, can produce a new class of ultrashort GRBs.

Keywords: Type Ic Supernovae — Hypercritical Accretion — Induced Gravitational Collapse — Gamma Ray Bursts – Gravitational Waves

## INTRODUCTION

Binary massive star systems evolve into a broad set of compact binaries from X-ray binaries consisting of stars accreting onto either BH or NS companions to the more exotic binary compact objects such NS-BH and NS-NS binaries. The formation scenarios of these compact binaries typically argue that, after the first SN explosion, the compact remnant enters a common envelope phase with its companion, tightening the orbit. If the system remains bound after the companion star collapses, a NS-BH or NS-NS binary is formed. A range of scenarios have been invoked [1–3], including exotic scenarios where both components expand off the main sequence concurrently, causing a single common envelope around two helium cores [4].

Recently, two independent communities have argued for a “new” evolutionary scenario forming these compact binaries where, after the collapse of the primary star to a NS, the system undergoes a series of mass transfer phases, ejecting both the hydrogen and helium shells of the secondary to produce a binary composed of a massive CO core and a NS. When the CO core collapses and produces a SN explosion, a compact binary system is formed. In the X-ray binary/SN community, these systems are called “ultra-stripped” binaries. In the past few years, such sys-

tems have been invoked to both explain the population of NS-NS binaries as well as a growing set of low-luminosity and/or rapid decay-rate SNe [5, 6]. Low-mass ejecta can match the observational features of these SNe and ultra-stripped binaries without hydrogen and helium layers in their pre-SN progenitor produce small cores with such low-mass explosions. The rate of these systems are predicted to be 0.1–1% of the total SN rate [5]. These binaries are extremely tight, and most of the systems studied have orbital periods lying between 3000 and 300,000 s. Proponents of the ultra-stripped systems argue that this scenario dominates the formation of NS-NS binaries and that there are virtually no systems that are formed where the CO core collapses directly to a BH.

The IGC scenario for GRBs [7–9] introduced a subset of extremely short-period CO-NS binaries where the ejecta from the exploding CO star accretes onto its NS companion, causing the NS, in some cases, to collapse to a BH. If ultra-stripped binaries dominate the formation of NS-NS binaries, this scenario would dominate the formation of NS-BH binaries. This collapse to a BH releases energy to drive the GRB emission [9, 10]. The CO core is a requirement to allow the tight orbits needed to produce sufficient accretion to cause the NS collapse, but it also provides a natural explanation for the fact that these GRBs are always associated with type Ic SNe. The recently introduced ultra-stripped binaries are a wel-

come support for the IGC scenario from the point of view of stellar evolution, with the only caveat that IGC progenitors are a small subset of the ultra-stripped binaries where the initial orbital separation and CO core mass are aligned to produce binaries with orbital periods lying in the 100–1000 s range. This requires fine-tuning both of the CO star mass and the binary orbit. From an astrophysical point of view the IGC scenario is uniquely characterized by the formation of the BH during the accretion process of the SN ejecta onto the companion NS and the associated GRB emission. Since the rate of the high-luminosity GRBs (BdHNe) explained through the IGC scenario is  $(1.1\text{--}1.3) \times 10^{-2} \text{ Gpc}^{-3} \text{ y}^{-1}$  [11], and 0.1–1% of the SN Ibc population could be ultra-stripped binaries [5], only 0.005–0.07% of the latter are needed to explain the BdHNe population (assuming a SN Ibc rate of  $2 \times 10^4 \text{ Gpc}^{-3} \text{ y}^{-1}$  [12]).

Studies of ultra-stripped binaries have expanded our understanding of stellar radii, confirming these results: CO cores with masses below  $2 M_{\odot}$  have radii of  $1\text{--}4 \times 10^9 \text{ cm}$  [13], in agreement with the assumptions used in IGC studies [10]. Even if some helium remains on the stripped core, it will be ejected if it expands to interact with its compact-object companion. These radii are sufficiently small to produce the tight orbits required to produce the rapid accretion of the ejecta onto the NS companion and the formation of the BH.

In typical systems, most of the binaries become unbound during the SN explosion because of the ejected mass and momentum imparted (kick) on the newly formed compact object in the explosion of the massive star. Under the instantaneous explosion assumption, if half of the binary system’s mass is lost in the SN explosion, the system is disrupted, forming two single compact objects. Although SN kicks may allow some systems to remain bound, in general, these kicks unbind even more systems. In general, it is believed that the fraction of massive binaries that can produce double compact object binaries is low:  $\sim 0.001\text{--}1\%$  [1–3].

For ultra-stripped binaries, the fate is very different. In these systems, the mass ejected is extremely low and, if the SN kick is low, these systems remain bound [5, 6]. In the tighter binaries leading to IGC progenitors, the assumption of instantaneous mass ejection is no longer valid. We demonstrate in this work that, removing this assumption, even with a strong SN kick nearly all of these systems will remain bound. In this case, even though IGC progenitors are rare, the compact binaries produced by these progenitors may dominate the total NS-BH binaries in the Universe, and lead to a new previously unaccounted family of GRBs.

We shall describe below the differences between these systems and typical massive star binaries, modeling these orbits through the SN explosion. We then calculate the evolution of these NS-BH binaries via GWs emission up to the merger point, and assess their detectability. We

conclude with a discussion of the additional observational predictions of these NS-BH binaries, introducing a new class of short GRBs, with specific observational signatures, here referred to as ultrashort GRBs.

## POST-EXPLOSION ORBITS

The mass ejected during the SN alters the binary orbit, causing it to become wider and more eccentric. Assuming that the mass is ejected instantaneously, the post-explosion semi-major axis is  $a/a_0 = (M_0 - \Delta M)/(M_0 - 2a_0\Delta M/r)$ , where  $a_0$  and  $a$  are the initial and final semi-major axes respectively,  $M_0$  is the total initial mass of the binary system,  $\Delta M$  is the change of mass (equal to the amount of mass ejected in the SN), and  $r$  is the orbital separation at the time of explosion [14]. For circular orbits, like the ones expected from our systems after going through a common envelope evolution, we find that the system is unbound if it loses half of its mass. But, for these close binaries, a number of additional effects can alter the fate of the binary.

The time it takes for the ejecta to flow past a companion in a SN is roughly 10–1000 s. These explosions follow a so-called homologous velocity profile where the velocity is proportional to the position. Although the shock front is moving above  $10,000 \text{ km s}^{-1}$ , the denser, lower-velocity ejecta can be moving at below  $1000 \text{ km s}^{-1}$ . Our estimates are based on simulated supernova explosions [10]. The broad range of times arises because the SN ejecta velocities varies from 100–10,000  $\text{km s}^{-1}$ . The accretion peaks as the slow-moving (inner) ejecta flows past the NS companion. Note that the initial SN explosion in this case is not a hypernova. The observed “hypernova” is actually produced when the GRB from the BH collapse sweeps up this SN (and circumstellar) material [15]. For normal binaries, this time is a very small fraction of the orbital period and the “instantaneous” assumption is perfectly valid. However, in the close binary systems considered here, the orbital period ranges from only 100–1000 s, and the mass loss from the SN explosion can no longer be assumed to be instantaneous.

This has already been pointed out in [16] where it was shown that in BdHNe the accretion process is fast and massive enough to produce the BH formation in a time-interval as short as the orbital period. We here deepen this analysis to study the effect of the SN explosion in such a scenario with a specific example, for which we have produced an orbit code using a simple staggered leapfrog integration (see [17] for details of this integration method). We have tested both stability (by modeling many orbits) and convergence (decreasing the time step by 2 orders of magnitude confirming identical results). We also reproduce the results of the instantaneous limit. From figure 1, as the ejecta timescale becomes just a fraction of the orbital timescale, the fate of the

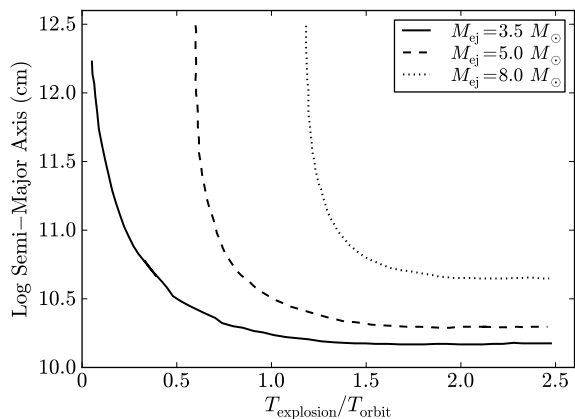


FIG. 1. Semi-major axis versus explosion time for 3 different mass ejecta scenarios:  $3.5 M_{\odot}$  (solid),  $5.0 M_{\odot}$  (dotted),  $8.0 M_{\odot}$  (dashed). The CO core collapse to form a  $1.5 M_{\odot}$  NS (its initial mass is the ejecta mass plus the NS mass), and the companion NS has a mass of  $2.0 M_{\odot}$ . If the explosion were instantaneous, all of our systems with ejecta masses above  $3.5 M_{\odot}$  would be unbound. For explosion times above 1.2 times the orbital time, not only are the systems bound, but the final orbital semi-major axis is less than 10 times the initial separation.

post-explosion binary can be radically altered. For these models, we assumed very close binaries with an initial orbital separation of  $7 \times 10^9$  cm in circular orbits (such close binaries are only formed through a common envelope phase which circularizes the orbit). With CO core radii of  $1-4 \times 10^9$  cm [13], such a separation is small, but achievable. We assume the binary consists of a CO core and a  $2.0 M_{\odot}$  NS companion. When the CO core collapses, it forms a  $1.5 M_{\odot}$  NS, ejecting the rest of the core. We then vary the ejecta mass and time required for most of the ejected matter to move out of the binary. Note that even if 70% of the mass is lost from the system (the  $8 M_{\odot}$  ejecta case), the system remains bound as long as the explosion time is just above the orbital time ( $T_{\text{orbit}} = 180$  s) with semi-major axes of less than  $10^{11}$  cm.

The short orbits (on ejecta timescales) are not the only feature of these binaries that alters the post-explosion orbit. The NS companion accretes both matter and momentum from the SN ejecta, reducing the mass lost from the system with respect to typical binaries with larger orbital separations and much less accretion. In addition, as with common envelope scenarios, the bow shock produced by the accreting NS transfers orbital energy into the SN ejecta. In figure 2, we show the final orbital separation of our same three binaries, including the effects of mass accretion (we assume  $0.5 M_{\odot}$  is accreted with the momentum of the SN material) and orbit coupling (30% of the orbital velocity is lost per orbit). With these effects, not only do the systems remain bound even for explosion times greater than  $1/2$  the orbital period but,

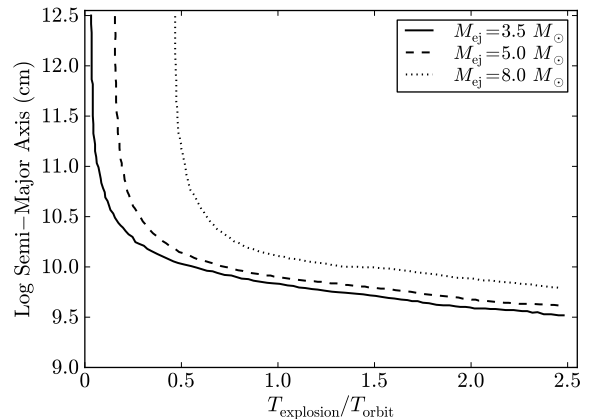


FIG. 2. Semi-major axis versus explosion time for the same 3 binary systems as in figure 1 including mass accretion and momentum effects. Including these effects, all systems with explosion times above 0.7 times the orbital time are bound and the final separations are on par with the initial separations.

if the explosion time is long, the final semi-major axis can be on par with the initial orbital separation.

The tight separation of these binaries facilitates tidal locking and the angular momentum axis of the CO core will be aligned with the orbital angular momentum. For many of the kick mechanisms in the literature, the kick is often aligned with the rotation axis. For example, both in neutrino-driven mechanisms [18, 19] and asymmetric explosions driven by convection [18, 20, 21] the kick is aligned with the rotation axis. However, it is still possible to have some misalignment leading to some eccentricity and “tumbling” of the system with specific signatures in the light curve following the prompt emission of the GRB. Hence, we here consider both kicks aligned with the rotation (and hence orbital) axis as well as random kicks. If the kick is aligned with the orbital plane, the system can remain bound even with kick velocities as high as  $1000 \text{ km s}^{-1}$ . However, if the kick is in the same direction as the star is moving, the systems can be disrupted if the kick is above  $500-700 \text{ km s}^{-1}$  if the accretion phase is longer than an orbital period.

The tight compact binaries produced in these explosions will emit GW emission, ultimately causing the system to merge. For typical massive star binaries, the merger time is many Myr. For BdHNe, the merger time is typically 10,000 y, or less (figure 3).

## GRAVITATIONAL WAVES FROM THE NS-BH BINARY

To better understand the GW signal from these mergers, we study the evolution of the orbital binding energy  $E_b$  up to the merger following the effective one-body

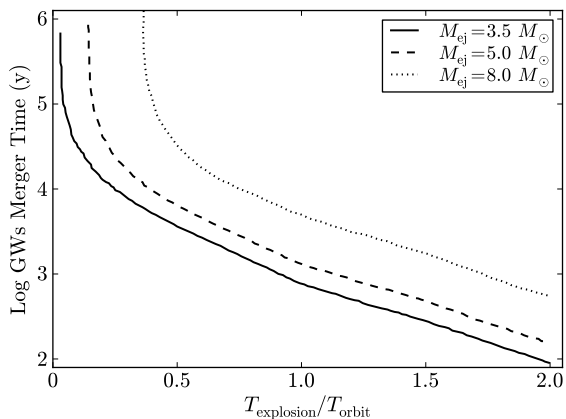


FIG. 3. Merger time due to GW emission as a function of explosion time for the same 3 binary as in figure 1 including mass accretion and momentum effects. Beyond a critical explosion time (0.1–0.6  $T_{\text{orbit}}$  depending on the system), the merger time is less than roughly 10,000 y. For most of our systems, the explosion time is above this limit and we expect most of these systems to merge quickly.

(EOB) formalism [22–25] up to the 4th Post-Newtonian approximation (see Refs. [26, 27] and references therein). We adopt here  $M_{\text{NS}} = 1.5 M_{\odot}$  and  $M_{\text{BH}} = 2.67 M_{\odot}$  [28], the latter corresponding to the critical mass  $M_{\text{crit}}$  of a non-rotating NS obeying the nuclear NL3 equation of state (EOS). Uncertainties in the EOS at supranuclear densities lead to a variety of NS mass-radius relations and consequently to different values of  $M_{\text{crit}}$ , hence of  $M_{\text{BH}}$ . Both rotation [29] and different binary parameters may lead to different amounts of angular momentum transferred to the NS, affecting its mass [30].

In order to assess the detectability of the GW emission by advanced LIGO (aLIGO), we compute the signal-to-noise ratio (SNR), averaged over all sky locations and binary orientations,  $\langle \text{SNR} \rangle$ , generated by the NS-BH spiraling-in binary up to the merger point [27]. Following [31], we adopt as a threshold for the aLIGO detection  $\langle \text{SNR} \rangle = 8$  in a single detector, which implies a GW horizon distance for these NS-BH binaries, which have a chirp mass  $\mathcal{M}_{\text{ch}} = (M_{\text{BH}} M_{\text{NS}})^{3/5} / (M_{\text{BH}} + M_{\text{NS}})^{1/5} \approx 1.73 M_{\odot}$ ,  $d_L \approx 335.4$  Mpc, or  $z \approx 0.075$ , using the maximum possible sensitive reachable by 2022. No BdHN has been up to now detected with such a low redshift. Figure 4 shows, for two sources shown to be consistent with the BdHN picture (GRB 130427A with  $z = 0.34$  [15] and GRB 061121 with  $z = 1.31$  [32]), the GW source amplitude spectral density,  $\sqrt{S_h} = 2|\tilde{h}(f_d)|\sqrt{f_d} = h_c(f_d)/\sqrt{f_d}$ , together with the one-sided ASD of the aLIGO noise,  $\sqrt{S_n}(f_d)$ . Here  $h_c(f_d)$  and  $\tilde{h}(f_d)$  are the characteristic strain and the Fourier transform of the signal and  $f_d$  the frequency of the GWs at the detector. For these sources,  $\langle \text{SNR} \rangle \approx 1.75$  and  $0.45$ , respectively. For an optimally located and polarized source, the SNR could increase by

up to a factor  $\approx 2.26$ , which implies that  $\text{SNR}=8$  could be obtained for a source as far as  $d_L \approx 2.26 \times 335.4$  Mpc  $\approx 758$  Mpc, or  $z \approx 0.160$ . Furthermore, the SNR scales as  $\mathcal{M}_{\text{ch}}^{5/6}$ , so it increases e.g. with larger BH masses. For rotating NS with the NL3 EOS, the maximum value of  $M_{\text{crit}}$  is  $\approx 3.4 M_{\odot}$  [29], which would increase the SNR only by  $\approx 1.1$ . For this largest BH mass, the GW horizon becomes  $d_L \approx 1.1 \times 758$  Mpc  $\approx 834$  Mpc, or  $z \approx 0.174$ . This largest possible GW horizon implies an upper limit of  $\sim 0.03$  detections per year, adopting a BdHN rate of  $1.2 \times 10^{-2} \text{ Gpc}^{-3} \text{ y}^{-1}$  [11].

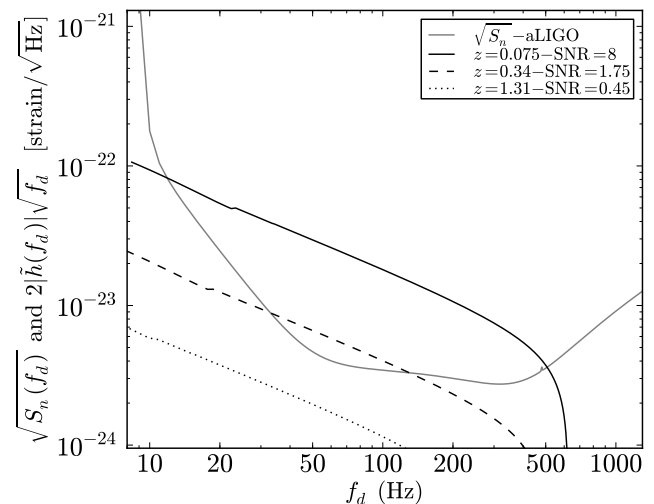


FIG. 4. ASD of the spiraling-in phase up to the merger,  $\sqrt{S_h} = 2|\tilde{h}(f_d)|\sqrt{f_d} = h_c(f_d)/\sqrt{f_d}$ , of the NS-BH binaries produced by two BdHNe, GRB 130427A at redshift  $z = 0.34$  and GRB 061121 at  $z = 1.31$ , compared with the noise ASD of aLIGO,  $\sqrt{S_n}(f_d)$ . We indicate the estimated SNR for these two sources and show the case of the NS-BH binary which would generate a positive detection with  $\text{SNR}=8$ . The binary dynamics is simulated via the EOB formalism up to the 4th Post-Newtonian approximation.

## CONCLUSION

The evolutionary scenario for BdHNe requires much tighter binaries than typically studied in the literature of ultra-stripped binaries and this produces unique features in the end-fate of these systems. The progenitor of this GRB engine begins with two massive stars, in contrast to the one based on a massive core collapsing to a BH [33]. A tight binary is produced after a succession of common envelope phases, producing a CO core near Roche-Lobe overflow orbiting a NS, a subset of the ultra-stripped binaries [5, 6, 34, 35]. Since 0.1–1% of the total SN Ibc are expected to be ultra-stripped binaries [5], we estimate that only 0.005–0.07% of the latter are needed to explain the observed population of BdHNe. The fate of such systems evolves very differently than the standard

picture. The NS can accrete appreciable material in the SN explosion and this accretion causes it to collapse to a BH and form a GRB. However, the tight binary invalidates many of the assumptions about orbital evolution in the SN. The SN explosion does not pass “instantaneously” across the NS, and correcting this assumption alone drastically alters the binary fate. Including the interaction of the orbit and the ejecta further exacerbates these differences, causing these NS-BH to be very different than the systems prediction in standard population synthesis models.

First and foremost, the fraction of the BdHNe that remain bound after the SN explosion is nearly 100% even with large  $\sim 500\text{--}1000 \text{ km s}^{-1}$  kicks imparted during the SN explosion instead of the  $\lesssim 1\%$  in standard scenarios. This means that even if BdHNe are rare, they may dominate the fraction of NS-BH binaries in the Universe. In addition, the merger timescales for these systems are typically  $<10,000 \text{ y}$ , producing a set of rapidly-merging binaries. In view of such a short lifetime due to GW emission, the current number of such events is likely to be comparable with the original rate of long GRBs produced by BdHNe following the IGC paradigm. Because of this rapid merger, the systems are unlikely to travel that far from the site of the SN explosion that formed the GRB. Even with large kicks, we expect these binaries to merge within 10 pc of the BdHNe and we expect the merger to occur within the radius swept clean by the BdHN, giving a characteristic imprint in the GRB emission. In view of the expected paucity of the baryonic contamination around the merger site, it is expected that the characteristic prompt radiation emission time of the GRB produced by these sources be dominated by the general relativistic timescale of the BH,  $GM/c^3 \approx 10^{-4}\text{--}10^{-5} \text{ s}$ , which justifies the attribution of the name of ultrashort GRBs to this new family of events.

Another observational feature of these binaries is that the BHs from these systems are low mass:  $\sim 3\text{--}4 M_{\odot}$ , of the order of the critical mass of rotating NSs [29, 30], instead of the  $5\text{--}10 M_{\odot}$  produced by standard scenarios. However, further accretion of mass and angular momentum from material kept bound into the system after the BdHN process might lead the BH to larger masses and to approach maximal rotation [30]. Although the NS in this NS-BH binary should be rapidly rotating, producing pulsed emission, the short timescale between formation and merger means that it will be difficult to observe such systems through steady pulsed emission. However, if these systems make up a sizable fraction of the NS-BH population, they could be detecting by their GW signal. Although it is difficult to get the exact component masses from aLIGO, evidence [36], or the lack thereof, for binaries with low-mass BHs could support, or limit the rate of, this scenario.

We would like to thank P. Podsiadlowski, T. Tauris

and Y. Suwa for many useful discussions about ultra-stripped binaries. Likewise, we would like to thank D. Arnett and S. O. Kepler for insightful discussions. J. A. R. acknowledges the support by the International Cooperation Program CAPES-ICRANet financed by CAPES Brazilian Federal Agency for Support and Evaluation of Graduate Education within the Ministry of Education of Brazil. F. G. O. acknowledges the support given by the International Relativistic Astrophysics Erasmus Mundus Joint Doctorate Program under the Grant 2012-1710 from EACEA of the European Commission.

- 
- [1] C. L. Fryer, S. E. Woosley, and D. H. Hartmann, *ApJ* **526**, 152 (1999), astro-ph/9904122.
  - [2] M. Dominik, K. Belczynski, C. Fryer, D. E. Holz, E. Berti, T. Bulik, I. Mandel, and R. O’Shaughnessy, *ApJ* **759**, 52 (2012), arXiv:1202.4901 [astro-ph.HE].
  - [3] K. A. Postnov and L. R. Yungelson, *Living Reviews in Relativity* **17**, 3 (2014), arXiv:1403.4754 [astro-ph.HE].
  - [4] G. E. Brown, *ApJ* **440**, 270 (1995).
  - [5] T. M. Tauris, N. Langer, T. J. Moriya, P. Podsiadlowski, S.-C. Yoon, and S. I. Blinnikov, *ApJL* **778**, L23 (2013), arXiv:1310.6356 [astro-ph.SR].
  - [6] T. M. Tauris, N. Langer, and P. Podsiadlowski, *MNRAS* **451**, 2123 (2015), arXiv:1505.00270 [astro-ph.SR].
  - [7] R. Ruffini, C. L. Bianco, F. Frascchetti, S.-S. Xue, and P. Chardonnet, *ApJL* **555**, L117 (2001).
  - [8] R. Ruffini, M. G. Bernardini, and C. L. Bianco et al., in *The Eleventh Marcel Grossmann Meeting*, edited by H. Kleinert, R. T. Jantzen, and R. Ruffini (2008) pp. 368–505.
  - [9] J. A. Rueda and R. Ruffini, *ApJL* **758**, L7 (2012), arXiv:1206.1684 [astro-ph.HE].
  - [10] C. L. Fryer, J. A. Rueda, and R. Ruffini, *ApJ* **793**, L36 (2014), arXiv:1409.1473 [astro-ph.HE].
  - [11] M. Muccino, F. G. Oliveira, J. A. Rueda, R. Ruffini, and et al., to be submitted (2015).
  - [12] D. Guetta and M. Della Valle, *ApJL* **657**, L73 (2007), astro-ph/0612194.
  - [13] Y. Suwa, T. Yoshida, M. Shibata, H. Umeda, and K. Takahashi, *ArXiv e-prints* (2015), arXiv:1506.08827 [astro-ph.HE].
  - [14] J. G. Hills, *ApJ* **267**, 322 (1983).
  - [15] R. Ruffini, Y. Wang, M. Enderli, M. Muccino, M. Kovacevic, C. L. Bianco, A. V. Penacchioni, G. B. Pisani, and J. A. Rueda, *ApJ* **798**, 10 (2015), arXiv:1405.5723 [astro-ph.HE].
  - [16] L. Becerra, F. Cipolletta, C. L. Fryer, J. A. Rueda, and R. Ruffini, *ApJ* **812**, 100 (2015), arXiv:1505.07580 [astro-ph.HE].
  - [17] C. K. Birdsall and A. B. Langdon, *Plasma Physics via Computer Simulation, The Adam Hilger Series on Plasma Physics*, edited by C. Birdsall and A. Langdon. Adam Hilger, Bristol, England (ISBN: 0-07-005371-5) (1991).
  - [18] C. L. Fryer and A. Heger, *ApJ* **541**, 1033 (2000), astro-ph/9907433.
  - [19] C. L. Fryer and A. Kusenko, *ApJS* **163**, 335 (2006), astro-ph/0512033.

- [20] T. Shimizu, S. Yamada, and K. Sato, *ApJL* **432**, L119 (1994).
- [21] C. L. Fryer and M. S. Warren, *ApJ* **601**, 391 (2004), [astro-ph/0309539](#).
- [22] A. Buonanno and T. Damour, *Phys. Rev. D* **59**, 084006 (1999), [gr-qc/9811091](#).
- [23] A. Buonanno and T. Damour, *Phys. Rev. D* **62**, 064015 (2000), [gr-qc/0001013](#).
- [24] T. Damour, P. Jaranowski, and G. Schäfer, *Phys. Rev. D* **62**, 084011 (2000), [gr-qc/0005034](#).
- [25] T. Damour, *Phys. Rev. D* **64**, 124013 (2001), [gr-qc/0103018](#).
- [26] D. Bini and T. Damour, *Phys. Rev. D* **87**, 121501 (2013), [arXiv:1305.4884 \[gr-qc\]](#).
- [27] F. G. Oliveira, J. A. Rueda, and R. Ruffini, *ApJ* **787**, 150 (2014).
- [28] R. Belvedere, D. Pugliese, J. A. Rueda, R. Ruffini, and S.-S. Xue, *Nuclear Physics A* **883**, 1 (2012).
- [29] F. Cipolletta, C. Cherubini, S. Filippi, J. A. Rueda, and R. Ruffini, *Phys. Rev. D* **92**, 023007 (2015), [arXiv:1506.05926 \[astro-ph.SR\]](#).
- [30] L. Becerra, F. Cipolletta, C. L. Fryer, J. A. Rueda, and R. Ruffini, *ArXiv e-prints* (2015), [arXiv:1505.07580 \[astro-ph.HE\]](#).
- [31] LIGO Scientific Collaboration, Virgo Collaboration, J. Aasi, J. Abadie, B. P. Abbott, R. Abbott, T. D. Abbott, M. Abernathy, T. Accadia, F. Acernese, and et al., *ArXiv e-prints* (2013), [arXiv:1304.0670 \[gr-qc\]](#).
- [32] R. Ruffini, L. Izzo, M. Muccino, G. B. Pisani, J. A. Rueda, Y. Wang, C. Barbarino, C. L. Bianco, M. Enderli, and M. Kovacevic, *A&A* **569**, A39 (2014), [arXiv:1404.1840 \[astro-ph.HE\]](#).
- [33] S. E. Woosley and J. S. Bloom, *Ann. Rev. A&A* **44**, 507 (2006), [astro-ph/0609142](#).
- [34] K. Belczyński and V. Kalogera, *ApJL* **550**, L183 (2001), [astro-ph/0012172](#).
- [35] J. D. M. Dewi and O. R. Pols, *MNRAS* **344**, 629 (2003), [astro-ph/0306066](#).
- [36] M. Hannam, D. A. Brown, S. Fairhurst, C. L. Fryer, and I. W. Harry, *ApJL* **766**, L14 (2013), [arXiv:1301.5616 \[gr-qc\]](#).

## ANGULAR MOMENTUM ROLE IN THE HYPERCRITICAL ACCRETION OF BINARY-DRIVEN HYPERNOVAE

L. BECERRA<sup>1,2</sup>, F. CIPOLLETTA<sup>1,2</sup>, CHRIS L. FRYER<sup>3</sup>, JORGE A. RUEDA<sup>1,2,4</sup>, AND REMO RUFFINI<sup>1,2,4</sup>

<sup>1</sup>Dipartimento di Fisica and ICRA, Sapienza Università di Roma, P.le Aldo Moro 5, I-00185 Rome, Italy

<sup>2</sup>ICRANet, P.zza della Repubblica 10, I-65122 Pescara, Italy

<sup>3</sup>CCS-2, Los Alamos National Laboratory, Los Alamos, NM 87545, USA

<sup>4</sup>ICRANet-Rio, Centro Brasileiro de Pesquisas Físicas, Rua Dr. Xavier Sigaud 150, 22290-180 Rio de Janeiro, Brazil

Received 2015 May 27; accepted 2015 September 4; published 2015 October 12

### ABSTRACT

The induced gravitational collapse paradigm explains a class of energetic,  $E_{\text{iso}} \gtrsim 10^{52}$  erg, long-duration gamma-ray bursts (GRBs) associated with Ic supernovae, recently named binary-driven hypernovae. The progenitor is a tight binary system formed of a carbon–oxygen (CO) core and a neutron star (NS) companion. The supernova ejecta of the exploding CO core trigger a hypercritical accretion process onto the NS, which reaches the critical mass in a few seconds, and gravitationally collapses to a black hole, emitting a GRB. In our previous simulations of this process, we adopted a spherically symmetric approximation to compute the features of the hypercritical accretion process. We here present the first estimates of the angular momentum transported by the supernova ejecta,  $L_{\text{acc}}$ , and perform numerical simulations of the angular momentum transfer to the NS during the hyperaccretion process in full general relativity. We show that the NS (1) reaches either the mass-shedding limit or the secular axisymmetric instability in a few seconds depending on its initial mass, (2) reaches a maximum dimensionless angular momentum value,  $[cJ/(GM^2)]_{\text{max}} \approx 0.7$ , and (3) can support less angular momentum than the one transported by supernova ejecta,  $L_{\text{acc}} > J_{\text{NS,max}}$ , hence there is an angular momentum excess that necessarily leads to jetted emission.

*Key words:* gamma-ray burst: general

### 1. INTRODUCTION

We have introduced the concept of induced gravitational collapse (IGC, Ruffini et al. 2008; Rueda & Ruffini 2012) and a family of systems that we have called binary-driven hypernovae (BdHNe, see Ruffini et al. 2014b, and references therein), in order to explain the subfamily of gamma-ray bursts (GRBs) with energies  $E_{\text{iso}} \gtrsim 10^{52}$  erg associated with type Ic supernovae. Within this paradigm, the supernova explosion and the GRB occur in the following time sequence taking place in a binary system composed of a carbon–oxygen (CO) core and a neutron star (NS) companion: (1) explosion of the CO core; (2) hypercritical accretion onto the NS that reaches the critical mass; (3) NS gravitational collapse to a black hole; (4) emission of the GRB. This sequence occurs on short timescales of  $\sim 100$  seconds in the source rest-frame, and it has been verified for several BdHNe with cosmological redshift  $z \leq 1$  (Pisani et al. 2013), all the way up to one of the farthest sources, GRB 090423, at  $z = 8.2$  (Ruffini et al. 2014a).

The first theoretical treatment of the IGC process (Rueda & Ruffini 2012) was based on a simplified model of the binary parameters and on the Bondi–Hoyle accretion formalism. More recently, Fryer et al. (2014) performed the first more realistic numerical simulations of the IGC by using more detailed supernova explosions coupled to hypercritical accretion models from previous simulations of supernova fallback (Fryer et al. 1996; Fryer 2009). The core-collapse of the CO core producing the supernova Ic was simulated in order to calculate realistic profiles for the density and expanding velocity of the supernova ejecta. The hydrodynamic evolution of the material falling into the accretion region of the NS was there followed numerically up to the surface of the NS. The accretion in these systems can proceed at very high rates that exceed by several orders of magnitude the Eddington limit due to the fact that the photons are trapped in the accreting material and the accretion energy is

lost through neutrino emission (see Fryer et al. 2014 and references therein for additional details).

In addition, Fryer et al. (2015b) have shown that BdHNe remain bound even if a large fraction of the binary initial total mass is lost in the explosion, exceeding the canonical 50% limit of mass loss. Indeed, these binaries evolve through the supernova explosion very differently than the compact binary progenitors studied for instance in population synthesis calculations due to the combined effects of (1) the hypercritical accretion onto the NS companion, (2) the explosion timescale comparable to the orbital period, and (3) the bow shock created as the accreting NS plows through the supernova ejecta transfer’s angular momentum, acting as a break on the orbit.

In previous simulations, we adopted a spherically symmetric approximation of the hypercritical accretion process. However, the angular momentum that the supernova ejecta carry, and eventually might transfer to the NS during the accretion process, could play an important role in the evolution and fate of the system. In this work, we give first, in Section 2, an estimate of the angular momentum transported by the part of the supernova ejecta that enters into the gravitational capture region (Bondi–Hoyle surface) of the NS and compute the Bondi–Hoyle accretion rate. In Section 3, we show that the material entering into the Bondi–Hoyle region possesses sufficient angular momentum to circularize around the NS, forming a disk-like structure. We then calculate, in Section 4, the accretion of both matter and angular momentum onto the NS from the matter that have circularized into a disk. The accretion process is assumed to occur from an inner disk radius given by the most bound circular orbit around a rotating NS. We show that, depending upon the initial mass of the NS, the NS might reach either the mass-shedding limit or the secular axisymmetric instability in a short time. In Section 5, we evaluate, instead, the binary parameters for which the accretion onto the NS is not high enough to lead it to its collapse to a BH.

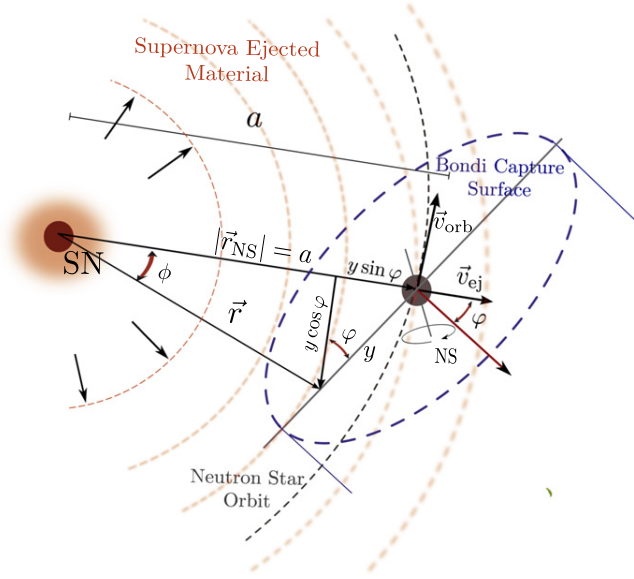


**Figure 1.** Scheme of the IGC scenario: the CO core undergoes SN explosion, the NS accretes part of the SN ejecta and then reaches the critical mass for gravitational collapse to a black hole, with consequent emission of a GRB.

The identification of such parameters defines a dichotomy in the final product of the CO-NS binary which has been recently discussed by Ruffini et al. (2015b): Family-1 long GRBs (i.e., BdHNe) in which the final system is a new NS binary, and Family-2 long GRBs in which an NS-BH binary is produced. Having introduced a typical CO core mass, the most important parameters that define such a dichotomy are the initial NS mass, the NS critical mass for the gravitational collapse to a BH, and the orbital period of the binary. We also discuss a possible evolutionary scenario leading to BdHN systems and compare and contrast our picture with existing binary evolution simulations in the literature. In the final discussion, in Section 6, we summarize the results of this work and, in addition, show that the total angular momentum transported by the supernova ejecta is larger than the maximum angular momentum supported by a maximally rotating NS. Therefore, we advance the possibility that such an excess of angular momentum constitutes a channel for the formation of jetted emission during the hyperaccretion process of BdHNe leading to possible observable non-thermal high-energy emission.

## 2. ANGULAR MOMENTUM TRANSPORTED BY THE SUPERNOVA EJECTA

The accretion rate of the supernova ejecta onto the NS (see Figure 1) can be estimated via the Bondi–Hoyle accretion formula (Hoyle & Lyttleton 1939; Bondi & Hoyle 1944; Bondi 1952):

$$\dot{M}_B(t) = \pi \rho_{\text{ej}} R_{\text{cap}}^2 \sqrt{v_{\text{rel}}^2 + c_{\text{s,ej}}^2}, \quad (1)$$

where  $\rho_{\text{ej}}$  is the density of the supernova ejecta,  $R_{\text{cap}}$  is the gravitational capture radius of the NS

$$R_{\text{cap}}(t) = \frac{2GM_{\text{NS}}(t)}{v_{\text{rel}}^2 + c_{\text{s,ej}}^2}, \quad (2)$$

with  $G$  the gravitational constant,  $M_{\text{NS}}$  the mass of the NS,  $c_{\text{s,ej}}$  the sound speed of the supernova ejecta, and  $v_{\text{rel}}$  the ejecta

velocity relative to the NS ( $v_{\text{rel}} = v_{\text{orb}} - v_{\text{ej}}$ , where  $v_{\text{orb}} = \sqrt{G(M_{\text{core}} + M_{\text{NS}})/a}$  is the orbital velocity of the NS around the CO core, and  $v_{\text{ej}}$  the velocity of the supernova ejecta).

Now, we are in a position to give an estimate of the angular momentum transported by the supernova material to the NS during the IGC process. In doing so, we “extrapolate” the results of Shapiro & Lightman (1976) and Wang (1981) for the accretion process from stellar wind in a binary system. Due to the motion of the material and the orbital motion of NS, see Figure 1, the material falls radially with a velocity  $v_{\text{rel}}$  making an angle  $\varphi$  with respect to the line that joins the stars’ centers of the binary (so,  $\sin \varphi = v_{\text{orb}}/v_{\text{rel}}$ ). Introducing Cartesian coordinates  $(y, z)$  in the plane perpendicular to  $v_{\text{rel}}$  ( $a$ ), and putting the origin on the NS position, the angular momentum per unit time that crosses a surface element  $dydz$  is

$$d^2\dot{L}_{\text{acc}} = \rho_{\text{ej}}(y, z) v_{\text{rel}}(y, z)^2 y \, dydz. \quad (3)$$

To first order in  $y$ ,  $\rho_{\text{ej}}$ , and  $v_{\text{rel}}$  can be written as:

$$\rho_{\text{ej}}(a) \simeq \rho_{\text{ej}}(a)(1 + \epsilon_{\rho}y) \quad \text{and} \quad v_{\text{rel}}(a) \simeq v_{\text{rel}}(a)(1 + \epsilon_{\nu}y), \quad (4)$$

and Equation (3) becomes

$$d^2\dot{L}_{\text{acc}} = \rho_{\text{ej}}(a) v_{\text{rel}}^2(a) [y + (\epsilon_{\rho} + 2\epsilon_{\nu})y^2] \, dydz. \quad (5)$$

Integrating over the area of the circle delimited by the capture radius

$$y^2 + z^2 = R_{\text{cap}}^2 = \left( \frac{2GM_{\text{NS}}}{v_{\text{rel}}^2(a, t)} \right)^2 (1 - 4\epsilon_{\nu}y), \quad (6)$$

where we have applied  $c_{\text{s,ej}} \ll v_{\text{ej}}$ , we obtain the angular momentum per unit time of the ejecta material falling into the gravitational attraction region of the NS

$$\dot{L}_{\text{acc}} = \frac{\pi}{2} \left( \frac{1}{2}\epsilon_{\rho} - 3\epsilon_{\nu} \right) \rho_{\text{ej}}(a, t) v_{\text{rel}}^2(a, t) R_{\text{cap}}^4(a, t). \quad (7)$$

Now, we have to evaluate the terms  $\epsilon_{\rho}$  and  $\epsilon_{\nu}$  of Equation (7). Following Anzer et al. (1987), we start expanding  $\rho_{\text{ej}}(r)$  and  $v_{\text{ej}}$  in Taylor series around the binary separation distance,  $r = a$ :

$$\rho_{\text{ej}}(r, t) \approx \rho_{\text{ej}}(a, t) \left( 1 + \frac{1}{\rho_{\text{ej}}(a, t)} \frac{\partial \rho_{\text{ej}}}{\partial r} \Big|_{(a,t)} \delta r \right), \quad (8)$$

$$v_{\text{ej}}(r, t) \approx v_{\text{ej}}(a, t) \left( 1 + \frac{1}{v_{\text{ej}}(a, t)} \frac{\partial v_{\text{ej}}}{\partial r} \Big|_{(a,t)} \delta r \right), \quad (9)$$

where we assumed  $\delta r = |r - r_{\text{NS}}| \ll 1$ , keeping only the first order terms. For the supernova material, the continuity equation implies

$$\frac{\partial \rho_{\text{ej}}}{\partial t} = -\nabla \cdot (\rho_{\text{ej}} v_{\text{ej}}), \quad (10)$$

and therefore we obtain

$$\epsilon_{\rho} = \left( \frac{\rho'_{\text{ej}}}{\rho_{\text{ej}}} \right)_{(a,t)} \sin \varphi = - \left( \frac{2}{r} + \frac{v'_{\text{ej}}}{v_{\text{ej}}} + \frac{1}{v_{\text{ej}}} \frac{\dot{\rho}_{\text{ej}}}{\rho_{\text{ej}}} \right)_{(a,t)} \sin \varphi. \quad (11)$$

On the other hand, defining  $\hat{x}$  as a unit vector in the direction of  $\mathbf{v}_{\text{rel}}(a)$ , the projection of  $\mathbf{v}_{\text{rel}}(r)$  on  $\hat{x}$  is

$$\hat{x} \cdot \mathbf{v}_{\text{rel}}(r) = v_{\text{ej}} \cos(\phi + \varphi) - v_{\text{orb}} \cos(\pi/2 - \varphi). \quad (12)$$

In the limit when  $\delta r \ll 1$ , also  $\delta r \simeq -y \sin \varphi$  and  $\sin \phi \simeq y/r \cos \phi$  (see Figure 1). Then, the last expression together with Equation (9) becomes

$$\begin{aligned} \hat{x} \cdot \mathbf{v}_{\text{rel}}(r) &\simeq v_{\text{ej}}(a) \cos \varphi + v_{\text{orb}} \sin \varphi \\ &- \left( \frac{v_{\text{ej}}}{r} + \frac{\partial v_{\text{ej}}}{\partial r} \right)_{(a,t)} y \cos \varphi \sin \varphi. \end{aligned} \quad (13)$$

We can write the relative velocity to the NS of the ejected material as

$$\mathbf{v}_{\text{rel}} \simeq \mathbf{v}_{\text{rel}}(a, t) + \delta \mathbf{v}_{\text{rel}}, \quad (14)$$

where

$$\begin{aligned} \delta \mathbf{v}_{\text{rel}} &\simeq \hat{x} \cdot [\mathbf{v}_{\text{rel}}(r) - \mathbf{v}_{\text{rel}}(a)] \\ &= - \left( \frac{v_{\text{ej}}}{r} + \frac{\partial v_{\text{ej}}}{\partial r} \right)_{(a,t)} y \cos \varphi \sin \varphi. \end{aligned}$$

Then, from a simple comparison of Equations (4) and (14), we obtain

$$\epsilon_\nu = - \left( \frac{v_{\text{ej}}}{r} + \frac{\partial v_{\text{ej}}}{\partial r} \right)_{(a,t)} \frac{\cos \varphi \sin \varphi}{v_{\text{rel}}(a)}. \quad (15)$$

In order to integrate Equation (1) and simulate the hypercritical accretion onto the NS, we need to implement a model for the supernova explosion from which we determine the velocity and the density of the ejecta near the capture region of the NS. We shall adopt for expansion of the supernova ejecta, i.e.,

$$v_{\text{ej}}(r, t) = n \frac{r}{t}. \quad (16)$$

Thus, the outermost layer of the ejecta, which we denote hereafter as  $R_{\text{star}}$ , evolves as

$$R_{\text{star}}(t) = R_{0\text{star}} \left( \frac{t}{t_0} \right)^n, \quad (17)$$

where  $t_0 > 0$  is the initial time of the accretion process and  $n$  is the so-called *expansion parameter* whose value depends on the hydrodynamical evolution of the ejecta and the circumstellar material, i.e.,  $n = 1$  corresponds to a free expansion,  $n > 1$  an accelerated expansion, and  $n < 1$  a decelerated one.

The condition of homologous expansion give us the density profile evolution (see Cox 1968 for details):

$$\rho_{\text{ej}}(X, t) = \rho_{\text{ej}}(X, t_0) \frac{M_{\text{env}}(t)}{M_{\text{env}}(t_0)} \left( \frac{R_{0\text{star}}}{R_{\text{star}}(t)} \right)^3 \quad X \equiv \frac{r}{R_{\text{star}}}, \quad (18)$$

where  $M_{\text{env}}(t)$  is the mass expelled from the CO core in the supernova explosion, and hence available to be accreted by the NS, and  $\rho_{\text{ej}}(X, t_0)$  is the density profile of the outermost layers of the CO core (i.e., a pre-supernova profile). Fryer et al. (2014) considered the density profile for three different low-metallicity stars with initial zero-age main-sequence (ZAMS) masses of  $M_{\text{ZAMS}} = 15, 20,$  and  $30 M_\odot$  using the *Kepler* stellar evolution code (Woosley et al. 2002). The CO envelope of such pre-

**Table 1**  
Properties of the Pre-supernova CO Cores

Progenitor $M_{\text{ZAMS}} (M_\odot)$	$\rho_{\text{core}}$ ( $\text{g cm}^{-3}$ )	$R_{\text{core}}$ (cm)	$M_{\text{env}}$ ( $M_\odot$ )	$R_{0\text{star}}$ (cm)	$m$
15	$3.31 \times 10^8$	$5.01 \times 10^7$	2.079	$4.49 \times 10^9$	2.771
20	$3.02 \times 10^8$	$7.59 \times 10^7$	3.89	$4.86 \times 10^9$	2.946
30	$3.08 \times 10^8$	$8.32 \times 10^7$	7.94	$7.65 \times 10^9$	2.801

**Note.** The CO cores are obtained for the low-metallicity ZAMS progenitors with  $M_{\text{ZAMS}} = 15, 20,$  and  $30 M_\odot$  of Woosley et al. (2002). The central iron core is assumed to have a mass  $M_{\text{Fe}} = 1.5 M_\odot$ , which will be the mass of the new NS formed out of the supernova process.

supernova configurations can be well approximated by a power law (see Figure 2 in Fryer et al. 2014):

$$\rho_{\text{ej}}(r, t_0) = \rho_{\text{core}} \left( \frac{R_{\text{core}}}{r} \right)^m, \quad \text{for } R_{\text{core}} < r \leq R_{0\text{star}}, \quad (19)$$

where the parameters are shown in Table 1.

In the accretion process, the NS baryonic mass evolves as

$$M_b(t) = M_b(t_0) + M_B(t), \quad (20)$$

and, in general, its total mass, which includes the gravitational binding energy, evolves as

$$\dot{M}_{\text{NS}} = \frac{\partial M_{\text{NS}}}{\partial M_b} \dot{M}_b + \frac{\partial M_{\text{NS}}}{\partial J_{\text{NS}}} \dot{J}_{\text{NS}} \quad (21)$$

where  $J_{\text{NS}}$  is the NS total angular momentum. The relation between  $M_b$  and  $M_{\text{NS}}$  for a rotating NS fully including the effects of rotation in general relativity, as well as other NS properties, are shown in the [appendix](#).

Taking into account the NS gravitational binding and considering the relations (2), (16), and (18), Equation (1) becomes

$$\frac{\dot{\mu}_B}{(1 - \chi \mu_B) M_{\text{NS}} (M_b)^2} = \frac{t_0}{\tau_B} \frac{\tau^{n(m-3)}}{\hat{r}^m} \left[ 1 + \eta \left( \frac{\hat{r}}{\tau} \right)^2 \right]^{-3/2}, \quad (22)$$

with

$$\tau \equiv \frac{t}{t_0}, \quad \mu_B \equiv \frac{M_B(\tau)}{M_{\text{NS}}(\tau = 1)}, \quad \hat{r} \equiv 1 - \frac{R_B}{a}.$$

The parameters  $\chi$ ,  $\eta$ , and  $\tau_B$  depend on the properties of the binary system before the SN explosion:

$$\begin{aligned} \tau_B &\equiv \frac{M_{\text{NS}}(\tau = 1) v_{\text{orb}}^3}{4\pi G^2 \rho_{\text{ej}}(a, \tau = 1)}, \quad \chi \equiv \frac{M_{\text{NS}}(\tau = 1)}{M_{\text{env}}(\tau = 1)}, \\ \eta &\equiv \left( \frac{n}{t_0} \frac{a}{v_{\text{orb}}} \right)^2. \end{aligned}$$

For the homologous explosion model adopted to describe the expansion dynamics of the ejecta, the parameters  $\epsilon_\rho$  and  $\epsilon_\nu$ ,

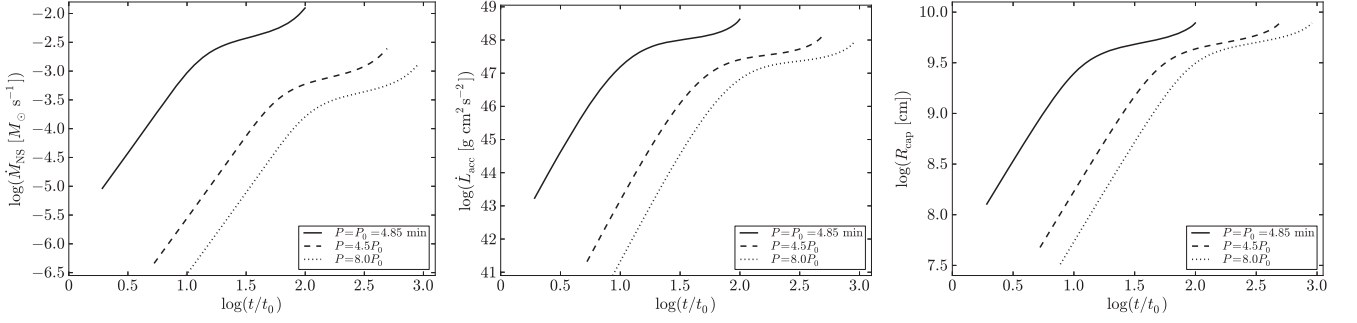


**Figure 2.** Time evolution of the mass accretion rate (left panel, in units of  $M_{\odot} \text{ s}^{-1}$ ), the angular momentum per unit time transported by the supernova ejecta (central panel, in units  $\text{g cm}^2 \text{ s}^{-2}$ ), and the Bondi–Hoyle capture radius of the NS (right panel, in units of  $10^9 \text{ cm}$ ).

using Equations (18) and (19), are given by

$$\begin{aligned} \epsilon_{\rho}(t) &= \frac{m}{a} \frac{v_{\text{orb}}}{v_{\text{rel}}(a, t)}, \\ \epsilon_{\nu}(t) &= \frac{2}{a} \left( \frac{v_{\text{ej}}}{v_{\text{rel}}(a, t)} \right)^2 \frac{v_{\text{orb}}}{v_{\text{rel}}(a, t)}. \end{aligned} \quad (23)$$

Replacing the above equations in Equation (7), the angular momentum per unit time transported by the ejecta crossing the capture region is

$$\begin{aligned} \dot{L}_{\text{acc}} &= 8\pi \rho_{\text{core}} \left( \frac{R_{\text{core}}}{a} \right)^m \\ &\times \frac{GM_{\text{NS}}(t_0) a^2}{(1+q)^3} H(\tau), \end{aligned} \quad (24)$$

where

$$\begin{aligned} H(\tau) &= \tau^{n(m-3)} \left( \frac{M_{\text{NS}}(\tau)}{M_{\text{NS}}(\tau=1)} \right)^4 (1 - \chi\mu_B) \\ &\times \left( 1 + \frac{\eta}{\tau^2} \right)^{-7/2} \left( \frac{m}{2} + \frac{6\eta}{\tau^2 + \eta} \right). \end{aligned}$$

Thus, we can write the specific angular momentum:

$$l_{\text{acc}} = \frac{\dot{L}_{\text{acc}}}{\dot{M}_B} = 2 \sqrt{\frac{GM_{\text{NS}}(\tau=1)a}{(1+q)^3}} G(\tau), \quad (25)$$

where

$$G(\tau) = \hat{r}^m \left( \frac{M_{\text{NS}}(\tau)}{M_{\text{NS}}(\tau=1)} \right)^2 \left( 1 + \frac{\eta}{\tau^2} \right)^{-3} \left( \frac{m}{2} + \frac{6\eta}{\tau^2 + \eta} \right).$$

Figure 2 shows the time evolution of the Bondi–Hoyle accretion rate, obtained from the numerical integration of Equation (22), and of the angular momentum transported by the ejecta, obtained from Equation (7). In these simulations, we have adopted, for the sake of example, the  $M_{\text{ZAMS}} = 30 M_{\odot}$  CO progenitor, an expansion parameter  $n = 1$ , a supernova ejecta velocity  $v_{0,\text{star}} = 2 \times 10^9 \text{ cm s}^{-1}$ , and an initial NS mass,  $M_{\text{NS}}(t_0) = 2.0 M_{\odot}$ . Following Fryer et al. (2014), we adopt binary parameters such that there is no Roche lobe overflow prior to the supernova explosion. For the above CO core and NS parameters, such a condition implies a minimum binary orbital period of  $P_0 = 4.85 \text{ min}$ .

In order to visualize the dynamics of the process, we show in Figure 3 the velocity field of the supernova ejecta at selected

times of the accretion process onto the NS. To produce this figure, we compute the SN velocity field considering just the effect of the NS gravitational attraction on the SN ejecta taking into account the changes in the NS position,  $\mathbf{r}_{\text{NS}}(t)$ , due to its own orbital motion and the evolution of the NS mass,  $M_{\text{NS}}(t)$ , estimated by the Bondi accretion formalism. The SN matter is seeing as a set of point-like particles, so the trajectory of each particle was followed by solving the Newtonian equation of motion:

$$\frac{d^2 \mathbf{r}_{\text{sn}}(t)}{dt^2} = -GM_{\text{NS}}(t) \frac{\mathbf{r}_{\text{sn}}(t) - \mathbf{r}_{\text{NS}}(t)}{|\mathbf{r}_{\text{sn}}(t) - \mathbf{r}_{\text{NS}}(t)|^3}, \quad (26)$$

setting as the reference frame the initial center of mass of the binary system. The simulation goes from time  $t = t_0$  until the collapse of the NS. The initial conditions for each SN particle come from the homologous velocity distribution, assuming a free expansion.

### 3. CIRCULARIZATION OF THE SUPERNOVA EJECTA AROUND THE NS

We turn now to the determination of whether or not the supernova ejecta possess enough angular momentum to circularize around the NS before being accreted by it. Since, initially, the NS is slowly rotating or non-rotating, we can describe the exterior spacetime of the NS before the accretion process by the Schwarzschild metric. A test-mass particle circular orbit of radius  $r_{\text{st}}$  possesses in this metric a specific angular momentum given by

$$l_{\text{st}} = c \sqrt{\frac{GM_{\text{NS}} r_{\text{st}}}{c^2} \left( 1 - \frac{3GM_{\text{NS}}}{c^2 r_{\text{st}}} \right)^{-1/2}}. \quad (27)$$

Assuming that there are no angular momentum losses once the ejected material enters the NS capture region, hence  $l_{\text{st}} = l_{\text{acc}} = \dot{L}_{\text{acc}}/\dot{M}_B$ , the material circularizes around the NS at the radii:

$$r_{\text{st}} = \frac{1}{2} \left[ \frac{l_{\text{acc}}^2}{GM_{\text{NS}}} + \sqrt{\left( \frac{l_{\text{acc}}^2}{GM_{\text{NS}}} \right)^2 - 12 \left( \frac{l_{\text{acc}}}{c} \right)^2} \right]. \quad (28)$$

$y$ -circular orbit around a non-rotating NS is located at a distance  $r_{\text{mb}} = 6GM_{\text{NS}}/c^2$  with an angular momentum per unit mass  $l_{\text{mb}} = 2\sqrt{3} GM_{\text{NS}}/c$ . The most bound circular orbit,  $r_{\text{mb}}$ , is located outside the NS surface for masses larger than  $1.57 M_{\odot}$ ,  $1.61 M_{\odot}$ , and  $1.68 M_{\odot}$  for the GM1, TM1, and NL3 equation of

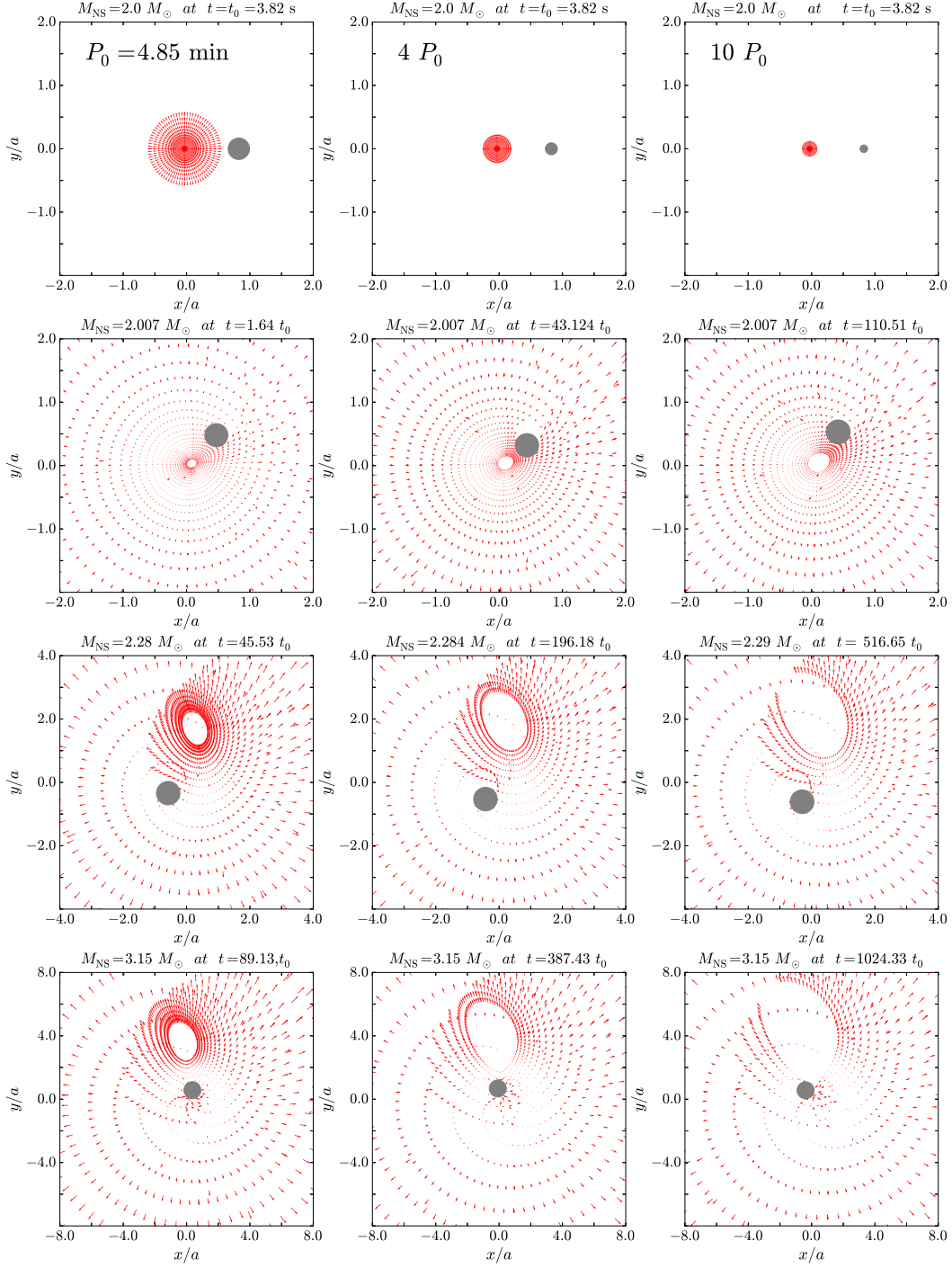


**Figure 3.** Supernova ejecta velocity field at selected times of the accretion process onto the NS. This set of images shows visibly the increase of mass of the NS as a function of time and manifestly evidence the physical reason why, as recently shown by Fryer et al. (2015b), contrary to the canonical supernova explosion occurring in binary progenitors studied in population synthesis calculations, BdHNe remain bound even if a large fraction of the binary system’s mass is lost in the explosion (i.e., well above the canonical 50% limit of mass loss). The reason is first, the hypercritical accretion onto the NS companion alters both the mass and momentum of the binary; second, the explosion timescale is comparable with the orbital period, hence the mass ejection cannot be assumed to be instantaneous; and finally, the bow shock created as the accreting NS plows through the supernova ejecta transfers angular momentum, acting as a break on the orbit. In the simulation represented in these snapshots, we have adopted the  $M_{\text{ZAMS}} = 30 M_{\odot}$  CO progenitor (see Table 1 for the corresponding pre-supernova CO core properties), an expansion parameter  $n = 1$ , an ejecta outermost layer velocity  $v_{\text{0star}} = 2 \times 10^9 \text{ cm s}^{-1}$ , and an initial NS mass,  $M_{\text{NS}}(t = t_0) = 2.0 M_{\odot}$ . We adopt binary parameters such that there is no Roche lobe overflow prior to the supernova explosion (Fryer et al. 2014), which imply for the present binary parameters a minimum orbital period of  $P_0 = 4.85$  minute. In the left, central, and right columns, we show the results for binary periods  $P = P_0, 4P_0,$  and  $10P_0$ , respectively. The Bondi–Hoyle surface, the filled gray circle, increases as the evolution continues mainly due to the increase of the NS mass. The  $x$ – $y$  positions refer to the center-of-mass reference frame. The last image in each column corresponds to the instant when the NS reaches the critical mass value. For the initial conditions of these simulations, the NS ends its evolution at the mass-shedding limit with a maximum value of the angular momentum  $J = 6.14 \times 10^{49} \text{ g cm}^2 \text{ s}^{-1}$  (or  $j_{\text{NS}} \approx 7$ ), and a corresponding critical mass of  $M_{\text{crit}}^{J=0} = 3.15 M_{\odot}$  (see, also, Figures 4 and 5).

state (EOS), respectively F. Cipolletta et al. (2015, in preparation). It is easy to check (see Figure 2) that the supernova ejected material has an angular momentum larger than this value, and therefore the ejecta entering into the NS capture region will necessarily circularize at radii  $r_{\text{st}} > r_{\text{mb}}$ . We have obtained from our simulations,  $r_{\text{st}}/r_{\text{mb}} \sim 10\text{--}10^3$ .

Even if the supernova ejecta possess enough angular momentum to form a disk around the NS, which would prevent it from falling rapidly onto the NS, the viscous forces (and other angular momentum losses) might allow the material to be accreted by the NS when it arrives at the inner boundary of the disk. In the  $\alpha$ -disk formalism, the kinetic viscosity is  $\nu = \eta/\rho = \alpha c_{s,\text{disk}} H$ , where  $\eta$  is the dynamical viscosity,  $H$  the disk scale height, and  $c_{s,\text{disk}}$  the sound velocity of the disk. Following Chevalier (1993), the infall time in a disk at radius  $r$  is

$$t_{\text{fall}} \sim \frac{r_{\text{st}}^2}{\alpha c_{s,\text{disk}} H} \sim \frac{r_{\text{st}}^{3/2}}{\alpha \sqrt{GM_{\text{NS}}}} \sqrt{1 - \frac{2GM_{\text{NS}}}{c^2 r_{\text{st}}}}, \quad (29)$$

where it is assumed that  $H \sim r_{\text{st}}$  (thick disk) and  $c_{s,\text{disk}}$  of the order of orbital velocity seen by an observer corotating with the particle. Finally,  $\alpha \sim 0.01\text{--}0.1$  is dimensionless and measures the viscous stress. In our simulations, we have obtained falling times  $t_{\text{fall}}/\Delta_{\text{acc}} \sim 10^{-3}$ , where  $\Delta_{\text{acc}}$  is the characteristic accretion time. Therefore, the supernova material can be accreted by the NS in a short time interval without introducing any significant delay.

With even a mild amount of angular momentum, this accretion drives a strong outflow along the axis of angular momentum (Fryer et al. 2006; Fryer 2009), ejecting up to 25% of the infalling material, removing much of the angular momentum. The ejecta may undergo rapid neutron capture producing  $r$ -process elements (Fryer et al. 2006). As the angular momentum increases, we expect the outflows to become more collimated, which might very well lead to the long sought explanation of the high-energy power-law MeV emission observed in the Episode 1 of BdHNe (see, e.g., Sections 5 and 7 in Izzo et al. 2012; Sections 3.2 and 3.3 in Ruffini et al. 2013; Ruffini & Izzo 2015a).

Much more work is needed to determine if there are any observation implications of these expelled materials.

#### 4. SPIN-UP OF THE NS AND REACHING OF THE INSTABILITY REGION

Our first estimate of the angular momentum transported by the supernova ejecta has shown that the materials have enough angular momentum to circularize around the NS for a short time and form a kind of thick disk. The viscous force torques in the disk (and other possible losses) allow a sufficient angular momentum loss until the material arrives at the inner boundary of the disk,  $R_{\text{in}}$ , then falling into the NS surface. Thus, from angular momentum conservation, the evolution of the NS angular momentum,  $J_{\text{NS}}$ , will be given by

$$\frac{dJ}{dt} = \xi l(R_{\text{in}}) \frac{dM_{\text{B}}}{dt} \quad (30)$$

where  $\xi$  is an efficiency angular momentum transfer parameter. In order to follow the NS spin-up during the accretion process, this equation must be integrated simultaneously with Equation (22). In Equation (30), the value of  $l(R_{\text{in}})$  corresponds to

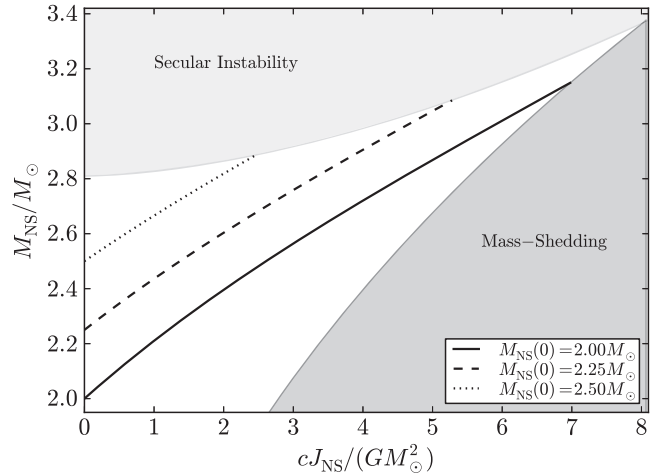


**Figure 4.** Neutron star mass as a function of its angular momentum gain for a selected efficient parameter  $\xi = 0.5$ . Three evolutionary paths of the NS are shown, each starting from a different initial NS mass  $M_{\text{NS}}(t = 0) = 2.0, 2.25,$  and  $2.5 M_{\odot}$ , and without loss of generality we have adopted the NL3 nuclear EOS.

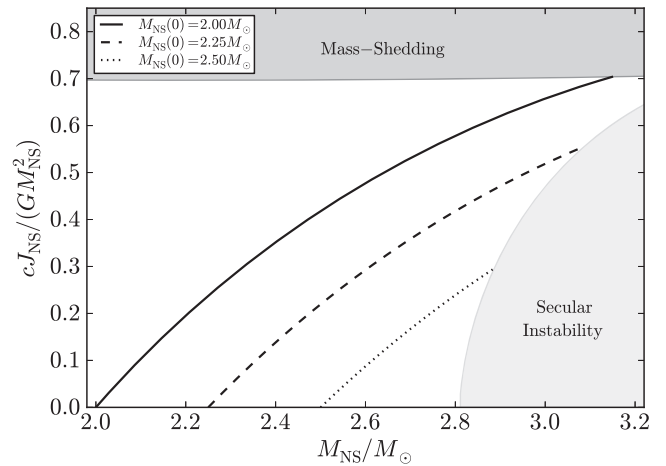


**Figure 5.** Dimensionless angular momentum gain of the NS as a function of the NS mass for a selected efficiency parameter  $\xi = 0.5$ . Three evolutionary paths of the NS are shown, each starting from a different initial NS mass  $M_{\text{NS}}(t = 0) = 2.0, 2.25,$  and  $2.5 M_{\odot}$ , and without loss of generality we have adopted the NL3 nuclear EOS.

the angular momentum of the mostly bound circular orbit, which for the axially symmetric exterior spacetime around the rotating NS can be written as (F. Cipolletta et al. 2015, in preparation):

$$l_{\text{mb}} = \frac{GM_{\text{NS}}}{c} \left[ 3.464 - 0.37 \left( \frac{J_{\text{NS}}}{M_{\text{NS}}} \right)^{0.85} \right]. \quad (31)$$

In Figure 4, we show the evolution of the NS mass as a function of its angular momentum during the accretion process for a selected efficiency parameter for the NS angular momentum rate,  $\xi = 0.5$ , and for selected values of the initial NS mass,  $M_{\text{NS}}(t = 0) = 2.0, 2.25,$  and  $2.5 M_{\odot}$ . We see how the NS starting with  $M_{\text{NS}}(t = 0) = 2.0 M_{\odot}$  reaches the mass-shedding limit while, for higher initial masses, the NS ends at the secular axisymmetric instability region.

Correspondingly, we show in Figure 5 the time evolution of the dimensionless angular momentum of the NS,  $cJ_{\text{NS}}/(GM_{\text{NS}}^2)$ ,

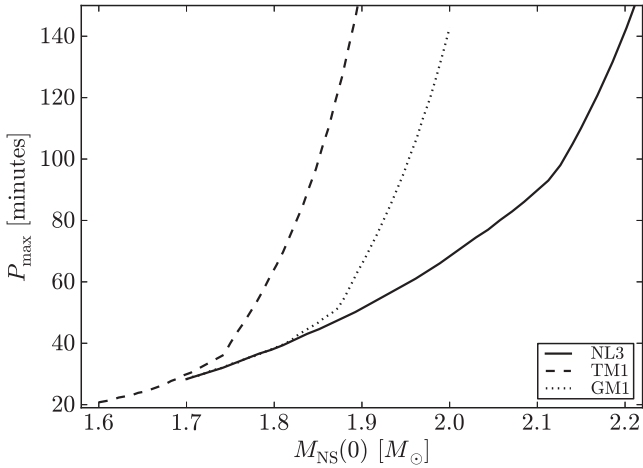


**Figure 6.** Maximum binary period for which the NS with initial mass  $M_{\text{NS}}(0)$  collapses to a BH, for three selected EOS.

as a function of the NS mass, in the case of an efficiency of angular momentum transfer to the NS  $\xi = 0.5$ . In line with the above result of Figure 4, we see here that only the NS that ends at the mass-shedding limit, i.e., the one with an initial mass  $M_{\text{NS}}(t=0) = 2.0 M_{\odot}$ , reaches the maximum possible value of the dimensionless angular momentum,  $cJ_{\text{NS}}/(GM_{\text{NS}}^2) \approx 0.7$ . The NSs with higher initial masses become secularly unstable with lower angular momentum.

#### 5. FAMILY-1 AND FAMILY-2 LONG GRBs AND THE EVOLUTIONARY SCENARIO

We have until now evidenced the binary parameters for which a new NS-BH binary system is produced out of the BdHNe. There exist limiting binary parameters leading to lower accretion rates onto the NS and to a total accreted matter not sufficient to bring the NS to the gravitational collapse to a BH, namely, not sufficient to reach the NS critical mass. The identification of such limiting parameters introduces a dichotomy in the final product of the CO-NS binary, with consequent different observational signatures, which have been recently discussed by Ruffini et al. (2015b): Family-1 long GRBs (BdHNe) in which the NS does not collapse to a BH, and the final system being a new NS binary; and Family-2 long GRBs (BdHNe) in which the NS collapses to a BH, leading to a new NS-BH binary.

Since we expect the accretion rate to become lower for wider (longer binary period) binaries, there must be a maximum binary period (of course having fixed the other system parameters, i.e., initial NS mass, CO core mass, and supernova velocity), which defines the aforementioned families' dichotomy. Therefore, we performed simulations increasing the binary period, starting from the minimum value  $P_0$ , for given  $M_{\text{NS}}(0)$ ,  $M_{\text{CO}}$ , and  $v_{0,\text{star}}$ . Figure 6 shows the results of the maximum binary period  $P_{\text{max}}$  for which we obtained a collapse to a BH of the NS companion, as a function of its initial mass,  $M_{\text{NS}}(0)$ , keeping the other binary parameters fixed. The results are shown for three selected nuclear EOS of the NS (NL3, TM1 and GM1). In particular, for the system, we have used as an example in the above figures, namely  $M_{\text{NS}}(0) = 2 M_{\odot}$ ,  $M_{\text{CO}} = 9.4 M_{\odot}$  ( $M_{\text{ZAMS}} = 30 M_{\odot}$ , see Table 1), and  $v_{0,\text{star}} = 2 \times 10^9 \text{ cm s}^{-1}$ , we obtained  $P_{\text{max}} \approx 73$  minute, for the NL3 EOS. Since the two other EOS (TM1 and GM1) lead

**Table 2**  
Critical Mass and Corresponding Radius for Selected Parameterizations of Nuclear EOS

EOS	$M_{\text{crit}}^{J=0}$ ( $M_{\odot}$ )	$R_{\text{crit}}^{J=0}$ (km)	$M_{\text{max}}^{J=0}$ ( $M_{\odot}$ )	$R_{\text{max}}^{J=0}$ (km)	$p$	$k$	$f_k$ (kHz)
NL3	2.81	13.49	3.38	17.35	1.68	0.006	1.34
GM1	2.39	12.56	2.84	16.12	1.69	0.011	1.49
TM1	2.20	12.07	2.62	15.98	1.61	0.017	1.40

**Note.** In the last column, we have also reported the rotation frequency of the critical mass configuration in the rotating case. This value corresponds to the frequency of the last configuration along the secular axisymmetric instability line, i.e., the configuration that intersects the Keplerian mass-shedding sequence.

**Reference.** Cipolletta et al. (2015).

to lower values of the critical NS mass with respect to the NL3 EOS (see Table 2 and Cipolletta et al. 2015), the maximum orbital period to have BH formation is longer for the same initial NS mass.

With the knowledge of the proper set of parameters for which the gravitational collapse of the NS to a BH is induced by accretion, and consequently, also the parameters for which such a process does not occur, it becomes appropriate to discuss the possible progenitors of such binaries. A possible evolutionary scenario was discussed by Rueda & Ruffini (2012), taking advantage of the following facts: (1) a viable progenitor for BdHN systems is represented by X-ray binaries such as Cen X-3 and Her X-1 (Schreier et al. 1972; Tananbaum et al. 1972; Wilson 1972; Leach & Ruffini 1973; Gursky & Ruffini 1975; Rawls et al. 2011); (2) evolution sequences for X-ray binaries, and evolution scenarios leading to systems in which two SN events occur during their life, had been already envisaged (see, e.g., Nomoto & Hashimoto 1988; Iwamoto et al. 1994). Thus, BdHNe could form following the evolution of an initial binary system composed of two main-sequence stars,  $M_1$  and  $M_2$ , with a mass ratio  $M_2/M_1 \gtrsim 0.4$ . Star 1 is likely  $M_1 \gtrsim 11 M_{\odot}$ , leaving an NS through a first core-collapse event. Star 2, now with  $M_2 \gtrsim 11 M_{\odot}$  after some almost conservative mass transfer, evolves filling its Roche lobe. It then starts a spiral-in of the NS into the envelope of star 2, i.e., a common-envelope phase occurs. If the binary system survives to this common-envelope phase, namely it does not merge, it will be composed of a helium star and an NS in tight orbit. The helium star then expands filling its Roche lobe and a non-conservative mass transfer to the NS, takes place. After loosing its helium envelope, the above scenario naturally leads to a binary system composed of a CO star and a massive NS whose fate has been discussed in the present work.

The above evolutionary path advanced by Rueda & Ruffini (2012), see Figure 7, is in agreement with the recent results of Tauris et al. (2015), who performed simulations of the evolution of a helium core in a tight binary with an NS companion. The helium envelope is stripped-off during the evolution as a result of both mass-loss and binary interactions and at the end it might lead to an SN of type Ib or Ic in the presence of the NS companion. Their simulations show the possibility of having binaries with orbital periods as short as  $\sim 50$  minute at the moment of the SN explosion. However, they were interested in the so-called ultra-stripped SNe and therefore they explored systems with helium stars of low initial masses

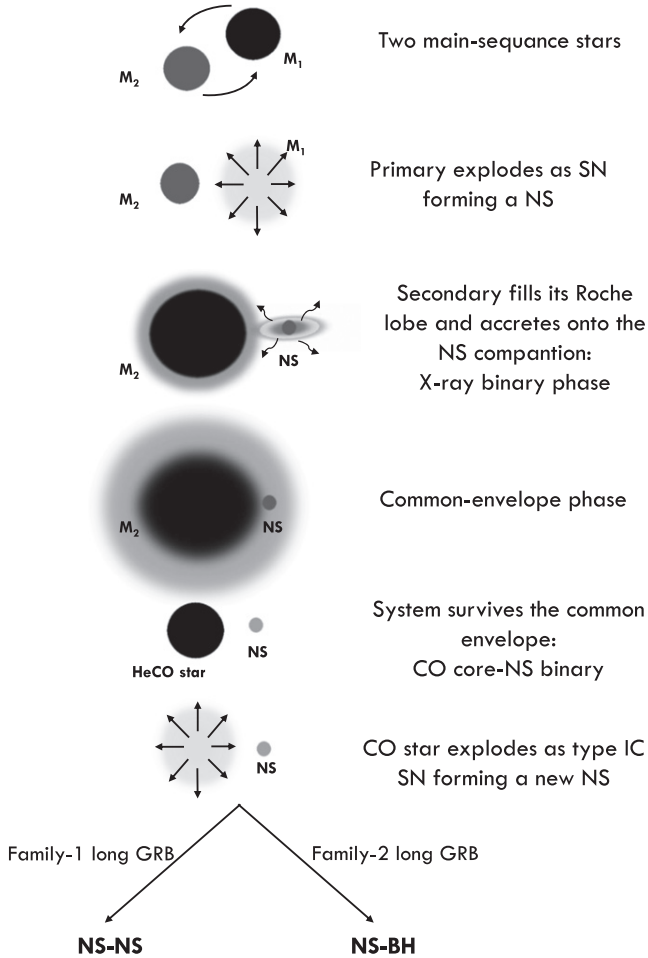


**Figure 7.** Scheme of a possible evolutionary scenario leading to BdHNe as outlined in Rueda & Ruffini (2012).

$M_{\text{He}} = 2.5\text{--}3.0 M_{\odot}$ , less massive than the ones we expect for the CO cores in BdHNe.

Besides comparing the value of the pre-SN core mass, it is also instructive to compare the radii we have assumed for the pre-SN CO core with the ones obtained by Tauris et al. (2015). For example, they obtained a radius of the metal core of the  $\approx 3 M_{\odot}$  helium star forming initially a binary of orbital period 0.1 day with an NS companion of  $1.35 M_{\odot}$ , is  $R \approx 0.024 R_{\odot}$ . The most similar case we can compare with, corresponds to the CO core formed by the  $M_{\text{ZAMS}} = 15 M_{\odot}$  progenitor (see Table 1),  $M_{\text{CO}} \approx 3.5 M_{\odot}$ , for which we have adopted a radius of  $\approx 4.5 \times 10^9 \text{ cm} \approx 0.06 R_{\odot}$ . This radius is  $\approx 2.5$  times larger than the above  $3 M_{\odot}$  helium star of Tauris et al. (2015). This implies that our assumption (Fryer et al. 2014) that, due to the three to four orders of magnitude of pressure jump between the CO core and helium layer, the star will not expand significantly when the helium layer is removed, seems to be appropriate. As we discussed in Fryer et al. (2014), differences of  $\sim 2$  in the value of the radius could be due to the different binary interaction ingredients as well as to subtleties of the numerical codes, e.g., between the MESA and the KEPLER codes.

On the other hand, the relatively long possible orbital periods we have obtained (with respect to our minimum value  $P_0$ ) to have BH formation weakens the role of the precise value of the

CO core radius on the accretion process and the final fate of the system. If the radius of the CO core is  $N$  times the radius of the core of the system with  $P = P_0$ , then the evolution of the system will be approximately the one of a system with orbital period  $P = N^{3/2} P_0$ . For example, we have adopted a radius  $R_{\text{CO}} \approx 7.7 \times 10^9 \text{ cm} \approx 0.1 R_{\odot}$  for the CO core with mass  $M_{\text{CO}} \approx 9.4 M_{\odot}$  (see Table 1), and thus a minimum orbital period (to have no Roche lobe overflow) of  $P_0 \approx 5$  minute, if it forms a binary with a  $2 M_{\odot}$  NS companion. The maximum value of the orbital period for which we obtained BH formation for those mass parameters was  $P_{\text{max}} \approx 73$  minute (for the NL3 EOS), which would imply that even with a CO core  $\approx 15^{2/3} \approx 6$  times larger, BH formation would occur. Despite this fact, the precise value of the CO core mass and radius depends on the binary interactions, hence on the evolutionary path followed by the system; therefore, it is appropriate to compute the binary evolution proposed in this work to confirm or improve our estimates for the CO core masses and radii.

## 6. CONCLUSIONS

We have first computed the angular momentum transported by the supernova ejecta expanding in the tight CO core-NS binary system progenitor of BdHNe. We have shown that the angular momentum of the ejecta is high enough to circularize, although for a short time, around the NS forming a kind of thick disk. We have then simulated the process of accretion onto the NS of the supernova ejecta falling into the Bondi–Hoyle region and forming the disk-like structure around the NS. We have computed both the evolution of the NS mass and angular momentum assuming that the material falls onto the NS surface from an inner disk radius position given by the mostly bound circular orbit around the NS. The properties of the mostly bound orbit, namely binding energy and angular momentum, have been computed in the axially symmetric case with full rotational effects in general relativity. We have computed the changes of these properties in a dynamical fashion accounting for the change of the exterior gravitational field due to the increasing NS mass and angular momentum.

In Figure 3, we have shown a set of snapshots of our simulation of the velocity field of the supernova ejecta falling into the NS. It is evident from the evolution the increase of size of the Bondi–Hoyle gravitational capture region of the NS with time due to the increase of the NS mass. It becomes also manifestly evident why, as shown by Fryer et al. (2015b), contrary to the canonical supernova explosion occurring in binary progenitors studied in population synthesis calculations, BdHNe remain bound even if a large fraction of the binary system’s mass is lost in the explosion. Indeed, they might exceed the canonical 50% limit of mass loss without being disrupted. This impressive result is the combined result of (1) the hypercritical accretion onto the NS companion which alters both the mass and momentum of the binary, (2) the explosion timescale which is on par with the orbital period, hence the mass ejection cannot be assumed to be instantaneous, and (3) the bow shock created, as the accreting NS plows through the supernova ejecta, transfers angular momentum acting as a break on the orbit.

We have shown that the fate of the NS depends on its initial mass: for example, we have seen how an NS with an initial mass  $M_{\text{NS}}(0) = 2.0 M_{\odot}$  reaches the mass-shedding limit, while for higher initial masses, e.g.,  $2.5 M_{\odot}$ , the NS ends at the secular axisymmetric instability limit (see Figure 4). Only

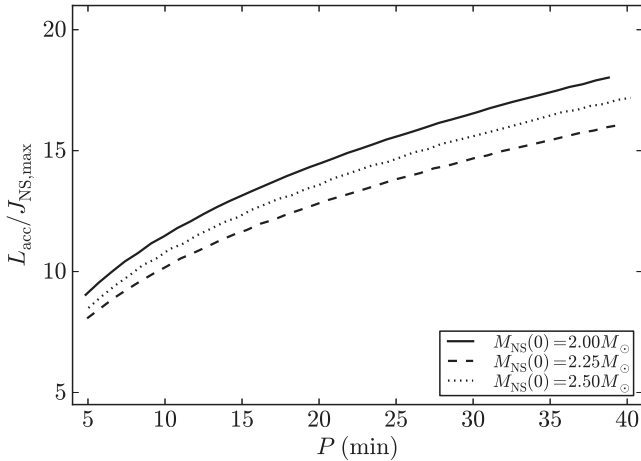


**Figure 8.** Ratio between the total angular momentum transported by the ejecta circularized around the NS and the maximum angular momentum of the NS when it reaches the instability point, for the NL3 EOS.

those NSs reaching the mass-shedding limit are spun-up up to the maximum value of the angular momentum,  $J_{\text{NS,max}} \approx 0.7G(M_{\text{crit}}^{J=0})^2/c$  (see Figure 5). Since the NS dimensionless angular momentum reaches a maximum value  $< 1$ , the new black hole formed out of the gravitational collapse of the NS is initially not maximally rotating. Further accretion of mass and angular momentum from material kept bound into the system after the BdHNe process might lead the black hole to approach maximal rotation; however it is out of the scope of this work to explore such a possibility and will be the subject of a forthcoming publication.

We can compute the total angular momentum transported by the supernova ejecta material,  $L_{\text{acc}}$ , by integrating the angular momentum per unit time  $\dot{L}_{\text{acc}}$  during the entire time interval of the accretion process up to the point when the NS reaches the instability region. If we compare the value of  $L_{\text{acc}}$  with the maximum possible angular momentum that an NS can support,  $J_{\text{NS,max}}$ , we reach the most important conclusion of this work: since  $L_{\text{acc}} > J_{\text{NS,max}}$ , see Figure 8, there is an excess of angular momentum in the system that might give rise to jetted emission in BdHNe with possible high-energy signatures.

We have explored the fate of the system for increasing the orbital period and as a function of the initial NS mass, for a fixed typical CO core mass. We have shown that, as expected, there exists a maximum orbital period,  $P_{\text{max}}$ , over which the NS does not accrete enough mass to become a BH. Despite the fact that this could be seen as an expected result, it has been quite unexpected, as shown in Figure 6, that the orbital period does not need to be as short as  $\sim 5$  minutes in order to produce the collapse of the NS to a BH. Indeed, for  $M_{\text{NS}0} = 2 M_{\odot}$  the orbital period can be as long as 73 minutes, for the NL3 EOS. Clearly, the value of  $P_{\text{max}}$  increases for lower values of the critical mass of the NS, i.e., the softer the EOS the longer the maximum orbital period up to which BH formation occurs, and vice versa. As discussed by Ruffini et al. (2015b), the existence of  $P_{\text{max}}$  and the precise value of the NS critical mass define a dichotomy in the long GRBs associated with SNe (BdHNe), namely two long GRB families with different observational signatures: Family-1 long GRBs in which a BH is not produced, and Family-2 long GRBs in which a BH is produced. The relative rate of Family-2 long GRBs with

respect to Family-1 long GRBs can give us crucial information on the value of the NS critical mass, hence on the stiffness of the nuclear EOS; and thus population synthesis analyses leading to theoretically inferred rates of events are needed to unveil this important information (see, e.g., Ruffini et al. 2014c; Fryer et al. 2015a, for the complementary case of short GRBs). As a first starting point toward such an analysis, we have discussed a possible evolutionary scenario leading to tight CO core-NS binaries (see Figure 7).

To conclude, in this work, we have advanced the first estimates of the role of the angular momentum transported by the supernova ejecta into the final fate of the NS companion in a BdHNe. In order to keep the problem tractable and to extract the main features of these complex systems, we have adopted a series of approximations. (1) We have applied the Bondi–Hoyle–Lyttleton formalism to compute the accretion rate onto the NS; BdHNe are time-varying systems that might challenge the validity of this framework which is valid for steady-state systems (see Edgar 2004 and references therein). (2) We have adopted Taylor series expansions of the supernova ejecta density and velocity around the NS under the assumption that the Bondi–Hoyle radius is small in comparison with the binary separation; this has to be considered a first order solution to the problem since for the conditions of BdHNe we have  $R_{\text{cap}} \sim 0.01\text{--}0.1 a$ . (3) We have adopted an homologous expansion model for the supernova ejecta that could lead to the suspicion of producing artificially higher accretion rates onto the NS due to the low-velocity inner layers of the ejecta. However, we have already shown (see Figure 3 in Fryer et al. 2014) that the homologous model leads to an accretion process lasting for a longer time with respect to more realistic explosion models, but with lower accretion rates such that the time-integrated accretion rate leads to a lower amount of accreted material by the NS. The reason for this is that, in a given time interval, some of the low-velocity ejecta do not have enough time to reach the gravitational capture region of the NS. (4) We have adopted some characteristic values for the homologous expansion parameter of the supernova ejecta ( $n = 1$ ), for the initial velocity of the outermost supernova ejecta layer ( $v_{0,\text{star}} = 2 \times 10^9 \text{ cm s}^{-1}$ ), for the efficiency of the angular momentum transfer from the circularized matter to the NS ( $\xi = 0.5$ ). Thus, a systematic analysis of simulations exploring the entire possible range of the above parameters as well as full 2D and/or 3D of the supernova explosion and accretion in BdHNe are required in order to validate and/or improve our results.

J.A.R. acknowledges the support by the International Cooperation Program CAPES-ICRANet financed by CAPES, Brazilian Federal Agency for Support and Evaluation of Graduate Education within the Ministry of Education of Brazil.

## APPENDIX NS STRUCTURE

The contents of this appendix are based on the recent work of Cipolletta et al. (2015). The interior and exterior metric of a uniformly rotating NS can be written in the form of the stationary axisymmetric spacetime metric

$$ds^2 = -e^{2\nu} dt^2 + e^{2\psi} (d\phi - \omega dt)^2 + e^{2\lambda} (dr^2 + r^2 d\theta^2), \quad (32)$$

where  $\nu$ ,  $\psi$ ,  $\omega$ , and  $\lambda$  depend only on variables  $r$  and  $\theta$ . It is useful to introduce the variable  $e^\psi = r \sin(\theta) B e^{-\nu}$ , being again  $B = B(r, \theta)$ . The energy–momentum tensor of the NS interior is given by

$$T^{\alpha\beta} = (\varepsilon + P)u^\alpha u^\beta + P g^{\alpha\beta}, \quad (33)$$

where  $\varepsilon$  and  $P$  denote the energy density and pressure of the fluid, and  $u^\alpha$  is the fluid 4-velocity. Thus, with the metric given by Equation (32) and the energy–momentum tensor given by Equation (33), one can write the field equations as (setting  $\zeta = \lambda + \nu$ ):

$$\begin{aligned} \nabla \cdot (B \nabla \nu) &= \frac{1}{2} r^2 \sin^2 \theta B^3 e^{-4\nu} \nabla \omega \cdot \nabla \omega \\ &+ 4\pi B e^{2\zeta - 2\nu} \left[ \frac{(\varepsilon + P)(1 + v^2)}{1 - v^2} + 2P \right], \end{aligned} \quad (34)$$

$$\nabla \cdot (r^2 \sin^2 \theta B^3 e^{-4\nu} \nabla \omega) = -16\pi r \sin \theta B^2 e^{2\zeta - 4\nu} \frac{(\varepsilon + P)v}{1 - v^2}, \quad (35)$$

$$\nabla \cdot (r \sin(\theta) \nabla B) = 16\pi r \sin \theta B e^{2\zeta - 2\nu} P, \quad (36)$$

$$\begin{aligned} \zeta_{,\mu} &= - \left\{ (1 - \mu^2) \left( 1 + r \frac{B_{,r}}{B} \right) \right. \\ &+ \left. \left[ \mu - (1 - \mu^2) \frac{B_{,r}}{B} \right]^2 \right\}^{-1} \\ &\times \left[ \frac{1}{2} B^{-1} \left\{ r^2 B_{,rr} - \left[ (1 - \mu^2) B_{,\mu} \right]_{,\mu} - 2\mu B_{,\mu} \right\} \right. \\ &\times \left. \left\{ -\mu + (1 - \mu^2) \frac{B_{,\mu}}{B} \right\} \right. \\ &+ r \frac{B_{,r}}{B} \left[ \frac{1}{2} \mu + \mu r \frac{B_{,r}}{B} + \frac{1}{2} (1 - \mu^2) \frac{B_{,\mu}}{B} \right] \\ &+ \frac{3}{2} \frac{B_{,\mu}}{B} \left[ -\mu^2 + \mu (1 - \mu^2) \frac{B_{,\mu}}{B} \right] \\ &- (1 - \mu^2) r \frac{B_{,\mu r}}{B} \left( 1 + r \frac{B_{,r}}{B} \right) \\ &- \mu r^2 (\nu_{,r})^2 - 2(1 - \mu^2) r \nu_{,\mu} \nu_{,r} \\ &+ \mu (1 - \mu^2) (\nu_{,\mu})^2 - 2(1 - \mu^2) r^2 B^{-1} B_{,r} \nu_{,\mu} \nu_{,r} \\ &+ (1 - \mu^2) B^{-1} B_{,\mu} \left[ r^2 (\nu_{,r})^2 - (1 - \mu^2) (\nu_{,\mu})^2 \right] \\ &+ (1 - \mu^2) B^2 e^{-4\nu} \left\{ \frac{1}{4} \mu r^4 (\omega_{,r})^2 + \frac{1}{2} (1 - \mu^2) r^3 \omega_{,\mu} \omega_{,r} \right. \\ &- \frac{1}{4} \mu (1 - \mu^2) r^2 (\omega_{,\mu})^2 + \frac{1}{2} (1 - \mu^2) r^4 B^{-1} B_{,r} \omega_{,\mu} \omega_{,r} \\ &- \frac{1}{4} (1 - \mu^2) r^2 B^{-1} B_{,\mu} \\ &\left. \left. \times \left[ r^2 (\omega_{,r})^2 - (-\mu^2) (\omega_{,\mu})^2 \right] \right\} \right], \end{aligned} \quad (37)$$

where, in the equation for  $\zeta_{,\mu}$ , we introduced  $\mu \equiv \cos(\theta)$ .

We can integrate numerically the above Einstein equations once a relation between  $\varepsilon$  and  $P$  is given, namely an EOS. The NS interior is made of a core and a crust. The core of the star

has densities higher than the nuclear value,  $\rho_{\text{nuc}} \approx 3 \times 10^{14} \text{ g cm}^{-3}$ , and it is composed of a degenerate gas of baryons (e.g., neutrons, protons, hyperons) and leptons (e.g., electrons and muons). The crust, in its outer region ( $\rho \leq \rho_{\text{drip}} \approx 4.3 \times 10^{11} \text{ g cm}^{-3}$ ), is composed of ions and electrons, and in the so-called inner crust ( $\rho_{\text{drip}} < \rho < \rho_{\text{nuc}}$ ), there are also free neutrons that drip out from the nuclei. For the crust, we adopt the Baym–Pethick–Sutherland EOS (Baym et al. 1971). For the core, we here adopt modern models based on relativistic mean-field theory, which have Lorentz covariance, intrinsic inclusion of spin, a simple mechanism of saturation for nuclear matter, and they do not violate causality. We use an extension of the formulation of Boguta & Bodmer (1977) with a massive scalar meson (sigma) and two vector meson (omega and rho) mediators, and possible interactions between them.

With the knowledge of the EOS, we can compute equilibrium configurations integrating the above equations for suitable initial conditions, for instance central density and angular momentum (or angular velocity) of the star. Then, after integrating the Einstein equations, properties of the NS can be obtained for the given central density and angular momentum such as the total gravitational mass, the total baryon mass, polar and equatorial radii, moment of inertia, quadrupole moment, etc.

For the present problem of accretion onto the NS, as we have mentioned in Section 2, an important relation to be obtained from the NS equilibrium properties, is the one between the total baryon rest-mass,  $M_{\text{b}}$ , and the gravitational mass,  $M_{\text{NS}}$ , namely the gravitational binding energy of the NS; see Equation (21). For non-rotating configurations, Cipolletta et al. (2015) obtained an EOS-independent relation

$$\frac{M_{\text{b}}}{M_{\odot}} = \frac{M_{\text{NS}}}{M_{\odot}} + \frac{13}{200} \left( \frac{M_{\text{NS}}}{M_{\odot}} \right)^2. \quad (38)$$

For the non-zero angular momentum configurations we are interested in, Cipolletta et al. (2015) obtained

$$\frac{M_{\text{b}}}{M_{\odot}} = \frac{M_{\text{NS}}}{M_{\odot}} + \frac{13}{200} \left( \frac{M_{\text{NS}}}{M_{\odot}} \right)^2 \left( 1 - \frac{1}{130} j_{\text{NS}}^{1.7} \right), \quad (39)$$

where  $j_{\text{NS}} \equiv c J_{\text{NS}} / (G M_{\odot}^2)$ . This formula is accurate within an error of 2% and it correctly generalizes the above Equation (38), approaching it in the limit  $j_{\text{NS}} \rightarrow 0$ .

The NS can accrete mass until it reaches a region of instability. There are two main instability limits for rotating NSs, namely the mass-shedding or Keplerian limit, and the secular axisymmetric instability. Cipolletta et al. (2015) have shown that the critical NS mass along the secular instability line, is approximately given by

$$M_{\text{NS}}^{\text{crit}} = M_{\text{NS}}^{J=0} (1 + k j_{\text{NS}}^p), \quad (40)$$

where the parameters  $k$  and  $p$  depend on the nuclear EOS (see Table 2). These formulas fit the numerical results with a maximum error of 0.45%.

In addition to the above relations, we have used in this work an analytic formula, Equation (31) obtained by F. Cipolletta et al. (2015, in preparation), which gives us the angular momentum of the mostly bound circular orbit around a uniformly rotating NS, as a function of the NS mass and angular momentum. Such a relation has allowed us to perform

the simulations of the evolution of the accreting NS in a semi-analytic fashion, including dynamically the feedback of the increase of the NS mass and angular momentum into the exterior geometry.

## REFERENCES

- Anzer, U., Boerner, G., & Monaghan, J. J. 1987, *A&A*, **176**, 235  
 Baym, G., Pethick, C., & Sutherland, P. 1971, *ApJ*, **170**, 299  
 Boguta, J., & Bodmer, A. R. 1977, *NuPhA*, **292**, 413  
 Bondi, H. 1952, *MNRAS*, **112**, 195  
 Bondi, H., & Hoyle, F. 1944, *MNRAS*, **104**, 273  
 Chevalier, R. A. 1993, *ApJL*, **411**, L33  
 Cipelletta, F., Cherubini, C., Filippi, S., Rueda, J. A., & Ruffini, R. 2015, *PhRvD*, **92**, 023007  
 Cox, J. P. 1968, *Principles of Stellar Structure*, Vol. 1 (New York: Gordon and Breach), 2  
 Edgar, R. 2004, *NewAR*, **48**, 843  
 Fryer, C. L. 2009, *ApJ*, **699**, 409  
 Fryer, C. L., Belczynski, K., Ramirez-Ruiz, E., et al. 2015a, arXiv:1504.07605  
 Fryer, C. L., Benz, W., & Herant, M. 1996, *ApJ*, **460**, 801  
 Fryer, C. L., Herwig, F., Hungerford, A., & Timmes, F. X. 2006, *ApJL*, **646**, L131  
 Fryer, C. L., Oliveira, F. G., Rueda, J. A., & Ruffini, R. 2015b, *PhRvL*, submitted (arXiv: 1505.02809)  
 Fryer, C. L., Rueda, J. A., & Ruffini, R. 2014, *ApJL*, **793**, L36  
 Gursky, H., & Ruffini, R. (ed.) 1975, *Proc. Annual Meeting 48, Neutron Stars, Black Holes and Binary X-ray Sources* (San Francisco, CA)  
 Hoyle, F., & Lyttleton, R. A. 1939, *PCPS*, **35**, 405  
 Iwamoto, K., Nomoto, K., Hoflich, P., et al. 1994, *ApJL*, **437**, L115  
 Izzo, L., Ruffini, R., Penacchioni, A. V., et al. 2012, *A&A*, **543**, A10  
 Leach, R. W., & Ruffini, R. 1973, *ApJL*, **180**, L15  
 Nomoto, K., & Hashimoto, M. 1988, *PhR*, **163**, 13  
 Pisani, G. B., Izzo, L., Ruffini, R., et al. 2013, *A&A*, **552**, L5  
 Rawls, M. L., Orosz, J. A., McClintock, J. E., et al. 2011, *ApJ*, **730**, 25  
 Rueda, J. A., & Ruffini, R. 2012, *ApJL*, **758**, L7  
 Ruffini, R., Bernardini, M. G., Bianco, C. L., et al. 2008, in *The Eleventh Marcel Grossmann Meeting*, ed. H. Kleinert, R. T. Jantzen, & R. Ruffini (Singapore: World Scientific), 368  
 Ruffini, R., Izzo, L., & Bianco, C. L. 2015a, *ARep*, **59**, 626  
 Ruffini, R., Izzo, L., Muccino, M., et al. 2014a, *A&A*, **569**, A39  
 Ruffini, R., Muccino, M., Bianco, C. L., et al. 2014b, *A&A*, **565**, L10  
 Ruffini, R., Muccino, M., Kovacevic, M., et al. 2014c, arXiv:1412.1018  
 Ruffini, R., Rueda, J. A., Barbarino, C., et al. 2013, arXiv:1311.7432  
 Ruffini, R., Wang, Y., Enderli, M., et al. 2015b, *ApJ*, **798**, 10  
 Schreier, E., Levinson, R., Gursky, H., et al. 1972, *ApJL*, **172**, L79  
 Shapiro, S. L., & Lightman, A. P. 1976, *ApJ*, **204**, 555  
 Tananbaum, H., Gursky, H., Kellogg, E. M., et al. 1972, *ApJL*, **174**, L143  
 Tauris, T. M., Langer, N., & Podsiadlowski, P. 2015, *MNRAS*, **451**, 2123  
 Wang, Y.-M. 1981, *AAP*, **102**, 36  
 Wilson, R. E. 1972, *ApJL*, **174**, L27  
 Woosley, S. E., Heger, A., & Weaver, T. A. 2002, *RvMP*, **74**, 1015

## GRB 140619B: A SHORT GRB FROM A BINARY NEUTRON STAR MERGER LEADING TO BLACK HOLE FORMATION

R. RUFFINI<sup>1,2,3,4</sup>, M. MUCCINO<sup>1,2</sup>, M. KOVACEVIC<sup>1,3</sup>, F. G. OLIVEIRA<sup>1,3</sup>, J. A. RUEDA<sup>1,2,4</sup>, C. L. BIANCO<sup>1,2</sup>,

M. ENDERLI<sup>1,3</sup>, A. V. PENACCHIONI<sup>4,5</sup>, G. B. PISANI<sup>1,2</sup>, Y. WANG<sup>1,2</sup>, AND E. ZANINONI<sup>4</sup>

<sup>1</sup>Dip. di Fisica and ICRA, Sapienza Università di Roma, Piazzale Aldo Moro 5, I-00185 Rome, Italy; ruffini@icra.it

<sup>2</sup>ICRANet, Piazza della Repubblica 10, I-65122 Pescara, Italy

<sup>3</sup>Université de Nice Sophia Antipolis, CEDEX 2, Grand Château Parc Valrose, Nice, France

<sup>4</sup>ICRANet-Rio, Centro Brasileiro de Pesquisas Físicas, Rua Dr. Xavier Sigaud 150, Rio de Janeiro, RJ, 22290-180, Brazil

<sup>5</sup>Instituto Nacional de Pesquisas Espaciais, Av. dos Astronautas, 1758, São José dos Campos, SP, 12227-010, Brazil

Received 2014 November 30; accepted 2015 June 15; published 2015 August 4

### ABSTRACT

We show the existence of two families of short gamma-ray bursts (GRBs), both originating from the merger of binary neutron stars (NSs): family-1 with  $E_{\text{iso}} < 10^{52}$  erg, leading to a massive NS as the merged core, and family-2 with  $E_{\text{iso}} > 10^{52}$  erg, leading to a black hole (BH). Following the identification of the prototype GRB 090227B, we present the details of a new example of family-2 short burst: GRB 140619B. From the spectral analysis of the early  $\sim 0.2$  s, we infer an observed temperature  $kT = (324 \pm 33)$  keV of the  $e^+e^-$ -plasma at transparency (P-GRB), a theoretically derived redshift  $z = 2.67 \pm 0.37$ , a total burst energy  $E_{e^+e^-}^{\text{tot}} = (6.03 \pm 0.79) \times 10^{52}$  erg, a rest-frame peak energy  $E_{p,i} = 4.7$  MeV, and a baryon load  $B = (5.52 \pm 0.73) \times 10^{-5}$ . We also estimate the corresponding emission of gravitational waves. Two additional examples of family-2 short bursts are identified: GRB 081024B and GRB 090510, remarkable for its well determined cosmological distance. We show that marked differences exist in the nature of the afterglows of these two families of short bursts: family-2 bursts, leading to BH formation, consistently exhibit high energy emission following the proper-GRB emission; family-1 bursts, leading to the formation of a massive NS, should never exhibit high energy emission. We also show that both the families fulfill an  $E_{p,i}-E_{\text{iso}}$  relation with slope  $\gamma = 0.59 \pm 0.07$  and a normalization constant incompatible with the one for long GRBs. The observed rate of such family-2 events is  $\rho_0 = (2.1_{-1.4}^{+2.8}) \times 10^{-4}$  Gpc<sup>-3</sup> yr<sup>-1</sup>.

*Key words:* gamma-ray burst: general

### 1. INTRODUCTION

The phenomenological classification of gamma-ray bursts (GRBs) based on their prompt emission observed  $T_{90}$  durations defines “long” and “short” bursts which are, respectively, longer or shorter than  $T_{90} = 2$  s (Dezalay et al. 1992; Klebesadel 1992, pp. 161–168; Kouveliotou et al. 1993; Tavani 1998). Short GRBs have been often indicated as originating from binary neutron star (NS) mergers (see, e.g., Goodman 1986; Paczynski 1986; Eichler et al. 1989; Narayan et al. 1991; Meszaros & Rees 1997; Rosswog et al. 2003; Lee et al. 2004; Berger 2014).

An ample literature exists of short GRBs with a measured redshift, isotropic burst energy  $E_{\text{iso}} < 10^{52}$  erg and rest-frame spectral peak energy  $E_{p,i} < 2$  MeV (see, e.g., Berger 2014 and references therein). Thanks to extensive data provided by the *Swift*-XRT instrument (Burrows et al. 2005), it is possible to observe the long lasting X-ray afterglow of these short bursts to identify their host galaxies and to compute their cosmological redshifts. They have been observed in both early- and late-type galaxies with older stellar population ages (see, e.g., Berger 2014 for details), and at systematically larger radial offsets from their host galaxies than long GRBs (Sahu et al. 1997; van Paradijs et al. 1997; Bloom et al. 2006; Troja et al. 2008; Fong et al. 2010; Berger 2011; Kopač et al. 2012). None of these afterglows appears to have the specific power law signature in the X-ray luminosity when computed in the source rest-frame, as found in some long GRBs (see, e.g., Ruffini et al. 2014).

In the meantime, considerable progress has been obtained in the theoretical understanding of the equilibrium configuration of NSs, in their mass–radius relation (see Figure 2 in Section 2), and especially in the theoretical determination of the value of the NS critical mass for gravitational collapse  $M_{\text{crit}}^{\text{NS}}$  (Rotondo et al. 2011; Rueda et al. 2011; Belvedere et al. 2012). This has led to a theoretical value  $M_{\text{crit}}^{\text{NS}} = 2.67 M_{\odot}$  (Belvedere et al. 2012). Particularly relevant to this determination has been the conceptual change of paradigm of imposing global charge neutrality (Belvedere et al. 2012) instead of the traditional local charge neutrality (LCN) still applied in the current literature (see, e.g., Haensel et al. 2007 and references therein).

Similarly, noteworthy progress has been achieved in the determination of the masses of galactic binary pulsars. Of the greatest relevance has been the direct observation of NS masses larger than  $2 M_{\odot}$  (see Antoniadis et al. 2013 and Section 2). In the majority of the observed cases of binary NSs the sum of the NS masses,  $M_1 + M_2$ , is indeed smaller than  $M_{\text{crit}}^{\text{NS}}$  and, given the above determination of the NS critical mass, their coalescence will never lead to a black hole (BH) formation (see Figure 3 in Section 2). This of course offers a clear challenge to the traditional assumption that all short GRBs originate from BH formation (see, e.g., Berger 2014 and references therein).

Motivated by the above considerations, we propose in this article the existence of two families of short GRBs, both originating from NS mergers: the difference between these two families depends on whether the total mass of the merged core

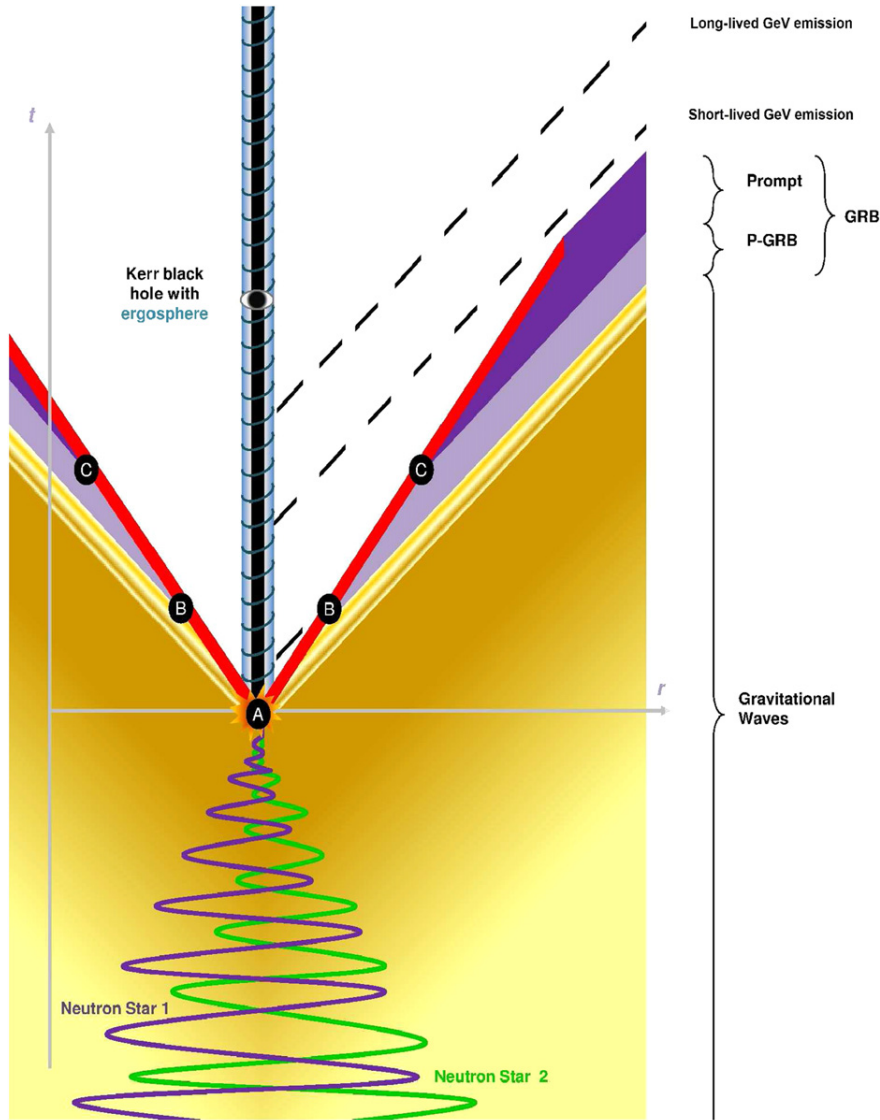


**Figure 1.** Space–time diagram of family-2 short GRBs. The orbital separation between the two NSs decreases due to the emission of GWs, until the merging occurs and a family-2 short GRB is emitted. Following the fireshell model (see Section 3): (A) vacuum polarization occurs while the event horizon is formed and a fireshell of  $e^+e^-$  plasma self-accelerates radially outwards; (B) the fireshell, after engulfing the baryons, keeps self-accelerating and reaches the transparency when the P-GRB is emitted; (C) the accelerated baryons interact with the local CBM giving rise to the prompt emission. The remnant of the merger is a Kerr BH. The accretion of a small (large) amount of orbiting matter onto the BH can lead to the short lived but very energetic 0.1–100 GeV emission observed in GRB 081024B, GRB 090510, and GRB 140619B. The absence of such an emission in GRB 090227B is due to the absence of observations of *Fermi*-LAT.

is smaller or larger than  $M_{\text{crit}}^{\text{NS}}$ . We assume that family-1 coincides with the above mentioned less energetic short GRBs with  $E_{\text{iso}} < 10^{52}$  erg and the coalescence of the merging NSs leads to a massive NS as the merged core. We assume that family-2 short bursts with  $E_{\text{iso}} > 10^{52}$  erg originate from a merger process leading to a BH as the merged core. The presence of the BH allows us to address the GRB nature within the fireshell model (Ruffini et al. 2001a, 2001b, 2001c) leading to specific signatures in the luminosity, spectra and time variability observed in two very different components: the proper-GRB (P-GRB) and the prompt emission (see Section 3). The prototype is GRB 090227B, which we already analyzed within the fireshell model in Muccino et al. (2013). We also assume that the BH gives rise to the short-lived ( $\lesssim 10^2$  s in the observer frame) and very energetic GeV emission which has been found to be present in all these family-2 short GRBs,

when *Fermi*-LAT data are available. This article is mainly dedicated to giving the theoretical predictions and the observational diagnostics to support the above picture.

In Section 4 we recall the results obtained in the case of the prototype of family-2 short GRBs: GRB 090227B (Muccino et al. 2013). The analysis of its P-GRB emission led to a particularly low value of the baryon load,  $B \sim 10^{-5}$ , as well as to the prediction of the distance corresponding to a redshift  $z = 1.61$ , and consequently to  $E_{e^+e^-}^{\text{tot}} = 2.83 \times 10^{53}$  erg. From the analysis of the spectrum and the light curve of the prompt emission we inferred an average circumburst medium (CBM) density  $\langle n_{\text{CBM}} \rangle \sim 10^{-5} \text{ cm}^{-3}$  typical of galactic halos of GRB host galaxies.

In Section 5 we summarize the observations of a second example of such family-2 short bursts, GRB 140619B, and our data analysis from 8 keV up to 100 GeV. We also point out the

lack of any observed X-ray afterglow following the prompt emission (Maselli & D’Avanzo 2014).

In Section 6 we address GRB 140619B within the fireshell model and compare and contrast the results with those of the prototype, GRB 090227B (Muccino et al. 2013). In Section 6.1, from the fireshell equations of motion, we theoretically estimate and predict the value of the redshift of the source,  $z = 2.67 \pm 0.37$ . Consequently, we derive the burst energy  $E_{\text{iso}} > 10^{52}$  erg and the value of the baryon load  $B \sim 10^{-5}$ . In Section 6.2 we infer an average density of the CBM  $\langle n_{\text{CBM}} \rangle \sim 10^{-5} \text{ cm}^{-3}$  from fitting the prompt emission light curve and spectra. This parameter is typical of the galactic halo environment and further confirms a NS–NS merger as the progenitor for GRB 140619B (see Section 6.3 and Figure 1).

In Section 7 we discuss the possibility for Advanced LIGO to detect the emission of gravitational waves (GWs) from such a binary NS progenitor. From the dynamics of the above system, the total energy emitted in GW radiation corresponds to  $E_{\text{GW}}^T = 7.42 \times 10^{52}$  erg, computed during the entire inspiral phase all the way up to the merger. This gives a signal below the sensitivity of the Advanced LIGO interferometer.

In Section 8 we focus on the short-lived ( $\Delta t \approx 4$  s) but significant 0.1–100 GeV emission (see Figure 1). We first address the issue of whether this is a peculiarity of GRB 140619B, or whether the GeV emission can be considered to be a common feature of all these family-2 short GRBs. We first return to GRB 090227B to see how to explain the absence of observations of the GeV emission from this source, and we find a simple reason: GRB 090227B was outside the nominal LAT field of view (FOV, see Ackermann et al. 2013, and Section 4). We then turn our attention to another source, GRB 090510, which presents many of the common features of the family-2 short GRBs. Especially noteworthy is the presence of a high energy GeV emission lasting  $\sim 10^2$  s, much longer than the one of GRB 140619B. The presence of an X-ray afterglow in GRB 090510 is fortunate and particularly important, though lacking a scaling law behavior (Ruffini et al. 2014), since it has allowed the optical identification of the source and the determination of its distance and its cosmological redshift  $z = 0.903$ . The corresponding isotropic energy and intrinsic peak spectral energy are, respectively,  $E_{\text{iso}} > 10^{52}$  erg and  $E_{p,i} = (7.89 \pm 0.76)$  MeV, typical again of family-2 short bursts. We then compare and contrast this high energy emission and their corresponding X-ray emissions in the family-2 short GRB 140619B and GRB 090510 with the afterglow of the family-1 short GRBs (see Figure 13 and Berger 2014).

In Section 9 we give an estimate for the rate of the family-2 short GRBs.

In Section 10 we discuss the existence of the new  $E_{p,i}-E_{\text{iso}}$  relation for all short GRBs introduced by Zhang et al. (2012) and Calderone et al. (2015), with a power-law similar to the one of the Amati relation (Amati et al. 2008) for long GRBs, but with a different amplitude. Finally we draw our conclusions.

## 2. MOTIVATION FROM GALACTIC BINARY NS AND NS THEORY

Recent theoretical progress has been achieved in the understanding of the NS equation of state and equilibrium configuration and of the value of its critical mass  $M_{\text{crit}}^{\text{NS}}$ . In Rotondo et al. (2011) it has been shown to be impossible to

impose the LCN condition on a self-gravitating system of degenerate neutrons, protons, and electrons in  $\beta$ -equilibrium within the framework of relativistic quantum statistics and the Einstein–Maxwell equations. The equations of equilibrium of NSs, taking into account strong, weak, electromagnetic, and gravitational interactions in general relativity and the equilibrium conditions based on the Einstein–Maxwell–Thomas–Fermi equations along with the constancy of the general relativistic Fermi energies of particles, the “Klein potentials,” throughout the configuration have been presented in Rueda et al. (2011) and Belvedere et al. (2012), where a theoretical estimate of  $M_{\text{crit}}^{\text{NS}} \approx 2.67 M_{\odot}$  has been obtained. The implementations of the above results by considering the equilibrium configurations of slowly rotating NSs by using the Hartle formalism has been presented in Belvedere et al. (2014a). Then in Rueda et al. (2014) a detailed study was made of the transition layer between the core and crust of NSs at the nuclear saturation density, and its surface tension and Coulomb energy have been calculated. A comprehensive summary of these results for both static and uniformly rotating NSs is discussed in Belvedere et al. (2014b). The absolute upper limit on the angular momentum of a rotating NS fulfilling the above microscopical conditions has been obtained in Cipolletta et al. (2015).

A vast number of tests have been performed in fitting the data of pulsars (Deneva et al. 2012; Lattimer 2012; Antoniadis et al. 2013; Kramer 2014). In particular, the high value of the recently measured mass of PSR J0348+0432,  $M = (2.01 \pm 0.04) M_{\odot}$  (Antoniadis et al. 2013), favors stiff nuclear equations of state, like the one adopted in Belvedere et al. (2012) based on relativistic nuclear mean field theory à la Boguta & Bodmer (1977), which leads to the above theoretical estimate of  $M_{\text{crit}}^{\text{NS}}$  (see also Figure 2). This value is supported by the above observational constraints, and in any case, is well below the absolute upper limit of  $3.2 M_{\odot}$  for a non-rotating NS (Rhoades & Ruffini 1974).

If we turn to the binary NSs within our Galaxy (see Figure 3) we notice that only in a subset of them is the total mass of the components larger than  $M_{\text{crit}}^{\text{NS}}$  and can lead to a BH in their merging process.<sup>6</sup>

Given this general understanding, we have identified the characteristic properties of family-2 short bursts, whose prototype was identified in GRB 090227B (Muccino et al. 2013). Equally important has been the identification of the observed characteristic features of family-1 short GRBs which will be discussed in the following sections.

<sup>6</sup> During the refereeing process, an approach by Fryer et al. (2015) based on a combination of binary NS merger nuclear physics models and population synthesis appeared. They infer that for a maximum nonrotating NS mass of  $M_{\text{crit}}^{\text{NS}}$  above 2.3–2.4  $M_{\odot}$ , less than 4% of the NS mergers produces short GRBs by gravitational collapse to a BH. Here we go one step further by indicating the theoretical predictions characterizing short GRBs originating from the massive NS formation (family-1) and the ones originating from BH formation (family-2). We indicate: (a) the specific spectral features, (b) the presence of the GeV emission originating from the BH, and (c) the fulfillment of the  $E_{p,i}-E_{\text{iso}}$  relation (see Zhang et al. 2012; Calderone et al. 2015, and Section 10). The paper by Fryer et al. (2015) was followed by Lawrence et al. (2015) where the authors examine the value of  $M_{\text{crit}}^{\text{NS}}$  for a family of equations of state and concluded that a reasonable fraction of double NS mergers may produce neither short GRBs nor BHs. Here we again go one step further by indicating that in the case of a merged core with a mass smaller than  $M_{\text{crit}}^{\text{NS}}$  leading to a massive NS, a less energetic short GRB with a softer emission tail indeed occurs (family-1 short bursts). We show also that these short GRBs fulfill the above  $E_{p,i}-E_{\text{iso}}$  relation (see Section 10).

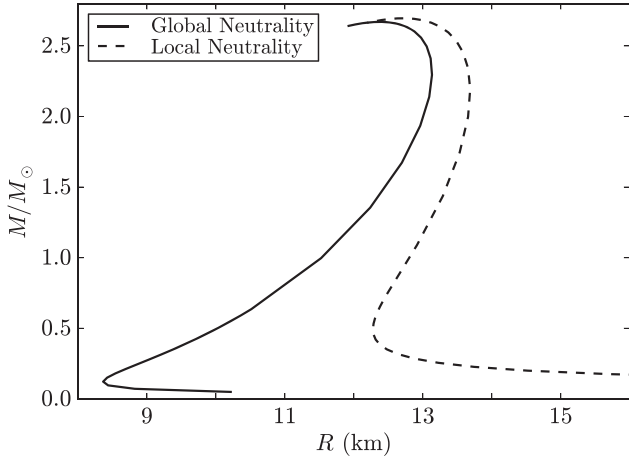


**Figure 2.** Mass–radius relation obtained with the local and the new global neutrality equilibrium configurations, by applying the NL3 nuclear model. Figure reproduced from Belvedere et al. (2012).

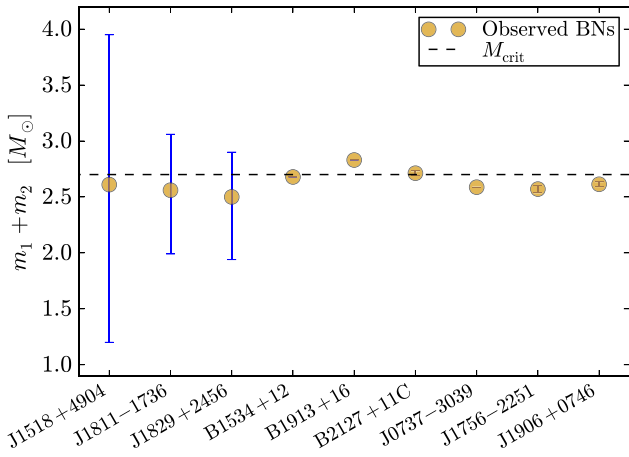


**Figure 3.** Plot of the binary NSs with known total masses ( $M_1 + M_2$ , in solar masses) and the corresponding uncertainties. The horizontal dashed line marks the critical NS mass of  $2.67 M_\odot$  (Belvedere et al. 2012). Systems beyond this value lead to BH formation. Masses taken from Zhang et al. (2011) and Antoniadis (2014).

The crucial role of  $M_{\text{crit}}^{\text{NS}}$  has been also shown in the corresponding analysis of long GRBs in distinguishing between the two different families (Ruffini et al. 2015) in the induced gravitational collapse paradigm (Izzo et al. 2012a; Rueda & Ruffini 2012; Fryer et al. 2014).

### 3. THE FIRESHELL MODEL

It is well known that the majority of the astrophysical community working on GRBs envisages the spectral and temporal analysis of both short and long GRBs considering their whole emission as a single event (see, e.g., Ackermann et al. 2013). This picture follows the conceptual framework of the “fireball model” (see, e.g., Sari et al. 1998; Piran 2005; Meszaros 2006, and reference therein).

The “fireshell model” (Ruffini et al. 2001a, 2001b, 2001c) has instead addressed a specific time-resolved spectral analysis leading to distinct signatures and to the identification of different astrophysical regimes within the same GRB (see, e.g., Izzo et al. 2010; Izzo et al. 2012b; Muccino et al. 2013; Ruffini et al. 2013 and references therein). This has led to introduction

of the concept of binary mergers of NS–NS and of FeCO–NS together with a set of new paradigms in order to describe the complexity of GRB phenomena within a “Cosmic-Matrix” approach (Ruffini 2015a).

In the fireshell model (Ruffini et al. 2001a, 2001b, 2001c) GRBs originate from an optically thick  $e^+e^-$  plasma (Damour & Ruffini 1975; Ruffini & Xue 2008; Ruffini et al. 2010) during the gravitational collapse to a BH. Such an  $e^+e^-$  plasma is confined to an expanding shell and reaches thermal equilibrium almost instantaneously (Aksenov et al. 2007). The annihilation of these pairs occurs gradually, while the expanding shell, called the *fireshell*, self-accelerates up to ultra relativistic velocities (Ruffini et al. 1999) and engulfs the baryonic matter (of mass  $M_B$ ) left over in the process of collapse. The baryon load thermalizes with the pairs due to the large optical depth (Ruffini et al. 2000).

Assuming spherical symmetry of the system, the dynamics in the optically thick phase is fully described by only two free initial parameters: the total energy of the plasma  $E_{e^+e^-}^{\text{tot}}$  and the baryon load  $B$  (Ruffini et al. 2000). Only solutions with  $B \leq 10^{-2}$  are characterized by regular relativistic expansion; for  $B \geq 10^{-2}$  turbulence and instabilities occur (Ruffini et al. 2000). The fireshell continues to self-accelerate until it reaches the transparency condition and a first flash of thermal radiation, the P-GRB, is emitted (Ruffini et al. 2001b). The radius  $r_{\text{tr}}$  at which the transparency occurs, the theoretical temperature (blueshifted toward the observer  $kT_{\text{blue}}$ ), the Lorentz factor  $\Gamma_{\text{tr}}$ , as well as the amount of the energy emitted in the P-GRB are functions of  $E_{e^+e^-}^{\text{tot}}$  and  $B$  (see, e.g., Ruffini et al. 2001b; Ruffini et al. 2009, and Figure 4).

After transparency, the residual expanding plasma of leptons and baryons collides with the CBM giving rise to multi-wavelength emission: the prompt emission. Assuming the fully radiative condition, the structures observed in the prompt emission of a GRB are described by two quantities associated with the environment: the CBM density profile  $n_{\text{CBM}}$ , which determines the temporal behavior of the light curve, and the fireshell surface filling factor  $\mathcal{R} = A_{\text{eff}}/A_{\text{vis}}$ , in which  $A_{\text{eff}}$  is the effective emitting area of the fireshell, and  $A_{\text{vis}}$  is its total visible area (Ruffini et al. 2002, 2005). This second parameter takes into account the inhomogeneities in the CBM and its filamentary structure (Ruffini et al. 2004).

The emission process of the collision between the baryons and the CBM is described in the comoving frame of the shell as a modified blackbody (BB) spectrum. This spectrum is obtained by the introduction of an additional phenomenological parameter  $\alpha$  which characterizes the departure of the slope of the low energy part of the comoving spectrum from the purely thermal one (see Patricelli et al. 2012, for details). The nonthermal spectral shape of the observed GRB is then produced by the convolution of a very large number of modified thermal spectra with different temperatures and different Lorentz and Doppler factors. This convolution is performed over the surfaces of constant arrival time for photons at the detector (EquiTemporal Surfaces, EQTS, Bianco & Ruffini 2005a, 2005b), encompassing the total observation time. The observed hard-to-soft spectral variation comes out naturally from the decrease with time of the comoving temperature and of the bulk Lorentz  $\Gamma$  factor. This effect is amplified by the curvature effect due to the EQTS which produces the observed time lag in the majority of the GRBs.

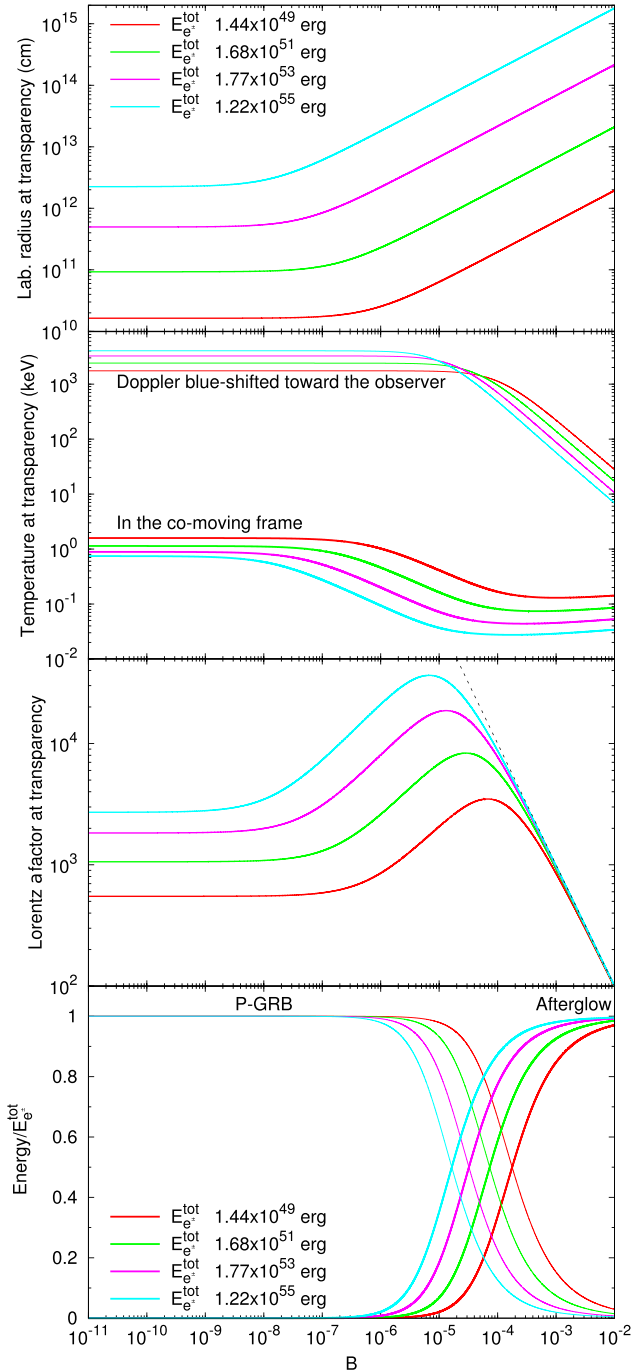


**Figure 4.** Main quantities of the fireshell model at transparency for selected values of  $E_{e^+e^-}^{\text{tot}}$ : the radius in the laboratory frame, the temperatures of the plasma in the co-moving frame and blueshifted toward the observer, the Lorentz  $\Gamma$  factor, and the fraction of energy radiated in the P-GRB and in the prompt emission as functions of  $B$ .

The canonical GRB light curve within the fireshell model is then characterized by a first (mainly thermal) emission due to the transparency of the  $e^+e^-$ -photon-baryon plasma, the P-GRB. A multi-wavelength emission, the prompt emission, follows due to the collisions between the accelerated baryons and the CBM.

The fireshell model has originally described the process of vacuum polarization due to the overcritical electromagnetic

field occurring at the moment of BH formation (Damour & Ruffini 1975). The formalism has been developed by considering a large number of relativistic quantum effects in the electrodynamics proposed for the NS crust (Belvedere et al. 2012, 2014a; Rueda et al. 2014), as well as on quantum-electrodynamics processes ongoing in the gravitational collapse (Han et al. 2012; Ruffini & Xue 2013). This has led to the results summarized in Figure 4.

The first description of the  $e^+e^-$  plasma within the fireshell model was performed under the simplified assumption of spherical symmetry (the dyadosphere; see, e.g., Preparata et al. 1998). The corresponding structure in the axially symmetric Kerr-Newman geometry has been considered (the dyadotorus; see, e.g., Cherubini et al. 2009; Ruffini 2009) and could possibly be tested.

The general formalism of the fireshell model can also be applied to any optically thick  $e^+e^-$  plasma in the presence of a baryon load, like the one created during the merging of binary NSs from  $\nu\bar{\nu} \rightarrow e^+e^-$  (see, e.g., Salmonson & Wilson 2002 and references therein).

The P-GRB addresses the fully relativistic fundamental physics aspects of the model, in particular the acceleration process of the  $e^+e^-$ -baryon plasma, the collapsing NS quantum-electrodynamics, and the BH physics. The prompt emission addresses the conceptually simpler problem of the interaction of the accelerated baryons with the CBM, which does not allow nor require, by its own nature, a detailed description.

#### 4. SUMMARY OF THE RESULTS FOR GRB 090227B: THE PROTOTYPE OF THE FAMILY-2 SHORT GRBS

GRB 090227B is a bright short burst with an overall emission lasting  $\sim 0.9$  s and total fluence of  $3.79 \times 10^{-5}$  erg  $\text{cm}^{-2}$  in the energy range 8 keV–40 MeV. This burst was significantly detected only in the LAT Low Energy (LLE) data since it was outside the nominal LAT FOV (Ackermann et al. 2013). However, only one transient-class event with energy above 100 MeV has been associated with the GRB (Ackermann et al. 2013).

The time-resolved spectral analysis on the time scale as short as 16 ms, made possible by the *Fermi*-GBM (Meegan et al. 2009), has allowed the identification of the P-GRB in the early 96 ms of emission. The corresponding thermal component has a temperature  $kT = (517 \pm 28)$  keV (see the upper plots of Figure 9 in Muccino et al. 2013). The subsequent emission, fit by a Band function (see lower plots of Figure 9 in Muccino et al. 2013), has been identified with the prompt emission.

Due to the absence of an optical identification, a direct measurement of the cosmological redshift was not possible. From the temperature and flux of the P-GRB thermal component it was possible to derive (see Figure 4) a theoretical cosmological redshift  $z = 1.61 \pm 0.14$ , as well as the baryon load  $B = (4.13 \pm 0.05) \times 10^{-5}$ , the total plasma energy  $E_{e^+e^-}^{\text{tot}} = (2.83 \pm 0.15) \times 10^{53}$  erg, and the extremely high Lorentz  $\Gamma$  factor at transparency  $\Gamma_{\text{tr}} = (1.44 \pm 0.01) \times 10^4$  (see Section 4.1 in Muccino et al. 2013). Consequently, an average CBM number density  $\langle n_{\text{CBM}} \rangle = (1.90 \pm 0.20) \times 10^{-5}$   $\text{cm}^{-3}$  has been determined which is typical of galactic halos where NS-NS mergers migrate, owing to natal kicks imparted to the binaries at birth (see, e.g., Narayan et al. 1992; Bloom et al. 1999; Fryer et al. 1999; Belczynski et al. 2006; Berger 2014).

In Muccino et al. (2013) it was concluded that the progenitor of GRB 090227B is a binary NS. For simplicity and as a lower limit, the masses of the two NS have been assumed to be the same, e.g.,  $M_1 = M_2 = 1.34 M_\odot$ , so that the total merged core mass is  $>M_{\text{crit}}^{\text{NS}}$  and therefore a BH is formed. This conclusion was drawn in view of the large total energy,  $E_{e^+e^-}^{\text{tot}} = 2.83 \times 10^{53}$  erg. Correspondingly, the energy emitted via GWs,  $\sim 9.7 \times 10^{52}$  erg, has been estimated in Oliveira et al. (2014).

## 5. OBSERVATIONS AND DATA ANALYSIS OF GRB 140619B

At 11:24:40.52 UT on 2014 June 19, the *Fermi*-GBM detector (Connaughton et al. 2014) triggered and located the short and hard burst GRB 140619B (trigger 424869883/140619475). The on-ground calculated location, using the GBM trigger data, was R.A.(J2000) =  $08^{\text{h}}54^{\text{m}}$  and decl. (J2000) =  $-3^\circ42'$ , with an uncertainty of  $5^\circ$  (statistical only). The location of this burst was  $32^\circ$  from the LAT boresight at the time of the trigger, and the data from the *Fermi*-LAT showed a significant increase in the event rate (Kocevski et al. 2014). The burst was also detected by *Suzaku*-WAM (Iwakiri et al. 2014), showing a single pulse with a duration of  $\sim 0.7$  s (50 keV–5 MeV). The analysis from 48.7 to 71.6 ks after the GBM trigger by the *Swift*-XRT instrument in the FOV of the *Fermi*-GBM and LAT, was completely in Photon Counting mode (Maselli & D’Avanzo 2014). No bright X-ray afterglow was detected within the LAT error circle. This set an upper limit on the energy flux in the observed 0.3–10 keV energy band of  $\approx 9.24 \times 10^{-14}$  erg/(cm<sup>2</sup> s), assuming a photon index  $\gamma = 2.2$ . Therefore, no optical follow-up was possible and thus the redshift of the source is unknown.

We have analyzed the *Fermi*-GBM and LAT data in the energy range 8 keV–40 MeV and 20 MeV–100 GeV, respectively. We have downloaded the GBM TTE (Time-Tagged Events) files,<sup>7</sup> suitable for short or highly structured events, and analyzed them by using the RMFIT package.<sup>8</sup> The LLE data<sup>9</sup>, between 20–100 MeV, and the high energy data<sup>10</sup>, between 100 MeV–100 GeV, were analyzed by using the Fermi-science tools.<sup>11</sup> In Figure 5 we have reproduced the 64 ms binned GBM light curves corresponding to detectors NaI-n6 (8–260 keV, top panel) and BGO-b1 (260 keV–20 MeV, second panel), the 64 ms binned LLE light curve (20–100 MeV, third panel) and the 192 ms binned high-energy channel light curve (0.1–100 GeV, bottom panel). All the light curves are background subtracted. The NaI-n6 light curve shows a very weak signal, almost at the background level, while the BGO-b1 signal is represented by a short hard pulse, possibly composed by two sub-structures, with a total duration of  $T_{90} \approx 0.7$  s. The vertical dashed line in Figure 5 represents the on-set of both LAT light curves, i.e.,  $\sim 0.2$  s after the GBM trigger. In principle, this allows us to determine the time interval within which the P-GRB emission takes place.

We have subsequently performed the time-integrated and time-resolved spectral analyses focused on the GBM data in the energy range 8 keV–40 MeV.

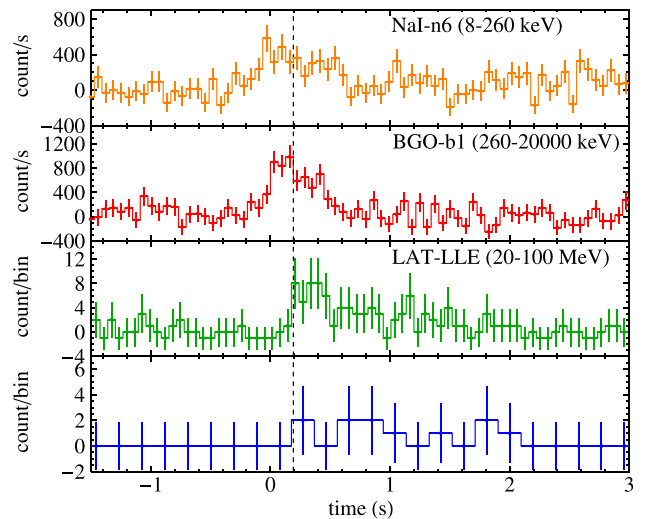


**Figure 5.** Background subtracted light curves of GRB 140619B from various detectors in various energy bands. From the top to the bottom panel: the 64 ms binned light curves from the NaI-n6 (8–260 keV, top panel) and BGO-b1 (260 keV–20 MeV, second panel) detectors, the 64 ms binned LLE light curve (20–100 MeV, third panel), and the 192 ms binned high-energy channel light curve (100 MeV–100 GeV, bottom panel).

### 5.1. Time-integrated Spectral Analysis

We have performed a time-integrated spectral analysis in the time interval from  $T_0 - 0.064$  s to  $T_0 + 0.640$  s, which corresponds to the  $T_{90}$  duration of the burst. We have indicated the trigger time by  $T_0$  and have considered the following spectral models: Comptonization (Compt) and a Band function (Band et al. 1993). The corresponding plots are shown in Figure 6 and the results of the fits are listed in Table 1. From a statistical point of view, the Compt model provides the best fit to the data. In fact the Band function, which has an additional parameter with respect to the Compt model, improves the fit by only  $\Delta\text{C-STAT} = 2.53$ , where  $\Delta\text{C-STAT}$  is the difference between the two C-STAT values of the Compt and Band models. If we consider  $\Delta\text{C-STAT}$  as a  $\chi^2$  variable for the change in the number of the model parameters  $\Delta n$  (in this case  $\Delta n = 1$ ), and assuming that the Compt model is nested within the Band model,<sup>12</sup> we conclude that the Band model improves the fit only at the 89% significance level, and anyway less than  $2\sigma$ . Therefore it is not enough to reject the Compt model. The most interesting feature of the Compt model consists of its low-energy index, which is consistent with  $\alpha \sim 0$ . We proceed now to a time-resolved analysis to investigate the possibility that in the early phases of the prompt emission the spectrum is consistent with a BB spectrum, i.e.,  $\alpha \approx 1$ , which corresponds to the signature of P-GRB emission.

### 5.2. Time-resolved Spectral Analysis

We performed the time-resolved spectral analysis by selecting time intervals with fluences larger than  $\approx 10^{-6}$  erg cm<sup>-2</sup> in order to collect enough photons. Consequently, we have selected two time intervals that correspond to the main spike and the less intense structure (see the BGO-b1 light curve in Figure 6). The first time interval, from  $T_0$  to

<sup>12</sup> The Compt model can be considered a particular case of the Band model with  $\beta \rightarrow -\infty$ .

<sup>7</sup> <ftp://legacy.gsfc.nasa.gov/fermi/data/gbm/bursts>

<sup>8</sup> [http://Fermi.gsfc.nasa.gov/ssc/data/analysis/rmf/fit/vc\\_rmf\\_fit\\_tutorial.pdf](http://Fermi.gsfc.nasa.gov/ssc/data/analysis/rmf/fit/vc_rmf_fit_tutorial.pdf)

<sup>9</sup> [http://fermi.gsfc.nasa.gov/ssc/observations/types/grbs/lat\\_grbs/](http://fermi.gsfc.nasa.gov/ssc/observations/types/grbs/lat_grbs/)

<sup>10</sup> <http://fermi.gsfc.nasa.gov/cgi-bin/ssc/LAT/LATDataQuery.cgi>

<sup>11</sup> <http://fermi.gsfc.nasa.gov/ssc/data/analysis/documentation/Cicerone/>

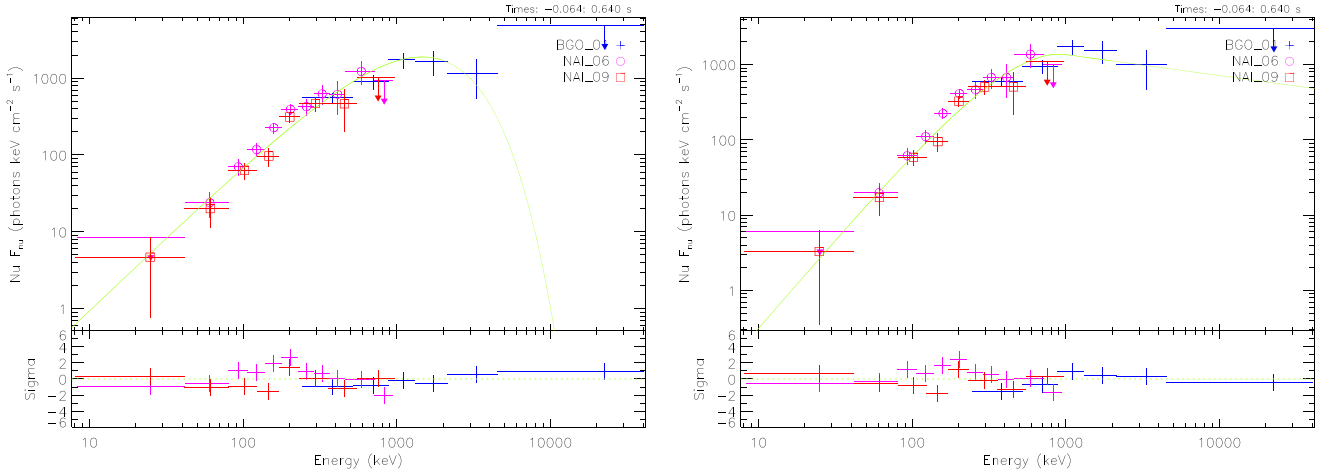


**Figure 6.** Combined NaI-n6, n9+BGO-b1  $\nu F_\nu$  spectra of GRB 140619B in the  $T_{90}$  time interval. The fit using the Compt spectral model is shown on the left, while the Band model fit is on the right.

**Table 1**  
Summary of the Time-integrated ( $T_{90}$ ) and Time-resolved ( $\Delta T_1$  and  $\Delta T_2$ ) Spectral Analyses

$\Delta T$	Model	$K$ (ph keV $^{-1}$ cm $^{-2}$ s $^{-1}$ )	$kT$ (keV)	$E_p$ (keV)	$\alpha$	$\beta$	$F_{\text{tot}}$ (erg cm $^{-2}$ s $^{-1}$ )	C-STAT/DOF
$T_{90}$	Compt	$(7.7 \pm 1.1) \times 10^{-3}$	...	$1456 \pm 216$	$-0.09 \pm 0.18$	...	$(5.75 \pm 0.75) \times 10^{-6}$	365.09/346
	Band	$(7.8 \pm 1.3) \times 10^{-3}$	...	$908 \pm 199$	$-0.38 \pm 0.37$	$-2.28 \pm 0.31$	$(7.4 \pm 1.8) \times 10^{-6}$	362.56/345
$\Delta T_1$	Compt	$(6.3 \pm 2.0) \times 10^{-3}$	...	$1601 \pm 287$	$0.26 \pm 0.32$	...	$(9.4 \pm 1.6) \times 10^{-6}$	318.92/346
	BB	$(7.5 \pm 2.2) \times 10^{-8}$	$324 \pm 33$	...	...	...	$(8.5 \pm 1.2) \times 10^{-6}$	323.86/347
$\Delta T_2$	Compt	$(7.2 \pm 1.4) \times 10^{-3}$	...	$1283 \pm 297$	$-0.11 \pm 0.26$	...	$(4.38 \pm 0.89) \times 10^{-6}$	391.65/346
	BB	$(3.8 \pm 1.1) \times 10^{-7}$	$156 \pm 15$	...	...	...	$(2.33 \pm 0.28) \times 10^{-6}$	392.23/347

**Note.** In each column are listed, respectively, the time interval  $\Delta T$ , the adopted spectral model, the normalization constant  $K$  of the fitting function, the BB temperature  $kT$ , the peak energy  $E_p$ , the low-energy  $\alpha$  and high-energy  $\beta$  photon indexes, the total energy flux  $F_{\text{tot}}$  in the range 8 keV–40 MeV, and the value of the C-STAT over the number of degrees of freedom (dof).

$T_0 + 0.192$  s, is hereafter referred to as  $\Delta T_1$ , while the subsequent emission, from  $T_0 + 0.192$  s to  $T_0 + 0.640$  s, is designated by  $\Delta T_2$ .

In the  $\Delta T_1$  time interval, to identify the P-GRB, we have performed a spectral analysis by considering the BB and Compt spectral models. The spectra and the corresponding fits are shown in Figure 7 and the best fit parameters are listed in Table 1. As reported in Table 1, the Compt and the BB models are both viable. However, the value of the low-energy index of the Compt model in the  $\Delta T_1$  time interval,  $\alpha = 0.26 \pm 0.32$ , is consistent within three  $\sigma$  with  $\alpha = 1$ , which is the low energy index of a BB. We conclude that the BB model is an acceptable fit to the data and the best “physical model” of the  $\Delta T_1$  time interval and therefore identify it with the P-GRB emission. The corresponding observed temperature is  $kT = (324 \pm 33)$  keV (see Table 1).

We then performed a spectral analysis on the time interval  $\Delta T_2$  to identify the prompt emission. We have again considered the Compt and BB spectral models (see Figure 8 and Table 1). By looking at Figure 8, it is immediately clear that the BB model does not adequately fit the data at energies larger than 1 MeV. Therefore the Compt model is favored. Its low-energy index,  $\alpha = -0.11 \pm 0.26$ , indicates that the spectral energy distribution in the  $\Delta T_2$  time interval is broader than that of the BB model. The Compt model is consistent with the spectral model adopted in the fireshell model and described in Patricelli et al. (2012) for the prompt emission.

In the next section we interpret the above data within the fireshell theoretical framework.

## 6. APPLICATION OF THE FIRESHLL MODEL TO GRB 140619B

After the P-GRB and the prompt emission identification, we have followed the same analysis described in Muccino et al. (2013) to determine the cosmological redshift, the baryon load and all the other physical quantities characterizing the plasma at the transparency point (see Figure 4). It is appropriate to underline that a remarkable difference between the long and the short GRBs is considered: the P-GRB emission in long GRBs represents on average the 1%–5% of the overall emission (see, e.g., the cases of GRB 970828, Ruffini et al. 2013, and GRB 090618, Izzo et al. 2012b), while in the cases of the short GRBs 090227B and 140619B (see Section 6.1), the P-GRB emissions represent  $\sim 40\%$  of the overall observed fluence.

### 6.1. Redshift Estimate in Fireshell Model

From the observed P-GRB and total fluences, respectively,  $S_{\text{BB}} = F_{\text{tot}}(\Delta T_1)\Delta T_1$  and  $S_{\text{tot}} = F_{\text{tot}}(T_{90})T_{90}$  (see values in Table 1), we have estimated the ratio

$$\frac{E_{\text{P-GRB}}}{E_{e^-e^+}^{\text{tot}}} \approx \frac{4\pi d_l^2 S_{\text{BB}}/(1+z)}{4\pi d_l^2 S_{\text{tot}}/(1+z)} = \frac{S_{\text{BB}}}{S_{\text{tot}}} = (40.4 \pm 7.8)\%, \quad (1)$$

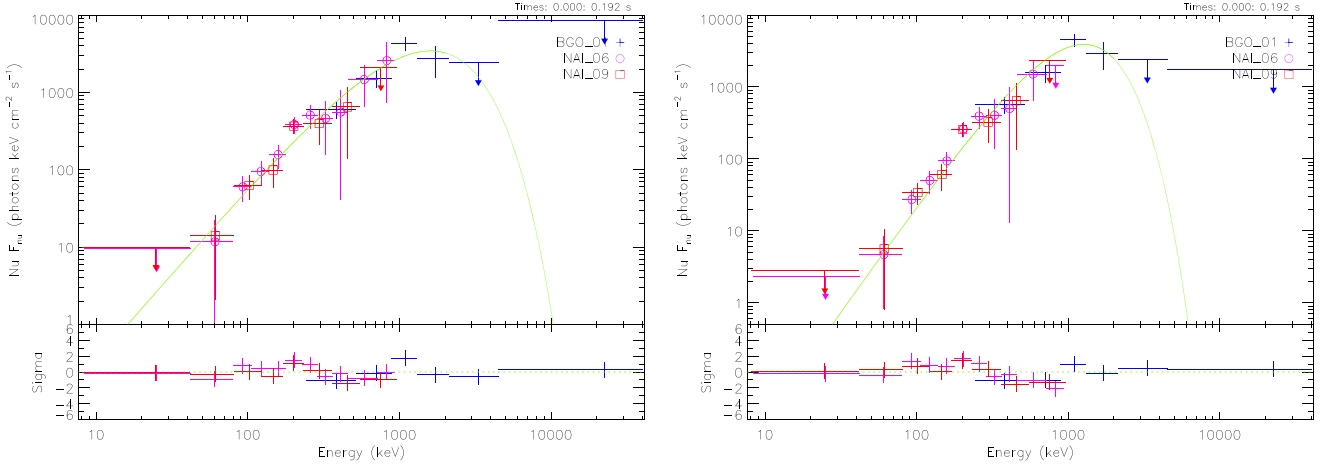


**Figure 7.** Same considerations as in Figure 6, in the  $\Delta T_1$  time interval, comparing Compt (left panel) and BB (right panel) models.

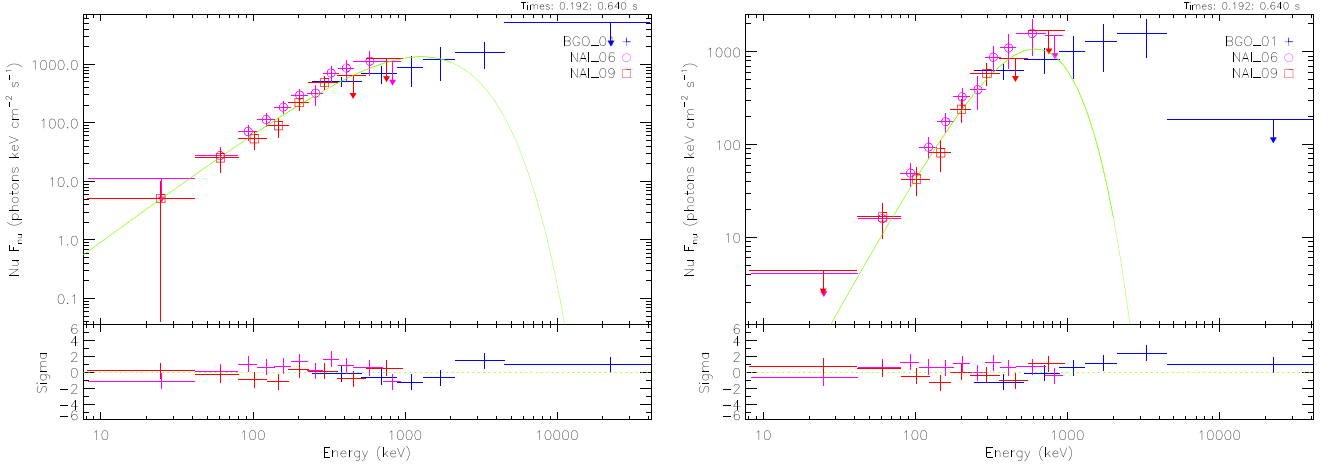


**Figure 8.** Same considerations as in Figure 6, in the  $\Delta T_2$  time interval, comparing Compt (left panel) and BB (right panel) models.

where the theoretically computed energy of the P-GRB,  $E_{P-GRB}$ , has been constrained by the observed thermal emission,  $E_{BB}$ , and we have imposed  $E_{e^+e^-}^{\text{tot}} \equiv E_{\text{iso}}$ . In Equation (1) the luminosity distance  $d_l$  and the redshift  $z$  of the source do not enter into the final computation.

From the last diagram in Figure 4, it is clear that for the value in Equation (1), we have different possible parameters ( $E_{e^+e^-}^{\text{tot}}$ ,  $B$ ) and for each of them we can determine the corresponding  $kT_{\text{blue}}$  (see the top diagram in Figure 4). Finally, from the ratio between  $kT_{\text{blue}}$  and the observed P-GRB temperature  $kT$ , we can estimate the redshift, i.e.,  $kT_{\text{blue}}/kT = (1+z)$ . To obtain the correct value of  $z$  and then the right parameters  $[E_{e^+e^-}^{\text{tot}}(z), B(z)]$ , we have made use of the isotropic energy formula

$$E_{\text{iso}} = 4\pi d_l^2 \frac{S_{\text{tot}}}{(1+z)} \frac{\int_{1/(1+z)}^{10000/(1+z)} E N(E) dE}{\int_8^{40000} E N(E) dE}, \quad (2)$$

in which  $N(E)$  is the photon spectrum of the burst and the integrals are due to the  $K$ -correction on  $S_{\text{tot}}$  (Schaefer 2007). From the initial constraint  $E_{\text{iso}} \equiv E_{e^+e^-}^{\text{tot}}$ , we have found  $z = 2.67 \pm 0.37$ , which leads to  $B = (5.52 \pm 0.73) \times 10^{-5}$

and  $E_{e^+e^-}^{\text{tot}} = (6.03 \pm 0.79) \times 10^{52}$  erg. All the quantities so determined are summarized in Table 2. The analogy with the prototypical source GRB 090227B, for which we have  $E_{P-GRB} = (40.67 \pm 0.12)\% E_{e^+e^-}^{\text{tot}}$  and  $B = (4.13 \pm 0.05) \times 10^{-5}$ , is very striking (Muccino et al. 2013).

We now proceed with the analysis of the subsequent emission to derive the properties of the surrounding CBM.

## 6.2. Analysis of the Prompt Emission

Having determined the initial conditions for the fireshell, i.e.,  $E_{e^+e^-}^{\text{tot}} = 6.03 \times 10^{52}$  erg and  $B = 5.52 \times 10^{-5}$ , the dynamics of the system is uniquely established. In particular, we obtain the Lorentz factor at transparency,  $\Gamma_{\text{tr}} = 1.08 \times 10^4$ , and we can simulate the light curve and the spectrum of the prompt emission. To reproduce the pulses observed especially in the BGO-b1 light curve (see Figure 5) we have derived the radial distributions of the CBM number density and of the filling factor  $\mathcal{R}$  around the burst site (see Table 3 and Figure 9). The errors in the CBM number density and in  $\mathcal{R}$  are defined as the maximum possible variation of the parameters to guarantee agreement between the simulated light curve and the observed data. The final simulation of the BGO-b1 light curve (260 keV–40 MeV) is shown in Figure 10.

**Table 2**

The Results of the Simulation of GRB 090227B in the Fireshell Model

Fireshell Parameter	Value
$E_{e^+e^-}^{\text{tot}}$ (erg)	$(6.03 \pm 0.79) \times 10^{52}$
$B$	$(5.52 \pm 0.73) \times 10^{-5}$
$\Gamma_{\text{tr}}$	$(1.08 \pm 0.08) \times 10^4$
$r_{\text{tr}}$ (cm)	$(9.36 \pm 0.42) \times 10^{12}$
$kT_{\text{blue}}$ (keV)	$(1.08 \pm 0.08) \times 10^3$
$z$	$2.67 \pm 0.37$
$\langle n_{\text{CBM}} \rangle$ ( $\text{cm}^{-3}$ )	$(4.7 \pm 1.2) \times 10^{-5}$

Interestingly, the average CBM number density in GRB 140619B,  $\langle n_{\text{CBM}} \rangle = (4.7 \pm 1.2) \times 10^{-5} \text{ cm}^{-3}$  (see Table 3), is very similar to that of the prototype GRB 090227B,  $\langle n_{\text{CBM}} \rangle = (1.90 \pm 0.20) \times 10^{-5} \text{ cm}^{-3}$ . In both the cases the CBM densities are typical of the galactic halo environment.

We turn now to the spectrum of the prompt emission using the spectral model described in Patricelli et al. (2012) with a phenomenological parameter  $\alpha = -1.11$ . From fitting the light curve in the energy range 260 keV–40 MeV, we have extended the simulation of the corresponding spectrum down to 8 keV to check overall agreement with the observed data. The final result is plotted in Figure 11, where the rebinned NaI-n6 and n9 and BGO-b1 data in the  $\Delta T_2$  time interval show their agreement with the simulation; the lower panel in Figure 11 shows the residuals of the data around the fireshell simulated spectrum.

The fireshell approach is different from the fireball one, where the sharp luminosity variations observed in the prompt emission are attributed to the prolonged and variable activity of the “inner engine” (see, e.g., Rees & Meszaros 1994; Ramirez-Ruiz & Fenimore 2000; Piran 2004).

In the fireshell model, the observed time variability of the prompt emission is produced by the interaction of the accelerated baryons of the fireshell with the CBM “clumps” (see, e.g., Ruffini et al. 2002, 2006; Patricelli et al. 2012). The issue of the time variability in GRB light curves has been long debated. Zhang et al. (2006) and Nakar & Granot (2007) indicated difficulties in producing short time variability from CBM inhomogeneities. The opposite point of view has been expressed by Dermer & Mitman (1999) and Dermer (2006, 2008). In the fireshell model it has been shown that, from the correct computation of the equations of motion of the shell, of the EQTS, and of the Lorentz factor (Bianco & Ruffini 2005a, 2005b, and Section 3), the short time scale variability of GRB light curves occurs in regimes with the larger values of the Lorentz factor, when the total visible area of the emission region is very small and “dispersion” in arrival time of the luminosity peaks is negligible. Therefore the short time scale variability indeed can be produced by the CBM inhomogeneities (see Section 3 in Patricelli et al. 2012). This has been verified in the present case of GRB 140619B, where the values of the Lorentz factor  $\Gamma$  and the total transversal size of the fireshell visible area  $d_v$  at the initial radius of the CBM cloud are explicitly indicated in Table 3. These values of  $d_v$  are smaller than the thickness of the inhomogeneities ( $\Delta r \approx 10^{16}$ – $10^{17}$  cm) and fully justify the adopted spherical symmetry approximation (Ruffini et al. 2002, 2006; Patricelli et al. 2012). Consequently, a finer description of each substructure in the spikes observed in the light curve is not necessary and does not

change the substantial agreement of the model with the observational data, which is provided by the average densities and the filling factors in Table 3.

### 6.3. The Progenitor System

In analogy with the case of GRB 090227B (see, e.g., Muccino et al. 2013; Oliveira et al. 2014), we conclude that the progenitor of GRB 140619B is a NS–NS merger. As a lower limit, we have considered the simplest case by assuming two NSs with the same mass  $M_{\text{NS}}$  such that the total mass would be larger than the NS critical mass  $M_{\text{crit}}^{\text{NS}}$ , e.g.,  $2M_{\text{NS}} \gtrsim M_{\text{crit}}^{\text{NS}}$ . This condition is clearly necessary for the formation of a BH and the consequent application of the fireshell model. It is also appropriate here to recall that only a subset of binary NSs mergers can fulfill this stringent requirement (see Figure 3). This will strongly affect the estimate of the rate of these family-2 short GRBs, when compared with the usual expected binary NS rate (see Section 9 and Conclusions).

Referring to the work of Belvedere et al. (2012) on nonrotating NSs in the global charge neutrality treatment with all the fundamental interactions taken into account properly, we have considered two NSs with mass  $M_{\text{NS}} = 1.34 M_{\odot} = 0.5M_{\text{crit}}^{\text{NS}}$  and corresponding radius  $R = 12.24$  km. As a working hypothesis we assume that in the NS merger the crustal material from both NSs contributes to the GRB baryon load, while the NS cores collapse to a BH. For each NS the crustal mass from the NL3 nuclear model is  $M_c = 3.63 \times 10^{-5} M_{\odot}$ , so the total NS merger crustal mass is  $M_{2c} = 2M_c = 7.26 \times 10^{-5} M_{\odot}$ . On the other hand, the baryonic mass engulfed by the  $e^+e^-$  plasma before transparency is  $M_B = E_{e^+e^-}^{\text{tot}} B/c^2 = (1.86 \pm 0.35) \times 10^{-6} M_{\odot}$ , so we can conclude that only a small fraction of the crustal mass contributes to the baryon load, namely  $M_B = (2.56 \pm 0.48)\% M_{2c}$ . This value is consistent with the global charge neutrality condition adopted in Belvedere et al. (2012). The usually adopted LCN condition leads instead to a crustal mass  $M_c^{\text{LCN}} \sim 0.2 M_{\odot}$  (see, e.g., Belvedere et al. 2012; Oliveira et al. 2014), which would be inconsistent with the small value of the baryon load inferred above.

## 7. ON THE GWS EMISSION AND THE DETECTABILITY OR ABSENCE THEREOF

Following the previous work on GRB 090227B (Oliveira et al. 2014), we now estimate the emission of GWs of the binary NS progenitor of the short GRB 140619B using the effective-one-body (EOB) formalism (Buonanno & Damour 1999, 2000; Damour et al. 2000; Damour 2001; Damour & Nagar 2010) and assess the detectability of the emission by the Advanced LIGO interferometer.<sup>13</sup> The EOB formalism maps the conservative dynamics of a binary system of nonspinning objects onto the geodesic dynamics of a single body of reduced mass  $\mu = M_1 M_2 / M$ , with total binary mass  $M = M_1 + M_2$ . The effective metric is a modified Schwarzschild metric with a rescaled radial coordinate,  $r = c^2 r_{12} / (GM)$ , where  $r_{12}$  is the distance between the two stars. The binary binding energy as a function of the orbital frequency  $\Omega$  is given by  $E_b(\Omega) = Mc^2 [\sqrt{1 + 2\nu(\hat{H}_{\text{eff}} - 1)} - 1]$ , where the effective Hamiltonian  $\hat{H}_{\text{eff}}^2 = A(u) + p_{\phi}^2 B(u)$  depends on the radial

<sup>13</sup> <http://www.advancedligo.mit.edu>

**Table 3**  
The Density and Filling Factor Masks of GRB 140619B

Cloud	Distance (cm)	$n_{\text{CBM}} \text{ (cm}^{-3}\text{)}$	$\mathcal{R}$	$\Gamma$	$d_v \text{ (cm)}$
1th	$1.50 \times 10^{15}$	$(1.2 \pm 0.2) \times 10^{-5}$	$(2.8 \pm 0.3) \times 10^{-11}$	$1.08 \times 10^4$	$2.76 \times 10^{11}$
2nd	$1.20 \times 10^{17}$	$(9.2 \pm 1.1) \times 10^{-6}$	...	$2.07 \times 10^3$	$1.16 \times 10^{14}$
3rd	$1.70 \times 10^{17}$	$(2.5 \pm 0.5) \times 10^{-4}$	$(3.5 \pm 0.6) \times 10^{-10}$	$1.84 \times 10^3$	$1.85 \times 10^{14}$

**Note.** In each column are listed, respectively, the CBM cloud, the corresponding initial radius away from the BH, the number density, the filling factor, the Lorentz factor, and the total transversal size of the fireshell visible area.

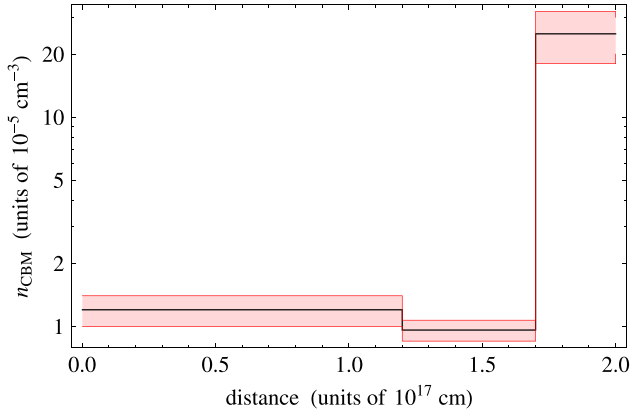


**Figure 9.** Radial CBM number density distribution of GRB 140619B (black line) and its range of validity (red shaded region).

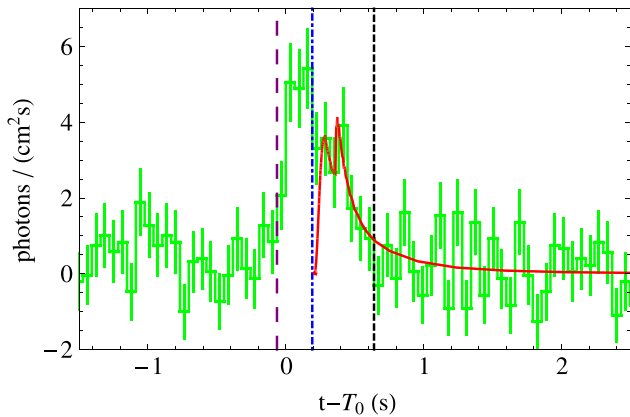


**Figure 10.** BGO-b1 (260 keV–40 MeV) simulated light curve of the prompt emission of GRB 140619B (solid red line). Each spike corresponds to the CBM number density profile described in Table 2 and Figure 9. The blue dotted–dashed vertical line marks the end of the P-GRB emission. The purple long-dashed and the black dashed vertical lines indicate, respectively, the starting and the ending times of the  $T_{90}$  time interval. Clearly visible outside of this time interval is the background noise level. The continuation of the simulation after  $T_{90}$  is due to the residual large angle emission of the EQTS (Bianco & Ruffini 2005a, 2005b) due to the density profile indicated in Table 3.

potential  $A(u)$  of the variable  $u = 1/r$  and  $B(u) = u^2 A(u)$ , while the angular momentum for the circular orbit is given by  $p_\phi^2 = -A'(u)/[u^2 A(u)]'$ , where a prime stands for the derivative with respect to  $u$  (see, e.g., Bini & Damour 2013 for further details). In order to obtain the derivative of the effective Hamiltonian  $\dot{H}_{\text{eff}}$  as a function of  $\Omega$ , we must use the chain rule together with the relation  $\Omega = \Omega(u)$  following from the angular

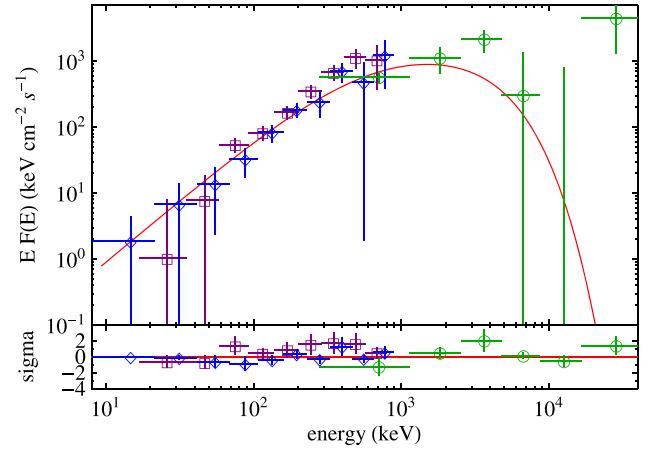


**Figure 11.** Top panel: comparison between the 8–900 keV data from the NaI-n6 (purple squares) and n9 (blue diamonds) detectors, and the 260 keV–40 MeV data from the BGO-b1 detector (green circles), and the simulation within the fireshell model (solid red curve) in the time interval  $\Delta T_2$ . Bottom panel: the residuals of the above mentioned data with the simulation.

Hamilton equation of motion in the circular case  $GM\Omega(u) = (1/u)\partial H/\partial p_\phi = MA(u)p_\phi(u)u^2/(H\dot{H}_{\text{eff}})$ , where  $G$  is the gravitational constant. Finally we obtain the rate of orbital energy loss through emission of GWs from the related derivative  $dE_b/d\Omega$ .

Using the well known matched filtering technique, we compute the signal-to-noise ratio (S/N) from the Fourier transform of the signal  $h(t) = h_+ F_+ + h_\times F_\times$ , where  $h_{+, \times}$  are functions that depend on the direction and polarization of the source and  $F_{+, \times}$  depend on the direction of the detector. By making an rms average over all possible source directions and wave polarizations, i.e.,  $\langle F_+^2 \rangle = \langle F_\times^2 \rangle = 1/5$ , we obtain (see Flanagan & Hughes 1998 for details)

$$\langle (S/N)^2 \rangle = \int_{f_{\min}}^{f_{\max}} df_d \frac{h_c^2(f_d)}{5f_d^2 S_h^2(f_d)}, \quad (3)$$

where  $S_h(f)$  is the strain noise spectral density (in units  $1/\sqrt{\text{Hz}}$ ) of the interferometer. We have also introduced the characteristic GW amplitude,  $h_c$ , defined using the Fourier transform of the GW form  $h(t)$ ,  $h_c(f) = f|\tilde{h}(f)|$ , and it is given by

$$h_c^2(f) = \frac{2(1+z)^2}{\pi^2 d_L^2} \frac{dE_b}{df} [(1+z)f_d], \quad (4)$$

with  $z$  the cosmological redshift,  $f_d = f/(1+z)$  the GW frequency at the detector,  $f = \Omega/\pi$  the frequency in the source frame,  $f_{\min}$  the minimal bandwidth frequency of the detector, and  $f_{\max} = f_c/(1+z)$  the maximal bandwidth frequency,

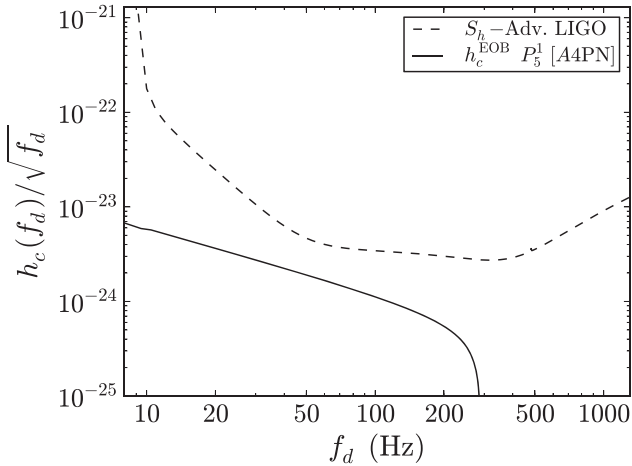


**Figure 12.** Sensitivity curve of Advanced LIGO  $S_h(f)$  (dashed black curve) and the characteristic gravitational amplitude  $h_c(f_d)/\sqrt{f_d}$  (solid black curve) of the binary NS progenitor of GRB 140619B, as a function of the frequency at the detector  $f_d$ . The EOB radial potential  $A(u)$  was calculated using values for the coefficients in the 4th order post-Newtonian (PN) approximation and  $P_5^1$  is the Padé approximant of order (1, 5).

where  $f_c = \Omega_c/\pi$  is the binary contact frequency and  $d_L$  is the luminosity distance. In Figure 12 we show the strain-noise sensitivity of Advanced LIGO,  $S_h(f)$ , and the characteristic gravitational amplitude per square root frequency,  $h_c(f_d)/\sqrt{f_d}$ , both plotted as functions of the frequency at the detector  $f_d$ .

Following the above procedure we obtained for the short GRB 140619B a very low value  $\langle S/N \rangle \approx 0.21$  compared to the value  $S/N = 8$  needed for an optimal positive detection. The low value of the  $S/N$  is clearly due to the large cosmological distance to the source,  $d \approx 21$  Gpc. Although the rms-averaged  $S/N$  we have computed might improve by a factor  $\approx 5/2$  for an optimally located and polarized source (e.g.  $\langle F_+^2 \rangle = 1$  and  $\langle F_\times^2 \rangle = 0$ ) with an optimal face-on orbit ( $\cos i = 1$ ), in the case of GRB 140619B it would increase only to a maximal value  $S/N(\text{opt}) \approx 0.5$ . From the dynamics of the system, we also find that this binary emits a total energy of  $E_{\text{GW}}^T = 7.42 \times 10^{52}$  erg in gravitational radiation during the entire inspiral phase all the way up to the merger.

## 8. CONSIDERATIONS ON THE GEV EMISSION OF GRB 140619B

In addition to the analogies with GRB 090227B, GRB 140619B presents a novelty of special interest: a short-lived emission ( $\sim 4$  s) observed at energies  $\gtrsim 0.1$  GeV. The light curve of this emission shows a rising part which peaks at  $\sim 2$  s, followed by a decaying tail emission lasting another  $\sim 2$  s in the observer frame (see Figure 13(b)). Since GRB 140619B was in the LAT FoV during the entire observational period, the absence of emission after  $\sim 4$  s has been attributed to a cut-off intrinsic to the source. We divided the overall emission into four time intervals (see Figure 13(b)), each of them lasting 1 s. The corresponding spectra are best fit by power-law models. The total isotropic energy of the 0.1–100 GeV emission is  $E_{\text{LAT}} = (2.34 \pm 0.91) \times 10^{52}$  erg.

In complete analogy with the GeV emission emitted in the binary-driven hypernovae (BdHNs), we attribute this high energy radiation to the newly formed BH. This identification is clearer here in view of the absence of a supernova (SN) and the

related constant power-law emission in X-rays, when measured in the cosmological rest-frame of the BdHN (Ruffini et al. 2014, 2015; Ruffini 2015b).

The presence of this GeV emission is not a peculiarity of GRB 140619B, but is a common feature of all these family-2 short GRBs. In line with this, the apparent absence of the GeV emission in GRB 090227B has already been discussed in Section 5: it can be explained simply by the fact that this source was outside the nominal LAT FoV. The significant detection in the LLE channel and the presence of only one transient-class event with energy above 100 MeV associated with the GRB (Ackermann et al. 2013) confirms that in optimal conditions the GeV emission from GRB 090227B should have been detected.

Now consider GRB 090510, which has the characteristics of the family-2 short GRBs ( $E_{\text{iso}} > 10^{52}$  erg and  $E_{p,i} > 2$  MeV), including the presence of a high energy GeV emission lasting  $\sim 10^2$  s. This high energy emission continues up to the signal goes below the LAT threshold (Ackermann et al. 2013). The new feature of GRB 090510, among the family-2 short GRBs, is a well determined cosmological redshift inferred from the optical observations. The corresponding distance indeed coincides with the one theoretically predicted in the fireshell binary merger model (M. Muccino et al. 2015, in preparation).

In Figure 13(a) we compare and contrast the afterglows of the traditional low energetic short GRBs (see Berger 2014, for a review) with those of the family-2 short GRB 140619B (see Figure 13(b)) and GRB 090510 (see Figure 13(c)). In Figure 1 we show the evolution of the NS–NS merger generating a family-2 short GRB. In this system the conservation laws for total energy and the total angular momentum have to be satisfied during and following the binary NS merger (J. A. Rueda et al. 2015, in preparation). One of the most important issues is the determination of the dimensionless angular momentum  $cJ/(GM^2)$  of the newly born BH (where  $J$  and  $M$  are, respectively, the BH spin angular momentum and mass). These considerations have been applied to GRB 090510 (M. Muccino et al. 2015, in preparation).

Before closing, we call attention to GRB 081024B, which we are currently addressing within the fireshell model (Y. Aimuratov et al. 2015, in preparation), and which shows all the typical features of the family-2 short GRBs, including a distinctive GeV emission. In conclusion, we can safely assert that all family-2 short GRBs, when the observational requirements are fulfilled, present a short-lived but very intense GeV emission, which in our interpretation originates from the newly formed BH.

In Table 4 we listed the redshift,  $E_{p,i}$ ,  $E_{\text{iso}}$ , and the GeV isotropic emission energy  $E_{\text{LAT}}$  in the rest-frame energy band 0.1–100 GeV of the three family-2 short GRBs discussed here. In computing  $E_{\text{iso}}$  we have inserted the energy computed in the rest-frame energy band 1–10000 keV.

## 9. THE RATE OF FAMILY-2 SHORT GRBS

With the identification of three family-2 short GRBs, namely GRB 090227B and GRB 140619B, with theoretically inferred redshifts, and GRB 090510 with a measured redshift, all of them detected by the *Fermi* satellite, we are now in a position to give an estimate of the expected rate  $\rho_0$  of such events. Following Soderberg et al. (2006) and Guetta & Della Valle (2007), for these sources we have computed the 1 s peak photon flux  $f_p$  in the energy band 1–1000 keV, which is 16.98

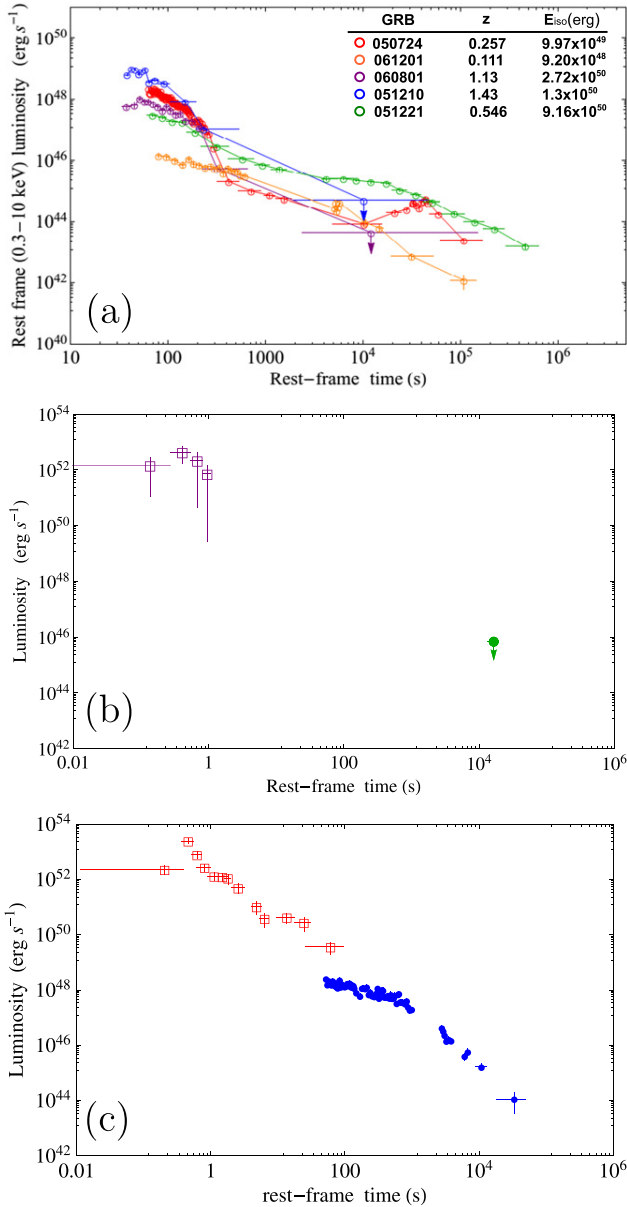


**Figure 13.** Top panel (a): the rebinned rest-frame 0.3–10 keV X-ray luminosities of weak short GRBs leading to massive NSs; the corresponding bursts, redshifts and energies are indicated in the legend. In their afterglows there is no regular power-law behavior at late times and no nesting (Ruffini et al. 2014). Middle panel (b): the short lived rest-frame 0.1–100 GeV isotropic luminosity light curve (purple squares) and the rest-frame 0.3–10 keV upper limit, as set from the analysis of GRB 140619B outlined in Section 3 (green circle). Bottom panel (c): the long lived rest-frame 0.1–100 GeV (red squares) and the rest-frame 0.3–10 keV (blue circles) isotropic luminosity light curves of GRB 090510.

photons  $\text{cm}^{-2} \text{s}^{-1}$  for GRB 090227B, 9.10 photons  $\text{cm}^{-2} \text{s}^{-1}$  for GRB 090510, and 4.97 photons  $\text{cm}^{-2} \text{s}^{-1}$  for GRB 140619B. From the spectral parameters for each source, we have computed  $f_p$  for various redshifts until it coincided with the corresponding threshold peak flux  $f_T$  which is the limiting peak photon flux allowing burst detection (see the analysis in Band 2003 for details). In this way we have evaluated for each source the maximum redshift  $z_{\text{max}}$  at which the burst would have been detected and, then, the corresponding maximum comoving volume  $V_{\text{max}}$ . For GRB 140619B we

**Table 4**

The Redshift, the Rest-frame Peak Spectral Energy, the Isotropic Energy  $E_{\text{iso}}$  in the Rest-frame Energy Band 1–10000 keV, and the GeV Isotropic Emission energy  $E_{\text{LAT}}$  in the Rest-frame Energy Band 0.1–100 GeV of the Four family-2 Short GRBs Discussed Here

GRB	$z$	$E_{p,i}$ (MeV)	$E_{\text{iso}}$ ( $10^{52}$ erg)	$E_{\text{LAT}}$ ( $10^{52}$ erg)
081024B	$>3.0$	$>8.2$	$>2.4$	$>2.7$
090227B	$1.61 \pm 0.14$	$5.89 \pm 0.30$	$28.3 \pm 1.5$	...
090510	$0.903 \pm 0.003$	$7.89 \pm 0.76$	$3.95 \pm 0.21$	$5.78 \pm 0.60$
140619B	$2.67 \pm 0.37$	$5.34 \pm 0.79$	$6.03 \pm 0.79$	$2.34 \pm 0.91$

**Note.** The values indicated for GRB 081024B will be Discussed in Y. Aimuraton et al. (2015, in preparation).

obtain  $f_p \equiv f_T = 1.03$  photons  $\text{cm}^{-2} \text{s}^{-1}$  at maximum redshift  $z_{140619B}^{\text{max}} = 5.49$ ; for GRB 090227B, which is the brightest one, we find  $f_p \equiv f_T = 1.68$  photons  $\text{cm}^{-2} \text{s}^{-1}$  at a maximum redshift  $z_{090227B}^{\text{max}} = 5.78$ ; finally, for GRB 090510, we get  $f_p \equiv f_T = 1.96$  photons  $\text{cm}^{-2} \text{s}^{-1}$  at a maximum redshift  $z_{090510}^{\text{max}} = 2.25$ . Correspondingly we have computed  $V_{\text{max}}$ .

The empirical rate can be evaluated as

$$\rho_0 = \left( \frac{\Omega_F}{4\pi} \right)^{-1} \frac{N}{V_{\text{max}} T_F}, \quad (5)$$

where  $N = 3$  is the number of identified energetic NS–NS short bursts,  $\Omega_F \approx 9.6$  sr is the average Fermi solid angle, and  $T = 6$  years is the Fermi observational period. We infer a local rate of  $\rho_0 = (2.6_{-1.9}^{+4.1}) \times 10^{-4} \text{ Gpc}^{-3} \text{ yr}^{-1}$ , where the attached errors are determined from the 95% confidence level of the Poisson statistic (Gehrels 1986). At  $z \geq 0.9$ , the above inferred rate provides an expected number of events  $N_{>} = 4_{-3}^{+6}$ , which is consistent with the above three observed events during the Fermi observational period. Also at  $z \leq 0.9$  our estimate  $N_{<} = 0.2_{-0.14}^{+0.31}$  is consistent with the absence of any family-2 short GRB detection.

With the inclusion of GRB 081024B, with a theoretically estimated redshift  $z > 3$  (more details will appear in Y. Aimuraton et al. 2015, in preparation), the above rate remains stable with smaller error bars, i.e.,  $\rho_0 = (2.1_{-1.4}^{+2.8}) \times 10^{-4} \text{ Gpc}^{-3} \text{ yr}^{-1}$ . This inferred rate is different from that of the long GRBs, recently estimated to be  $\rho_{\text{L-GRB}} = 1.3_{-0.6}^{+0.7} \text{ Gpc}^{-3} \text{ yr}^{-1}$  (Wanderman & Piran 2010), and also from the estimates of the family-1 short GRBs given in the literature (without a beaming correction  $\rho_{\text{short}} = 1\text{--}10 \text{ Gpc}^{-3} \text{ yr}^{-1}$ ; see e.g., Berger 2014 and Clark et al. 2014).

Such a low rate can be explained based upon the existing data of binary NSs within our Galaxy (see Section 2). From Figure 3 we notice that only a subset of them has the sum of the masses of the components larger than the critical NS mass and can collapse to a BH in their merger process. Only this subset can lead to a family-2 short GRB.

## 10. THE FAMILY-2 SHORT GRBS AND THE $E_{p,i}$ – $E_{\text{ISO}}$ RELATION FOR SHORT GRBS

Now we discuss some general considerations for the new  $E_{p,i}$ – $E_{\text{iso}}$  relation for short GRBs (Zhang et al. 2012; Calderone et al. 2015), with a power law similar to the one of the Amati

relation for long GRBs (Amati et al. 2008), but different amplitude. This yet unexplained difference discourages the use of the Amati relation as an astronomical tool. All four family-2 short GRBs satisfy this new  $E_{p,i}-E_{\text{iso}}$  relation (see the quantities listed in Table 4). We call attention to the need to investigate the physical reasons for the validity of this universal  $E_{p,i}-E_{\text{iso}}$  relation, which appears to be satisfied by family-1 short bursts, where the binary NS merger does not lead to BH formation, and also the family-2 short bursts, where BHs are formed and reveal their presence by giving rise to the short-lived but significant GeV emission.

## 11. CONCLUSIONS

In this article we have predicted the occurrence of two different kinds of short GRBs originating from binary NS mergers, based on

- (a) the analysis of GRB 090227B, the prototype of short bursts originating from a binary NS leading to BH formation (Muccino et al. 2013),
- (b) the recent progress in the determination of the mass–radius relation of NSs and the determination of their critical mass  $M_{\text{crit}}^{\text{NS}} \approx 2.67 M_{\odot}$  (Rotondo et al. 2011; Rueda et al. 2011, 2014; Belvedere et al. 2012, 2014a, 2014b), and
- (c) the recently measured mass of PSR J0348+0432,  $M = (2.01 \pm 0.04) M_{\odot}$  (Antoniadis et al. 2013), establishing an absolute lower limit on  $M_{\text{crit}}^{\text{NS}}$ , and the remarkable information gained from radio observations of binary NS systems in our own Galaxy (Zhang et al. 2011; Antoniadis 2014).

The first kind of short GRBs, which we call family-1, are the most common ones with  $E_{\text{iso}} < 10^{52}$  erg and rest-frame spectral peak energy  $E_{p,i} < 2$  MeV, originating from binary NS mergers with merged core mass smaller than  $M_{\text{crit}}^{\text{NS}}$  and leading, therefore, to a massive NS, possibly with a companion. We identify these family-1 short bursts with the ones extensively quoted in literature (see, e.g., Berger 2014 for a review).

The second kind of short GRBs, which we call family-2, are those with  $E_{\text{iso}} > 10^{52}$  erg and harder spectra with  $E_{p,i} > 2$  MeV, originating from binary NS mergers with merged core mass larger than  $M_{\text{crit}}^{\text{NS}}$ . These family-2 short bursts satisfy the necessary condition to form a BH, following the example of the prototype GRB 090227B (Muccino et al. 2013).

The application of the fireshell model (Ruffini et al. 2001a, 2001b, 2001c) to the family-2 short GRB 140619B analyzed here has allowed the determination of the physical parameters of this source: the identification of the P-GRB emission in the early  $\sim 0.2$  s of its light curve, the theoretical cosmological redshift of  $z = 2.67 \pm 0.37$  and consequently the total burst energy  $E_{e^+e^-}^{\text{tot}} = (6.03 \pm 0.79) \times 10^{52}$  erg, the baryon load  $B = (5.52 \pm 0.73) \times 10^{-5}$ , and a Lorentz  $\Gamma$  factor at transparency  $\Gamma_{\text{tr}} = (1.08 \pm 0.08) \times 10^4$ . The analysis of the prompt emission has also led to the determination of the CBM density,  $\langle n_{\text{CBM}} \rangle = (4.7 \pm 1.2) \times 10^{-5} \text{ cm}^{-3}$ , typical of the galactic halo environment, where NS–NS binaries migrate to, due to natal kicks imparted to them at birth (see, e.g., Narayan et al. 1992; Bloom et al. 1999; Fryer et al. 1999; Belczynski et al. 2006; Berger 2014), clearly supporting the binary NS merger hypothesis of this source. Unexpectedly, we have found the existence of a short-lived and

very intense GeV emission, just after the P-GRB occurrence and during and after the prompt emission phase, which has led us to conclude that this high energy emission originates from the newly formed BH.

While this article was being refereed, we have discovered three additional examples of these family-2 short bursts: GRB 081024B, GRB 090510, and GRB 090227B. These have given evidence that all these family-2 short bursts indeed show the existence of high energy emission, with the sole exception of GRB 090227B, which at the time of the observation was outside the nominal LAT FOV.

In summary we formulate some norms and theoretical predictions.

- (1) All family-1 short GRBs have an extended X-ray afterglow (see, e.g., Figure 13(a) and Berger 2014). When computed in the rest-frame 0.3–10 keV energy band they do not show any specific power-law behavior (Pisani et al. 2013) or the “nesting” properties (Ruffini et al. 2014) which have been discovered in some long GRBs. We predict that family-1 short GRBs, originating from a binary merger to a massive NS, should never exhibit high energy emission. The upper limit of  $10^{52}$  erg can be simply understood in terms of a merger leading to a massive NS.
- (2) All family-2 short GRBs have been observed not to have prominent X-ray or optical afterglows. They all have short-lived but very energetic GeV emissions (see, e.g., Figures 13(b) and (c)), when LAT data are available. The upper limit of  $10^{54}$  erg can be also simply understood in terms of a merger leading to BH formation.
- (3) The high energy emission episode in family-2 short GRBs always occurs at the end of the P-GRB emission, during and after the prompt emission phase. This fact uniquely links the high energy emission to the occurrence of the newly born BH. The prompt emission phase studied within the fireshell model has also allowed the determination of a large number of essential astrophysical parameters, both of the source (e.g.,  $E_{e^+e^-}^{\text{tot}}$  and  $B$ ) and of the CBM (e.g.,  $\alpha$ ,  $n_{\text{CBM}}$ , and  $\mathcal{R}$ ).

It is interesting that the very simplified conditions encountered in the short GRBs in the absence of a SN event, which characterize the long GRBs (Ruffini et al. 2015), have allowed definite progress in understanding some fundamental GRB properties, e.g., the correlation of high energy emission to the BH formation. They can be adapted to the case of long GRBs. The points summarized above go a long way toward reaching a better understanding of family-1 and family-2 long GRBs (Ruffini et al. 2015), as well as of the BdHNe (Ruffini et al. 2014). We are confident that GRB 140619B is one of the best examples of short GRBs obtained with the current space technology. We sincerely hope that the results of our research will lead to new missions with greater collecting area and time resolution in X- and gamma-rays.

We thank the referee for requesting additional observational support for our theoretical fireshell binary merger model. This has motivated us to improve the connection of our theoretical work with the observations, resulting in this new version of the manuscript. We are especially grateful to S. Campana and C. L. Fryer for useful suggestions in improving some conceptual and observational arguments, and to L. Izzo for the detailed analysis of the high energy emission. M.E., M.K. and F.G.O.

are supported by the Erasmus Mundus Joint Doctorate Program by grant Nos. 2012-1710, 2013-1471, and 2012-1710, respectively, from the EACEA of the European Commission. A.V.P. and E.Z. acknowledge the support by the International Cooperation Program CAPES-ICRANet financed by CAPES-Brazilian Federal Agency for Support and Evaluation of Graduate Education within the Ministry of Education of Brazil. This work made use of data supplied by the UK *Swift* Science Data Centre at the University of Leicester.

## REFERENCES

- Ackermann, M., Ajello, M., Asano, K., et al. 2013, *ApJS*, **209**, 11
- Aksenov, A. G., Ruffini, R., & Vereshchagin, G. V. 2007, *PhRvL*, **99**, 125003
- Amati, L., Guidorzi, C., Frontera, F., et al. 2008, *MNRAS*, **391**, 577
- Antoniadis, J. 2015, in *Gravitational Wave Astrophysics*, ed. C. F. Sopuerta (Cham, Switzerland: Springer International Publishing), 1
- Antoniadis, J., Freire, P. C. C., Wex, N., et al. 2013, *Sci*, **340**, 448
- Band, D., Matteson, J., Ford, L., et al. 1993, *ApJ*, **413**, 281
- Band, D. L. 2003, *ApJ*, **588**, 945
- Belczynski, K., Perna, R., Bulik, T., et al. 2006, *ApJ*, **648**, 1110
- Belvedere, R., Boshkayev, K., Rueda, J. A., & Ruffini, R. 2014a, *NuPhA*, **921**, 33
- Belvedere, R., Pugliese, D., Rueda, J. A., Ruffini, R., & Xue, S.-S. 2012, *NuPhA*, **883**, 1
- Belvedere, R., Rueda, J. A., & Ruffini, R. 2014b, *JKPS*, **65**, 897
- Berger, E. 2011, *NewAR*, **55**, 1
- Berger, E. 2014, *ARA&A*, **52**, 43
- Bianco, C. L., & Ruffini, R. 2005a, *ApJL*, **633**, L13
- Bianco, C. L., & Ruffini, R. 2005b, *ApJL*, **620**, L23
- Bini, D., & Damour, T. 2013, *PhRvD*, **87**, 121501
- Bloom, J. S., Prochaska, J. X., Pooley, D., et al. 2006, *ApJ*, **638**, 354
- Bloom, J. S., Sigurdsson, S., & Pols, O. R. 1999, *MNRAS*, **305**, 763
- Boguta, J., & Bodmer, A. R. 1977, *NuPhA*, **292**, 413
- Buonanno, A., & Damour, T. 1999, *PhRvD*, **59**, 084006
- Buonanno, A., & Damour, T. 2000, *PhRvD*, **62**, 064015
- Burrows, D., Hill, J., Nousek, J., et al. 2005, *SSRv*, **120**, 165
- Calderone, G., Ghirlanda, G., Ghisellini, G., et al. 2015, *MNRAS*, **448**, 403
- Cherubini, C., Geralico, A., J. A. Rueda, H., & Ruffini, R. 2009, *PhRvD*, **79**, 124002
- Cipolletta, F., Cherubini, C., Filippi, S., Rueda, J. A., & Ruffini, R. 2015, *PhRvD*, submitted (arXiv:1506.05926)
- Clark, J., Evans, H., Fairhurst, S., et al. 2014, arXiv:1409.8149
- Connaughton, V., Zhang, B.-B., Fitzpatrick, G., & Roberts, O. 2014, *GCN*, 16419, 1
- Damour, T. 2001, *PhRvD*, **64**, 124013
- Damour, T., Jaranowski, P., & Schäfer, G. 2000, *PhRvD*, **62**, 084011
- Damour, T., & Nagar, A. 2010, *PhRvD*, **81**, 084016
- Damour, T., & Ruffini, R. 1975, *PhRvL*, **35**, 463
- Deneva, J. S., Freire, P. C. C., Cordes, J. M., et al. 2012, *ApJ*, **757**, 89
- Dermer, C. D. 2006, *NCimB*, **121**, 1331
- Dermer, C. D. 2008, *ApJ*, **684**, 430
- Dermer, C. D., & Mitman, K. E. 1999, *ApJL*, **513**, L5
- Dezalay, J.-P., Barat, C., Talon, R., et al. 1992, AIP Conf. Ser. 265, ed. W. S. Paciesas & G. J. Fishman (Melville, NY: AIP), 304
- Eichler, D., Livio, M., Piran, T., & Schramm, D. N. 1989, *Natur*, **340**, 126
- Flanagan, É. É., & Hughes, S. A. 1998, *PhRvD*, **57**, 4535
- Fong, W., Berger, E., & Fox, D. B. 2010, *ApJ*, **708**, 9
- Fryer, C. L., Belczynski, K., Ramirez-Ruiz, E., et al. 2015, *ApJ*, submitted (arXiv:1504.07605)
- Fryer, C. L., Rueda, J. A., & Ruffini, R. 2014, *ApJL*, **793**, L36
- Fryer, C. L., Woosley, S. E., & Hartmann, D. H. 1999, *ApJ*, **526**, 152
- Gehrels, N. 1986, *ApJ*, **303**, 336
- Goodman, J. 1986, *ApJL*, **308**, L47
- Guetta, D., & Della Valle, M. 2007, *ApJL*, **657**, L73
- Haensel, P., Potekhin, A. Y., & Yakovlev, D. G. (ed.) 2007, *Astrophysics and Space Science Library 326, Neutron Stars 1: Equation of State and Structure* (New York: Springer)
- Han, W.-B., Ruffini, R., & Xue, S.-S. 2012, *PhRvD*, **86**, 084004
- Iwakiri, W., Tashiro, M., Terada, Y., et al. 2014, *GCN*, 16457, 1
- Izzo, L., Bernardini, M. G., Bianco, C. L., et al. 2010, *JKPS*, **57-3**, 551
- Izzo, L., Rueda, J. A., & Ruffini, R. 2012a, *A&A*, **548**, L5
- Izzo, L., Ruffini, R., Penacchioni, A. V., et al. 2012b, *A&A*, **543**, A10
- Klebesadel, R. W. 1992, in *Gamma-Ray Bursts—Observations, Analyses and Theories*, ed. C. Ho, R. I. Epstein, & E. E. Fenimore (Cambridge: Cambridge Univ. Press)
- Kocevski, D., Longo, F., Vianello, G., et al. 2014, *GCN*, 16421, 1
- Kopač, D., D'Avanzo, P., Melandri, A., et al. 2012, *MNRAS*, **424**, 2392
- Kouveliotou, C., Meegan, C. A., Fishman, G. J., et al. 1993, *ApJL*, **413**, L101
- Kramer, M. 2014, *IJMPD*, **23**, 30004
- Lattimer, J. M. 2012, *ARNPS*, **62**, 485
- Lawrence, S., Tervala, J. G., Bedaque, P. F., & Miller, M. C. 2015, *ApJ*, in press (arXiv:1505.00231)
- Lee, W. H., Ramirez-Ruiz, E., & Page, D. 2004, *ApJL*, **608**, L5
- Maselli, A., & D'Avanzo, P. 2014, *GCN*, 16424, 1
- Meegan, C., Lichti, G., Bhat, P. N., et al. 2009, *ApJ*, **702**, 791
- Meszáros, P. 2006, *RPPH*, **69**, 2259
- Meszáros, P., & Rees, M. J. 1997, *ApJL*, **482**, L29
- Muccino, M., Ruffini, R., Bianco, C. L., Izzo, L., & Penacchioni, A. V. 2013, *ApJ*, **763**, 125
- Nakar, E., & Granot, J. 2007, *MNRAS*, **380**, 1744
- Narayan, R., Paczynski, B., & Piran, T. 1992, *ApJL*, **395**, L83
- Narayan, R., Piran, T., & Shemi, A. 1991, *ApJL*, **379**, L17
- Oliveira, F. G., Rueda, J. A., & Ruffini, R. 2014, *ApJ*, **787**, 150
- Paczynski, B. 1986, *ApJL*, **308**, L43
- Patricelli, B., Bernardini, M. G., Bianco, C. L., et al. 2012, *ApJ*, **756**, 16
- Piran, T. 2004, *RvMP*, **76**, 1143
- Piran, T. 2005, *RvMP*, **76**, 1143
- Pisani, G. B., Izzo, L., Ruffini, R., et al. 2013, *A&A*, **552**, L5
- Preparata, G., Ruffini, R., & Xue, S. 1998, *A&A*, **338**, L87
- Ramirez-Ruiz, E., & Fenimore, E. E. 2000, *ApJ*, **539**, 712
- Rees, M. J., & Meszáros, P. 1994, *ApJL*, **430**, L93
- Rhoades, C. E., & Ruffini, R. 1974, *PhRvL*, **32**, 324
- Rosswog, S., Ramirez-Ruiz, E., & Davies, M. B. 2003, *MNRAS*, **345**, 1077
- Rotondo, M., Rueda, J. A., Ruffini, R., & Xue, S.-S. 2011, *PhLB*, **701**, 667
- Rueda, J. A., & Ruffini, R. 2012, *ApJL*, **758**, L7
- Rueda, J. A., Ruffini, R., Wu, Y.-B., & Xue, S.-S. 2014, *PhRvC*, **89**, 035804
- Rueda, J. A., Ruffini, R., & Xue, S.-S. 2011, *NuPhA*, **872**, 286
- Ruffini, R. 2009, in *The Kerr Spacetime*, ed. D. L. Wiltshire, M. Visser, & S. Scott (Cambridge: Cambridge Univ. Press)
- Ruffini, R. 2015a, ARep, in press
- Ruffini, R. 2015b, Proc. of the 2nd Cesar Lattes Meeting, ed. U. Barres de Almeida et al., in press
- Ruffini, R., Aksenov, A. G., Bernardini, M. G., et al. 2009, AIP Conf. Ser. 1132, ed. M. Novello & S. Perez (Melville, NY: AIP), 199
- Ruffini, R., Bernardini, M. G., Bianco, C. L., et al. 2005, AIP Conf. Ser. 782, Xlth Brazilian School of Cosmology and Gravitation, ed. M. Novello & S. E. Perez Bergliaffa (Melville, NY: AIP), 42
- Ruffini, R., Bernardini, M. G., Bianco, C. L., et al. 2006, AIP Conf. Ser. 836, Gamma-Ray Bursts in the Swift Era, ed. S. S. Holt, N. Gehrels & J. A. Nousek (Melville, NY: AIP), 103
- Ruffini, R., Bianco, C. L., Chardonnet, P., Frascchetti, F., & Xue, S. 2002, *ApJL*, **581**, L19
- Ruffini, R., Bianco, C. L., Frascchetti, F., Xue, S.-S., & Chardonnet, P. 2001a, *ApJL*, **555**, L117
- Ruffini, R., Bianco, C. L., Frascchetti, F., Xue, S.-S., & Chardonnet, P. 2001b, *ApJL*, **555**, L113
- Ruffini, R., Bianco, C. L., Frascchetti, F., Xue, S.-S., & Chardonnet, P. 2001c, *ApJL*, **555**, L107
- Ruffini, R., Bianco, C. L., Xue, S.-S., et al. 2004, *IJMPD*, **13**, 843
- Ruffini, R., Izzo, L., Muccino, M., et al. 2013, ARep, submitted (arXiv:1311.7432)
- Ruffini, R., Muccino, M., Bianco, C. L., et al. 2014, *A&A*, **565**, L10
- Ruffini, R., Salmonson, J. D., Wilson, J. R., & Xue, S. 2000, *A&A*, **359**, 855
- Ruffini, R., Salmonson, J. D., Wilson, J. R., & Xue, S.-S. 1999, *A&A*, **350**, 334
- Ruffini, R., Vereshchagin, G., & Xue, S.-S. 2010, *PhR*, **487**, 1
- Ruffini, R., Wang, Y., Enderli, M., et al. 2015, *ApJ*, **798**, 10
- Ruffini, R., & Xue, S.-S. 2008, AIP Conf. Ser. 1059, ed. D.-S. Lee & W. Lee (Melville, NY: AIP), 72
- Ruffini, R., & Xue, S.-S. 2013, *PhLA*, **377**, 2450
- Sahu, K. C., Livio, M., Petro, L., et al. 1997, *Natur*, **387**, 476
- Salmonson, J. D., & Wilson, J. R. 2002, *ApJ*, **578**, 310
- Sari, R., Piran, T., & Narayan, R. 1998, *ApJL*, **497**, L17
- Schaefer, B. E. 2007, *ApJ*, **660**, 16
- Soderberg, A. M., Kulkarni, S. R., Nakar, E., et al. 2006, *Natur*, **442**, 1014
- Tavani, M. 1998, *ApJL*, **497**, L21
- Troja, E., King, A. R., O'Brien, P. T., Lyons, N., & Cusumano, G. 2008, *MNRAS*, **385**, L10
- van Paradijs, J., Groot, P. J., Galama, T., et al. 1997, *Natur*, **386**, 686
- Wanderman, D., & Piran, T. 2010, *MNRAS*, **406**, 1944
- Zhang, B., Fan, Y. Z., Dyks, J., et al. 2006, *ApJ*, **642**, 354
- Zhang, C. M., Wang, J., Zhao, Y. H., et al. 2011, *A&A*, **527**, A83
- Zhang, F.-W., Shao, L., Yan, J.-Z., & Wei, D.-M. 2012, *ApJ*, **750**, 88

**Fast rotating neutron stars with realistic nuclear matter equation of state**F. Cipolletta,<sup>1,\*</sup> C. Cherubini,<sup>2,3,†</sup> S. Filippi,<sup>2,3,‡</sup> J. A. Rueda,<sup>1,4,5,§</sup> and R. Ruffini<sup>1,4,5,||</sup><sup>1</sup>*Dipartimento di Fisica and International Center for Relativistic Astrophysics-ICRA, Sapienza Università di Roma, P.le Aldo Moro 5, I-00185 Rome, Italy*<sup>2</sup>*Nonlinear Physics and Mathematical Modeling Lab, University Campus Bio-Medico of Rome, Via A. del Portillo 21, I-00128 Rome, Italy*<sup>3</sup>*International Center for Relativistic Astrophysics-ICRA, University Campus Bio-Medico of Rome, Via A. del Portillo 21, I-00128 Rome, Italy*<sup>4</sup>*International Center for Relativistic Astrophysics Network-ICRANet, Piazza della Repubblica 10, I-65122 Pescara, Italy*<sup>5</sup>*International Center for Relativistic Astrophysics Network-ICRANet-Rio, Centro Brasileiro de Pesquisas Físicas, Rua Dr. Xavier Sigaud 150, Rio de Janeiro 22290-180, Brazil*

(Received 19 February 2015; published 13 July 2015)

We construct equilibrium configurations of uniformly rotating neutron stars for selected relativistic mean-field nuclear matter equations of state (EOS). We compute, in particular, the gravitational mass ( $M$ ), equatorial ( $R_{\text{eq}}$ ) and polar ( $R_{\text{pol}}$ ) radii, eccentricity, angular momentum ( $J$ ), moment of inertia ( $I$ ) and quadrupole moment ( $M_2$ ) of neutron stars stable against mass shedding and secular axisymmetric instability. By constructing the constant frequency sequence  $f = 716$  Hz of the fastest observed pulsar, PSR J1748-2446ad, and constraining it to be within the stability region, we obtain a lower mass bound for the pulsar,  $M_{\text{min}} = [1.2-1.4]M_{\odot}$ , for the EOS employed. Moreover, we give a fitting formula relating the baryonic mass ( $M_b$ ) and gravitational mass of nonrotating neutron stars,  $M_b/M_{\odot} = M/M_{\odot} + (13/200)(M/M_{\odot})^2$  [or  $M/M_{\odot} = M_b/M_{\odot} - (1/20)(M_b/M_{\odot})^2$ ], which is independent of the EOS. We also obtain a fitting formula, although not EOS independent, relating the gravitational mass and the angular momentum of neutron stars along the secular axisymmetric instability line for each EOS. We compute the maximum value of the dimensionless angular momentum,  $a/M \equiv cJ/(GM^2)$  (or “Kerr parameter”),  $(a/M)_{\text{max}} \approx 0.7$ , found to be also independent of the EOS. We then compare and contrast the quadrupole moment of rotating neutron stars with the one predicted by the Kerr exterior solution for the same values of mass and angular momentum. Finally, we show that, although the mass quadrupole moment of realistic neutron stars never reaches the Kerr value, the latter is closely approached from above at the maximum mass value, as physically expected from the no-hair theorem. In particular, the stiffer the EOS, the closer the mass quadrupole moment approaches the value of the Kerr solution.

DOI: [10.1103/PhysRevD.92.023007](https://doi.org/10.1103/PhysRevD.92.023007)

PACS numbers: 97.10.Kc, 04.25.D-, 04.40.Dg, 26.60.Kp

**I. INTRODUCTION**

Understanding the physics of neutron stars and being able to describe the spacetime in the interior and around such compact objects is one of the most important objectives for modern astrophysics, as from one side it could be an excellent test for general relativity and on the other the strong forces acting and the high level of densities reached cannot be tested anywhere on the Earth.

Although we are actually incapable of describing these concepts exactly, some observational limits have already been determined, via simplifying assumptions (such as a spherical configuration in the x-ray binaries observation). Other general considerations on the nature of neutron stars and pulsars are often extracted in the literature from the use

of fiducial structure parameters: a canonical neutron star (NS) of mass  $M = 1.4M_{\odot}$ , radius  $R = 10$  km, and moment of inertia  $I = 10^{45}$  g cm<sup>2</sup> (see, e.g., Ref. [1] and references therein). Based on these parameters together with the thus-inferred surface magnetic field from the classic pointlike magnetodipole rotating model [2,3], NSs have been traditionally classified according to the assumed nature of the energy source powering their observed emission. Neutron stars are also thought to possibly participate in the most powerful explosions in the Universe, gamma-ray bursts (GRBs), e.g., via NS mergers in the case of short GRBs (see, e.g., Ref. [4] and references therein) and hypercritical accretion processes leading to gravitational collapse to a black hole (BH) in the case of long GRBs associated with supernovae (see, e.g., Refs. [5,6] and references therein).

There are still, however, many open issues regarding the above global picture of NSs, both from the physics and the astrophysics points of view (see, e.g., Refs. [7,8]). On the other hand, our theoretical and observational knowledge on NSs has largely increased in the intervening years from the first general relativistic description of a NS by

\*cipo87@gmail.com

†c.cherubini@unicampus.it

‡s.filippi@unicampus.it

§jorge.rueda@icra.it

||ruffini@icra.it

Oppenheimer and Volkoff in 1939 [9]. Eventually, a more complex equation of state (EOS), interior structure, and consequently exterior gravitational field of nonrotating, slowly rotating, and fast rotating stars were acquired, and massive NSs of  $\approx 2M_{\odot}$ , drastically constraining the nuclear EOS stiffness, were observed [10,11]. Thus, general conclusions based on fiducial parameters and corresponding observables might be premature, and a more exhausting exploration of the consequences of adopting different NS parameters appears to be necessary.

For instance, as recently shown in [12] for the high-magnetic field pulsar class, thought to be intermediate objects linking pulsars and magnetars, for the understanding of their magnetic field values and their energy source, we need precise knowledge of the entire set of possible structure parameters of a NS and a self-consistent general relativistic description of the pulsar observables. Indeed, it was shown there how the magnetic field of a pulsar is overestimated, and how the rotational energy is underestimated, by the classic magnetic rotating dipole model and the use of fiducial NS parameters.

The description of the rotational and thermal evolution, as well as the emitted radiation of isolated and accreting NS, requires knowledge of the structure properties and the corresponding exterior metric. For instance, we have recently compared and contrasted the cooling evolution of neutral NSs satisfying local charge neutrality and global charge neutrality [13]. In that work we have shown that, owing to their different crust structure (mass and thickness) for the same value of the total mass, their thermal relaxation time (the time to form an isothermal core) can be very different, and therefore, the signatures of the structure of the NS might be accessed via early cooling observations.

There have been recent numerical relativity computations of the structure of uniformly rotating NSs which have mainly focused on the existence of universal relations between, e.g., the quadrupole moment, the moment of inertia, and the Love number of NSs (see, e.g., Refs. [14–17]), considered in a slow rotation regime. Other works (e.g., Refs. [18,19]) also tried to recover these relations in a full rotation regime, with a numerical method based on the one first implemented in [20].

In this work, through a full rotation approach (treated by numerical relativity methods), we focus on additional structure properties of uniformly rotating NSs relevant for astrophysical applications such as mass, polar and equatorial radii, eccentricity, angular momentum, angular velocity, moment of inertia, and quadrupole moment, for a selected sample of EOS (describing nuclear matter with relations of different stiffness) within relativistic mean-field nuclear theory, not analyzed in the set of EOS of previous works.

This article is organized as follows. In Sec. II we briefly review the axisymmetric system of Einstein's equations to be integrated for a given EOS which we describe in Sec. III. The stability conditions (mass-shedding and secular instability) are outlined in Sec. IV, and the mass radius of

rotating NSs is shown in Sec. V. The eccentricity and the moment of inertia are shown in Sec. VI, while the quadrupole moment is discussed in Sec. VII. We finally summarize and discuss our results in Sec. VIII.

## II. STRUCTURE EQUATIONS

We consider the equilibrium equations for a self-gravitating, rapidly rotating NS, within a fully general relativistic framework. We start with the stationary axisymmetric spacetime metric (see, e.g., Ref. [21]):

$$ds^2 = -e^{2\nu} dt^2 + e^{2\psi} (d\phi - \omega dt)^2 + e^{2\lambda} (dr^2 + r^2 d\theta^2), \quad (1)$$

where  $\nu$ ,  $\psi$ ,  $\omega$  and  $\lambda$  depend only on variables  $r$  and  $\theta$ . It is useful to introduce the variable  $e^{\psi} = r \sin(\theta) B e^{-\nu}$ , with again  $B = B(r, \theta)$ . The above form of the metric is obtained under two assumptions: (1) there are two Killing vector fields, one timelike,  $t^a$ , and one relative to the axial symmetry,  $\phi^a$ ; (2) the spacetime is asymptotically flat. Then, one can introduce quasi-isotropic coordinates, which in the nonrotating limit tend to isotropic ones.

Turning to the physical matter content in the NS interior, if one neglects sources of nonisotropic stresses, viscosity, and heat transport, then the energy-momentum tensor becomes one of a perfect fluid,

$$T^{\alpha\beta} = (\varepsilon + P) u^{\alpha} u^{\beta} + P g^{\alpha\beta}, \quad (2)$$

where  $\varepsilon$  and  $P$  denote the energy density and pressure of the fluid, and  $u^{\alpha}$  is the fluid 4-velocity. In terms of the two Killing vectors,

$$u^{\alpha} = \frac{e^{-\nu} (t^{\alpha} + \Omega \phi^{\alpha})}{\sqrt{1 - v^2}}, \quad (3)$$

where  $v$  is the fluid 3-velocity with respect to the local zero angular-momentum observer (ZAMO),

$$v = (\Omega - \omega) e^{\psi - \nu} \quad (4)$$

with  $\Omega \equiv u^{\phi} / u^t = d\phi / dt$  the angular velocity in the coordinate frame, equivalent to the one measured by an observer at rest at infinity.

Thus, with the metric given by Eq. (1) and the energy-momentum tensor given by Eq. (2), one can write the field equations as (analogously to Ref. [22] setting  $\zeta = \lambda + \nu$ )

$$\begin{aligned} \nabla \cdot (B \nabla \nu) &= \frac{1}{2} r^2 \sin^2 \theta B^3 e^{-4\nu} \nabla \omega \cdot \nabla \omega \\ &+ 4\pi B e^{2\zeta - 2\nu} \left[ \frac{(\varepsilon + P)(1 + v^2)}{1 - v^2} + 2P \right], \end{aligned} \quad (5)$$

$$\nabla \cdot (r^2 \sin^2 \theta B^3 e^{-4\nu} \nabla \omega) = -16\pi r \sin \theta B^2 e^{2\zeta - 4\nu} \frac{(\varepsilon + P)v}{1 - v^2}, \quad (6)$$

$$\nabla \cdot (r \sin(\theta) \nabla B) = 16\pi r \sin \theta B e^{2\zeta - 2\nu} P, \quad (7)$$

$$\begin{aligned} \zeta_{,\mu} = & - \left\{ (1 - \mu^2) \left( 1 + r \frac{B_{,r}}{B} \right)^2 + \left[ \mu - (1 - \mu^2) \frac{B_{,r}}{B} \right]^2 \right\}^{-1} \left[ \frac{1}{2} B^{-1} \{ r^2 B_{,rr} - [(1 - \mu^2) B_{,\mu}]_{,\mu} - 2\mu B_{,\mu} \} \right. \\ & \times \left\{ -\mu + (1 - \mu^2) \frac{B_{,\mu}}{B} \right\} + r \frac{B_{,r}}{B} \left[ \frac{1}{2} \mu + \mu r \frac{B_{,r}}{B} + \frac{1}{2} (1 - \mu^2) \frac{B_{,\mu}}{B} \right] + \frac{3}{2} \frac{B_{,\mu}}{B} \left[ -\mu^2 + \mu(1 - \mu^2) \frac{B_{,\mu}}{B} \right] \\ & - (1 - \mu^2) r \frac{B_{,\mu r}}{B} \left( 1 + r \frac{B_{,r}}{B} \right) - \mu r^2 (\nu_{,r})^2 - 2(1 - \mu^2) r \nu_{,\mu} \nu_{,r} + \mu(1 - \mu^2) (\nu_{,\mu})^2 - 2(1 - \mu^2) r^2 B^{-1} B_{,r} \nu_{,\mu} \nu_{,r} \\ & + (1 - \mu^2) B^{-1} B_{,\mu} [r^2 (\nu_{,r})^2 - (1 - \mu^2) (\nu_{,\mu})^2] + (1 - \mu^2) B^2 e^{-4\nu} \left\{ \frac{1}{4} \mu r^4 (\omega_{,r})^2 + \frac{1}{2} (1 - \mu^2) r^3 \omega_{,\mu} \omega_{,r} \right. \\ & \left. - \frac{1}{4} \mu (1 - \mu^2) r^2 (\omega_{,\mu})^2 + \frac{1}{2} (1 - \mu^2) r^4 B^{-1} B_{,r} \omega_{,\mu} \omega_{,r} - \frac{1}{4} (1 - \mu^2) r^2 B^{-1} B_{,\mu} [r^2 (\omega_{,r})^2 - (-\mu^2) (\omega_{,\mu})^2] \right\} \Big], \quad (8) \end{aligned}$$

where, in the equation for  $\zeta_{,\mu}$ , we introduced  $\mu \equiv \cos(\theta)$ .

The projection of the conservation of the energy-momentum tensor, normal to the 4-velocity,  $(\delta_b^c + u^c u_b) \nabla_a T^{ab} = 0$ , leads to the hydrostationary equilibrium equation:

$$P_{,i} + (\varepsilon + P) \left[ \nu_{,i} + \frac{1}{1 - v^2} \left( -v v_{,i} + v^2 \frac{\Omega_{,i}}{\Omega - \omega} \right) \right] = 0, \quad (9)$$

where  $i = 1, 2, 3$  and, as usual,  $A_{,i} \equiv \partial A / \partial x^i$ .

For a barotropic EOS,  $P = P(\varepsilon)$ , and in the case of uniform rotation which we adopt in this work, the above hydrostationary equilibrium equation has a first integral that can be written as

$$\int_0^P \frac{dP}{\varepsilon + P} - \ln(u^a \nabla_a t) = \nu|_{\text{pole}}, \quad (10)$$

where the constant of motion has been obtained, for instance, at the pole of the star (see, e.g., Ref. [21]).

### III. EQUATION OF STATE

To obtain a solution to the field equations, the matter EOS must be supplied. In general, a NS is composed of two regions, namely, the core and the crust. The core, with densities overcoming the nuclear saturation value,  $\rho_{\text{nuc}} \approx 3 \times 10^{14} \text{ g cm}^{-3}$ , is composed of a degenerate gas of baryons (e.g., neutrons, protons, hyperons) and leptons (e.g., electrons and muons). The crust, in its outer region ( $\rho \leq \rho_{\text{drip}} \approx 4.3 \times 10^{11} \text{ g cm}^{-3}$ ), is composed of ions and electrons, while in its inner region ( $\rho_{\text{drip}} < \rho < \rho_{\text{nuc}}$ ), there is an additional component of free neutrons dripped out from nuclei. For the crust, we adopt the Baym-Pethick-Sutherland

(BPS) EOS [23]. For the core, here we adopt modern models based on relativistic mean-field (RMF) theory. Indeed, RMF models have become the most used ones in NS literature; with their success mainly owing to important properties such as Lorentz covariance, intrinsic inclusion of spin, a simple mechanism of saturation for nuclear matter, and being consistently relativistic, they do not violate causality (see, e.g., Ref. [24]). We adopt, as is now becoming traditional, an extension of the original formulation of Boguta and Bodmer [25] in which nucleons interact via massive meson mediators of different nature providing the attractive long range (scalar  $\sigma$ ) and repulsive short range (vector  $\omega$ ) of the nuclear force, isospin and surface effects (vector  $\rho$ ). Meson-meson interactions can also be present; for instance, in the version of Boguta and Bodmer [25] a self-interacting scalar field potential is present in the form of a quartic polynomial with adjustable coefficients. Here we consider the possibility of including, in addition to such a potential, vector-vector interactions of the  $\omega$  meson. For a very recent and comprehensive analysis of the performance of several RMF models in the description of observed properties of ordinary nuclei, we refer the reader to Ref. [26], and for a brief historical and chronological reconstruction of the developments of the RMF models, see Ref. [27].

Thus, we constrain ourselves to models in which the energy density and pressure are given by (in units with  $\hbar = c = 1$ ) [26]

$$\begin{aligned} \varepsilon = & \frac{1}{2} m_\sigma^2 \sigma^2 + \frac{g_{\sigma 2}}{3} \sigma^3 + \frac{g_{\sigma 3}}{4} \sigma^4 - \frac{1}{2} m_\omega^2 \omega_0^2 - \frac{g_{\omega 3}}{4} (g_\omega^2 \omega_0^2)^2 \\ & - \frac{1}{2} m_\rho^2 \rho_0^2 + g_\omega \omega_0 n_B + \frac{g_\rho}{2} \rho_0 n_3 + \sum_{i=n,p,e,\mu} \varepsilon_i, \quad (11a) \end{aligned}$$

$$P = -\frac{1}{2}m_\sigma^2\sigma^2 - \frac{g_{\sigma 2}}{3}\sigma^3 - \frac{g_{\sigma 3}}{4}\sigma^4 + \frac{1}{2}m_\omega^2\omega_0^2 + \frac{g_{\omega 3}}{4}(g_\omega^2\omega_0^2)^2 + \frac{1}{2}m_\rho^2\rho_0^2 + \sum_{i=n,p,e,\mu} P_i, \quad (11b)$$

where  $m_{\sigma,\omega,\rho}$  are the masses of the scalar and vector mesons,  $g_{\sigma 2,3}$ ,  $g_\omega$ ,  $g_{\omega 3}$  are coupling constants,  $\sigma$  denotes the scalar meson and  $\omega_0$  and  $\rho_0$ , denote the time component of the  $\omega$  and  $\rho$  vector mesons, respectively. The components  $\varepsilon_i$  and  $P_i$  for each kind of particle considered are

$$\varepsilon_{n,p} = \frac{2}{(2\pi)^3} \int_0^{k_{n,p}^F} \sqrt{k^2 + (m_{n,p}^*)^2} d^3k, \quad (12a)$$

$$\varepsilon_{e,\mu} = \frac{2}{(2\pi)^3} \int_0^{k_{e,\mu}^F} \sqrt{k^2 + (m_{e,\mu})^2} d^3k, \quad (12b)$$

$$P_{n,p} = \frac{1}{3} \frac{2}{(2\pi)^3} \int_0^{k_{n,p}^F} \frac{k^2}{\sqrt{k^2 + (m_{n,p}^*)^2}} d^3k, \quad (12c)$$

$$P_{e,\mu} = \frac{1}{3} \frac{2}{(2\pi)^3} \int_0^{k_{e,\mu}^F} \frac{k^2}{\sqrt{k^2 + (m_{e,\mu})^2}} d^3k, \quad (12d)$$

where  $m_i^*$  is the effective mass of baryons.

The scalar, isospin, and baryon densities are given, respectively, by

$$n_s = \frac{2}{(2\pi)^3} \sum_{i=n,p} \int_0^{k_i^F} \frac{m_i^*}{\sqrt{k^2 + (m_i^*)^2}} d^3k, \quad (13a)$$

$$n_3 = n_p - n_n, \quad (13b)$$

$$n_B = n_p + n_n, \quad (13c)$$

where  $n_i = (k_i^F)^3 / (3\pi^2)$  are the particle number densities, with  $k_i^F$  the particle Fermi momenta.

The equations of motion of the meson fields within the RMF approximation are

$$m_\sigma^2\sigma = g_\sigma n_s - g_{\sigma 2}\sigma^2 - g_{\sigma 3}\sigma^3, \quad (14a)$$

$$m_\omega^2\omega_0 = g_\omega n_B - g_{\omega 3}g_\omega(g_\omega\omega_0)^3, \quad (14b)$$

$$m_\rho^2\rho_0 = \frac{g_\rho}{2} n_3. \quad (14c)$$

A barotropic EOS can be obtained iff additional closure relations are supplied. The first condition to be imposed is the request of the stability of matter against beta decay. The second closure equation that has been traditionally adopted is the condition of local charge neutrality of the system. It has recently been shown that the latter condition is not fully consistent with the equilibrium equations in the presence of

multicomponent charged constituents such as protons and electrons (see [27] and references therein). Instead, one has to request only global charge neutrality. The new system of equations, referred to as Einstein-Maxwell-Thomas-Fermi (EMTF) equations, self-consistently introduce the Coulomb interactions in addition to the strong, weak, and gravitational interactions within a full general relativity framework. It is worth noting that in this case no perfectlike form of the total energy-momentum tensor is obtained since the presence of electromagnetic fields breaks the pressure isotropy. Static NSs fulfilling the EMTF equations were constructed in Ref. [27], and uniformly rotating configurations in the second-order Hartle approximation can be found in Ref. [28]. To construct rotating NSs beyond the slow rotation regime, we take advantage of existing public numerical codes (e.g., the RNS code; see Sec. V) that solve the field equations without any limitation of the rotation rate of the star. However, an implementation of the equations and boundary conditions of the EMTF system within these codes is not yet available. Thus, as a first step, we adopt the condition of local charge neutrality, bearing in mind the necessity of a future implementation of the EMTF equations of equilibrium in the fast rotation regime.

With both the beta equilibrium and the local charge neutrality conditions, a numerical relation between the energy density and the pressure can be obtained. Here we adopt the nuclear parametrizations (for the specific values of the coupling constants, particle, and meson field masses) NL3 [29], TM1 [30], and GM1 [31,32]. In Fig. 1, we compare and contrast the three selected EOS used in this work in the nuclear and supranuclear regimes, relevant for NS cores. In Sec. V, we show how this selection of EOSs is physically relevant, as well as from the astrophysical point of view.

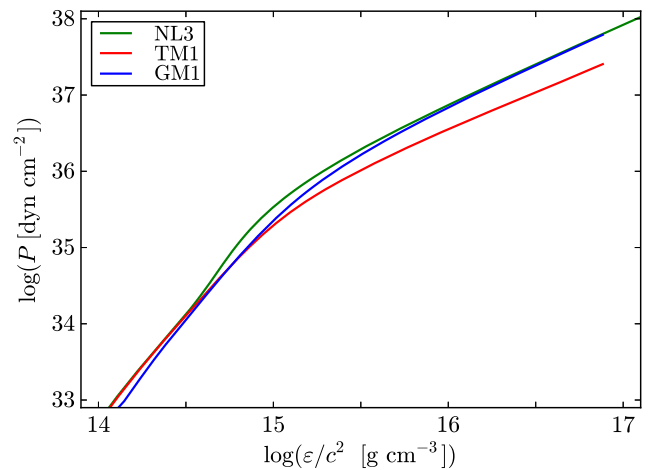


FIG. 1 (color online). Pressure-energy density relation for the three EOS (TM1, GM1, and NL3) used in the present article.

#### IV. STABILITY OF EQUILIBRIUM MODELS

To solve the system of field equations (5)–(8) and the hydrostationary equilibrium equation (10), one has to fix one (in the spherical static case) or two parameters (in the rotating case). The first quantity one has to fix is the central value of the energy density,  $\varepsilon_c$ . For a rotating model, one can choose the second parameter among different possibilities: the axes ratio ( $r_{\text{pol}}/r_{\text{eq}}$ ) of coordinate radii, angular velocity ( $\Omega$ ), dimensionless angular momentum ( $j$ ), gravitational mass ( $M$ ), or baryonic mass ( $M_b$ ). Thus, it is always possible to construct a sequence of rotating models by fixing a value of the second parameter and letting the central energy density vary in a given range which is constrained to stability limits that we now discuss.

The first limit on the stability of uniformly rotating configurations which we take into account is given by the sequence of maximally rotating stars, also referred to as the Keplerian or mass-shedding sequence. In all the stars belonging to such a sequence, the gravitational force equals the centrifugal force at the star equator, in such a way that faster rotation rates would induce the expulsion of mass from the star. The RNS code calculates this sequence by decreasing the axis ratio (which corresponds to an increase in angular velocity) until the angular velocity equals the one of a particle orbiting the star at its equator.

Another limit to the physically relevant models is determined by the so-called secular axisymmetric instability. For static configurations, the maximum stable mass (the critical mass) coincides with the first maximum of a sequence of configurations with increasing central density, namely, the first point where  $\partial M/\partial \varepsilon_c = 0$ , with  $M$  the mass of a configuration with central density  $\varepsilon_c$ . At this point, the frequency of the radial perturbations vanishes. For higher densities, imaginary frequencies are obtained which lead to nonoscillatory perturbations, hence an instability. Thus, for static configurations, a turning point of the  $M - \varepsilon_c$  relation locates the onset of unstable configurations. This instability proceeds on secular timescales, i.e., not dynamical, so that it proceeds for long times, allowing the star to accommodate itself to the energy loss that occurs when going from one equilibrium point to another during gravitational collapse (see, e.g., Ref. [33] and references therein). As shown by Friedman, Ipser, and Sorkin in [33], the turning-point method leading to points of secular instability can also be used in uniformly rotating stars as follows. In a constant angular-momentum sequence, the turning point of a sequence of configurations with increasing central density separates secularly stable from secularly unstable configurations. Namely, secular axisymmetric instability sets in at

$$\left. \frac{\partial M(\varepsilon_c, J)}{\partial \varepsilon_c} \right|_{J=\text{constant}} = 0, \quad (15)$$

and therefore, the curve connecting all the maxima (turning points) limits the stability region. The intersection of such a limiting curve with the Keplerian sequence gives the fastest

possible configuration. It is important to mention that the numerical code adopted (described in the next section) builds sequences of constant dimensionless angular momentum, defined as

$$j \equiv \frac{cJ}{GM_\odot^2}, \quad (16)$$

which is the quantity we refer to in the sequel.

The angular momentum  $J$  is computed from the definition

$$J = \int_\Sigma T_{ab} \phi^a \hat{n}^b dV, \quad (17)$$

with  $\Sigma$  a spacelike 3-surface,  $\hat{n}^a = \nabla_a t / |\nabla_b t \nabla^b t|$  the unit normal vector field to the  $t$ -constant spacelike hypersurfaces, and  $dV = \sqrt{|^3g|} d^3x$  the proper 3-volume element (with  $^3g$  the determinant of the 3-metric). With this, Eq. (17) becomes [22]

$$J = \int B^2 e^{2\zeta - 4\nu} \frac{(\varepsilon + P)v}{1 - v^2} r^3 \sin^2(\theta) dr d\theta d\phi. \quad (18)$$

#### V. MASS-RADIUS RELATION, OBSERVATIONAL CONSTRAINTS, AND STABILITY REGION

In the literature there are many different numerical schemes and, consequently, codes to compute relativistic, rotating figures of equilibrium. For the numerical integration of the equilibrium equations, in this work we use the public code RNS [34] by Stergioulas and Friedman [35]. This code is a numerical implementation based on the scheme by Cook, Shapiro, and Teukolsky [36] (first implemented for realistic NS EOS in [20]), which is a modified version of the method envisaged by Komatsu, Eriguchi, and Hachisu [37]. We refer the reader to Ref. [21] for further details on the numerical schemes.

The major intuitive effect of rotation is to deform the figure of equilibrium with respect to the spherical static counterpart. This can be seen from many points of view. For instance, we can compute sequences of constant angular velocity  $\Omega$ . An important aspect should be taken into account however: the RNS code builds fast rotating models starting from a spherical (static) guess and decreases the polar to an equatorial radii ratio until the fixed parameter (e.g., the angular velocity) is reached with a prescribed accuracy. Thus, the axes ratio is a parameter used intrinsically by the numerical method, while other parameters (see the beginning of the previous section for a list) can be chosen but are reached by spanning decreasing values of the axis ratio. In particular, as an example, the code does not converge for every value of fixed angular velocity in every range of central energy density, and the range of convergence is reduced by decreasing the angular velocity. To be more precise, choosing fixed rotation frequencies below 300 Hz, the code fails to converge in the entire range in which equilibrium models should exist

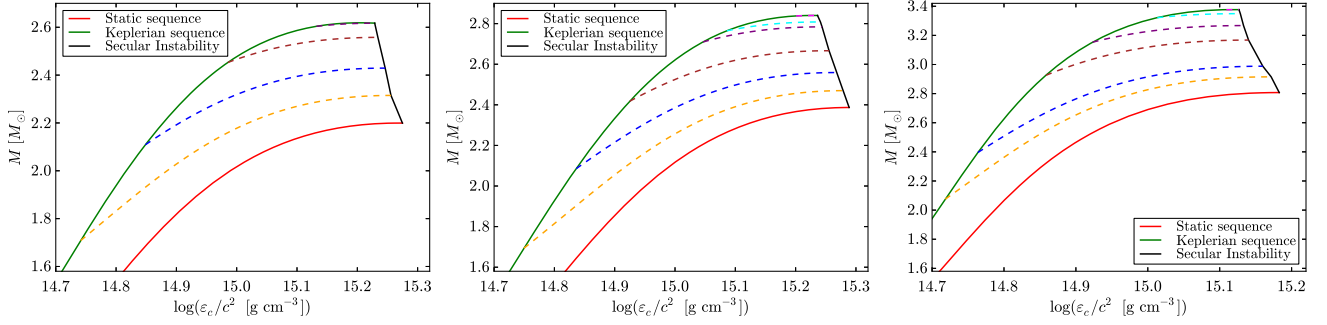


FIG. 2 (color online). Gravitational mass is plotted against central energy density for  $j$ -constant sequences obtained with the EOS TM1, GM1, and NL3 (from top to bottom). In this plot and hereafter, the red, green, and black curves represent, respectively, the static sequence, the Keplerian sequence, and the limit for secular stability. Here, other colors stand for various  $j$ -constant sequences.

(thus between the Keplerian and secular instability limits), even adopting a very dense numerical grid (300 angular times 600 radial points), different accuracy and tolerance values (down to  $10^{-16}$ ), or values of a relaxation factor from 1 to 0.8. Effectively, the code does converge for this kind of rotation frequency, but in very limited ranges of energy density. Thus, how can the slow rotation regime be recovered for every meaningful density? As technical advice, we mention that one could first compute sequences keeping various values of the axes ratio constant (in the vicinity of unity) and then select, in this set of models, the ones with small values of a particular angular velocity. With this simple method we construct the sequences with low rotation frequency (e.g., models from 50 Hz to 200 Hz). For other values of rotation frequency and for all other constant parameter sequences, we achieved optimal convergence using a 300 angular times 600 radial points numerical grid, and accuracy and tolerance of  $10^{-8}$ , while the relaxation parameter was not necessary.

Figure 2 shows the total mass-central energy density plane for the selected EOS TM1, GM1, and NL3. We also show the stability limits discussed above in Sec. IV and show explicitly some constant angular-momentum sequences.

Figure 3 shows instead the total mass-central energy density plane, but in this case, we show explicitly some selected constant rotation frequency sequences ranging from 50 Hz all the way up to the rotation frequency of the fastest observed pulsar, PSR J1748–2446ad, with  $f = \Omega/(2\pi) \approx 716$  Hz [38].

In Fig. 4 we plot the same  $\Omega$ -constant sequences to show the relation between  $M$  and the equatorial radius,  $R_{\text{eq}}$ .

With the knowledge of the mass-radius relations predicted by the theory, we are now in a position to compare and contrast them with existing observational constraints, in order to validate the selection of EOS of the present work, not only from the already-presented physical aspects, but also from the astrophysical ones. Current observational constraints on the mass-radius relation of NSs are as follows (see Fig. 5):

- (i) *Most massive NS observed.*—The mass value of the most massive NS observed is the one of PSR

J1614–2230 with  $2.01 \pm 0.04M_{\odot}$  [39]. The rotation frequency of this pulsar is 46 Hz; thus, the deviations from spherical symmetry are negligible. This implies that every mass-radius relation for nonrotating NSs must have a maximum stable mass larger than this value.

- (ii) *Fastest observed NS.*—The highest rotation frequency observed in a pulsar is the one from PSR J1748–2446ad with  $f = 716$  Hz [38]. The constant frequency sequence of this value for any mass-radius relation must have at least one stable configuration that supports such a rotation frequency; namely, the constant frequency sequence for this pulsar must lie within the region of stability. This is actually a very weak constraint since most NS models allow much higher rotation frequencies. Interestingly, as we show below, the construction of the constant frequency sequence for PSR J1748–2446ad allows us to infer a lower mass for this pulsar.
- (iii) *Constraints on the NS radius.*—Since the surface temperatures of not-so-young NSs ( $t > 10^3$ – $10^4$  y) are of the order of a million degrees (see, e.g., Ref. [13]), their thermal spectrum is expected to peak in the soft x rays. Thus, the modeling of the NS x-ray emission appears to be, at present, one of the most promising methods to obtain information on the NS radius. Systems that are currently used to this aim are isolated NSs, quiescent low-mass x-ray binaries (qLMXBs), NS bursters, and rotation-powered millisecond pulsars (see Ref. [40] and references therein). From the modeling of the observed spectrum, the radius of the NS as measured by an observer at infinity,  $R_{\infty} = R/\sqrt{1 - 2GM/(c^2R)}$ , can be extracted.<sup>1</sup> The observation of a preferable

<sup>1</sup>Actually, accurate spectra modeling leads to preferable values for both mass and radius; however, for a simpler comparison between different results from different methods and for a simple test of the mass-radius relation, it is sufficient to plot the constraints obtained from the values of  $R_{\infty}$  consistent with the data [41].

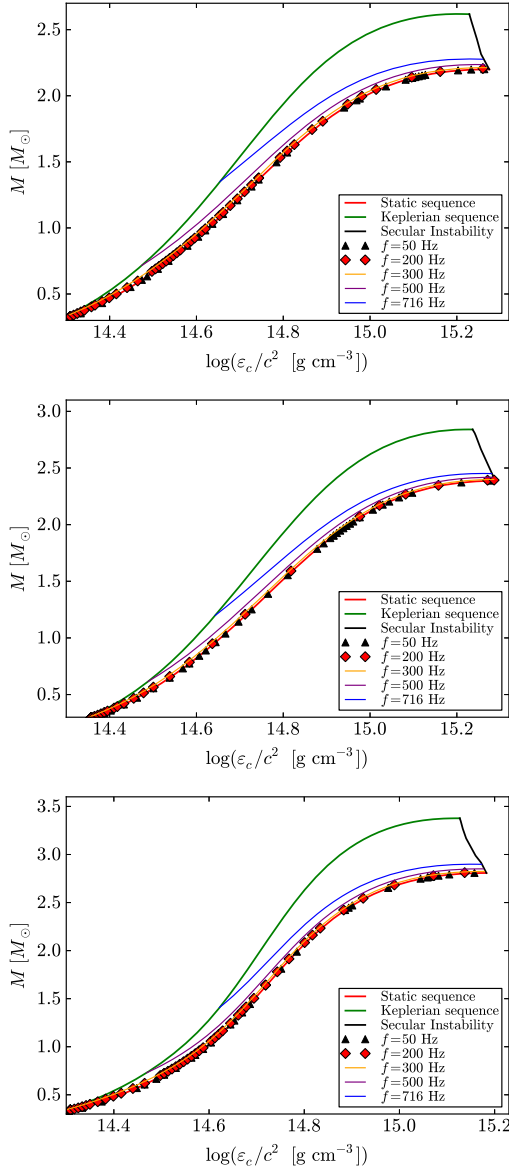


FIG. 3 (color online). Mass versus central energy density using the EOS TM1, GM1, and NL3 (from top to bottom) set of parameters. Red and green curves represent the static and Keplerian sequences. Other colors correspond to constant frequency sequences of values 716 Hz (fastest observed pulsar; blue), 500 Hz (purple), 300 Hz (orange), 200 Hz (red diamonds), and 50 Hz (black triangles).

radius at infinity clearly represents a constraint on the NS mass-radius relation since the above definition for  $R_\infty$  can be rewritten as  $2GM/c^2 = R - R^3/(R_\infty^3)$ . In Ref. [42] (see, also, Ref. [43]), the x-ray emission from the NSs in the qLMXBs M87, NGC 6397, M13,  $\omega$  Cen, and NGC 6304 was revisited, and in Ref. [41] the one from the NS X7 in the Globular Cluster 47 Tucanae was examined. From the extracted values of  $R_\infty$  consistent with these observational data at 90% confidence level, we

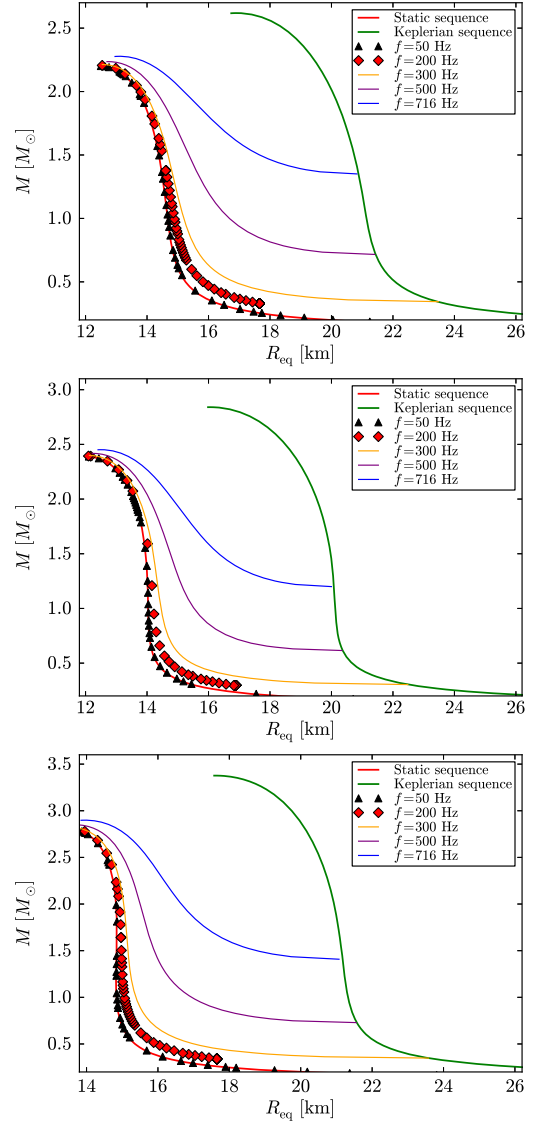


FIG. 4 (color online). Mass versus equatorial radius using the EOS TM1, GM1, and NL3 (from top to bottom) set of parameters for the same sequences as in Fig. 3. The convention of the plot colors and symbols is the same as in Fig. 3.

can conclude that the current x-ray data very weakly constrains the mass-radius relation, allowing radii in the interval  $R_\infty = [7.64, 18.86]$ , where the lower limit is obtained for NGC 6304 and the upper one for X7. It is important to mention that x-ray measurements suffer from a variety of uncertainties, which are the main reason for the very large spread in possible NS radii. The spectra modeling depends on the atmosphere composition, magnetic fields, accurate knowledge of the distance to the source, hence the extinction, and, to some extent, on the NS exterior geometry that could be affected by the rotation of the NS in the case of some LMXBs which could harbor NSs rotating with frequencies of

a few hundreds of Hz (see, e.g., Ref. [44] for details). In these latter cases, a more reliable comparison between theory and the above data constraints, which assume spherical symmetry, could be obtained by plotting the mass-radius relation using, instead of the equatorial radius, a mean or average spherical radius such as the authalic radius,  $\langle R \rangle = (2R_{\text{eq}} + R_{\text{pol}})/3$ . However, for the purposes of this work, it is sufficient to make a comparison with the mass-radius relation produced by the nonrotating configurations.

An additional constraint to the mass-radius relation might come from the request of causality to the EOS, namely, the condition that the speed of sound in the NS interior cannot exceed the speed of light. However, for the present set of EOS, this condition is automatically satisfied by construction since the models are relativistic. One can therefore see from Fig. 5 that the spherical (static) models (solid curves) obtained by the EOS selection of this work are in good agreement with the current constraints of the NS mass-radius relation determined by the most updated observational data.

An often useful physical quantity to be computed is the binding energy of the configurations, or the relation between the baryonic mass and the gravitational mass.

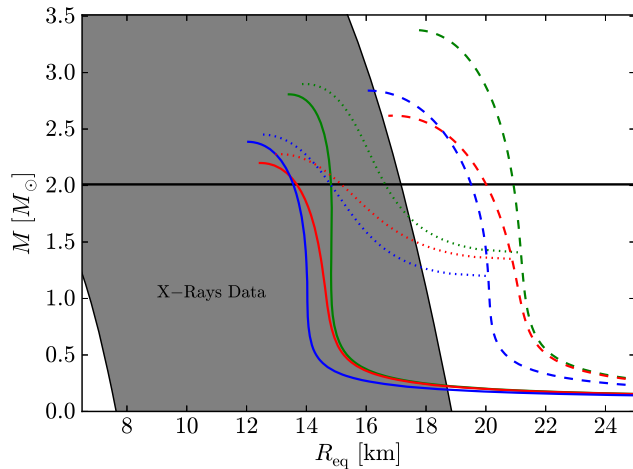


FIG. 5 (color online). Mass versus equatorial radius relation using the TM1, GM1, and NL3 EOS (red, blue, and green, respectively), plotted together with up-to-date observational constraints. Solid color curves represent static NS configurations; dotted color curves represent the sequence of models rotating with spin frequency of the fastest observed pulsar (PSR J1748–2446ad),  $f = 716$  Hz; and dashed color curves represent sequences of models rotating at the Keplerian frequency. The gray-shaded region corresponds to the constraints given by the x-ray data, while the horizontal lines are the lower and upper bounds to the mass of the most massive observed pulsar, PSR J1614–2230, namely,  $M = 2.01 \pm 0.04 M_{\odot}$ . Further details of these constraints can be found in the text.

For nonrotating NSs, we found that for the three analyzed EOS, the following relations hold:

$$\begin{aligned} \frac{M_b}{M_{\odot}} &\approx \frac{M}{M_{\odot}} + \frac{13}{200} \left( \frac{M}{M_{\odot}} \right)^2, \\ \frac{M}{M_{\odot}} &\approx \frac{M_b}{M_{\odot}} - \frac{1}{20} \left( \frac{M_b}{M_{\odot}} \right)^2, \end{aligned} \quad (19)$$

where  $M_b$  is the baryonic mass. The apparent universality of these relations for the present set of EOS points to a universal behavior of the binding energy, namely independent of the EOS. The maximum relative errors obtained for nonrotating sequences of GM1, TM1, and NL3 are, respectively, 1.4%, 1.3%, and 0.99%. For rotating configurations,  $M = M(M_b, J)$  or  $M_b = M_b(M, J)$ , we find that for our set of EOS, there is indeed a common relation given by

$$\frac{M_b}{M_{\odot}} = \frac{M}{M_{\odot}} + \frac{13}{200} \left( \frac{M}{M_{\odot}} \right)^2 \left( 1 - \frac{1}{130} j^{1.7} \right), \quad (20)$$

which is accurate within an error of 2%, and which duly generalizes Eq. (19).

Turning back to the above plots, we can clearly see that, as expected, the higher the frequency of rotation, the higher the value of the mass at which the departures from the nonrotating mass-radius relation begin. We find that for rotation frequencies  $\lesssim 200$  Hz (or rotation periods  $\gtrsim 5$  ms), the nonrotating star becomes an accurate representation of the object. This is in accordance with previous results; see, e.g., Fig. 5 in Ref. [45], where it was shown that the moment of inertia of sequences computed with different EOS starts to deviate considerably from the static and the slow rotation Hartle’s approximations for frequencies above  $\sim 0.2$  kHz. As we show below, this is also the case for the moment of inertia in the same range of frequencies (thus, the moment of inertia of nonrotating configurations can be safely approximated with the one of spinning configurations, with frequencies below the aforementioned limit, and vice versa). For higher frequencies, full rotation effects are needed for an accurate description. This is especially important for objects with masses lower than the maximum value, where departures from a nonrotating or slow rotation approximation become more and more evident.

Following this reasoning, it is important to see how a constant frequency sequence imposes structure constraints on a pulsar. Particularly interesting is the case of the  $f = 716$  Hz sequence (blue curve), which corresponds to the fastest observed pulsar, PSR J1748–2446ad. The constant frequency sequence intersects the stability region in two points: at the maximally rotating Keplerian sequence, defining a minimum mass for the pulsar, and at the secular axisymmetric instability limit, in the upper part, defining the maximum possible mass for the given frequency. Clearly, these minimum and maximum mass values depend upon the EOS. For the EOS employed here, we can see that the mass

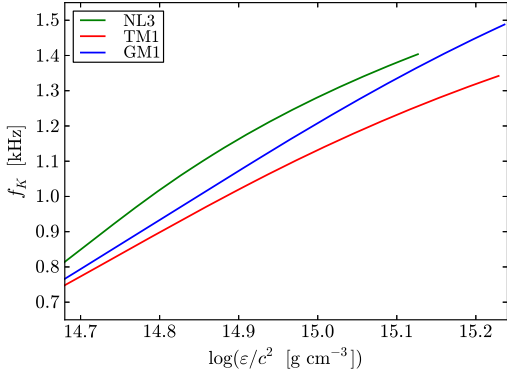


FIG. 6 (color online). Frequency of the maximally rotating configurations (Keplerian sequence) as a function of the total NS mass for the TM1, GM1, and NL3 EOS. The curves end at the maximum frequency configuration, which is located at the intersection between the Keplerian and the secular axisymmetric instability sequences.

of PSR J1748–2446ad has to be  $\gtrsim [1.41, 1.35, 1.20]M_{\odot}$  for NL3, TM1, and GM1, respectively.

We now determine the maximum rotation frequency of NSs. The fastest configuration for a given EOS is the one that terminates the Keplerian sequence, namely, the configuration at the intersection between the Keplerian and the secular axisymmetric instability sequences. We show in Fig. 6 the rotation frequency of the maximally rotating configurations, i.e., the frequencies of the NSs along the Keplerian sequence.

Another important quantity for this discussion is the dimensionless angular momentum (“Kerr parameter”),  $a/M \equiv cJ/(GM^2)$ , which we show in Fig. 7 as a function

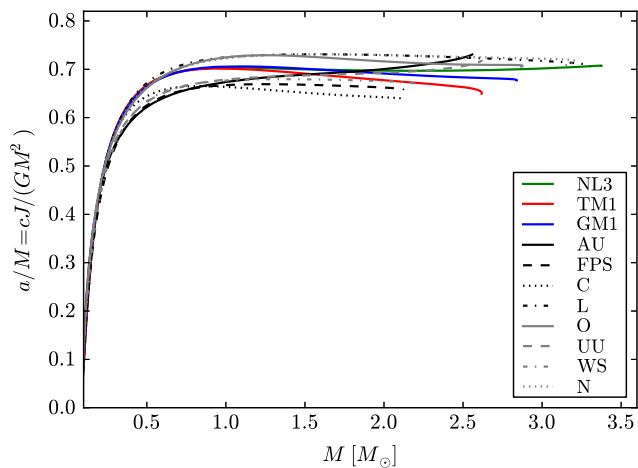


FIG. 7 (color online). Dimensionless angular momentum (“Kerr parameter”),  $a/M \equiv cJ/(GM^2)$ , as a function of the total NS mass along the Keplerian sequence for the EOS selected in this work (colored curves). For comparison, we show the results for additional EOS, taken from a set supplied by the RNS code (EOS.INDEX file). We refer the reader to the RNS web page and references therein for further details of these EOS.

of the total mass for the maximally rotating configurations, namely, the Keplerian sequence. It can be seen that the maximum value attained by the NS,  $(a/M)_{\max} \approx 0.7$ , holds for all the selected EOS. The maximum value is reached for the mass  $[0.96, 1.05, 3.37]M_{\odot}$  for the TM1, GM1, and NL3 EOS, respectively. The existence of such a particular maximum (see, also [46]) EOS-independent, value of  $a$  possibly implies the existence of universal limiting values of the NS compactness and the rotational to gravitational energy ratio. This is a conjecture which deserves further exploration. In the same plot, the same sequences obtained with other already-known EOS (represented by differently dashed curves), assuming widely different kinds of interactions and via different many-body theories, are shown, and the reader can notice a general universal behavior of the dimensionless angular momentum, even if for these other EOS, the exact maximal values of this dimensionless parameter are slightly different. On the other hand, such a general behavior of the  $a$  parameter is not surprising in fact, as it was already shown in Ref. [19], it can be chosen as a parameter to establish a universal I-Love-Q relation. Nevertheless, the important argument here is that, although with different stiffness, our chosen set of EOS presents a common maximal dimensionless angular momentum  $a/M$ .

In Table I we summarize a few relevant quantities of NSs; the maximum stable mass in the nonrotating case, the maximum mass in the case of uniform rotation, the maximum rotation frequency, and the maximum value of the dimensionless angular momentum.

Before closing this section, we would like to provide a formula, useful for astrophysical applications, for the masses of the NSs lying along the secular axisymmetric instability line. Using the dimensionless angular momentum  $j$ , defined in Eq. (16) and related to the Kerr parameter by  $j = (M/M_{\odot})^2 a$ , we obtain

$$M = M_{\max}^{J=0} (1 + k j^l), \quad (21)$$

where the values of  $M_{\max}^{J=0}$  are given in Table I,  $k = [0.017, 0.011, 0.0060]$  and  $l = [1.61, 1.69, 1.68]$  for the EOS TM1, GM1, NL3, respectively. The maximum relative errors obtained for values of mass along the secular axisymmetric instability line with respect to fits for each EOS are, respectively,  $[0.33\%, 0.44\%, 0.45\%]$ .

TABLE I. Some properties of NSs for the selected EOS: critical mass for nonrotating case,  $M_{\max}^{J=0}$ ; maximum mass in uniform rotation,  $M_{\max}^{J \neq 0}$ ; maximum rotation frequency,  $f_{\max}$ ; and maximum dimensionless angular momentum (“Kerr parameter”),  $(a/M)_{\max} \equiv [cJ/(GM^2)]_{\max}$ .

EOS	$M_{\max}^{J=0} [M_{\odot}]$	$M_{\max}^{J \neq 0} [M_{\odot}]$	$f_{\max} [\text{kHz}]$	$(a/M)_{\max}$
TM1	2.20	2.62	1.34	0.70
GM1	2.39	2.84	1.49	0.71
NL3	2.81	3.38	1.40	0.71

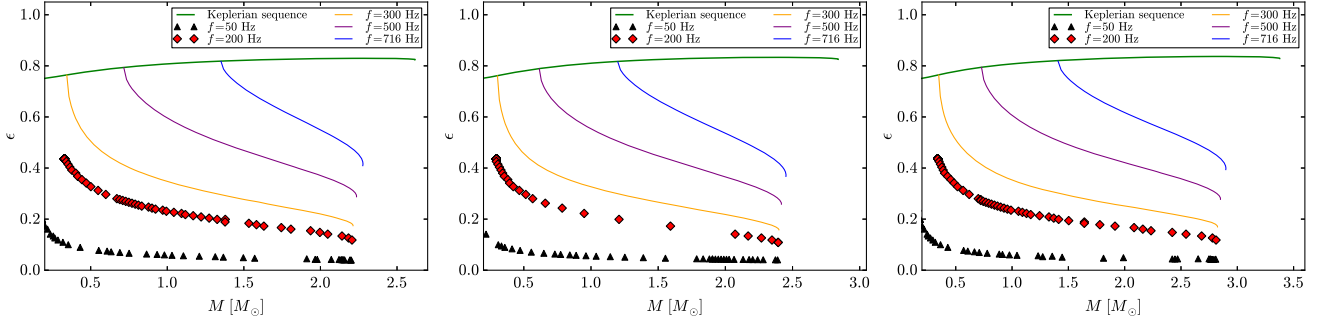


FIG. 8 (color online). Eccentricity versus gravitational mass using EOS with the TM1, GM1, and NL3 (from left to right) set of parameters for the same sequences as in Fig. 3.

## VI. ECCENTRICITY AND MOMENT OF INERTIA

In order to see how a figure of equilibrium becomes deformed by rapid rotation, we compute the eccentricity

$$\epsilon = \sqrt{1 - \left(\frac{R_{\text{pol}}}{R_{\text{eq}}}\right)^2}, \quad (22)$$

which we plot in Fig. 8 as a function of the mass  $M$  for the same constant  $\Omega$  sequences of the previous figures.

It is also interesting to investigate the distribution of the energy density within the figure of equilibrium for both the static and rotational cases for the different EOS. In Fig. 9 we show the contours of constant energy density of a model with central value  $\epsilon_c = 10^{15} \text{ g cm}^{-3}$ , both in the static case and in the rotational one with dimensionless angular momentum  $j = 4$ , for the sake of example, for the GM1 EOS.

We now compute the moment of inertia of the star, which is one of the most relevant properties in pulsar analysis. The moment of inertia can be estimated as [21]

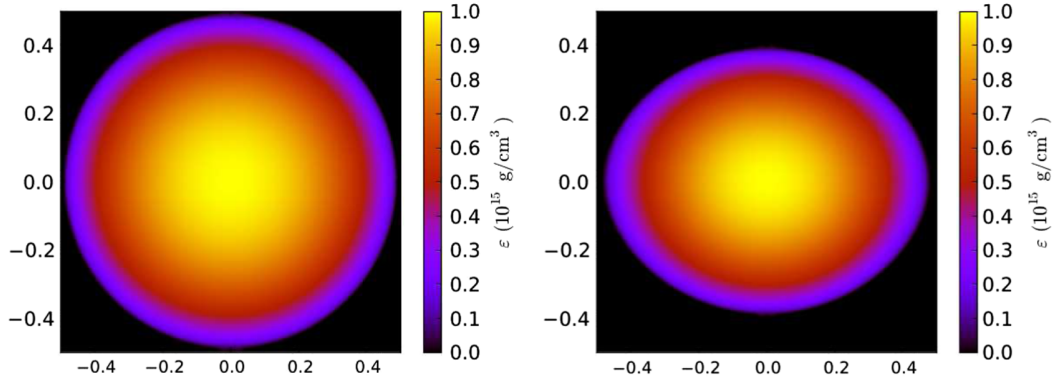


FIG. 9 (color online). Contours of constant energy density of a model with central value  $\epsilon_c = 10^{15} \text{ g cm}^{-3}$ , both in the static case (left plot) and in the rotational one with dimensionless angular momentum  $j = 4$  (right plot) for the GM1 EOS.

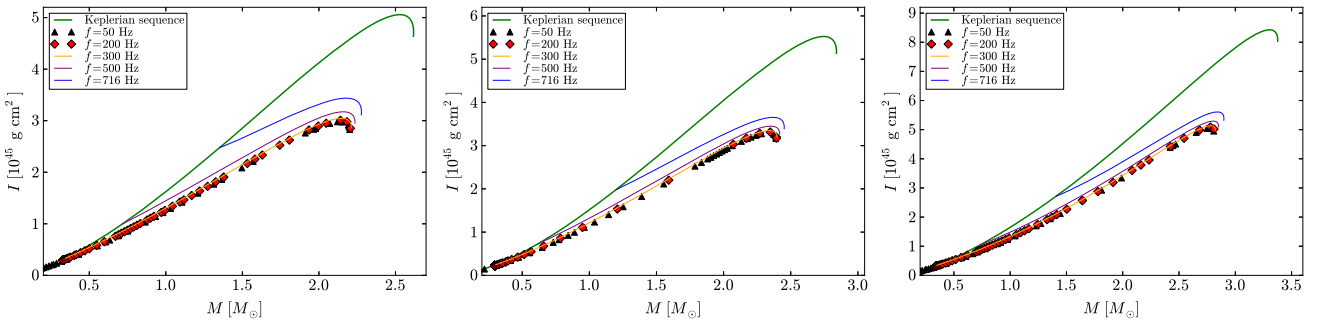


FIG. 10 (color online). Moment of inertia versus mass relation using the EOS TM1, GM1, and NL3 (from top to bottom) set of parameters for the same sequences as in Fig. 3.

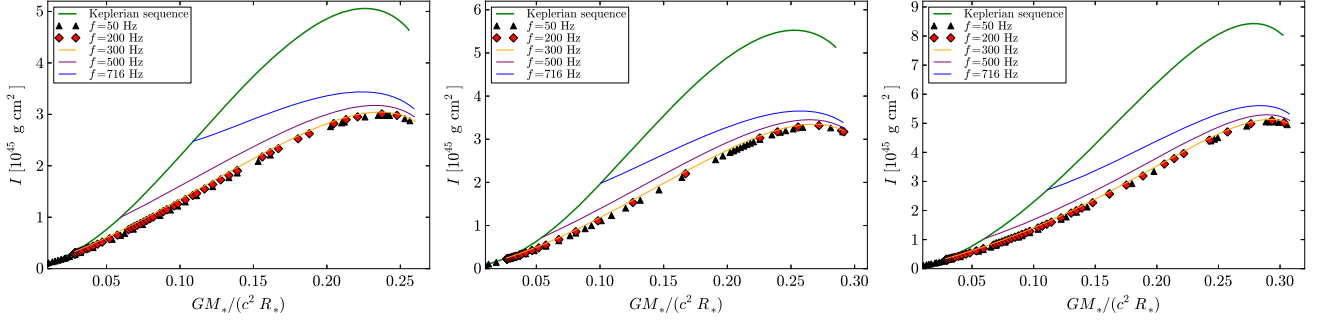


FIG. 11 (color online). Moment of inertia versus compactness using EOS with the TM1, GM1, and NL3 (from left to right) set of parameters for the same sequences as in Fig. 3.

$$I = \frac{J}{\Omega}, \quad (23)$$

where  $J$  is the star angular momentum which is given by Eq. (18).

In Fig. 10 we plot the moment of inertia as a function of the mass for some  $\Omega$ -constant sequences together with the Keplerian sequence, while in Fig. 11 we show the relations between  $I$  and the compactness,  $GM_*/(c^2 R_*)$ , where  $M_*$  and  $R_*$  are the mass and the radius of the spherical configuration with the same central density as the rotating one,  $\varepsilon_c$ .

The above figures confirm that for rotation frequencies  $\lesssim 200$  Hz, or rotation periods  $\gtrsim 5$  ms, the deformation of the star is very small and, indeed, the nonrotating or the

slow rotation regimes can be safely adopted as accurate approximations of the rotating NS.

## VII. QUADRUPOLE MOMENT

The quadrupole moment in the RNS code is given by

$$M_2 = \frac{1}{2} r_{\text{eq}}^3 \int_0^1 \frac{s'^2 ds'}{(1-s')^4} \int_0^1 P_2(\mu') \tilde{S}_\rho(s', \mu') d\mu', \quad (24)$$

where  $r_{\text{eq}}$  is the value of the coordinate radius at the equator,  $\rho \equiv 2\nu - \ln(B)$ ,  $s = r/(r + r_{\text{eq}}) \in [0, 1]$  is a compacted radial coordinate,  $\mu = \cos(\theta)$ ,  $P_2(\mu)$  is the Legendre polynomial of second order, and  $\tilde{S}_\rho = r^2 S_\rho$ , with  $S_\rho$  a source function defined as

$$S_\rho(r, \mu) = e^{\frac{\rho}{2}} \left[ 8\pi e^{2\lambda} (\varepsilon + P) \frac{1+u^2}{1-u^2} + r^2 e^{-2\rho} \left[ \omega_{,r}^2 + \frac{1}{r^2} (1-\mu^2) \omega_{,\mu}^2 \right] + \frac{1}{r} \gamma_{,r} - \frac{1}{r^2} \mu \gamma_{,\mu} \right] + \frac{\rho}{2} \left\{ 16\pi e^{2\lambda} - \gamma_{,r} \left( \frac{1}{2} \gamma_{,r} + \frac{1}{r} \right) \frac{1}{r^2} \gamma_{,\mu} \left[ \frac{1}{2} \gamma_{,\mu} (1-\mu^2) - \mu \right] \right\}, \quad (25)$$

with  $\gamma = \ln(B)$ . However, as shown in Ref. [14], Eq. (24) is not the actual quadrupole moment of the rotating source according to the Geroch-Hansen multipole moments [47–49]. Indeed, the quadrupole moment extracted via Ryan’s expansion method [50] is [14,15]

$$M_2^{\text{corr}} = M_2 - \frac{4}{3} \left( \frac{1}{4} + b_0 \right) M^3, \quad (26)$$

$$b_0 = - \frac{16\sqrt{2\pi} r_{\text{eq}}^4}{M^2} \int_0^{\frac{1}{2}} \frac{s'^3 ds'}{(1-s')^5} \times \int_0^1 d\mu' \sqrt{1-\mu'^2} P(s', \mu') e^{\gamma+2\lambda} T_0^{\frac{1}{2}}(\mu'), \quad (27)$$

where  $M_2$  is given by Eq. (24) and  $T_0^{\frac{1}{2}}$  is the Gegenbauer polynomial of order 0 with normalization  $T_0^{1/2} = \sqrt{2/\pi} C_0$ , with  $C_0$  the traditional 0th-order Gegenbauer polynomial.

Following Refs. [14,15], we numerically computed the correction factor  $b_0$  given by Eq. (27), and then obtained the corrected quadrupole moment through Eq. (26). In Fig. 12 the modulus of  $M_2^{\text{corr}}$  is plotted in logarithmic scale against the gravitational mass for selected constant frequency sequences. Each sequence was stopped at the secular instability limit. We can see that the quadrupole moment is a decreasing function of the mass along a constant frequency sequence, while it is an increasing function along the Keplerian sequence.

We now compare and contrast the above mass quadrupole moment with the one from the Kerr solution,

$$M_2^{\text{Kerr}} = \frac{J^2}{M}. \quad (28)$$

The reason for this is twofold. First, we point out the long-discussed question in astrophysics of whether the Kerr

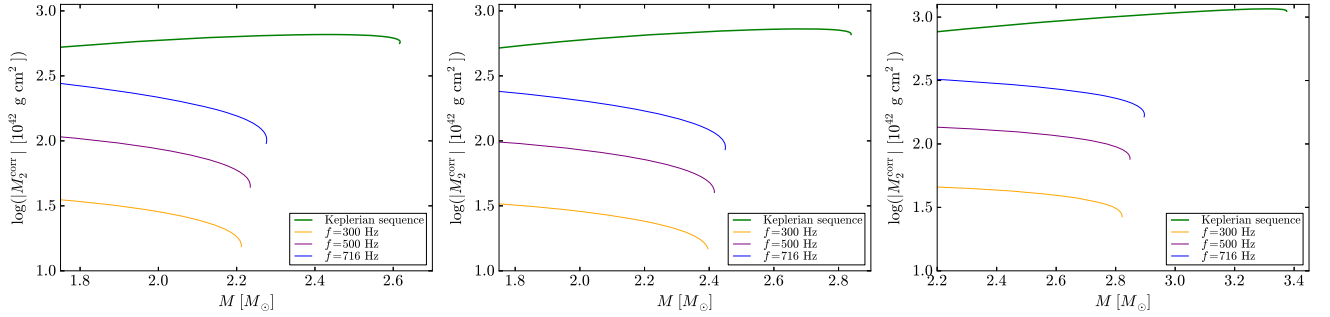


FIG. 12 (color online). The modulus of the corrected value for the mass quadrupole (in logarithmic scale) obtained via Eq. (26) is plotted against gravitational mass for the same constant frequency sequences of Fig. 3.

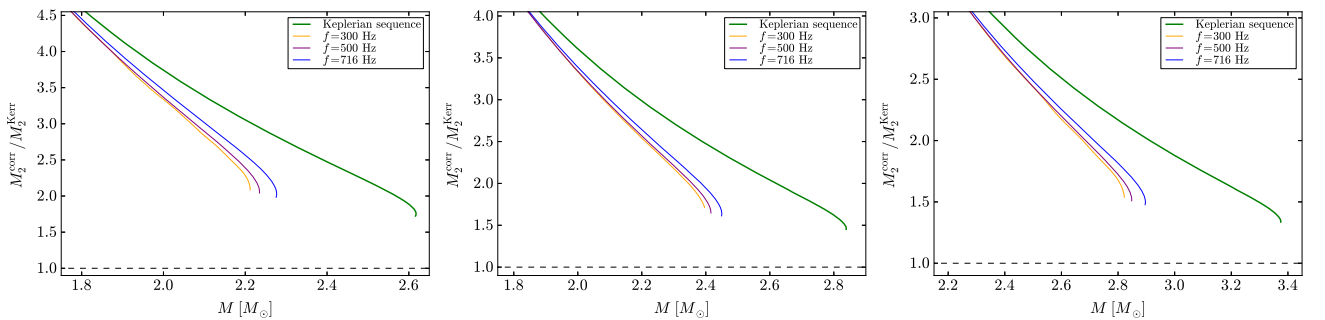


FIG. 13 (color online).  $M_2^{\text{corr}}/M_2^{\text{Kerr}}$  ratio for the same selected sequences of constant frequency of Fig. 12 and EOS TM1, GM1, and NL3 (from left to right). We show here only the region of large masses where  $M_2^{\text{corr}}$  starts to approach the Kerr value  $M_2^{\text{Kerr}}$ .

solution may describe the exterior gravitational field of a realistic astrophysical source besides a black hole; namely, is there any matter content which could generate a Kerr exterior field? (See, e.g., Refs. [51,52] and references therein.) Second, if the answer to the previous question is negative, then one can distinguish a NS from a black hole with the same mass and angular momentum from the knowledge of the quadrupole moment (see, e.g., Ref. [53] and references therein).

In Fig. 13 we show the ratio between the NS quadrupole moment  $M_2^{\text{corr}}$ , given by Eq. (26), and the Kerr solution quadrupole moment  $M_2^{\text{Kerr}}$ , for selected constant frequency sequences. We find that  $M_2^{\text{corr}}$  starts to approach  $M_2^{\text{Kerr}}$ , as intuitively expected, for masses close to the maximum stable value. An interesting feature that we can see from Fig. 13 is that the stiffer the EOS the more the quadrupole moment approaches the Kerr value. This result is in good accordance with previous results that showed that the compactness of the star increases, and also the moment of inertia, Love numbers, and mass quadrupole approach the ones of a black hole, though they will never coincide (see, e.g., Ref. [17]). Moreover, we confirm, in the full rotation regime, the previous result obtained in the slow rotation Hartle approximation [54], that the ratio  $M_2^{\text{corr}}/M_2^{\text{Kerr}}$  is a decreasing function of the NS mass, hence reaching its lowest value at the maximum mass

configuration. Indeed, as we can see from Fig. 13, the larger the maximum mass attained by a NS model, the more the NS quadrupole moment approaches the Kerr solution value, reaching even values  $< 1.5$  for stiff EOS such as the NL3 model.

## VIII. DISCUSSIONS AND CONCLUSIONS

We have computed uniformly rotating NSs for the selected relativistic mean-field nuclear matter model EOS (TM1, GM1, and NL3). Specifically, we have calculated their gravitational mass, equatorial and polar radii, eccentricity, angular momentum, moment of inertia, and quadrupole moment. We have established the region of stability against mass shedding and the secular axisymmetric instability. We have provided plots of all these physical quantities, e.g., as a function of the mass of the configurations. We have also constructed sequences of constant rotation frequency and approximately determined the rotation rate at which deviations of the structure parameters from the spherically symmetric (or slowly rotating) values start, obtaining  $f \approx 200$  Hz, a value in agreement with previous works (see, e.g., Ref. [45]).

From the astrophysical point of view, we have obtained a lower bound for the mass of the fastest observed pulsar, PSR J1748–2446ad with  $f = 716$  Hz, by constructing its

constant rotation frequency sequence and constraining it to be within the stability region: we obtained  $M_{\min} = [1.2\text{--}1.4]M_{\odot}$ , for the EOS used in this work, a prediction submitted for observational verification. We have also obtained a fitting formula relating the baryonic and gravitational mass of nonrotating NSs [see Eq. (19)], independent of the EOS. We have computed a formula for the masses of NSs on the secular instability line as a function of their angular momentum [see Eq. (21)]. We studied the Kerr parameter (dimensionless angular momentum) of NSs and found that it reaches a maximum value  $(a/M)_{\max} \approx 0.7$ , independent of the EOS. This result brings us to the important conclusion that the gravitational collapse of a uniformly rotating NS, constrained to mass-energy and angular-momentum conservation, cannot lead to a maximally rotating Kerr black hole, which, by definition, has  $(a/M)_{\text{BH,max}} = 1$ . We have also shown that the quadrupole moment of realistic NSs does not reach the Kerr value (for the same values of mass and angular momentum), but this is closely approached from above at the maximum mass value, in physical agreement with the no-hair theorem. We have also found that the stiffer the EOS, the more the Kerr solution is approached.

It is important to stress that the results shown in this work for some specific nuclear EOS likely will remain valid in the case of other different models, provided they are

consistent with current observational constraints, especially the mass of PSR J0348 + 0432,  $M = 2.01 \pm 0.04M_{\odot}$  [11]. The existence of such a massive NS clearly favors stiff nuclear EOS, such as the ones obtained via RMF theory, which leads to a critical NS mass higher than this constraint.

To conclude, as already mentioned in Sec. III, we would like to note the importance of considering a global charge neutrality condition for the system, instead of a local one, which needs a new and more complete code to treat these kinds of problems, including the case of fast rotating strange quark stars with crust, which show similar features in the core-crust transition.

## ACKNOWLEDGMENTS

C. C. and S. F. would like to acknowledge GNFM-INdAM and ICRANet for partial support. It is a pleasure to thank D. P. Menezes and R. C. R. de Lima for discussions on the equation of state of NSs and for supplying the EOS tables. J. A. R. acknowledges support from the International Cooperation Program CAPES-ICRANet financed by CAPES—Brazilian Federal Agency for Support and Evaluation of Graduate Education within the Ministry of Education of Brazil.

- 
- [1] P. A. Caraveo, *Annu. Rev. Astron. Astrophys.* **52**, 211 (2014).
  - [2] F. Pacini, *Nature (London)* **216**, 567 (1967).
  - [3] T. Gold, *Nature (London)* **218**, 731 (1968).
  - [4] F. G. Oliveira, J. A. Rueda, and R. Ruffini, *Astrophys. J.* **787**, 150 (2014).
  - [5] J. A. Rueda and R. Ruffini, *Astrophys. J. Lett.* **758**, L7 (2012).
  - [6] C. L. Fryer, J. A. Rueda, and R. Ruffini, *Astrophys. J. Lett.* **793**, L36 (2014).
  - [7] A. K. Harding, *Front. Phys.* **8**, 679 (2013).
  - [8] T. M. Tauris, V. M. Kaspi, R. P. Breton, A. T. Deller, E. F. Keane, M. Kramer, D. R. Lorimer, M. A. McLaughlin, A. Possenti, P. S. Ray, B. W. Stappers, and P. Weltevrede, *Proc. Sci.*, AASKA14 (2015) 039.
  - [9] J. R. Oppenheimer and G. M. Volkoff, *Phys. Rev.* **55**, 374 (1939).
  - [10] J. Antoniadis, M. H. van Kerkwijk, D. Koester, P. C. C. Freire, N. Wex, T. M. Tauris, M. Kramer, and C. G. Bassa, *Mon. Not. Roy. Astron. Soc.* **423**, 3316 (2012).
  - [11] J. Antoniadis *et al.*, *Science* **340**, 1233232 (2013).
  - [12] R. Belvedere, J. A. Rueda, and R. Ruffini, *Astrophys. J.* **799**, 23 (2015).
  - [13] S. M. de Carvalho, R. Negreiros, J. A. Rueda, and R. Ruffini, *Phys. Rev. C* **90**, 055804 (2014).
  - [14] G. Pappas and T. A. Apostolatos, *Phys. Rev. Lett.* **108**, 231104 (2012).
  - [15] K. Yagi, K. Kyutoku, G. Pappas, N. Yunes, and T. A. Apostolatos, *Phys. Rev. D* **89**, 124013 (2014).
  - [16] K. Yagi and N. Yunes, *Science* **341**, 365 (2013).
  - [17] K. Yagi and N. Yunes, *Phys. Rev. D* **88**, 023009 (2013).
  - [18] D. D. Doneva, S. S. Yazadjiev, N. Stergioulas, and K. D. Kokkotas, *Astrophys. J. Lett.* **781**, L6 (2014).
  - [19] S. Chakrabarti, T. Delsate, N. Gürlebeck, and J. Steinhoff, *Phys. Rev. Lett.* **112**, 201102 (2014).
  - [20] G. B. Cook, S. L. Shapiro, and S. A. Teukolsky, *Astrophys. J.* **424**, 823 (1994).
  - [21] N. Stergioulas, *Living Rev. Relativity* **6**, 3 (2003).
  - [22] E. M. Butterworth and J. R. Ipser, *Astrophys. J.* **204**, 200 (1976).
  - [23] G. Baym, C. Pethick, and P. Sutherland, *Astrophys. J.* **170**, 299 (1971).
  - [24] J. A. Rueda, R. Ruffini, Y.-B. Wu, and S.-S. Xue, *Phys. Rev. C* **89**, 035804 (2014).
  - [25] J. Boguta and A. R. Bodmer, *Nucl. Phys.* **A292**, 413 (1977).
  - [26] M. Dutra, O. Lourenço, S. S. Avancini, B. V. Carlson, A. Delfino, D. P. Menezes, C. Providência, S. Typel, and J. R. Stone, *Phys. Rev. C* **90**, 055203 (2014).
  - [27] R. Belvedere, D. Pugliese, J. A. Rueda, R. Ruffini, and S.-S. Xue, *Nucl. Phys.* **A883**, 1 (2012).

- [28] R. Belvedere, K. Boshkayev, J. A. Rueda, and R. Ruffini, *Nucl. Phys.* **A921**, 33 (2014).
- [29] G. A. Lalazissis, J. König, and P. Ring, *Phys. Rev. C* **55**, 540 (1997).
- [30] Y. Sugahara and H. Toki, *Nucl. Phys.* **A579**, 557 (1994).
- [31] N. K. Glendenning and S. A. Moszkowski, *Phys. Rev. Lett.* **67**, 2414 (1991).
- [32] S. Pal, D. Bandyopadhyay, and W. Greiner, *Nucl. Phys.* **A674**, 553 (2000).
- [33] J. L. Friedman, J. R. Ipser, and R. D. Sorkin, *Astrophys. J.* **325**, 722 (1988).
- [34] <http://www.gravity.phys.uwm.edu/rns/>.
- [35] N. Stergioulas and J. L. Friedman, *Astrophys. J.* **444**, 306 (1995).
- [36] G. B. Cook, S. L. Shapiro, and S. A. Teukolsky, *Astrophys. J.* **398**, 203 (1992).
- [37] H. Komatsu, Y. Eriguchi, and I. Hachisu, *Mon. Not. Roy. Astron. Soc.* **237**, 355 (1989).
- [38] J. W. T. Hessels, S. M. Ransom, I. H. Stairs, P. C. C. Freire, V. M. Kaspi, and F. Camilo, *Science* **311**, 1901 (2006).
- [39] P. B. Demorest, T. Pennucci, S. M. Ransom, M. S. E. Roberts, and J. W. T. Hessels, *Nature (London)* **467**, 1081 (2010).
- [40] M. Fortin, J. L. Zdunik, P. Haensel, and M. Bejger, *Astron. Astrophys.* **576**, A68 (2015).
- [41] C. O. Heinke, G. B. Rybicki, R. Narayan, and J. E. Grindlay, *Astrophys. J.* **644**, 1090 (2006).
- [42] J. M. Lattimer and A. W. Steiner, *Eur. Phys. J. A* **50**, 40 (2014).
- [43] C. O. Heinke, H. N. Cohn, P. M. Lugger, N. A. Webb, W. C. G. Ho, J. Anderson, S. Campana, S. Bogdanov, D. Haggard, A. M. Cool, and J. E. Grindlay, *Mon. Not. Roy. Astron. Soc.* **444**, 443 (2014).
- [44] M. Bauböck, F. Özel, D. Psaltis, and S. M. Morsink, *Astrophys. J.* **799**, 22 (2015).
- [45] O. Benhar, V. Ferrari, L. Gualtieri, and S. Marassi, *Phys. Rev. D* **72**, 044028 (2005).
- [46] K.-W. Lo and L.-M. Lin, *Astrophys. J.* **728** (2011) 12.
- [47] R. Geroch, *J. Math. Phys. (N.Y.)* **11**, 1955 (1970).
- [48] R. Geroch, *J. Math. Phys. (N.Y.)* **11**, 2580 (1970).
- [49] R. O. Hansen, *J. Math. Phys. (N.Y.)* **15**, 46 (1974).
- [50] F. D. Ryan, *Phys. Rev. D* **52**, 5707 (1995).
- [51] L. A. Pachón, J. A. Rueda, and J. D. Sanabria-Gómez, *Phys. Rev. D* **73**, 104038 (2006).
- [52] K. Boshkayev, H. Quevedo, and R. Ruffini, *Phys. Rev. D* **86**, 064043 (2012).
- [53] L. A. Pachón, J. A. Rueda, and C. A. Valenzuela-Toledo, *Astrophys. J.* **756**, 82 (2012).
- [54] M. Urbanec, J. C. Miller, and Z. Stuchlík, *Mon. Not. Roy. Astron. Soc.* **433**, 1903 (2013).

**Energy decomposition within Einstein-Born-Infeld black holes**Jonas P. Pereira<sup>1,2,\*</sup> and Jorge A. Rueda<sup>2,3,†</sup><sup>1</sup>*Université de Nice Sophia Antipolis, 28 Avenue de Valrose, 06103 Nice Cedex 2, France*<sup>2</sup>*Dipartimento di Fisica and ICRA, Università di Roma “La Sapienza”,  
Piazzale Aldo Moro 5, I-00185 Rome, Italy*<sup>3</sup>*International Center for Relativistic Astrophysics Network (ICRANet), Coordinating Center,  
Piazza della Repubblica 10, 65122 Pescara, Italy*  
(Received 30 January 2015; published 20 March 2015)

We analyze the consequences of the recently found generalization of the Christodoulou-Ruffini black hole mass decomposition for Einstein-Born-Infeld black holes [characterized by the parameters  $(Q, M, b)$ , where  $M = M(M_{\text{irr}}, Q, b)$ ,  $b$  scale field,  $Q$  charge,  $M_{\text{irr}}$  “irreducible mass,” physically meaning the energy of a black hole when its charge is null] and their interactions. We show in this context that their description is largely simplified and can basically be split into two families depending upon the parameter  $b|Q|$ . If  $b|Q| \leq 1/2$ , then black holes could have even zero irreducible masses and they always exhibit single nondegenerated horizons. If  $b|Q| > 1/2$ , then an associated black hole must have a minimum irreducible mass (related to its minimum energy) and has two horizons up to a transitional irreducible mass. For larger irreducible masses, single horizon structures raise again. By assuming that black holes emit thermal uncharged scalar particles, we further show in light of the black hole mass decomposition that one satisfying  $b|Q| > 1/2$  takes an infinite amount of time to reach the zero temperature, settling down exactly at its minimum energy. Finally, we argue that depending on the fundamental parameter  $b$ , the radiation (electromagnetic and gravitational) coming from Einstein-Born-Infeld black holes could differ significantly from Einstein-Maxwell ones. Hence, it could be used to assess such a parameter.

DOI: 10.1103/PhysRevD.91.064048

PACS numbers: 04.20.-q, 04.70.Dy, 11.10.Ef

**I. INTRODUCTION**

Although solving Einstein equations for a classical charged black hole (BH) (Reissner-Nordström one) is a relatively simple task [1], such an approach does not make evident the relationship between its two parameters, namely its mass ( $M$ ) and charge ( $Q$ ). Intuitively, this relation must exist since electromagnetic energies have their origin in charges, and it can be found in a variety of ways. An interesting notably physical manner was put forward by Christodoulou [2] and Christodoulou and Ruffini [3], by introducing the concept of BH reversible transformations [2]. Such transformations are the only ones that could bring back the BH parameters to their original values after any transformation processed by a test particle with parameters  $m$  and  $q$  (where  $M \gg m$  and  $Q \gg q$ ). Another known approach was due to Bardeen *et al.* [4], which takes advantage of the spacetime symmetries.

It has been recently shown [5], in the context of spherically symmetric spacetimes, that reversible transformations are fully equivalent to the constancy of the event horizon upon such changes for any nonlinear theory of the electromagnetism  $L(F)$  that leads to asymptotically flat solutions. Due to the generality of the analysis, such a constant must be  $2M_{\text{irr}}$ , where  $M_{\text{irr}}$  is the irreducible BH

mass given by the total mass energy of the system in the uncharged case, namely when  $Q = 0$ . Due to this fact,  $M_{\text{irr}}$  must be always positive. The aforementioned equivalence allows us to exchange the problem of solving nonlinear differential equations for nonlinear theories by the problem of solving algebraic equations. This procedure works only for the cases where event horizons are present. We recall that after the seminal work of Bekenstein [6], it is known that the entropy of a black hole is equivalent to its  $M_{\text{irr}}$ . Nevertheless, it is more appealing to our reasoning to make use of the original concept of irreducible mass,  $M_{\text{irr}}$ .

The aim of this work is to elaborate on the consequences of the mass-energy decomposition for nonlinear BHs and their interactions. In order to do it, we use the specific nonlinear theory of electromagnetism due to Born and Infeld (BI) [7]. Such a theory has regained interest due to its analogous emergence as an effective theory to string theory [8]. It was constructed with the purpose of remedying the singular behavior in terms of energy of a pointlike charged particle. The theory introduces a parameter  $b$  identified with the absolute upper limit of the electric field of a system when just electric aspects are present. Born and Infeld fixed this parameter by imposing that in the Minkowski spacetime the associated electromagnetic energy coming from a pointlike electron equals its rest mass (unitarian viewpoint [7]). Nevertheless, the dualistic viewpoint [7] could equally well have been assumed and the parameter  $b$  should be determined by a theory relying on it, such as quantum

\*jonaspedro.pereira@icranet.org  
†jorge.rueda@icra.it

mechanics [7]. Actually, the BI theory has been applied to the description of the hydrogen atom, both the nonrelativistic and relativistic one [9,10], and their numerical analyses show that  $b$  must be much larger than the value initially proposed by BI. Notwithstanding, a definite value has not been obtained.

Rasheed [8] has analyzed mathematically the validity of the zeroth and first laws of black hole mechanics and concluded that they do hold for any nonlinear Lagrangian of the electromagnetism. Although Rasheed concluded that the black hole mass formula for such a case does not keep the same simple functional form as for the Maxwellian Lagrangian, a further scrutiny of the consequences of this fact was not performed. Following our results in Ref. [5], we instead shall analyze in this work some consequences of the black hole mass formula in the case of Einstein-Born-Infeld black holes, and their interactions. Since such a relation establishes a constraint for the parameters of the theory, physically based on conservation laws, the description is expected to be greatly simplified, as it will turn out to be exactly the case. To the best of our knowledge, this has not been done before.

The article is organized as follows. In the next section, the mathematical approach for reversible transformations is briefly elaborated and the mass decomposition for  $L(F)$  theories in the spherically symmetric case is exhibited. In Sec. III, we revisit some aspects of the Einstein-Born-Infeld black hole solution and exhibit the black hole mass decomposition for this theory. In Sec. IV, we analyze some properties of the above-mentioned mass decomposition and show that when  $b$  is finite, there are always intrinsic nonclassical islands of black hole solutions where each member has a single, nondegenerated horizon. Section V is devoted to the study of the consequences of assuming that Einstein-Born-Infeld black holes evaporate within the framework of the mass decomposition. In Sec. VI we analyze the radiation emitted by two interacting Einstein-Born-Infeld black holes and show by means of a toy model that in principle there are alternative ways to infer the constant  $b$  even from astrophysical scenarios. Section VII closes the paper with an analysis of the main points raised.

Units are such that  $c = G = 1$  and the signature of the spacetime is  $-2$ .

## II. BLACK HOLE MASS DECOMPOSITION FOR ANY NONLINEAR THEORY

In the context of spherically symmetric solutions to general relativity minimally coupled to nonlinear Lagrangians of the electromagnetism, it can be shown that the general solution to the metric is [11]

$$ds^2 = e^{\nu(r)} dt^2 - e^{-\nu(r)} dr^2 - r^2(d\theta^2 + \sin^2\theta d\varphi^2), \quad (1)$$

where [5]

$$\begin{aligned} e^{\nu(r)} &= 1 - \frac{2M}{r} + \frac{8\pi}{r} \int_r^\infty r'^2 T^0_0(r') dr' \\ &= 1 - \frac{2M}{r} + \frac{2QA_0}{r} - \frac{2\mathcal{N}}{r}, \end{aligned} \quad (2)$$

$$E_r \doteq -\frac{\partial A_0}{\partial r}, \quad T^\mu_\nu = \frac{4L_F F^{\mu\beta} F_{\nu\beta} - L\delta^\mu_\nu}{4\pi}, \quad \frac{\partial \mathcal{N}}{\partial r} \doteq -Lr^2. \quad (3)$$

We are assuming that the Lagrangian describing the electromagnetic interactions is  $L = L(F)$ ,  $F \doteq F^{\mu\nu} F_{\mu\nu}$ , where  $F_{\mu\nu}$  is the electromagnetic field tensor [1,12]. Besides,  $L_F$  was defined as the derivative of  $L(F)$  with respect to the invariant  $F$  and  $T^\mu_\nu$  is the energy-momentum tensor of the matter fields [1,12], here the electromagnetic fields described by  $L(F)$ . In the above expressions,  $E_r$  is the radial component of the electric field and  $A_0$  is its associated potential. In the expressions for  $A_0$  and  $\mathcal{N}$ , it has been chosen a gauge where they are null at infinity. We stress that for obtaining  $A_0(r)$  and  $\mathcal{N}(r)$  from given  $E_r(r)$  and  $L(F)$ , it is tacit one has to integrate from an arbitrary  $r$  to infinity, since we are interested in black hole solutions [13]. The radial electric field satisfies the equation

$$L_F E_r r^2 = -\frac{Q}{4} \quad \text{or} \quad \frac{\partial L}{\partial E_r} = \frac{Q}{r^2}. \quad (4)$$

In a spherically symmetric spacetime, infinitesimal reversible transformations are defined by

$$\delta M = \delta Q A_0(r_+), \quad (5)$$

where  $r_+$  is the outermost horizon from a given black hole theory, defined as the largest zero of Eq. (3). For a general transformation, one has the formal replacement “ $= \rightarrow \geq$ ” in the above equation.

The customary approach for obtaining the mass formula (energy decomposition) would be integrating Eq. (5), given the outer horizon in terms of the parameters coming from the electromagnetic theory under interest and the spacetime. In general, it turns out to be impossible to work analytically for  $L(F)$  theories in such a case. Since one knows that there is a correlation between black holes and thermodynamics [4,14], one would suspect that Eq. (5) (thermodynamics) is somehow inside the equations of general relativity (or vice versa). It can be shown easily that this is indeed the case, provided that the outer horizon keeps constant under reversible transformations [5]. Since it is so, it follows that the outer horizon must be identified with its associated Schwarzschild horizon (where  $Q = 0$ ), and it will be denoted by  $r_+ = 2M_{\text{irr}}$ .

For the nonlinear theories where the electric potential  $A_0$  is independent of the parameter  $M$ , it follows from the above reasoning and Eq. (3) that

$$\begin{aligned}
M &= M_{\text{irr}} + QA_0|_{r=2M_{\text{irr}}} - \mathcal{N}|_{r=2M_{\text{irr}}} \\
&= M_{\text{irr}} + 4\pi \int_{2M_{\text{irr}}}^{\infty} r'^2 T^0_0(r') dr'. \quad (6)
\end{aligned}$$

The above equation is the way of decomposing the total energy in terms of intrinsic ( $M_{\text{irr}}$ ) and extractable quantities ( $M - M_{\text{irr}}$ ). It can be shown with ease [5] that it implies the so-called generalized first law of black hole mechanics for nonlinear electrodynamics [8], thus superseding it. Notice from the above equation that one could not associate all  $M_{\text{irr}}$  (given  $M$  and  $T^0_0$ ) with the outer horizon. The reason for this is simple: Eq. (6) was defined by  $e^{\nu(2M_{\text{irr}})} = 0$ , which encompasses also  $M_{\text{irr}}$  related to the inner horizon. Nevertheless, it is uncomplicated to single out the set of  $M_{\text{irr}}$  corresponding to the outer horizon. One knows that the condition that leads to the degeneracy of the horizons is the common solution to  $e^{\nu(2M_{\text{irr}})} = 0$  and  $de^{\nu}/dr|_{r=2M_{\text{irr}}} = 0$ . These requirements and Eq. (6) imply that the horizons of black holes are degenerated at the critical points of  $M$  as a function of  $M_{\text{irr}}$ . Hence, since outer horizons are larger than inner ones, it follows that the set of irreducible masses relevant in our analysis is the one that always gives  $dM/dM_{\text{irr}} \geq 0$ . In the mass decomposition approach the region inside the outer horizon is not of physical relevance.

### III. BORN-INFELD LAGRANGIAN

The Born-Infeld Lagrangian  $L_{\text{BI}}$  can be written as (compatible with our previous definitions)

$$L_{\text{BI}} = b^2 \left( 1 - \sqrt{1 + \frac{F}{2b^2}} \right), \quad (7)$$

where  $b$  is the fundamental parameter of the theory and counts for the maximum electric field exhibited by an electrically charged and at rest particle in flat spacetime [7]. This parameter naturally defines a scale to the Born-Infeld theory.

Putting Eq. (7) into Eqs. (3) and (3) and performing the integral from a given arbitrary radial coordinate  $r$  up to infinity, one gets (see for instance Ref. [13])

$$e^{\nu(r)} = 1 - \frac{2M}{r} - \frac{2}{3}b^2 y^2 + \frac{2Q^2}{3\sqrt{|\beta|r}} \mathcal{F}\left[x(r), \frac{1}{\sqrt{2}}\right], \quad (8)$$

where we have defined

$$x(r) \doteq \arccos\left(\frac{r^2 - |\beta|}{r^2 + |\beta|}\right), \quad y^2 \doteq \sqrt{r^4 + \beta^2} - r^2, \quad (9)$$

$$\beta^2 \doteq \frac{Q^2}{b^2}, \quad \mathcal{F}\left[x(r), \frac{1}{\sqrt{2}}\right] = 2 \int_{\frac{r}{\sqrt{|\beta|}}}^{\infty} \frac{du}{\sqrt{1+u^4}}, \quad (10)$$

where  $\mathcal{F}[x(r), 1/\sqrt{2}]$  is the elliptic function of first kind [15].

The modulus of the radial electric field and its scalar potential in this case, as given by the first term of Eqs. (3) and (4), are

$$E_r(r) = \frac{Q}{\sqrt{r^4 + \beta^2}}, \quad A_0(r) = \frac{Q}{2\sqrt{|\beta|}} \mathcal{F}\left[x(r), \frac{1}{\sqrt{2}}\right]. \quad (11)$$

As it is clear from Eq. (11), the electric field of a pointlike charged particle is always finite, as well as its associated scalar potential and they are positive monotonically decreasing functions of the radial coordinate. Hence, from Eq. (5), it implies that the necessary and sufficient condition for extracting energy from an Einstein-Born-Infeld black hole is to use test particles with an opposite charge to the hole.

### IV. ANALYSIS OF THE EINSTEIN-BORN-INFELD MASS FORMULA

The metric given by Eqs. (8), (9) and (10) has been studied in detail in Ref. [13]. It has been pointed out there that the dimensionless quantities  $\tilde{M} \doteq bM$ ,  $\alpha \doteq Q/M$  and  $u \doteq r/M$  are convenient to scrutinize the properties of such a metric. Nevertheless, apparently some interesting properties of Eq. (8) have not been stressed. Under the above definitions, Eq. (8) may be written as

$$\begin{aligned}
e^{\nu(u)} &= 1 - \frac{2}{u} + \frac{2}{3}\tilde{M}^2 u^2 \left( 1 - \sqrt{1 + \frac{\alpha^2}{\tilde{M}^2 u^4}} \right) \\
&\quad + \frac{2\alpha^2}{3u} \sqrt{\frac{\tilde{M}}{|\alpha|}} \mathcal{F}\left[\arccos\left(\frac{\tilde{M}u^2 - |\alpha|}{\tilde{M}u^2 + |\alpha|}\right), \frac{1}{\sqrt{2}}\right]. \quad (12)
\end{aligned}$$

The horizons are obtained as the zeros of the above equation. As a result, one can verify that Eq. (12) has no minimum, and hence it is a monotonic function iff

$$b < \frac{9M^2}{|Q|^3 \mathcal{F}^2\left[\pi, \frac{1}{\sqrt{2}}\right]} \approx \frac{0.654M^2}{|Q|^3}, \quad (13)$$

which can also be cast as

$$M > M_0, \quad M_0 \doteq \frac{\sqrt{b|Q|^3}}{3} \mathcal{F}\left[\pi, \frac{1}{\sqrt{2}}\right]. \quad (14)$$

As the limit of  $u$  going to zero in Eq. (12) shows us, Eq. (13) also guarantees that the associated spacetime will always exhibit just one horizon (not degenerated). The above inequality has no classical counterpart, since it can be formally obtained by taking the limit of  $b$  going to infinity. Equation (13) sets a fundamental inequality

concerning the parameters  $Q$ ,  $b$  and  $M$ . Whenever it is not verified, it does automatically imply the existence of a minimum. A simple analysis shows us that such a requirement can be cast as

$$u_+ \leq \frac{\sqrt{4\tilde{M}^2\alpha^2 - 1}}{2\tilde{M}}, \quad \frac{d}{du}(e^\nu)|_{u=u_+} = 0, \quad (15)$$

which is just the consequence of imposing that  $e^{\nu(u_+)} \leq 0$ ,  $u_+$  being the critical point of  $e^\nu$ , thus guaranteeing the existence of an outer horizon. Just as a reference, in the limit when  $\tilde{M}$  goes to infinity, the above condition reduces to  $|\alpha| \leq 1$ , as it is well known from the Reissner-Nordström solution for assuring the existence of horizons. As the above inequality suggests, the term  $(4b^2Q^2 - 1)$  plays a fundamental role into the horizon description. We shall see that this is also the case in the approach related to the energy decomposition. Specialized to the Born-Infeld Lagrangian, Eq. (7), the total mass [see Eq. (6)] of an Einstein-Born-Infeld black hole can be decomposed as

$$M = M_{\text{irr}} - \frac{8}{3}b^2M_{\text{irr}}^3 \left( \sqrt{1 + \frac{\beta^2}{16M_{\text{irr}}^4}} - 1 \right) + \frac{\sqrt{b|Q|^3}}{3} \mathcal{F} \left[ \arccos \left( \frac{4M_{\text{irr}}^2 - |\beta|}{4M_{\text{irr}}^2 + |\beta|} \right), \frac{1}{\sqrt{2}} \right]. \quad (16)$$

From now on we shall assume that Eq. (16) is a valid decomposition to the total energy of a Einstein-Born-Infeld black hole. A simple analysis tells us that whenever

$$2b|Q| > 1 \quad (17)$$

is valid for the parameter  $Q$ , given  $b$ , Eq. (16) does have a minimum with respect to  $M_{\text{irr}}$ , associated with the critical irreducible mass

$$M_{\text{irr}}^c \equiv M_{\text{irr}}^{\text{min}} = \frac{\sqrt{4b^2Q^2 - 1}}{4b}. \quad (18)$$

Note that  $M_{\text{irr}}^c$  is always related to the case where the horizons are degenerated (extreme black holes), as we have pointed out in Sec. II, and it is always smaller than its classical counterpart,  $|Q|/2$  (where  $M = |Q|$ ). From our previous discussions, the relevant irreducible masses to the analysis for reversible transformations for black holes are  $M_{\text{irr}} \geq M_{\text{irr}}^c$ . Substituting the above critical irreducible mass into Eq. (16), one has that its associated minimum total energy is

$$M_{\text{min}} = \frac{\sqrt{4b^2Q^2 - 1}}{6b} + \frac{\sqrt{b|Q|^3}}{3} \mathcal{F} \left[ x \left( \frac{\sqrt{4b^2Q^2 - 1}}{2b} \right), \frac{1}{\sqrt{2}} \right], \quad (19)$$

which is naturally positive and it can be verified to be smaller than  $M_0$  defined by Eq. (14). For the case  $2b|Q| > 1$ , one can check that an immediate solution to  $M = M_0$  is  $M_{\text{irr}} = 0$  (not of relevance for us for the present case). There also is a nontrivial solution that cannot be expressed analytically in general, that we shall denote by  $M_{\text{irr}}^t$ . This solution is very important since it will delimit the transition from spacelike singularities to timelike ones with respect to the radial coordinate. This signifies that the range of irreducible masses that generalizes Reissner-Nordström black holes (with two horizons) is  $M_{\text{irr}}^{\text{min}} \leq M_{\text{irr}} < M_{\text{irr}}^t$ . An arbitrary black hole with  $M_{\text{irr}} \geq M_{\text{irr}}^t$  shall present a sole horizon and hence when test particles have crossed it, their fate is unavoidably its associated singularity. Note that Reissner-Nordström black holes are such that  $M_{\text{irr}}^t \rightarrow \infty$  and the existence of  $M_{\text{irr}}^t$  for Einstein-Born-Infeld black holes is only due to the finiteness of  $b$ . Figure 1 exemplifies the analysis from the previous sentences for a selected value of the parameter  $b|Q|$  for the case  $2b|Q| > 1$ .

We consider now the case where Eq. (17) is violated. In this case,  $M$ , as given by Eq. (16), is a monotonic function of  $M_{\text{irr}}$ . Since it is given by Eq. (14) when  $M_{\text{irr}} = 0$  and it is monotonic, we conclude that Eq. (14) is always satisfied and therefore the associated singularity is unavoidable for test particles. Just for completeness, Fig. 2 compactifies the above-mentioned properties for a selected value of the parameter  $b|Q|$  such that  $2b|Q| \leq 1$ . Besides, in Fig. 3 we depicted all the different classes associated with the parameter  $b|Q|$ , assuming in all cases it is fixed.

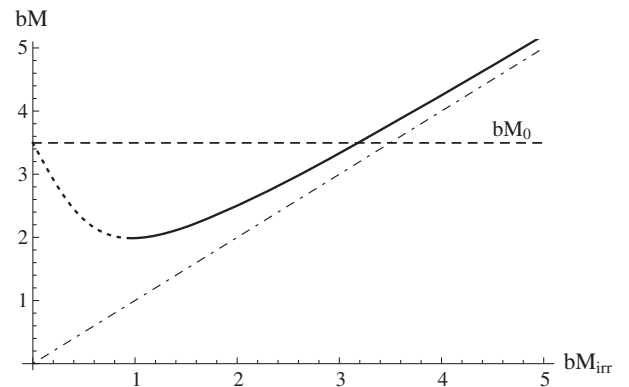


FIG. 1. Mass formula (thick plus dotted curves), Eq. (16), when the parameter  $b|Q|$  satisfies Eq. (17), chosen here as 2. The dashed curve represents  $bM_0$ , as given by Eq. (14). The dot-dashed curve is the asymptote to  $M$ ,  $M_{\text{irr}}$ . Besides,  $bM$  exhibits a minimum at the critical point  $M_{\text{irr}}^c b \approx 0.97$  (where the horizons become degenerated) and for  $M_{\text{irr}}^c b \leq M_{\text{irr}} b < M_{\text{irr}}^t b \approx 3.18$ , we have the range of irreducible masses that generalize Reissner-Nordström black holes. For  $M_{\text{irr}} \geq M_{\text{irr}}^t$ , there is a sole horizon (not degenerated), whose radial coordinate inside of it is always spacelike. The irreducible masses associated with the outer horizon are  $M_{\text{irr}} \geq M_{\text{irr}}^c$ . The dotted curve is related to the inner horizon solutions (for given configurations) and is not relevant to the analyses concerning the black hole mass decomposition.

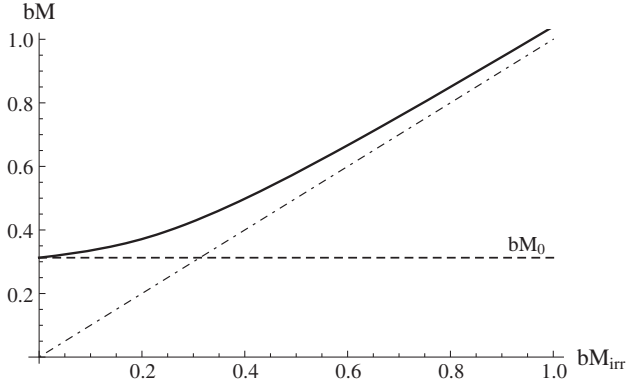


FIG. 2. Mass decomposition when the parameter  $b|Q|$  does not satisfy Eq. (17) and is chosen to be 0.4. The curves have the same meaning as the ones in Fig. 1. From the solid curve we see that  $M$  is a monotonic function and always larger than  $M_0$ . This means that such a case characterizes a scenario where there is always a sole event horizon and there is no classical analogue to it.

An important general remark is here in order, especially for astrophysical analyses. Assume that  $b|Q| = C_1$  and  $M/|Q| = C_2$ , where  $C_1$  and  $C_2$  are given constants. This means that  $Mb = C_1C_2$  is also known. Assuming that  $0 \leq C_1 < \infty$  and from the fact that  $bM \geq (bM)_{\min} \geq 0$ , we first conclude that  $C_2$  cannot be any, but  $C_2 \geq (bM)_{\min}/C_1$ . This means that  $|\alpha| \doteq |Q|/M \leq C_1/(bM)_{\min}$  and this is the condition that guarantees the presence of an outer horizon in an Einstein-Born-Infeld black hole. In the classical case for instance, where  $(bM)_{\min} = b|Q|$  [see Eq. (19) in the limit  $b \rightarrow \infty$ ], the previous inequality means  $|\alpha| \leq 1$ , as it is already known. Finally, after one chooses arbitrarily another parameter to be  $M$  or  $|Q|$  or  $b$ , all the remaining ones are automatically fixed, which could be assessed by

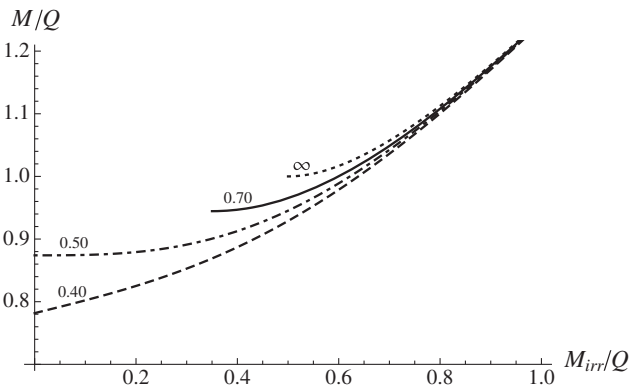


FIG. 3. Mass formula for selected values of the parameter  $b|Q|$  (numbers on the curves) that encompasses all physically distinct classes of black holes for the Born-Infeld Lagrangian. The dotted curve represents the mass formula for the Maxwell Lagrangian. The dot-dashed curve demarcates the transition from two horizon solutions (as given by the thick curve) to a single one (as given by the dashed curve), where its associated inner horizon is null. The branches related to the inner horizons were removed.

the aforesaid choice. It is not complicated to see that when  $M_{\text{irr}}/|Q|$  is given instead of  $M/|Q|$ , a similar reasoning as the above one also ensues.

## V. HAWKING RADIATION FROM EINSTEIN-BORN-INFELD BLACK HOLES

Subsequent to the work of Hawking on the semiclassical quantization of scalar fields in some curved spacetimes [16], it is widely accepted that black holes radiate thermally, although this view has still some criticisms [17,18]. Motivated by the first law of black hole thermodynamics, which is a direct consequence of the mass decomposition expression given by Eq. (6) [5], and the results from the aforesaid semiclassical quantization, we shall now study the consequences of conjecturing that clothed black holes should behave like blackbodies to observers at infinity (no backreaction effects are considered here), radiating at temperatures proportional to their surface gravity [16]. In the spherically symmetric case, such a quantity is proportional to  $de^\nu/dr|_{r=r_+}$  [14,19]. From Eq. (12) and preceding definitions, one has

$$T \propto \frac{1 + 8b^2M_{\text{irr}}^2 - 2b\sqrt{16b^2M_{\text{irr}}^4 + Q^2}}{M_{\text{irr}}}. \quad (20)$$

We notice some particularities of the insertion of the parameter  $b$  into the description of the electromagnetic fields. As in the classical case,  $b \rightarrow \infty$ , it is possible to attain  $T = 0$ , but now as far as

$$M_{\text{irr}}^{(T=0)} = \frac{\sqrt{4b^2Q^2 - 1}}{4b}. \quad (21)$$

Notice that  $M_{\text{irr}}^c = M_{\text{irr}}^{(T=0)}$ . This is not surprising, since from our previous comments, the condition for null temperature of a black hole with charge  $Q$  occurs exactly at the critical points of the energy with respect to its irreducible mass. When Eq. (17) holds, one sees that the temperatures of the associated clothed black holes must decrease with the decrease of their irreducible masses until they eventually reach zero, for  $M_{\text{irr}} = M_{\text{irr}}^{(T=0)}$ . This would mean that black holes where Eq. (17) is valid should radiate off finite amounts of energy, namely  $M(M_{\text{irr}}) - M(M_{\text{irr}}^{(T=0)})$ . Besides, from the analyses of the energy decomposition, black holes could never have negative temperatures. For the case Eq. (17) does not hold, it is impossible to have  $T = 0$  and the temperature increases with the decrease of the irreducible mass. Figure 4 compactifies the dependence of the temperature upon the irreducible mass for selected values of  $b|Q|$ .

We elaborate now on the temperature evolution of evaporating blackbodies. For an arbitrary black hole case where  $2b|Q| > 1$ , as we know, the temperature decreases as

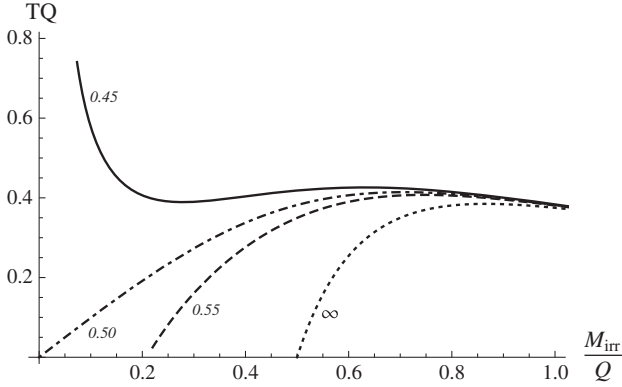


FIG. 4. Einstein-Born-Infeld black hole temperature as a function of the irreducible mass for selected values of the parameter  $b|Q|$ . The temperature goes to infinity as the irreducible mass tends to zero whenever  $2b|Q| \leq 1$  (thick curve). Whenever  $2b|Q| > 1$  (dashed curve), it decreases with the decrease of the irreducible mass (keeping the charge constant), always being null for a finite value of the latter. The temperature experiences a transitional behavior for  $2b|Q| = 1$  (dot-dashed curve), being null just when the irreducible mass of the system is so [see Eq. (20)], albeit it cannot be seen directly from this plot. Finally,  $b|Q| \rightarrow \infty$  (dotted curve) corresponds to the Reissner-Nordström case.

the irreducible mass of the system does so (see Fig. 4). Hence, it would allow us to conceive a situation where just the emission of uncharged scalar particles are present. For this simplified case, the charge of a hole would remain constant. Given that the black holes would behave like blackbodies for observers located at infinity (where there is a meaning to talk about the total energy of a black hole), their energy loss could be estimated by Stefan's law [20]

$$\frac{dM}{d\lambda} = -M_{\text{irr}}^2 T^4, \quad (22)$$

where  $\lambda$  is proportional to the observer's time receiving the radiation. For the emission of uncharged scalar particles, the above equation and Eq. (16) imply that

$$\frac{d\tilde{M}_{\text{irr}}}{d\lambda} \propto - \frac{\left(1 + 8\tilde{M}_{\text{irr}}^2 - 2\sqrt{16\tilde{M}_{\text{irr}}^4 + \tilde{Q}^2}\right)^3}{\tilde{M}_{\text{irr}}^2}. \quad (23)$$

In the above equation, for an arbitrary quantity  $A$ ,  $\tilde{A} \doteq bA$ . We show now that for this case the temperature never reaches the absolute zero. Since the irreducible mass can decrease until  $M_{\text{irr}}^{\text{min}}$ , after a convenient transient time interval, the right-hand side of Eq. (23) can always be expanded about  $M_{\text{irr}}^{\text{min}}$ , leading to

$$\frac{d\tilde{M}_{\text{irr}}}{d\lambda} = - \left( \tilde{M}_{\text{irr}} - \frac{1}{4} \sqrt{4\tilde{Q}^2 - 1} \right)^3, \quad (24)$$

where  $\tilde{\lambda}$  is proportional to  $\lambda$  and other terms that are constants and not important to our analysis. The above equation has an analytic solution and when the limit of  $\tilde{\lambda}$  going to infinity is taken, one obtains  $\tilde{M}_{\text{irr}}(\infty) = \tilde{M}_{\text{irr}}^{\text{min}}$ . This means an associated black hole never reaches the absolute zero and tends asymptotically to have just one horizon. Our analyses in light of the energy decomposition give the same known mathematical results for the thermodynamics for Reissner-Nordström black holes [20,21], but in a simpler way.

For an arbitrary black hole satisfying  $2b|Q| \leq 1$ , it seems that a juncture shall arrive where its thermal energy will be sufficient to create pairs that could even neutralize the hole. This would happen since in this case the thermal energy of a black hole would augment with the diminution of its irreducible mass (see Fig 4). Hence its description would be much more elaborated than the former one. Black holes with  $2b|Q| \leq 1$  are expected to evaporate after finite amounts of time, as corroborated by numerical analyses from Eq. (23). We shall not pursue further into these issues in this work.

## VI. ENERGY LOSS OF INTERACTING EINSTEIN-BORN-INFELD BLACK HOLES

In this section we shall make use of the energy decomposition given by Eq. (16) to find the imprint the parameter  $b$  has on the energy radiated off by two interacting Einstein-Born-Infeld black holes. For accomplishing such a goal, we shall also utilize the second law of black hole mechanics [1,4]. Such a theorem implies that the area of the resultant black hole can never be smaller than the sum of the areas of the initially (far away) interacting black holes [1,4]. For simplifying the reasoning, we will assume that all the black holes involved are spherically symmetric Einstein-Born-Infeld ones. This problem can easily be solved for Einstein-Maxwell black holes (Einstein theory minimally coupled to the Maxwell Lagrangian), because their outer horizons are analytical. For nonlinear black holes, in general just numerical solutions are possible. In the mass decomposition approach, it is possible to carry out the analytical investigations further. The key for this is that whenever the mass formula is taken into account, the outer horizon must be always proportional to its associated irreducible mass for any theory.

Assume that the two initially interacting black holes have irreducible masses  $M_{i1}$  and  $M_{i2}$ , respectively, giving rise to another (final) one of the same kind with irreducible mass  $M_{if}$ . Concerning its final charge, if one assumes that just radiation is allowed to leave the system (carried away by neutral particles), it must be the sum of the charges of the two initial black holes [1]. Since the irreducible masses are proportional to the horizon areas, Hawking's theorem (or the second law of black hole mechanics) implies that

$$M_{if}^2 \geq M_{i1}^2 + M_{i2}^2. \quad (25)$$

Invoking the first law of black hole mechanics for an isolated system [1], the final energy of the two interacting black holes  $M_f$  can never be larger than  $M_1 + M_2$ . The difference in the energy balance is due to the emission of radiation (here gravitational and electromagnetic), hence,  $W_{\text{rad}} = M_1 + M_2 - M_f \geq 0$ . By the cognizance of the minimum final energy of the system, it is even possible to obtain its maximum energy radiated off, a point we shall not pursue here.

For fixing ideas, let us analyze first the classical case, namely two Reissner-Nordström black holes interacting in a way to lead to another Reissner-Nordström black hole. We know that the total energy of each black hole can be written as [3]

$$M_a = M_{ia} + \frac{Q_a^2}{4M_{ia}}, \quad (26)$$

where we have defined  $Q_a$  as the charge of the  $a$ th black hole. It is easy to see that just  $M_{if}^- \leq M_{if} \leq M_{if}^+$  with

$$M_{if}^\pm = \frac{M_1 + M_2 \pm \sqrt{(M_1 + M_2)^2 - (Q_1 + Q_2)^2}}{2} \quad (27)$$

is in agreement with the above-mentioned positivity of  $W_{\text{rad}}$ . Naturally, choices for  $M_{if}$  must satisfy simultaneously Eqs. (25) and (27). When nonlinear theories are present, it is clear that in general the above range of final irreducible masses will not agree with the classical (Einstein-Maxwell black holes) case. It means that many possible classical situations will not exist in the nonlinear case and vice versa even in the simple case of symmetry conserved binary interactions. This could possibly lead to significant deviations for the amounts of radiation emitted by some systems when they are treated classically or not.

In the Einstein-Born-Infeld theory, the physical interval for  $M_{if}$  cannot be determined (numerically) unless the fundamental parameter  $b$  is given. What is known [9] is that  $b > b_0 \approx 10^{-9} \text{ cm}^{-1}$ , where  $b_0$  is the value for the scale field determined by Born and Infeld using the unitarian viewpoint [7].

Let us take a closer look at the Einstein-Born-Infeld black holes when compared to their classical counterparts. Assume just for simplicity that  $M_{i1} = M_{i2}$  and  $Q_1 = Q_2 \equiv Q > 0$ . For this choice, Eq. (27) gives us  $-\sqrt{1/\alpha^2 - 1} \leq M_{if}/Q - 1/\alpha \leq \sqrt{1/\alpha^2 - 1}$ , where  $\alpha$  is here defined as the charge-to-mass ratio of the initially interacting black holes. Let us choose, just for simpleness,  $M_{if}/Q = 1/\alpha$ . From the Einstein-Maxwell case, one can check easily that for the above analysis  $W_{\text{rad}(\text{clas})}/Q = (1 - \alpha^2)/\alpha$ . For the above choice of parameters, one can show that Eq. (25) is just satisfied if

$\alpha \geq \sqrt{2(\sqrt{2} - 1)} \approx 0.91$ . Such cases are of theoretical interest since they would evidence the departures of the Born-Infeld theory from the Maxwell theory. For investigating smaller values of  $\alpha$ , one should select different final irreducible masses for the black holes.

Figure 5 compactifies the possibilities for the above chosen  $M_{if}$  for  $\alpha = 0.95$ , due to miscellaneous values of  $bQ$ . One sees in this case that nonlinear and linear black holes may radiate off very different amounts of energy. Besides, the energy released for interacting Born-Infeld black holes is always larger than its Maxwellian counterpart. Notice finally that  $Q = \alpha M$ ,  $M$  being the mass of any of the black holes when they are far apart, which would also allow one to compare the energies radiated off by the black holes during their process of interaction with the total initial energy of the system.

Some simple estimates can be done here assessing astrophysical scenarios where Fig. 5 could be of relevance. As we stressed before, from the hydrogen atom one knows that  $b \gg b_0 \approx 10^{-9} \text{ cm}^{-1} \approx 10^{15}$  electrostatic unit. We also commented at the end of Sec. IV that with fixed  $M_{\text{irr}}/|Q|$  or  $M/|Q|$  and  $b|Q|$ , one still has freedom to choose arbitrarily another parameter, such as  $M$ , even having already taken into account the mass formula. Let us choose, as it is reasonable under the point of view of black hole interactions coming from neutron stars,  $M \approx M_\odot \approx 1.48 \times 10^5 \text{ cm}$ , where  $M_\odot$  is the mass of the Sun. Let us focus our attention at a given value of  $b|Q|$  such that the associated radiated energy may differ considerably from its classical counterpart. As a simple inspection in Fig. 5 reveals, one could take as a

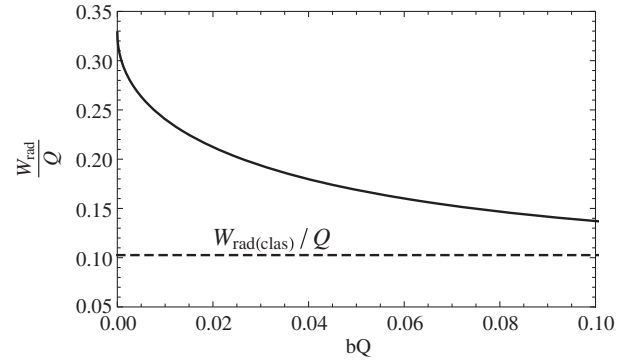


FIG. 5. Total radiation (gravitational plus electromagnetic)  $W_{\text{rad}}/Q$  released in the process of coalescence of two identical Einstein-Born-Infeld black holes with  $\alpha = 0.95$  under the assumption it leads to another one of the same type with the same parameters as their classical counterparts. The thick curve represents such a case. The dashed curve stands for the radiation encountered in the Einstein-Maxwell theory,  $W_{\text{rad}(\text{clas})}/Q$ . The associated radiation tends to its classical counterpart when  $bQ$  goes to infinity. The energy released in the case of nonlinear black hole interaction is always larger than the one coming from its classical counterpart, for a given charge  $Q$ .

good example of this case  $b|Q| = 0.1$ , where the energy radiated off by Born-Infeld black holes is around 30% more than Maxwellian ones with identical parameters. Besides, we recall that we have already chosen  $\alpha = 0.95$  for plotting Fig. 5. From this case, we have  $bM_0 \approx 4 \times 10^{-2}$  [see Eq. (14)], which shows that  $|\alpha| = 0.95$  is a perfectly good candidate for the case  $2b|Q| \leq 1$ , the one we are interested in here. For this case we know that  $Q = M/C_2 = 1.4 \times 10^5 \text{ cm} = 1.6 \times 10^{20} \text{ C}$  and finally  $b = C_1 C_2 / M = 7.1 \times 10^{-7} \text{ cm}^{-1}$ , which is about 1000 times larger than  $b_0$  and hence in agreement with the bound given by the hydrogen atom, the only remaining physical constraint. Therefore, the above example suggests that the radiation coming from coalescing astrophysical black holes could be a good tool to access and discriminate their electro-dynamical properties.

## VII. DISCUSSION

Foremost, it is clear that the approach of analyzing a given black hole solution just from its metric and the one from its metric and energy decomposition expression must be consistent since both approaches use intrinsic properties of the spacetime. Nevertheless, the latter approach is much more restrictive than the former one. It must be stressed that the energy decomposition (black hole thermodynamics) is mandatory for the proper description of any (clothed) black hole phenomenon, since it is in accord with conservation laws. Such a constraint equation (energy decomposition) in turn automatically evidences the physically relevant cases in black hole physics, hence leading to a pellucid description of them.

The energy decomposition analysis within Einstein-Born-Infeld black holes leads us to their split into two fundamental families of black holes. Whenever  $2b|Q| \leq 1$ , independent of their irreducible masses, one is led to an associated black hole whose singularity cannot be forestalled after test particles cross its sole nondegenerated horizon. Besides, the previous inequality naturally leads to an absolute upper limit to the charge of approximately  $10^8 \text{ cm} \approx 10^3 M_\odot \approx 10^{23} \text{ C}$ , given that  $b > 10^{-9} \text{ cm}^{-1}$  [9]. Finally, we notice that for this class of black holes, the extractable energy could be up to 100%, since black holes with  $2b|Q| \leq 1$  could even have  $M_{\text{irr}} = 0$ . We stress that the previous conclusions are strictly nonclassical consequences of the finiteness of  $b$ .

The second family of black holes is defined by those satisfying  $2b|Q| > 1$ , where  $M_{\text{irr}} \geq M_{\text{irr}}^{\text{min}}$  [see Eqs. (18) and (19)] for each black hole associated. It constitutes the family that generalizes Einstein-Reissner-Nordström black holes for irreducible masses smaller than transitional values, the nontrivial solutions of  $M = M_0$ , and larger than  $M_{\text{irr}}^{\text{min}}$  (related to their minimum energies), whose associated energies (masses) are always smaller than  $M_0$ . Above such transitional irreducible masses, again due to the finiteness of  $b$ , nonclassical black holes with single

horizons also rise, all of them having masses larger than  $M_0$ . The total amount of energy that could be extracted [ $M - M_{\text{irr}}$ , see Eq. (16)] in this case is always inferior to half of the total energy of the hole (as it occurs for Reissner-Nordström black holes, see [3]), here due to the self-interactions present.

Black holes satisfying  $2b|Q| > 1$  should radiate off (suppose by emitting uncharged scalar particles) until their temperatures reach  $T = 0$ , taking for doing so an infinite amount of time, settling down exactly at their lowest energy state, as one would intuitively expect and here as a direct consequence of the mass formula. Further energy could be extracted from them (obviously by means of other processes rather than the emission of uncharged scalar particles) even when  $T = 0$ , since they still have an ergosphere. For the case  $2b|Q| \leq 1$ , it is impossible to have  $T = 0$  and they are expected to keep radiating, with a much more complex dynamics, until their total evaporation likely after a finite amount of time as measured by the observer who receives the radiation. Whenever charged scalar fields are taken into account, the phenomenon of superradiance could also take place, rendering their dynamics even more cumbersome. Superradiance is of interest for charged nonlinear black holes, since it is another energy extraction mechanism for them and would couple to the nonlinearities of the electromagnetic field. We let more precise analyses of this case to be done elsewhere.

Concerning the issue of energies radiated off due to the interaction of black holes, as we showed here with a toy model, the changes imprinted by the Einstein-Born-Infeld black holes with respect to their classical counterparts may be significant, depending on  $\alpha$  for a range of values of the fundamental parameter  $b|Q|$ . This could be important for gravitational wave detectors calibrated based on classical results. Besides, if it is possible to identify sources of radiation, then measurements upon such a quantity could give us information about electromagnetic interactions. We analyzed the radiated energies due to charged black hole interactions. This means that also electromagnetic radiation is always present in such processes. Identifying and analyzing this part of the radiation would give direct information about astrophysical electro-dynamical processes.

We further point out that all the above conclusions remain valid even in the case where the systems present a slow rotation (when the rotational parameter  $a \doteq J/M$ ,  $J$  being the total angular momentum of the system as seen by distant observers, is much smaller than the outer horizon area or the mass of the hole). This is the case since the energy decomposition must be an even power of  $a$ , due to invariance requirements. Thereby, the previous analyses are in a sense stable against rotational perturbations.

Summing up, in this work we tried to emphasize the need of also taking into account the mass decomposition of a

charged black hole for talking about the physical aspects it could display. Conceptually speaking this is of relevance since it could give us acumen of where and how to search experimentally for charged black holes and their interactions. In this regard, it would be also of interest to investigate the aspects of the electromagnetic radiation coming from the coalescence of charged black holes; because it could be much more easily observed, it would give us direct information about electromagnetic phenomena and of the coalescence process itself. It also seems that quasi periodic oscillations could also shed a light on the illation of black hole charges and the role played by the nonlinearities of the electromagnetism in the astrophysical scope, since they talk about phenomena that take place in the innermost regions of black holes (see [22]

and references therein). We let this issue be elaborated elsewhere.

### ACKNOWLEDGMENTS

We are indebted to Dr. Andrea Geralico for insightful comments and discussions within the theme of this work. J. P. P. acknowledges the support given by the Erasmus Mundus Joint Doctorate Program within the IRAP Ph.D., under the Grant No. 2011–1640 from Education, Audiovisual and Culture Executive Agency (EACEA) of the European Commission. J. A. R. acknowledges the support by the International Cooperation Program CAPES-ICRANet financed by CAPES–Brazilian Federal Agency for Support and Evaluation of Graduate Education within the Ministry of Education of Brazil.

- 
- [1] C. W. Misner, K. S. Thorne, and J. A. Wheeler, *Gravitation* (W.H. Freeman and Co., San Francisco, 1973).
- [2] D. Christodoulou, *Phys. Rev. Lett.* **25**, 1596 (1970).
- [3] D. Christodoulou and R. Ruffini, *Phys. Rev. D* **4**, 3552 (1971).
- [4] J. M. Bardeen, B. Carter, and S. W. Hawking, *Commun. Math. Phys.* **31**, 161 (1973).
- [5] J. P. Pereira, H. J. Mosquera Cuesta, J. A. Rueda, and R. Ruffini, *Phys. Lett. B* **734**, 396 (2014).
- [6] J. D. Bekenstein, *Phys. Rev. D* **7**, 2333 (1973).
- [7] M. Born and L. Infeld, *Proc. R. Soc. A* **144**, 425 (1934).
- [8] D. A. Rasheed, [arXiv:hep-th/9702087](https://arxiv.org/abs/hep-th/9702087).
- [9] H. Carley and M. K.-H. Kiessling, *Phys. Rev. Lett.* **96**, 030402 (2006).
- [10] J. Franklin and T. Garon, *Phys. Lett. A* **375**, 1391 (2011).
- [11] J. Diaz-Alonso and D. Rubiera-Garcia, *Gen. Relativ. Gravit.* **45**, 1901 (2013).
- [12] L. D. Landau and E. M. Lifshitz, *The Classical Theory of Fields* (Pergamon Press, Oxford, 1975).
- [13] N. Bretón, *Classical Quantum Gravity* **19**, 601 (2002).
- [14] D. Kothawala, S. Sarkar, and T. Padmanabhan, *Phys. Lett. B* **652**, 338 (2007).
- [15] I. S. Gradshteyn, I. M. Ryzhik, A. Jeffrey, and D. Zwillinger, *Table of Integrals, Series, and Products* (Elsevier Academic Press, New York, 2007).
- [16] S. W. Hawking, *Commun. Math. Phys.* **43**, 199 (1975).
- [17] V. A. Belinski, *Phys. Lett. A* **209**, 13 (1995).
- [18] V. A. Belinski, *Phys. Lett. A* **354**, 249 (2006).
- [19] E. Poisson, *A Relativist's Toolkit* (Cambridge University Press, Cambridge, England, 2004).
- [20] R. M. Wald, *General Relativity* (University of Chicago Press, Chicago, 1984).
- [21] W. Israel, *Phys. Rev. Lett.* **57**, 397 (1986).
- [22] N. Glendenning, *Compact Stars. Nuclear Physics, Particle Physics and General Relativity* (Springer-Verlag, New York, 1996).

## RADIAL STABILITY IN STRATIFIED STARS

JONAS P. PEREIRA<sup>1,2</sup> AND JORGE A. RUEDA<sup>2,3,4</sup>

<sup>1</sup> Université de Nice Sophia Antipolis, CEDEX 2, Grand Château Parc Valrose, BP 2135, F-06103 Nice, France; [jonaspedro.pereira@icranet.org](mailto:jonaspedro.pereira@icranet.org)

<sup>2</sup> Dipartimento di Fisica and ICRA, Sapienza Università di Roma, P.le Aldo Moro 5, I-00185 Rome, Italy; [jorge.rueda@icra.it](mailto:jorge.rueda@icra.it)

<sup>3</sup> ICRA Net, P.zza della Repubblica 10, I-65122 Pescara, Italy

<sup>4</sup> ICRA Net-Rio, Centro Brasileiro de Pesquisas Físicas, Rua Dr. Xavier Sigaud 150, Rio de Janeiro, RJ 22290-180, Brazil

Received 2014 November 12; accepted 2014 December 29; published 2015 February 26

### ABSTRACT

We formulate within a generalized distributional approach the treatment of the stability against radial perturbations for both neutral and charged stratified stars in Newtonian and Einstein’s gravity. We obtain from this approach the boundary conditions connecting any two phases within a star and underline its relevance for realistic models of compact stars with phase transitions, owing to the modification of the star’s set of eigenmodes with respect to the continuous case.

*Key words:* stars: fundamental parameters – stars: interiors – stars: neutron – stars: oscillations

### 1. INTRODUCTION

There is theoretical evidence that compact stars, such as neutron stars, are made up of several matter phases (Shapiro & Teukolsky 1986). This is a consequence of the astonishingly high density excursion they could attain in their inner regions. For instance, a neutron star is in general thought to be composed of at least two different regions: the crust and the core. Starting from very low densities of a few grams per cubic centimeter close to their surfaces, and up to densities on the order of the nuclear saturation value,  $\rho_{\text{nuc}} \approx 2.7 \times 10^{14} \text{ g cm}^{-3}$ , the crust of a neutron star is thought to be in a *solid-like* state. The core, with densities that might be greater by orders of magnitude than  $\rho_{\text{nuc}}$ , is instead thought to be in a *liquid-like* state. The details of the treatment of the thermodynamic transition (Maxwell or Gibbs phase construction), as well as the conditions of density and pressure at which such a transition occurs, are still a matter of debate. The application of the Gibbs construction with more than one conserved charge (for example, baryon and electric) leads to the appearance of mixed phases in between the pure phases, with an equilibrium pressure that varies with the density, leading to a spatially extended phase-transition region of nonnegligible thickness with respect to the star’s radius (Glendenning 1992, 2001; Glendenning & Pei 1995; Christiansen & Glendenning 1997; Glendenning & Schaffner-Bielich 1999; Christiansen et al. 2000). In contrast, in the traditional Maxwell construction the phases are in “contact” with each other. It is worth mentioning that in these treatments the pure phases are subject to the condition of local charge neutrality, so they do not account for the possible interior Coulomb fields. Indeed, the complete equilibrium of the multicomponent fluid in the cores of compact stars needs the presence of a Coulomb potential formed by electric charge separation due to gravito-polarization effects (Rotondo et al. 2011; Rueda et al. 2011), favoring a sharp core–crust transition that ensures the global, but not the local, charge neutrality (see Belvedere et al. 2012, 2014, and references therein). Other than the core–crust transition, additional phase transitions, such as the ones allowed by quantum chromo-dynamics, could occur within the core of the star itself (see, e.g., Glendenning 1996, and references therein). From all of the above we can conclude that ultradense stars such as neutron stars necessarily show a nontrivial stratification. Between any two phases, which can be

very different, it is reasonable to investigate the situation where some quantities are discontinuous, such as the energy density and the pressure. Such discontinuities can be harnessed by appropriate surface tensions. These surface quantities influence the stability of a system, adding new boundary conditions to the problem that, as we shall show here, modify the set of eigenfrequencies and eigenmodes of a star.

In this work we analyze the problem of perturbations in systems constituted of various phases that are split by surfaces that host nontrivial degrees of freedom. This analysis is thought to be a generalization of the treatment for continuous systems (see Herrera & Santos 1997 and references therein for a comprehensive analysis of properties, types, and stability of continuous anisotropic fluids also in the presence of radiation and heat flux). By investigating the dynamics of perturbations, we are automatically probing the stability of systems. We shall restrict ourselves to the simplest possible case: spherically symmetric extended bodies where radial perturbations take place. In order to model the problem, we shall assume that these surfaces of discontinuity separating two arbitrary phases are very thin, and a generalized distributional approach (Poisson 2004; Raju 1982b) shall be adopted. We start our analysis in the Newtonian case in order to gain some intuition into the relevant aspects of the problem, and finally we generalize it to general relativity. Our purpose is solely to expound the problem and seek to solve it as generically as we can. Our analysis is far from complete and must be considered as a first step toward deeper investigations, and scrutinies of specific cases will be the object of later studies.

We show in this work that phase transitions in the presence of surface degrees of freedom can be enclosed in additional boundary conditions on the problem. Our formalism also tells us that such boundary conditions are only self consistent when the set of eigenfrequencies of the perturbation modes is related to the global system, not with individual phases. This is consistent with the well-known results from coupled springs, where there are only global frequencies. The presence of further boundary conditions naturally modifies the possible set of eigenfrequencies because we are inserting further restrictive aspects to the physical oscillation modes. Therefore, measurements on the pulsation modes in a star could tell us very precisely about its internal structure, being a sort of fingerprint that could help us understand better the nature of these systems.

The article is organized as follows. In Section 2 we formulate the problem of radial perturbations of stars with interfaces in the classical Newtonian case. For the sake of example, we compute the specific solution of the stability equation in Section 3 for the simple case of incompressible stars, scrutinizing which circumstances deliver us enough arbitrary constants to fix additional boundary conditions. In Section 4 we give the formulation in the case of systems with electric charge but still within Newtonian gravity. The formulation in the case of general relativity in the neutral case is presented in Section 5, and in Section 6 we extend the general relativistic treatment to systems endowed with electric charge. Finally, in Section 7 we summarize and discuss the main results of this work. We use units such that  $c = G = 1$  and the metric signature  $-2$  throughout the article, unless otherwise stated.

## 2. STABILITY OF CLASSICAL SYSTEMS WITH PHASE TRANSITIONS

Assume a continuous classical astrophysical system with spherical symmetry. When its volume elements are perturbed radially, it is well known (see, e.g., Shapiro & Teukolsky 1986) that the evolution of perturbations of the form

$$\tilde{\xi}(r, t) = \xi(r)e^{i\omega t}, \quad (1)$$

with  $\omega$  an arbitrary constant, is described by

$$\frac{d}{dr} \left[ \Gamma P \frac{1}{r^2} \frac{d(r^2 \xi)}{dr} \right] - \frac{4}{r} \frac{dP}{dr} \xi + \omega^2 \rho \xi = 0, \quad (2)$$

where  $P(r)$  is the pressure of the background system under hydrostatic equilibrium and

$$\Gamma \doteq \frac{\rho}{P} \frac{\partial P}{\partial \rho}, \quad (3)$$

with  $\rho(r)$  the mass density of the system. Formulated in this way, we have at hand an eigenvalue problem. For continuous systems, the boundary conditions to be added to Equation (2) are quite simple. They are directly related to the spherical symmetry of the system, as well as to the vanishing of its pressure on its border even in the presence of perturbations (other situations where a surface tension is present could also be envisaged, and we shall attempt to elaborate on them below). In other words, we impose that

$$\xi(0) = 0, \quad \text{and} \quad \xi(R_s) = \text{finite}, \quad (4)$$

where  $R_s$  is defined as the radius of the star, such that  $P(R_s) = 0$ . For further details about these boundary conditions see Shapiro & Teukolsky (1986). Equation (2) supplemented with Equation (4) constitutes a Sturm–Liouville problem, where the aspects of its solutions are already known. Concerning the eigenfrequencies,  $\omega^2$ , they are all real and form a discrete hierarchical set. When one seeks stable solutions to Equation (2), one seeks solutions with positive  $\omega^2$ , especially for its fundamental mode. As can be seen from Equation (1), negative values of  $\omega^2$  indicate instabilities in the assumed background system, which leads to the conclusion that they do not linger on in time. They would either implode or explode.

We now turn to the more involved problem of permitting the system to be stratified and harboring surface degrees of freedom on the interface of two given phases. Such degrees of

freedom have themselves a dynamic, described generically by the thin-shell formalism or Darmois–Israel formalism (Israel 1966, 1967; Lobo & Crawford 2005; Poisson 2004). We are here, however, particularly interested in another aspect of the problem, namely understanding the role such degrees of freedom play in the stability of the system when its parts (defined naturally by the hypersurface that hosts the aforesaid degrees of freedom) are perturbed. Therefore, before anything, it is assumed that, for it to be meaningful to talk about this scenario, one has that the hypersurfaces of discontinuity themselves are stable (see Pereira et al. 2014 for further details). If this is not the case, any displacement of the hypersurface of discontinuity would trigger a cataclysmic set of events that would result in the disruption of the system.

One expects that the stratified problem could be accounted for additional boundary conditions to the system. The reason for this is that the perturbations in the upper and lower regions with respect to a given surface of discontinuity would be described by the same physics (for example Equation (2)), as well as the totality of the matches. The only missing points would be their connection (allowing combinations of solutions to also be solutions to the physical equations involved) and generalization by means of surface quantities. For example, the existence of a surface tension would account for an extra surface force term. The same ensues with the presence of a surface mass (enclosed by a surface mass density) and the associated presence of a surface gravitational force. Therefore, in order to properly describe stratified systems, which need the addition of surface boundary conditions to match different regions, one must make use of distributions (Poisson 2004; Raju 1982b).

We proceed now with the distributional generalization of the equations describing continuous fluids under gravitational fields. Assume that a surface harboring surface degrees of freedom in a system in equilibrium is at  $r = R$ . The first equation to be generalized in terms of distributions in this case is the equation of hydrostatic equilibrium. This should now read

$$\frac{dP}{dr} + \rho g(r) - \frac{2\mathcal{P}}{R} \delta(r - R) = 0, \quad (5)$$

where  $g(r)$  has been defined as the norm of the gravitational field, the solution to (the distributional) Poisson's equation  $\nabla \cdot \mathbf{g} = -4\pi G\rho$ ,  $\mathbf{g} = -g(r)\hat{r}$ , which can always be written as

$$g(r) = \frac{GM(r)}{r^2}, \quad M(r) \doteq 4\pi \int_0^r \rho(\bar{r})\bar{r}^2 d\bar{r}. \quad (6)$$

In addition,  $\mathcal{P}$  in Equation (5) stands for the surface tension (Peters 2013) on the surface of a discontinuity at  $r = R$ . The expression on the aforesaid equation is the result of restoring surface forces (this is the reason they have a direction opposite to the pressure gradient) in a small surface area (the factor 2 comes from the principal curvatures in a surface element, which in the spherically symmetric case are equal). The gravitational force from the sheet of mass at  $r = R$  is naturally incorporated into the distributional definitions of  $\rho$  and  $g(r)$ , as we will show below. The mass density, on the other hand, must be expressed as

$$\rho(r) = \rho^-(r)\theta(R - r) + \rho^+(r)\theta(r - R) + \sigma\delta(r - R), \quad (7)$$

with  $\theta(r - R)$  the Heaviside function, whose derivative is the Dirac delta function  $\delta(r - R)$  in the sense of distributions. From the existence of a surface mass density, it can be checked that the gravitational field is discontinuous at a given surface

of discontinuity of the system (at  $R$ ):

$$[g(R)]_{\pm}^{\pm} = 4\pi G\sigma, \quad (8)$$

where we have introduced the convention  $[A]_{\pm}^{\pm} \doteq A^+ - A^-$ , the jump of  $A(r)$  across  $r = R$ . Therefore,  $g(r)$  could be represented distributionally as

$$g = g^+(r)\theta(r - R) + g^-(r)\theta(R - r). \quad (9)$$

The above equation means that the associated distributional gravitational potential  $\phi(r)$  ( $\mathbf{g} = -\nabla\phi$ ,  $\mathbf{g} = -g\hat{r}$ ) is always a continuous function, although not differentiable at the surface of a discontinuity.

We will also assume that the pressure can be discontinuous at  $r = R$  and hence written as

$$P(r) = P^-(r)\theta(R - r) + P^+(r)\theta(r - R). \quad (10)$$

The reason this is so will be clarified when we deal with our original problem in the scope of general relativity. The heuristic argument corroborating the validity of Equation (10) is that it is meaningless to colligate a surface term to the radial pressure because its associated force would necessarily be normal to it and therefore would not lie on the surface. Only tangential pressures should be tied within their surface terms. From Equations (10), (7), (6), (8), and (9) we have

$$\mathcal{P} = \frac{R}{2}[P(R)]_{\pm}^{\pm} + \frac{G}{16\pi R^3}[M^2(R)]_{\pm}^{\pm} \quad (11)$$

and

$$\frac{dP^{\pm}}{dr} + \rho^{\pm}(r)g^{\pm}(r) = 0. \quad (12)$$

The arithmetic average present in Equation (11) (see the definition of  $g(r)$  and the value of  $\sigma$ ) is a general consequence of the product of delta functions with Heaviside ones in the generalized sense of distributions (Raju 1982a, 1982b). Note from Equation (11) that its first term is the known Young–Laplace equation for spherical surfaces at equilibrium (see, e.g., Rodríguez-Valverde et al. 2003; Peters 2013), where only geometric aspects are taken into account for the surface tension. Its second term, though, is the gravitational surface tension, uniquely due to the nonzero surface mass. If the surface tension were null, the pressure jump could not be arbitrary but is proportional to the surface mass density and must be a monotonically decreasing function of the radial coordinate (see Equations (8) and (11)). From Equation (11), one sees further that the force per unit area associated with the surface tension is exactly the one necessary to counterbalance both of the forces coming from the pressure gradient at  $R$  and the surface gravitational force, as it should be.

One sees that the above procedure generalizes our notion of hydrostatic equilibrium in each phase the stratified system has (see Equation (12)) and automatically gives the surface tension at  $R$  that guarantees the hydrostatic equilibrium for arbitrary pressure jumps and surface masses. We will keep the same philosophy now concerning the generalization of Equation (2). From our generalized hydrostatic equilibrium equation, we have that an important term for the deduction of the equation governing radial perturbations would be the application of the Lagrangian operator  $\Delta$  ( $\Delta A \doteq A(t, r + \tilde{\xi}) - A_0(t, r)$ ,  $A_0$  and  $A$  being a physical quantity in the equilibrium and perturbed

cases, respectively) on the surface force in Equation (5) (see Equation (20)):

$$\Delta \left[ \frac{\mathcal{P}}{R}\delta(r - R) \right] \doteq \frac{\Delta\mathcal{P}}{R}\delta(r - R) - \frac{\mathcal{P}\tilde{\xi}}{R^2}\delta(r - R) \quad (13)$$

because  $\Delta\delta(r - R) = 0$  and  $\Delta R = \tilde{\xi}$ . Now we assume that  $\mathcal{P} = \mathcal{P}(\sigma)$ . This means that we are endowing the fluid at the surface of a discontinuity with adiabatic properties, and the underlying microphysics is not contemplated in this procedure. For continuous media, the total mass in the interface of two phases is generally not a constant. This means that mass fluxes are allowed to take place. This generically would render the mass of each phase not constant, an aspect not taken into account in Equation (2). Nevertheless, if the displacements of the surface of a discontinuity are small and oscillatory, we have that on average the masses on each phase are conserved (here it becomes clear why the surface of a discontinuity should be stable). For adiabatic processes, we have

$$\Delta\mathcal{P} = \eta^2\Delta\sigma, \quad \eta^2 \doteq \frac{\partial\mathcal{P}}{\partial\sigma}, \quad (14)$$

with  $\eta^2$  the square of the speed of sound in the fluid at the surface of a discontinuity. The missing term  $\Delta\sigma$  can be found via the thin-shell formalism when the classical limit is taken there. Generically, in the static and spherically symmetric case,  $\sigma$  can be written as (Lobo & Crawford 2005)

$$\sigma = -\frac{c^2}{4\pi GR}[e^{-\beta(R)}]_{\pm}^{\pm}, \quad (15)$$

with the classical limit  $\beta(r) \approx GM(r)/(rc^2) \ll 1$ . It is easy to check that Equation (15) reduces to Equation (8) in the aforementioned limit. When perturbed, it can be shown that  $\beta \rightarrow \beta + \delta\beta$ , with  $\delta\beta = -4\pi Gr\rho_0 e^{2\beta_0}\tilde{\xi}/c^2$  (Misner et al. 1973),  $\rho_0$  here meaning the mass density in the hydrostatic background solution. Hence,

$$\Delta\sigma = \delta\sigma + \sigma'_0\tilde{\xi} = -[\rho_0\tilde{\xi}]_{\pm}^{\pm} + \sigma'_0\tilde{\xi}, \quad (16)$$

where we also considered  $\sigma_0$  the background solution (Equation (8)).

Another simpler way of obtaining Equation (16) would be through the dynamics of  $\delta g$  ( $\delta\mathbf{g} = -(\delta g)\hat{r}$ ). In the spherically symmetric case we have  $\delta g = -4\pi G\rho_0\tilde{\xi}$  (Shapiro & Teukolsky 1986), and because  $\delta g \doteq g - g_0$ , with  $g_0$  the norm of the gravitational field without the perturbation  $\tilde{\xi}$ , from Equation (8), we finally obtain

$$\Delta\sigma = \frac{[\delta g(R)]_{\pm}^{\pm}}{4\pi G} + \sigma'_0(R)\tilde{\xi} = \sigma'_0(R)\tilde{\xi} - [\rho_0\tilde{\xi}]_{\pm}^{\pm}. \quad (17)$$

In addition, from Equations (6) and (8), for the case when the jump of  $\tilde{\xi}$  is null at the surface of a discontinuity (which will be justified below), one shows that the above equation can be further simplified to

$$\Delta\sigma = -\frac{2}{r}\sigma\tilde{\xi}. \quad (18)$$

Now we show the general equation governing the propagation of radial perturbations. For  $P$  defined as in Equation (10),  $\rho$  in terms of Equation (7),  $g$  as given by Equation (9), and finally

$$\tilde{\zeta}(r, t) = \tilde{\zeta}^+(r, t)\theta(r - R) + \tilde{\zeta}^-(r, t)\theta(R - r), \quad (19)$$

the equation governing the evolution of perturbations in a given volume element of the fluid is

$$\Delta \left\{ \rho \frac{dv_r}{dt} + \frac{\partial P}{\partial r} + \rho g(r) - \left[ \frac{2P}{R} + \frac{\sigma}{2} (\dot{v}_r^+ + \dot{v}_r^-) \right] \delta(r - R) \right\} = 0. \quad (20)$$

Note that we assumed that  $\dot{v}_r$  is a distribution like  $\tilde{\xi}$ . Physically this must be taken because the phases are always ‘‘localizable’’ and do not mix. In other words, this constraint reflects the intuitive fact that the surface of a discontinuity should be well defined. The mathematical reason for this will be given below, and it is related to the well-posedness of the problem.

When developed, taking into account the hydrostatic equilibrium equation (see Equation(5)), it can be simplified to

$$\begin{aligned} \frac{\partial}{\partial r} \left[ \frac{\Gamma P}{r^2} \frac{\partial}{\partial r} (r^2 \tilde{\xi}) \right] - \frac{4}{r} \frac{\partial P}{\partial r} \tilde{\xi} - \frac{d^2 \tilde{\xi}}{dt^2} \rho = & \left[ \frac{2\tilde{\xi}}{R^2} (2\eta^2 \sigma - 3P) \right. \\ & \left. - \frac{\sigma}{2} \left( \frac{d^2 \tilde{\xi}^+}{dt^2} + \frac{d^2 \tilde{\xi}^-}{dt^2} \right) \right] \delta(r - R). \end{aligned} \quad (21)$$

First note that coefficients multiplied by  $\delta^2(r - R)$  or  $\delta'(r - R)$  in Equation (21) must all be null. Taking into account Equation (19), this means that

$$[\tilde{\xi}]_{\pm}^+ = 0. \quad (22)$$

This automatically warrants  $\tilde{\xi}$  as a distribution without Dirac deltas, as we have advanced previously. In order to obtain Equation (21), we used the results that for a distribution  $A(r) = A^+(r)\theta(r - R) + A^-(r)\theta(R - r)$ ,

$$\Delta A = \delta A + \frac{\partial A}{\partial r} \tilde{\xi} - [A]_{\pm}^+ \tilde{\xi} \delta(r - R), \quad (23)$$

$$\begin{aligned} \Delta \left( \frac{\partial A}{\partial r} \right) = & \frac{\partial}{\partial r} (\Delta A) - \frac{\partial \tilde{\xi}}{\partial r} \frac{\partial A}{\partial r} \\ & + \frac{1}{2} \left[ \frac{\partial \tilde{\xi}^+}{\partial r} + \frac{\partial \tilde{\xi}^-}{\partial r} \right] [A(R)]_{\pm}^+ \delta(r - R). \end{aligned} \quad (24)$$

In addition to the above mathematical properties, we have also made use of

$$\Delta \rho = -\frac{\rho}{r^2} \frac{\partial}{\partial r} (r^2 \tilde{\xi}) + \frac{\sigma}{2} \left( \frac{\partial \tilde{\xi}^+}{\partial r} + \frac{\partial \tilde{\xi}^-}{\partial r} \right) \delta(r - R), \quad (25)$$

which is a direct consequence of assuming that the total mass in each phase is constant, even in the presence of perturbations. This is only guaranteed if the surface of a discontinuity is stable, a prime hypothesis for having a well-posed stability problem. We also have assumed that  $P = P(\rho)$ , which implies that  $\Delta P^{\pm} = \Gamma^{\pm} P^{\pm} \Delta \rho^{\pm} / \rho^{\pm}$ . In deriving Equation (21), we further took into account Equation (11). We finally stress that a simpler way to obtain Equation (21) is to recall that  $\Delta M = 0$ , which guarantees that  $\Delta g = -2g\tilde{\xi}/r$ . The fact that  $\Delta M = 0$  means that observers comoving with the fluid do not note a mass change. The aforementioned result can also be directly shown by Equations (6), (24), and (25).

It can be seen that only solutions of the type  $\tilde{\xi}^{\pm}(r, t) = e^{i\omega^{\pm} t} \xi^{\pm}(r)$  for Equation (21) are meaningful if

$$\omega^+ = \omega^- \doteq \omega. \quad (26)$$

This is the only way to eliminate the time dependence above in Equation (21) and also to guarantee that the jump of  $\tilde{\xi}$  is null for any surface of discontinuity at any time. Therefore, we arrive at the important conclusion that even a stratified system where oscillatory perturbations take place should be described by a sole set of frequencies. Each member of this set describes the eigenfrequency of a whole system, instead of one or another phase. Nevertheless, we recall that at the surface of a discontinuity the frequencies are in principle not defined. Bearing in mind the above conclusions, we have that, using Equation (1),

$$\xi(r) = \xi^-(r)\theta(R - r) + \xi^+(r)\theta(r - R) \quad (27)$$

and the boundary condition

$$[\xi(R)]_{\pm}^+ = 0, \quad \text{or} \quad \xi^+(R) = \xi^-(R) \doteq \xi(R), \quad (28)$$

and therefore the only meaningful  $\Gamma$  are given by

$$\Gamma(r) = \Gamma^-(r)\theta(R - r) + \Gamma^+(r)\theta(r - R). \quad (29)$$

Gathering the above equations in Equation(21), we obtain

$$\begin{aligned} \frac{d}{dr} \left[ \frac{\Gamma P}{r^2} \frac{\partial}{\partial r} (r^2 \xi) \right] - \frac{4}{r} \frac{dP}{dr} \xi + \omega^2 \rho \xi \\ = -\xi(R) \left[ \frac{2}{R^2} (3P - 2\eta^2 \sigma) - \omega^2 \sigma \right] \delta(r - R). \end{aligned} \quad (30)$$

Ones sees from Equation (30) that in the case where  $\mathcal{P}$  and  $\sigma$  are null, the classical expression, Equation (2), is recovered.

Summing up, substituting Equations (27) and (7) into Equation (30), one sees that the only way to satisfy such an equation is by imposing that

$$\frac{d}{dr} \left[ \Gamma^{\pm} P^{\pm} \frac{1}{r^2} \frac{d}{dr} (r^2 \xi^{\pm}) \right] - \frac{4}{r} \frac{dP^{\pm}}{dr} \xi^{\pm} + \omega^2 \rho^{\pm} \xi^{\pm} = 0, \quad (31)$$

$$\left[ \Gamma P \frac{d}{dr} (r^2 \xi) \right]_{\pm}^+ + 2(3P - 2\eta^2 \sigma - 2R[P(R)]_{\pm}^+) \xi(R) = 0, \quad (32)$$

and for completeness, condition (28). Equation (31) is obtained here as a consequence of our distributional search for solutions to the radial Lagrangian displacements. This is exactly what one expects under physical arguments. Equations (32) and (28) are our desired boundary conditions to be further taken into account (besides Equation (4)) at the interface of any two phases.

For the case where  $[P(R)]_{\pm}^+ = [\Gamma(R)]_{\pm}^+ = \sigma = \mathcal{P} = 0$ , we have that the derivative of  $\xi$  is also continuous, and therefore  $\xi$  is a differentiable function anywhere, as it should be because we are defining here a continuous system. Nevertheless, whenever the aforementioned conditions do not take place, richer scenarios arise. Even in the case of a phase transition at constant pressure and negligible surface mass, the discontinuity of  $\Gamma$  and the existence of  $\mathcal{P}$  generally render the derivative of  $\xi$  discontinuous.

### 3. A SPECIFIC EXAMPLE: UNIFORM-DENSITY STARS

We would like to stress that the boundary condition we have derived previously is actually very restrictive. This is because the physically acceptable cases (solutions to Equations (31) associated with a surface of discontinuity at  $r = R$ ) are only the ones that deliver enough arbitrary constants of integration

to satisfy Equations (27) and (32). This should be taken into account together with the physical requirement of only admitting finite  $\xi$  everywhere and that are null at the origin (see Equation (4)). In the following, we shall see a particular example where all of these aspects are evidenced.

Let us now investigate a star made of two phases, each with a uniform mass density. Let us assume also, for the sake of simplicity and example, that the associated  $\Gamma$  for each region is an arbitrary constant. As we will see, although this can be considered only as a first academic example, it already evidences some aspects that stratified systems should have. For this case it is straightforward to solve Poisson's equation and the equation of hydrostatic equilibrium (see, e.g., Shapiro & Teukolsky 1986, for further details), and we have for  $r < R$

$$P^-(r) = \frac{2\pi G\rho_-^2}{3}(R^2 - r^2), \quad \mathcal{R} \doteq \frac{3p_0^-}{2\pi G\rho_-^2}, \quad (33)$$

where  $p_0^-$  is an arbitrary constant that corresponds to the pressure of the system at the origin. For  $r > R$ , instead

$$P^+(r) = \frac{2\pi G\rho_+^2}{3}(R_s^2 - r^2). \quad (34)$$

The constant mass density in the inner and outer regions has been defined as  $\rho^-$  and  $\rho^+$ , respectively. The pressure at the origin  $p_0^-$  could always be chosen such that it matches the pressure at the base of the outer phase, and as can be seen from Equation (34), we have also introduced the condition of having a null pressure at the star's surface. Substituting Equations (33) and (34) into Equation (31), we are led to

$$(1 - x_{\pm}^2) \frac{d^2\xi_{\pm}}{dx_{\pm}^2} + \left(\frac{2}{x_{\pm}} - 4x_{\pm}\right) \frac{d\xi_{\pm}}{dx_{\pm}} + \left(A_{\pm} - \frac{2}{x_{\pm}^2}\right) \xi_{\pm} = 0, \quad (35)$$

where we assumed that  $x_+ \doteq r/R_s$ ,  $x_- \doteq r/R$  and

$$A_{\pm} \doteq \frac{3\omega_{\pm}^2}{2\pi G\rho_{\pm}\Gamma_{\pm}} + \frac{8}{\Gamma_{\pm}} - 2. \quad (36)$$

We now solve Equation (35) by the method of Frobenius. For the sake of simplicity, we drop the  $\pm$  notation. We therefore assume solutions of the form

$$\xi = \sum_{n=0}^{\infty} a_n x^{n+s}, \quad (37)$$

where  $a_n$  and  $s$  are arbitrary constants to be fixed by primarily demanding that the first condition of Equation (4) is satisfied, as well as  $\xi(x)$  always being finite. By substituting Equation (37) into Equation (35), it can be checked that the solutions to  $s$  are either  $s = 1$  or  $s = -2$ . The associated recurrence relation obtained generally is

$$a_{m+2} = \frac{(m+s)(m+s+3) - A}{(m+s+2)(m+s+3) - 2} a_m, \quad (38)$$

with  $m = 0, 2, 4, \dots$ , and  $a_1 = a_3 = a_5 = \dots = 0$ . Let us analyze first the inner region. It is clear in this case that the associated  $a_0$  for  $s = -2$  must be null, as a consequence of one of our boundary conditions. From Equation (38), one clearly sees that the power series given by Equation (37) does not converge. Therefore, in order to satisfy the finiteness anywhere of  $\xi$ , we

have to impose that the series be truncated somewhere, rendering it actually a polynomial. Hence

$$A_{m,s=1}^- = (m+1)(m+4). \quad (39)$$

From Equation (36), one sees that only discrete frequencies (given by Equation (39)) are possible in this region. From Equations (36) and (39), to have the frequency of the fundamental mode ( $m = 0$ ) positive, one should have  $\Gamma^- \geq 4/3$ . Summing up, the physically relevant solution to this case just leaves out an arbitrary constant of integration, as required due to the scaling law present for  $\xi$  from Equation (31).

Let us now analyze the outer region. This is the most physically interesting region because the problems at the star's center are absent, and therefore in principle one could even have two linearly independent solutions to  $\xi$ . Because of the finiteness of  $\xi$  in this region, the outer counterpart of Equation (39) must again take place. Nevertheless, for  $s = -2$ , one should also impose

$$A_{m,s=-2}^+ = (m-2)(m+1). \quad (40)$$

From Equation (36), one sees from this case that its associated fundamental mode ( $m = 0$ ) is unstable. This means in principle that this solution to the outer region should be excluded, leaving out just the one from the case  $s = 1$ , where we should consider

$$A_{m,s=1}^+ = (m+1)(m+4). \quad (41)$$

Still, our previous analysis exhibits clear problems: there are not enough arbitrary constants to fix Equations (28) and (32), and the eigenfrequencies in each region are different. However, we shall show that the condition of having a same eigenfrequency for the whole system, as required by our formalism, addresses all of the problems. Obviously, the stable eigenfrequencies of the star are only related to the solution  $s = 1$ . However, they could arise here from aspects of either the inner or outer phases of the star. Let us see what ensues from this conclusion. Assume initially that the only possible  $\omega$  are given by Equation (39), associated with the modes  $m_{s=1}^-$ . So, for having finite  $\xi^+$  related to  $s = 1$ , one must impose that there exists a  $m_{s=1}^+$  to the outer phase such that the numerator of the associated recurrence relation is null. It can be shown that this is only the case if

$$m_{s=1}^+ = \frac{-5 + \sqrt{9 + 4A_{s=1}^+(m_{s=1}^-)}}{2}. \quad (42)$$

Therefore, Equation (42) demands that

$$9 + 4A_{s=1}^+ = (2p+1)^2, \quad p \geq 2, \quad p \in \mathbb{N}. \quad (43)$$

For the case  $s = -2$  to  $\xi^+$ , it can be shown that the condition for the existence of a  $m_{s=-2}^+$  related to  $a_{m_{s=-2}^+} = 0$  is exactly given by Equation (43). The mode itself is

$$m_{s=-2}^+ = \frac{1 + \sqrt{9 + 4A_{s=1}^+(m_{s=1}^-)}}{2}. \quad (44)$$

Summarizing: if Equation (43) is satisfied for any natural  $p \geq 2$ , there always exist modes, characterized by Equations (42) and (44), that guarantee the finiteness of  $\xi^+$  as a linear combination of solutions for  $s = 1$  and  $s = -2$ , associated with a given eigenfrequency  $\omega_{m_{s=1}^-}$  that only takes into account aspects of the inner phase of the system. In this case,

one is able to come up with two arbitrary constants of integration, which would then guarantee that the additional boundary conditions raised by the stratification, Equations (28) and (32), are satisfied. It is immediately apparent that a reasoning similar to the above ensues if one now chooses  $\omega_{m_{s=1}^+}$  as coming from aspects of the outer region, given now by Equations (36) and (41). For this case, we will now find an  $m_{s=1}^-$  and an  $m_{s=-2}^+$  associated with  $\omega_{m_{s=1}^+}$ , as given by Equations (42) and (44), with the condition given by Equation (43), replacing  $A_{s=1}^+(m_{s=1}^-)$  by  $A_{s=1}^-(m_{s=1}^+)$ . Because  $\Gamma^\pm$  and  $\rho^\pm$  are given quantities, one sees that the only possible eigenfrequencies for a system should satisfy  $9 + 4A_{s=1}^\pm = (2p + 1)^2$ . This constraint is uniquely imposed because of the extra boundary conditions to the problem and is very restrictive. We have just shown a simple example where some of the aspects imprinted by stratification arise. Whenever there are two arbitrary solutions to  $\xi$  in a given phase, it will be always possible to satisfy the constraints (28) and (32).

#### 4. SYSTEMS WITH AN ELECTROMAGNETIC STRUCTURE

Now we attempt to take a further step in our classical generalization, by endowing the phases (as well as the surface of a discontinuity) with an electromagnetic structure. Just for clarity, let us work with a system that exhibits just an electric field. The first point to be taken into account is the additional electric force present in the system. This would have the same structure as the gravitational force, and therefore its generalization is straightforward. Now one should also define a distributional solution to the charge density. The surface force associated with the surface tension should have the same form as previously, but now it should also take into account the present electric aspects. The pressure in this case would also change because of the presence of the electric field, and its jump over a surface of discontinuity could still be kept free.

From the (distributional) Maxwell equations in the spherically symmetric case, one has that

$$E(r) = \frac{Q(r)}{r^2}, \quad Q(r) \doteq 4\pi \int_0^r \rho_c(\bar{r})\bar{r}^2 d\bar{r}, \quad (45)$$

where  $\rho_c(r)$  is the charge density at  $r$ . The associated ‘‘force density’’ is  $d\mathbf{F}_{el}/dv = \rho_c E(r)\hat{r}$ . Therefore, the equation of hydrostatic equilibrium now reads

$$\frac{dP}{dr} + \rho(r)g(r) - \rho_c(r)E(r) - \frac{2P_Q}{R}\delta(r - R) = 0. \quad (46)$$

Therefore, like the gravitational field, the electric field also presents a jump at any surface of a discontinuity (at  $r = R$ ) endowed with surface charges. We write the charge density as

$$\rho_c(r) = \rho_c^-(r)\theta(R - r) + \rho_c^+(r)\theta(r - R) + \sigma_c\delta(r - R), \quad (47)$$

and the distributional electric field is

$$E(r) = E^-(r)\theta(R - r) + E^+(r)\theta(r - R), \quad [E(R)]_\pm^+ = 4\pi\sigma_c. \quad (48)$$

By substituting now Equations (10), (45), (47), and (48) into Equation (46), we have that the surface tension at equilibrium should read

$$\mathcal{P}_Q = \frac{R}{2}[P(R)]_\pm^+ + \frac{G}{16\pi R^3}[M^2(R)]_\pm^+ - \frac{1}{16\pi R^3}[Q^2(R)]_\pm^+. \quad (49)$$

Note that the existence of a surface mass would lead to  $[M^2(R)]_\pm^+ > 0$ , and  $[Q^2(R)]_\pm^+$  could in principle be any. The appearance of the last term in Equation (49) is consistent with the expected and long ago known contribution of electric double layers to the surface tension and surface energy of metals, as recalled by Frenkel (1917) in his seminal work. The existence of such surface electric fields is well known in materials science, and it has been determined experimentally from the photoelectric phenomenon by measuring the amount of work done by electrons to escape from a metal’s surface. There is a vast literature on the role of electric double layers on surface phenomena in metals and contact surfaces, and we refer the reader for instance to Huang & Wyllie (1949) and Israelachvili (2011), and references therein, for further details on this subject.

Because in the presence of an electric field the hydrostatic equilibrium equation and the surface tension changes, it can be checked that Equation (30) keeps the same functional form. In drawing this conclusion, it was also assumed that the total charge of the system is a constant. This also means that  $\Delta Q = 0$ . One also sees immediately that the main results concerning the stability of the stratified charged case are totally analogous to the neutral one, obtained by simply making the replacement  $\mathcal{P} \rightarrow \mathcal{P}_Q$ .

#### 5. STRATIFIED SYSTEMS IN GENERAL RELATIVITY

Now we generalize the analysis of stratified systems to general relativity. From the classical analysis, we have learned that surface quantities must also be inserted into the generalized equation of hydrostatic equilibrium. Therefore, in a certain sense, we must find the proper generalization of the surface forces in general relativity. This will not be difficult bearing in mind the thin-shell formalism, as we shall see below. Such a formalism states that in order to search for distributional solutions to general relativity, one has to consider an energy-momentum tensor at a surface of discontinuity, which we shall name  $\Sigma$ . It is precisely this surface content that leads to the jump of quantities that are related to physical observables, such as the extrinsic curvature. We now outline the formalism succinctly. Let us work just in the spherically symmetric case, where  $\Sigma$  is defined as  $\Phi = r - R(\tau) = 0$ , with  $\tau$  the proper time of an observer on the aforesaid hypersurface. Assume that the metrics in the regions above and below  $\Sigma$  (with respect to the normal vector to it), described by the coordinate systems  $x_\pm^\mu \doteq (t_\pm, r_\pm, \theta_\pm, \text{ and } \varphi_\pm)$ , respectively, are given by

$$ds_\pm^2 = e^{2\alpha_\pm(r_\pm)} dt_\pm^2 - e^{2\beta_\pm(r_\pm)} dr_\pm^2 - r_\pm^2 d\Omega_\pm^2, \quad (50)$$

where

$$d\Omega_\pm^2 = d\theta_\pm^2 + \sin^2\theta_\pm d\varphi_\pm^2. \quad (51)$$

Assume that the (three-dimensional) hypersurface  $\Sigma$  is described by the (intrinsic) coordinates  $y^a \doteq (\tau, \theta, \varphi)$  such that at the hypersurface  $t_\pm = t_\pm(\tau)$ ,  $\theta_\pm = \theta$  and  $\varphi_\pm = \varphi$  and obviously  $r_\pm = R(\tau)$ . In order to render the procedure consistent, one has to impose primarily that the intrinsic metric to  $\Sigma$  is unique. This fixes the coordinate transformations  $x_\pm^\mu = x_\pm^\mu(y^a)$ . This is the generalization of the continuity of the gravitational potential across a surface harboring surface degrees of freedom. Now, if the jump of the extrinsic curvature is nonnull, the existence of a surface energy-momentum tensor (Poisson 2004) is automatically guaranteed that in the spherically symmetric case can always be cast as  $S^a_b = \text{diag}(\sigma, -\mathcal{P}, -\mathcal{P})$ , with

(see, e.g., Lobo & Crawford 2005)

$$\sigma = -\frac{1}{4\pi R} \left[ \sqrt{e^{-2\beta} + \dot{R}^2} \right]_+^-, \quad (52)$$

$$\mathcal{P} = -\frac{\sigma}{2} + \frac{1}{8\pi R} \left[ \frac{R\alpha'(e^{-2\beta} + \dot{R}^2) + \ddot{R}R + \beta'R\dot{R}^2}{\sqrt{e^{-2\beta} + \dot{R}^2}} \right]_+^-, \quad (53)$$

where generically  $A' \doteq \partial A/\partial r$  and  $\dot{A} \doteq dA/d\tau$ . Finally, the discontinuity of the extrinsic curvature is the generalization of the discontinuity of the gravitational field across a surface with nontrivial degrees of freedom. The case of interest to be analyzed here is the static and stable (upon radial displacements of  $\Sigma$ ) one,  $\dot{R} = \ddot{R} = 0$ , i.e., an equilibrium point.

Let us see now how the generalization of the surface forces appears in this formalism. First of all, we know that

$$T_{\mu\nu} = T_{\mu\nu}^+ \theta(r - R) + T_{\mu\nu}^- \theta(R - r) + e_\mu^a e_\nu^b S_{ab} \delta(r - R), \quad (54)$$

where  $e_\mu^a \doteq \partial y^a/\partial x^\mu$  and  $S_{ab} = h_{ac} S_b^c$ ,  $h_{ab} \doteq e_a^\mu e_b^\nu g_{\mu\nu}$ . Note that  $e_\mu^a$  is itself defined as a distribution. For  $h_{ab}$ , it does not matter what side of  $\Sigma$  one takes to evaluate it, because it must be unique. Let us constrain ourselves first to the case of perfect fluids (locally neutral) on each side of  $\Sigma$ . One sees from Equation (54) and the coordinate transformations at  $\Sigma$  that

$$T_0^0 \doteq \rho = \rho^+ \theta(r - R) + \rho^- \theta(R - r) + \sigma \delta(r - R), \quad (55)$$

$$T_1^1 \doteq -P = -P^+ \theta(r - R) - P^- \theta(R - r), \quad (56)$$

and

$$T_2^2 = T_3^3 \doteq -P_t = -P - \mathcal{P} \delta(r - R). \quad (57)$$

From Equation (56), we note that there are no associated surface stresses. This is exactly what we advanced in the classical case with heuristic arguments and obtained here as a general consequence of distributional solutions to general relativity. Let us search formally for solutions to Einstein's equations with the energy momentum given by Equations (55)–(57) with the ansatz

$$ds^2 = e^{2\alpha} dt^2 - e^{2\beta} dr^2 - r^2(d\theta^2 + \sin^2\theta d\varphi^2). \quad (58)$$

The distributional nature of Equation (58) will be evidenced by Equation (54). As the solution, we have

$$e^{-2\beta} = 1 - \frac{2m(r)}{r}, \quad m(r) \doteq 4\pi \int_0^r \rho(\bar{r}) \bar{r}^2 d\bar{r}. \quad (59)$$

Note from the above equation that  $\rho$  is given by Equation (55), and therefore  $e^{-2\beta}$  is a distribution generally discontinuous at  $R$ . For  $\alpha$  we have, though,

$$\alpha' = \frac{e^{2\beta}}{r^2} [4\pi P r^3 + m(r)], \quad (60)$$

where  $P$  is given by Equation (56). From Equations (59) and (60), we see that  $\alpha'$  is a distribution with no Dirac delta function terms. Therefore, this implies that  $[\alpha]_\pm^+ = 0$ . In other words, the function  $\alpha$  is generally continuous though not differentiable at  $R$ . Nevertheless, from the conservation law of the energy-momentum tensor given by Equation (54), we also have

$$\alpha'_\pm (\rho_\pm + P_\pm) = -P'_\pm. \quad (61)$$

We note that  $T^{\mu\nu}{}_{;v} = 0$ , taking into account Equation (54), would give us in principle terms dependent upon Heaviside functions, Dirac delta functions, and their derivatives. The terms associated with the Heaviside functions are null because of the validity of Einstein's equations on each side of  $\Sigma$ . The nullity of the remaining terms is associated with identities that the surface energy-momentum tensor has to satisfy (see, e.g., Mansouri & Khorrami 1996). It is not difficult to show that such identities are automatically satisfied when one takes into account Equations (52) and (53) (see, e.g., Lobo & Crawford 2005). This shows that the thin-shell formalism is consistent, and the surface terms must indeed be taken as the aforesaid equations.

In order to put Equation (61) in the form that would allow us to consider Equations (55) and (56), we mandatorily should add surface terms. The correct way of doing it is

$$\begin{aligned} \frac{dP}{dr} = & -(\rho + P)\alpha' + \frac{2P}{R} \delta(r - R) + \left\{ [P(R)]_+^+ \right. \\ & \left. + \frac{\sigma}{2} [\alpha'_+(R) + \alpha'_-(R)] + \frac{\sigma}{R} - \frac{[\alpha' e^{-\beta}]_+^+}{4\pi R} \right\} \delta(r - R). \end{aligned} \quad (62)$$

Now we show that, in the classical limit, Equation (62) reduces exactly to Equation (5), and thus it is its proper generalization. First of all, note that in such a limit,  $\alpha = \phi(r)$ ,  $\phi(r)$  the gravitational potential. It can be also shown that in such a case

$$\sigma = \frac{1}{4\pi R^2} [M(R)]_+^+, \quad (63)$$

where the above quantities are in cgs units. In Equation (63) one recognizes the jump of the gravitational field  $g(r) = \phi' = GM(r)/r^2$  at  $r = R$ , as exactly given by Equation (8). Therefore,

$$\frac{\sigma}{2} \{\alpha'_+(R) + \alpha'_-(R)\} \simeq \frac{G[M^2(R)]_+^+}{8\pi R^4}. \quad (64)$$

Substituting Equation (64) into Equation (62), we see that the term inside the curly brackets of the latter equation is null (see Equations (53) and (11)). Hence, the remaining term in front of the delta function is exactly  $2P/R$ , as we already advanced and expected (see Equation (5)).

Now we are in a position to talk about perturbations in the general relativistic scenario. When they take place, metric and fluid quantities change at a given spacetime point from their static counterparts. It is customary to assume that such departures are small, which allows us to work perturbatively. The primary task is to find such changes from the system of equations coming from relativistic hydrodynamics and general relativity. Nevertheless, these solutions are already very well known (Misner et al. 1973). Our ultimate task is simply to generalize them to the distributional case.

The equation governing the evolution of the fluid displacements on each side of  $\Sigma$  is the general relativistic Euler equation, related to the orthogonal projection of  $T^{\mu\nu}{}_{;v}$  (perfect fluids) onto  $u^\mu$ :

$$(\rho + P)u^\nu{}_{;\mu} u^\mu \doteq (\rho + P)a^\nu = (g^{\mu\nu} - u^\mu u^\nu)P_{,\mu}, \quad (65)$$

where the labels  $\pm$  for each term in the above equation were omitted just to not overload the notation.

In the hydrostatic case, we have only that  $u'_{\pm} = e^{-\alpha_{\pm}^{\pm}}$ . When perturbations are present (Misner et al. 1973),

$$u'_{\pm} = e^{-\alpha^{\pm}} = e^{-\alpha_0^{\pm}}(1 - \delta\alpha^{\pm}), \quad (66)$$

where  $\delta\alpha$  is the change of the static solution  $\alpha_0$  in the presence of perturbations at a given spacetime point. For the  $u'_{\pm}$  component, using the normalization condition  $u'_{\pm} u'_{\mu} = 1$ , one shows that (Misner et al. 1973)

$$u'_{\pm} = e^{-\alpha_0^{\pm}} \dot{\xi}_{\pm}^{\pm}, \quad (67)$$

with  $\dot{\xi}^{\pm} \doteq \partial \tilde{\xi}^{\pm} / \partial t^{\pm}$ . Just for completeness,  $u^{\theta}_{\pm} = u^{\varphi}_{\pm} = 0$ . For the components of  $u'_{\pm}$  given by Equations (66) and (67), the left-hand side of Equation (65) gives as the only nontrivial component  $a'_{\pm} = -e^{-2\beta^{\pm}} a'_{r^{\pm}}$ , with

$$-a'_{r^{\pm}} = \alpha'_{0\pm} + \delta\alpha'_{\pm} + e^{2(\beta_0^{\pm} - \alpha_0^{\pm})} \ddot{\xi}_{\pm}^{\pm} \quad (68)$$

and the associated equation of motion

$$(\rho^{\pm} + P^{\pm})(-a'_{r^{\pm}}) = -\frac{\partial P^{\pm}}{\partial r_{\pm}}. \quad (69)$$

From Equation (68), Equation (69) can be cast as

$$(\rho_0^{\pm} + P_0^{\pm})e^{2(\beta_0^{\pm} - \alpha_0^{\pm})} \ddot{\xi}_{\pm}^{\pm} = -\frac{\partial P^{\pm}}{\partial r_{\pm}} - (\rho^{\pm} + P^{\pm})\alpha'_{\pm}. \quad (70)$$

Therefore, in terms of distributions, Equation (70) reads

$$\begin{aligned} (\rho_0 + P_0)e^{2(\beta_0 - \alpha_0)} \ddot{\xi} &= -\frac{\partial P}{\partial r} - (\rho + p)\alpha' + \frac{2P}{R}\delta(r - R) \\ &+ \left[ \frac{\sigma}{R} - \frac{[\alpha' e^{-\beta}]_{\pm}^{\pm}}{4\pi R} + [P(R)]_{\pm}^{\pm} \right. \\ &\left. + \frac{\sigma}{2} \left\{ e^{2(\beta_0^+ - \alpha_0^+)} \ddot{\xi}_{+}^+ + e^{2(\beta_0^- - \alpha_0^-)} \ddot{\xi}_{-}^- + \alpha'_{+} + \alpha'_{-} \right\} \right] \delta(r - R), \end{aligned} \quad (71)$$

where  $\rho$  and  $P$  are given by Equations (55) and (56), respectively, and now

$$\tilde{\xi}(r, t) = \tilde{\xi}^+(r^+, t^+)\theta(r^+ - R) + \tilde{\xi}^-(r^-, t^-)\theta(R - r^-). \quad (72)$$

Note that in Equation (71) we are considering jumps and symmetrizations of quantities defined in the presence of perturbations. As we stated previously, such perturbations change slightly the value of the physical quantities with respect to their hydrostatic values. The square brackets term of Equation (71) is the proper generalization of the curly brackets term in Equation (20). Naturally, the reasoning for the eigenfrequencies of  $\tilde{\xi}$  in the general relativistic case is the same as in the classical case. The same can be said about the continuity, though not differentiability, of  $\tilde{\xi}$  at any surface of a discontinuity.

Now, in order to have the proper generalization of Equation (30), we should evaluate Equation (71) at  $r + \tilde{\xi}$  and then subtract it from its evaluation at  $r$  concerning the static solution. In order to do it properly, one should take into account the general results for the case of Lagrangian displacements coming from the standard procedure (see, e.g., Misner et al. 1973), but now in the sense of distributions, by recalling that

$\Delta A \doteq A(r + \tilde{\xi}, t) - A_0(r, t)$ , where  $A_0$  concerns the quantity  $A$  at equilibrium.

It is not difficult to see that we have the following results in the general relativistic distributional case (see, e.g., Misner et al. 1973, for the treatment of a continuous system):

$$\Delta\beta = -\alpha'_0 \tilde{\xi}, \quad (73)$$

$$\Delta\alpha' = 4\pi r e^{2\beta_0} [\delta P + 2\delta\beta P_0] + \frac{e^{2\beta_0}}{r} \delta\beta + \alpha'_0 \tilde{\xi}, \quad (74)$$

$$\Delta P = -\gamma P_0 \left[ \frac{e^{-\beta_0} (r^2 e^{\beta_0} \tilde{\xi})'}{r^2} + \delta\beta \right], \quad (75)$$

$$\begin{aligned} \Delta\rho &= -(\rho_0 + P_0) \left[ \frac{1}{r^2} \frac{\partial}{\partial r} (r^2 \tilde{\xi}) \right] + \left( \frac{\sigma}{2} \left\{ \frac{\partial \tilde{\xi}^+}{\partial r} + \frac{\partial \tilde{\xi}^-}{\partial r} \right\} \right. \\ &\left. + \Delta\sigma + \frac{2\sigma_0 \tilde{\xi}}{R} + [P_0]_{\pm}^{\pm} \tilde{\xi} \right) \delta(r - R) - \frac{dP_0}{dr} \tilde{\xi}, \end{aligned} \quad (76)$$

$$\gamma \doteq \frac{\rho_0 + P_0}{P_0} \left( \frac{\partial P}{\partial \rho} \right)_{s=\text{const}}, \quad (77)$$

$$\Delta\sigma = -\frac{2\sigma_0 \tilde{\xi}}{R} - \tilde{\xi} \left( [e^{\beta_0} P_0]_{\pm}^{\pm} + \frac{[\cosh \beta_0]_{\pm}^{\pm}}{4\pi R^2} \right). \quad (78)$$

We stress that Equation (75) assumes adiabatic processes, in which one considers  $P = P(\rho)$ , and we have made use of  $[\tilde{\xi}]_{\pm}^{\pm} = 0$  for the above equations.

We shall seek solutions to the perturbations as  $\tilde{\xi} = e^{i\omega t} \xi(r)$  with  $\omega$  the same for all of the phases the system may have. We just need to worry about the Dirac delta function term because it gives us the desired boundary condition valid for the separation of each two phases. The terms in front of the Heaviside functions by default will be the ones found in continuous media. It is not hard to see that the surface terms at the end should satisfy the condition

$$\frac{\Delta\sigma}{R} (2\eta^2 + 1) - \frac{\Delta[\alpha' e^{\beta}]_{\pm}^{\pm}}{4\pi R} = 0, \quad (79)$$

where we have used Equation (24). When the last term on the left-hand side of the above equation is expanded by using Equations (60) and (73), Equation (79) can be further simplified to

$$\frac{2\eta^2 \Delta\sigma}{R} - \Delta \left[ \frac{[\cosh \beta]_{\pm}^{\pm}}{4\pi R^2} \right] = \left[ \frac{2P}{R^2} - [P e^{\beta} \alpha']_{\pm}^{\pm} \right] \tilde{\xi} + [\Delta P e^{\beta_0}]_{\pm}^{\pm}. \quad (80)$$

One sees from Equation (80) that Equation (32) is recovered in the classical limit by recalling that  $\beta = M(r)/r$ , which implies that the last term on the left-hand side of the above equation is  $4\sigma(g^+ + g^-)/(2R)$ . In this limit we take  $P \rightarrow 0$  and  $e^{\beta} \rightarrow 1$  for the remaining terms.

The case where electromagnetic interactions are also present is also of interest because its associated energy-momentum

tensor is anisotropic. This naturally influences the equation of hydrostatic equilibrium, because it now becomes

$$\alpha'(P + \rho) = -P' - \frac{2}{r}(P_t - P), \quad (81)$$

where  $P$ ,  $P_t$ , and  $\rho$  are the resultant radial pressure, tangential pressure, and energy density of the fluid, respectively. For the electromagnetic fields, clearly  $(P_t - P)$  is solely related to them. Because of the aforementioned aspects, the latter should also influence the dynamics of the radial perturbations, as we will show in the next section.

## 6. ELECTROMAGNETIC INTERACTIONS IN STRATIFIED SYSTEMS WITHIN GENERAL RELATIVITY

We consider now the inclusion of electromagnetic interactions within the scope of stratified systems in general relativity. An important comment at this level is in order. Because we are dealing with electromagnetic fields in stars, it would be more reasonable to assume the Maxwell equations in material media. Nevertheless, because our knowledge of the structures constituting the stars is not yet precise, it is difficult to assess their realistic dielectric properties. Because working with Maxwell equations in the absence of material media gives us upper limits to the fields under normal circumstances, this seems to be a good first tool to evaluate the relevance and effects of electromagnetism in stars. For the time being we will follow this approach. The energy-momentum tensor of each layer of the system we are now interested in should also have the electromagnetic one<sup>5</sup>:

$$4\pi T_{\mu\nu}^{(em)} = -F_{\mu\alpha}F_{\nu\beta}g^{\alpha\beta} + g_{\mu\nu}\frac{F^{\alpha\beta}F_{\alpha\beta}}{4}, \quad (82)$$

where we defined  $F_{\mu\nu} \doteq \partial_\mu A_\nu - \partial_\nu A_\mu$ . Solving Einstein–Maxwell equations on each layer of a stratified system leads us to the following equilibrium condition (Bekenstein 1971):

$$\frac{\partial P}{\partial r} = \frac{Q(r)Q'(r)}{4\pi r^4} - \alpha'_Q(\rho + P), \quad (83)$$

where

$$Q(r) \doteq \int_0^r 4\pi r'^2 \rho_c e^{\beta_Q} dr', \quad E(r) = e^{\alpha_Q + \beta_Q} \frac{Q(r)}{r^2}, \quad (84)$$

$$e^{-\beta_Q} = 1 - \frac{2m_Q(r)}{r} + \frac{Q^2(r)}{r^2} \quad (85)$$

$$\alpha'_Q = \frac{e^{2\beta_Q}}{r^2} \left[ 4\pi r^3 P + m_Q(r) - \frac{Q^2(r)}{r} \right] \quad (86)$$

and

$$m_Q(r) \doteq \int_0^r 4\pi r'^2 \rho dr' + \frac{Q^2}{2r} + \frac{1}{2} \int_0^r \frac{Q^2}{r^2} dr. \quad (87)$$

Equations (84), (85), (86), and (87) are the charge, radial, and time components of the metric and the energy of the system up to a radial coordinate  $r$ , respectively. In Equation (84), we also showed the electric field  $E(r)$  in the context of general relativity, obtained by means of the definition  $F_{tr} \doteq E(r) = -\partial_r A_0$ . We stress that  $\rho_c$  is the physical charge density of the system, defined in terms of the four-current by  $j^\mu \doteq e^{-\alpha_Q} u^\mu$ , where  $u^\mu$  is the

four-velocity of the fluid with respect to the coordinate system  $(t, r, \theta, \varphi)$  (see Landau & Lifshitz 1975, for further details).

From Equation (83) one sees that in the scope of general relativity the effect of the charge is not merely to counterbalance the gravitational pull. For certain cases, it could even contribute to it. This is due to the contribution of the electromagnetic energy to the final mass of the system, as clearly given by Equation (87). Note from Equation (87) that we have assumed that the mass at the origin is null, in order to avoid singularities there. More generically, one could assume point or surface mass contributions in Equation (87) by conveniently adding Dirac delta functions in  $\rho$ . Finally, we stress that Equation (84) can indeed be seen as the generalization of the charge in general relativity because it takes into account the nontrivial contribution coming from the spacetime warp due to its energy-momentum content.

Note that the classical limit to Equation (83) can be shown to coincide with Equation (46), by recalling that  $E_{\text{clas}}(r) = Q_{\text{clas}}(r)/r^2$  and, from Equation (84),  $Q'_{\text{clas}}(r) = 4\pi r^2 \rho_c$ . In addition, we recall that when converted to cgs units, the term  $Q^2/r$  (here in geometric units) becomes  $Q^2/(c^2 r)$ , which is null in the classic nonrelativistic limit, as well as any pressure term on the right-hand side of the aforementioned equation.

Now, consider the analysis of a charged system constituted of two parts, connected by a surface of discontinuity (at  $r^\pm = R$ ) that hosts surface degrees of freedom, such as an energy density, a charge density, and a surface tension. Its generalization to an arbitrary number of layers is immediate because each surface of discontinuity is only split by two phases. The proper description of the charge density in this case would be given by the generalization of Equation (47). Therefore, one would have at equilibrium that

$$Q(r) = Q^-(r^-)\theta(R - r^-) + Q^+(r^+)\theta(r^+ - R), \quad (88)$$

and for  $Q'(r)$ , a Dirac delta will rise due to  $\rho_c$ .

Let us define the distribution

$$\bar{\rho}_c \doteq \rho_c e^{\beta_Q} \doteq \bar{\rho}_c^+ \theta(r - R) + \bar{\rho}_c^- \theta(R - r) + \bar{\sigma}_c \delta(r - R), \quad (89)$$

where  $\bar{\rho}_c^\pm = \bar{\rho}_c^\pm(r^\pm)$ . From the above definition, we have that  $Q' = 4\pi r^2 \bar{\rho}_c$ . It implies that the total charge is the same as the one associated with  $\bar{\rho}_c$  in a Euclidean space. Therefore, all classical results apropos of the charge densities and total charges that we deduced in the previous sections ensue here for  $\bar{\rho}_c$ .

We seek now the distributional generalization of Equation (83). This can be easily done by following the same reasoning from the previous section, which finally leads us to

$$\begin{aligned} \frac{dP}{dr} = & \frac{Q(r)\bar{\rho}_c}{r^2} - (\rho + P)\alpha'_Q + \frac{2P_Q}{R}\delta(r - R) \\ & + \left\{ [P(R)]_-^+ + \frac{\sigma_Q}{2} [\alpha'_{Q^+}(R) + \alpha'_{Q^-}(R)] + \frac{\sigma_Q}{R} \right. \\ & \left. - \frac{[\alpha'_{Q^-} e^{-\beta_Q}]_-^+}{4\pi R} - \frac{\bar{\sigma}_c}{2R^2} [Q_+(R) + Q_-(R)] \right\} \delta(r - R), \end{aligned} \quad (90)$$

where we are assuming that surface quantities with the subindex  $Q$  are related to the charged versions of Equations (52) and (53) (see also Equations (85) and (86)). It is easy to show that in the classical limit Equation (49) naturally rises, implying that in such a limit the curly brackets in Equation (90) are null.

<sup>5</sup> We restrict our analyses to the Maxwell Lagrangian,  $-F^{\mu\nu}F_{\mu\nu}/4 \doteq -F/4$ .

We consider now the case where radial perturbations take place in our charged system. This case is more involved than the neutral case because the charged particles also feel an electric force. The equation describing the evolution of the displacements can be shown to be generalized to (see Anninos & Rothman 2002, for the dynamics of the radial perturbations in a given phase)

$$\begin{aligned}
 (\rho_0 + P_0)e^{2(\beta_{Q0} - \alpha_{Q0})} \ddot{\xi} &= -\frac{\partial P}{\partial r} - (\rho + P)\alpha'_Q \\
 &+ \frac{Q(r)\bar{\rho}_c}{r^2} + \frac{2P_Q}{R}\delta(r - R) + \left[ \frac{\sigma_Q}{R} - \frac{[\alpha'_Q e^{-\beta_Q}]^+}{4\pi R} \right. \\
 &+ \frac{\sigma_Q}{2} \left\{ e^{2(\beta_{Q0}^+ - \alpha_{Q0}^+)} \ddot{\xi}^+ + e^{2(\beta_{Q0}^- - \alpha_{Q0}^-)} \ddot{\xi}^- + \alpha'_{Q+} + \alpha'_{Q-} \right\} \\
 &\left. - \frac{\bar{\sigma}_c}{2R^2} [Q_+(R) + Q_-(R)] + [P(R)]^+ \right] \delta(r - R). \quad (91)
 \end{aligned}$$

For the change in  $Q(r)$ , it can be shown (see Bekenstein 1971) that in the comoving frame there are no currents. This means that the Lagrangian displacements of  $Q$  are null,  $\Delta Q = 0$ . Equation (91) takes into account the values of the physical quantities in the presence of perturbations at  $r$ . In order to obtain the generalization of Equation (30), we should evaluate Equation (91) at  $r + \tilde{\xi}$  and subtract it from Equation (90). This is due to the definition of the Lagrangian displacement of a given physical quantity, intrinsically related to the notion of observers comoving with the fluid, who naturally could describe its thermodynamics.

In order to simplify Equation (91), we have in the generalized charged case (see Anninos & Rothman 2002 for the treatment in a phase of a charged system)

$$\Delta\beta_Q = -\alpha'_{Q0}\tilde{\xi}, \quad (92)$$

$$\begin{aligned}
 \Delta\alpha'_Q &= 4\pi r e^{2\beta_{Q0}} \left[ \delta P + 2\delta\beta_Q \left( P_0 - \frac{Q_0^2}{8\pi r^4} \right) \right] \\
 &+ \frac{e^{2\beta_{Q0}}}{r} \delta\beta_Q + \alpha'_{Q0}\tilde{\xi} + \frac{4\pi e^{2\beta_{Q0}} \bar{\rho}_c Q_0}{r} \tilde{\xi} - \frac{2\pi \bar{\sigma}_c \tilde{\xi}}{R} \\
 &\times (Q_0^+ e^{2\beta_0^+} + Q_0^- e^{2\beta_0^-}) \delta(r - R), \quad (93)
 \end{aligned}$$

$$\Delta P = -\gamma P_0 \left[ \frac{e^{-\beta_{Q0}} (r^2 e^{\beta_{Q0}} \tilde{\xi})'}{r^2} + \delta\beta_Q \right], \quad (94)$$

$$\begin{aligned}
 \Delta\rho &= -(\rho_0 + P_0) \left[ \frac{1}{r^2} \frac{\partial}{\partial r} (r^2 \tilde{\xi}) \right] - \left[ \frac{dP_0}{dr} - \frac{Q_0 \bar{\rho}_c}{r^2} \right] \tilde{\xi} \\
 &+ \left( \frac{\sigma_{Q0}}{2} \left\{ \frac{\partial \tilde{\xi}^+}{\partial r} + \frac{\partial \tilde{\xi}^-}{\partial r} \right\} + \Delta\sigma_Q + \frac{2\sigma_{Q0}\tilde{\xi}}{R} + [P_0]^- \tilde{\xi} \right. \\
 &\left. - \frac{\bar{\sigma}_c \tilde{\xi}}{2R^2} [Q_+ + Q_-] \right) \delta(r - R), \quad (95)
 \end{aligned}$$

$$\gamma \doteq \frac{\rho_0 + P_0}{P_0} \left( \frac{\partial P}{\partial \rho} \right)_{s=\text{const}}, \quad (96)$$

$$\Delta\sigma_Q = - \left[ \frac{2\sigma_{Q0}}{R} + [e^{\beta_{Q0}} P_0]^- + \frac{[\cosh \beta_{Q0}]^+}{4\pi R^2} \right] \tilde{\xi}. \quad (97)$$

The additional 0 subindex in a physical quantity means that its value at equilibrium was taken. We just stress that Equation (96) is the general relativistic definition of the adiabatic index and assumes the existence of an equation of state linking the pressure and density of the system,  $P = P(\rho)$ . In this sense, it generalizes  $\Gamma$  as defined by Equation (3).

By seeking solutions for  $\tilde{\xi} = e^{i\omega t} \xi(r)$ , one can see that Equation (91) only gives meaningful boundary conditions when a frequency  $\omega$  is the same for all of the phases present in the system. We emphasize that this is a universal property of the approach developed here, due to the surface degrees of freedom and the well-posedness of the problem of radial perturbations in stratified systems. The associated boundary condition arising from this analysis leads us to the conclusion that generically  $\xi(r)$  is not differentiable at a surface of discontinuity, though continuous. It can be shown that the associated boundary condition to be taken into account here is functionally the same as Equation (79) (or Equation (80)), where now the metric and surface quantities should be related to the charged case.

## 7. CONCLUSIONS

In this article we have developed a formalism for assessing the stability of a stratified star against radial perturbations. We have derived the relevant equations defining this boundary-value problem for both neutral and charged stars and in Newtonian and Einstein's gravity. It makes use of the generalized theory of distributions: we assumed that the surfaces of discontinuity are thin, that they host surface degrees of freedom, and that the phases separated by them do not mix. We showed that although the phases may be very different among themselves, when perturbations take place, they lead to the notion of a set of eigenfrequencies describing the whole system, instead of an independent set for each phase. As a consequence, our formalism also gave us the proper additional boundary conditions to take into account when working with stratified systems. Such boundary conditions encompass surface degrees of freedom in the surfaces of discontinuities and generically modify the set of eigenfrequencies with respect to their continuous counterpart. This should be a generic fingerprint of stratified systems with nontrivial surface degrees of freedom. Our analyses are relevant for the assessment of the stability of realistic star models because they ensue the precise notion of boundary conditions. It was not our objective to systematically apply our formalism here, but simply to derive and expound it. It is clear that for precise and realistic numerical stability calculations, it would be ideal to have the microphysical knowledge of the properties of the interfacial surfaces. However, this a difficult problem that has been elusive even in the most advanced fields of materials science, where laboratory data of material surface properties are accessible, but there is still a lack of a complete physical theory for their explanation (Israelachvili 2011). Thus, the measurement of the star's eigenmodes becomes of major relevance because it could give information not only on the star's bulk structure but also on the possible existence of interior interfaces and their associated microphysical and electromagnetic phenomena.

The radial instabilities shown in our analyses should be interpreted analogously for continuous stars because, even in the stratified case, a global set of eigenfrequencies arises. Thus,

stratified stars would either implode or explode when they are radially unstable. Although we were concerned only with radial perturbations, it is of interest to investigate the additional oscillation modes owing to nonradial perturbations. The only point to be added, with respect to continuous stars, is the proper redefinition of the surfaces of discontinuity when such perturbations take place. This is clearly a richer scenario that inserts additional degrees of freedom into the system, leading to the appearance of additional modes such as the gravitational  $g$  modes (see, e.g., Reisenegger & Goldreich 1992). Such an analysis, however, is a second step that goes beyond the goal of the present work and that we are planning to investigate elsewhere.

We are grateful to Professor Thibault Damour for discussions on various occasions at the International Relativistic Astrophysics (IRAP) PhD-Erasmus Mundus Joint Doctorate Schools held in Nice. We are likewise grateful to Professor Luis Herrera. J.P.P. acknowledges the support given by the Erasmus Mundus Joint Doctorate Program within the IRAP PhD, under Grant Number 2011-1640 from EACEA of the European Commission. J.A.R. acknowledges the support by the International Cooperation Program CAPES-ICRANet financed by CAPES–Brazilian Federal Agency for Support and Evaluation of Graduate Education within the Ministry of Education of Brazil.

#### REFERENCES

- Anninos, P., & Rothman, T. 2002, [PhRvD](#), **65**, 024003
- Bekenstein, J. D. 1971, [PhRvD](#), **4**, 2185
- Belvedere, R., Boshkayev, K., Rueda, J. A., & Ruffini, R. 2014, [NuPhA](#), **921**, 33
- Belvedere, R., Pugliese, D., Rueda, J. A., Ruffini, R., & Xue, S.-S. 2012, [NuPhA](#), **883**, 1
- Christiansen, M. B., & Glendenning, N. K. 1997, [PhRvC](#), **56**, 2858
- Christiansen, M. B., Glendenning, N. K., & Schaffner-Bielich, J. 2000, [PhRvC](#), **62**, 025804
- Frenkel, J. 1917, [PMag](#), **33**, 297
- Glendenning, N. 1996, *Compact Stars. Nuclear Physics, Particle Physics and General Relativity* (New York: Springer)
- Glendenning, N. K. 1992, [PhRvD](#), **46**, 1274
- Glendenning, N. K. 2001, [PhR](#), **342**, 393
- Glendenning, N. K., & Pei, S. 1995, [PhRvC](#), **52**, 2250
- Glendenning, N. K., & Schaffner-Bielich, J. 1999, [PhRvC](#), **60**, 025803
- Herrera, L., & Santos, N. O. 1997, [PhR](#), **286**, 53
- Huang, K., & Wyllie, G. 1949, [PPSA](#), **62**, 180
- Israel, W. 1966, [NCimB](#), **44**, 1
- Israel, W. 1967, [NCimB](#), **48**, 463
- Israelachvili, J. N. 2011, *Intermolecular and Surface Forces* (3rd ed.)
- Landau, L. D., & Lifshitz, E. M. 1975, *The Classical Theory of Fields* (Oxford: Pergamon)
- Lobo, F. S. N., & Crawford, P. 2005, [CQGra](#), **22**, 4869
- Mansouri, R., & Khorrami, M. 1996, [JMP](#), **37**, 5672
- Misner, C. W., Thorne, K. S., & Wheeler, J. A. 1973, *Gravitation* (San Francisco, CA: W.H. Freeman)
- Pereira, J. P., Coelho, J. G., & Rueda, J. A. 2014, [PhRvD](#), **90**, 123011
- Peters, T. 2013, [ConPh](#), **54**, 60
- Poisson, E. 2004, *A Relativist's Toolkit* (Cambridge: Cambridge Univ. Press)
- Raju, C. K. 1982a, [JPhA](#), **15**, 3915
- Raju, C. K. 1982b, [JPhA](#), **15**, 381
- Reisenegger, A., & Goldreich, P. 1992, [ApJ](#), **395**, 240
- Rodríguez-Valverde, M. A., Cabrerizo-Vílchez, M. A., & Hidalgo-Álvarez, R. 2003, [EJPh](#), **24**, 159
- Rotondo, M., Rueda, J. A., Ruffini, R., & Xue, S. 2011, [PhL](#), **B701**, 667
- Rueda, J. A., Ruffini, R., Xue, S.-S., & Pugliese, D. 2011, [NuPh](#), **A872**, 286
- Shapiro, S. L., & Teukolsky, S. A. 1986, *Black Holes, White Dwarfs and Neutron Stars: The Physics of Compact Objects*

## ON THE MAGNETIC FIELD OF PULSARS WITH REALISTIC NEUTRON STAR CONFIGURATIONS

R. BELVEDERE<sup>1,2,3</sup>, JORGE A. RUEDA<sup>1,2,3</sup>, AND R. RUFFINI<sup>1,2,3</sup>

<sup>1</sup> Dipartimento di Fisica and ICRA, Sapienza Università di Roma P.le Aldo Moro 5, I-00185 Rome, Italy;

[riccardo.belvedere@icra.it](mailto:riccardo.belvedere@icra.it), [jorge.rueda@icra.it](mailto:jorge.rueda@icra.it), [ruffini@icra.it](mailto:ruffini@icra.it)

<sup>2</sup> ICRA Net, P.zza della Repubblica 10, I-65122 Pescara, Italy

<sup>3</sup> ICRA Net-Rio, Centro Brasileiro de Pesquisas Físicas, Rua Dr. Xavier Sigaud 150, Rio de Janeiro 22290-180, Brazil

Received 2014 April 29; accepted 2014 November 7; published 2015 January 13

### ABSTRACT

We have recently developed a neutron star model fulfilling global and not local charge neutrality, both in the static and in the uniformly rotating cases. The model is described by the coupled Einstein–Maxwell–Thomas–Fermi equations, in which all fundamental interactions are accounted for in the framework of general relativity and relativistic mean field theory. Uniform rotation is introduced following Hartle’s formalism. We show that the use of realistic parameters of rotating neutron stars, obtained from numerical integration of the self-consistent axisymmetric general relativistic equations of equilibrium, leads to values of the magnetic field and radiation efficiency of pulsars that are very different from estimates based on fiducial parameters that assume a neutron star mass  $M = 1.4 M_{\odot}$ , radius  $R = 10$  km, and moment of inertia  $I = 10^{45}$  g cm<sup>2</sup>. In addition, we compare and contrast the magnetic field inferred from the traditional Newtonian rotating magnetic dipole model with respect to the one obtained from its general relativistic analog, which takes into account the effect of the finite size of the source. We apply these considerations to the specific high-magnetic field pulsar class and show that, indeed, all of these sources can be described as canonical pulsars driven by the rotational energy of the neutron star, and have magnetic fields lower than the quantum critical field for any value of the neutron star mass.

*Key words:* equation of state – gravitation – pulsars: general – stars: neutron – stars: rotation

### 1. INTRODUCTION

The traditional formula used in pulsar astrophysics literature to infer the pulsar’s magnetic field originated from the pioneering hypothesis of Gold (1968) and Pacini (1968), who first stressed the role of the rotational energy of the neutron star as an energy reservoir for the pulsar’s activity. The surface magnetic field of pulsars has since been estimated (see, e.g., Gunn & Ostriker 1969; Ostriker & Gunn 1969; Ferrari & Ruffini 1969) by equating the rotation energy loss of the neutron star,

$$\dot{E}_{\text{rot}} = -4\pi^2 I \frac{\dot{P}}{P^3}, \quad (1)$$

to the radiating power of a rotating magnetic point dipole in a vacuum,

$$P_{\text{dip}} = -\frac{2}{3} \frac{\mu_{\perp}^2 \Omega^4}{c^3}. \quad (2)$$

Here  $\Omega$  is the rotation angular velocity of the star,  $\mu_{\perp} = \mu \sin \chi$  is the component of the magnetic dipole  $\mu = BR^3$  perpendicular to the rotation axis, which is  $B$ , the magnetic field at the equator, and  $\chi$  denotes the inclination angle of the magnetic dipole with respect to the rotation axis. Under these assumptions, the magnetic field is estimated as

$$B \sin \chi = \left( \frac{3c^3}{8\pi^2} \frac{I}{R^6} P \dot{P} \right)^{1/2}, \quad (3)$$

where  $P = 2\pi/\Omega$  and  $\dot{P}$  are the rotational period and the spin-down rate of the pulsar, which are observational properties, while the moment of inertia  $I$  and the radius  $R$  of the star are model-dependent properties.

It is worth noting that the electromagnetic power of the above simplified rotating magnetic point dipole model, given by Equation (2), coincides, in regards to the so-called *wave zone* approximation ( $r \gg c/\Omega = 1/k = \lambda/2\pi$ , where  $k$

is the wave number and  $\lambda$  the wavelength), with the one obtained from the classic work by Deutsch (1955), where the exterior (vacuum) electromagnetic field of a uniformly rotating, perfectly conducting star with a misaligned magnetic dipole was obtained as an exact closed-form analytic solution of the Maxwell equations in flat spacetime.

General considerations on the nature of pulsars are often extracted in the literature from the application of the above formulas with fiducial parameters of a pulsar: a canonical neutron star of mass  $M = 1.4 M_{\odot}$ , radius  $R = 10$  km, and moment of inertia  $I = 10^{45}$  g cm<sup>2</sup>, (see, e.g., Caraveo 2014, and references therein). For these fiducial parameters, Equation (1) becomes

$$\dot{E}_{\text{rot}}^f = -3.95 \times 10^{46} \frac{\dot{P}}{P^3} \text{ ergs}^{-1}, \quad (4)$$

and Equation (3) becomes

$$B_f \sin \chi = 3.2 \times 10^{19} (P \dot{P})^{1/2} \text{ G}. \quad (5)$$

We focus in this work on the interesting class referred to as high-magnetic field pulsars (see, e.g., Ng & Kaspi 2011). In Table 1 (Ng & Kaspi 2011; Zhu et al. 2011), we show samples of the high-magnetic field pulsar class with their properties as inferred from the fiducial formulas (5), and (4) for the surface magnetic field and rotational energy loss (see second and fourth column of the table, respectively). Notice that magnetic fields with values higher than the critical field for quantum electro-dynamical effects,

$$B_c = \frac{m_e^2 c^2}{e\hbar} = 4.41 \times 10^{13} \text{ G}, \quad (6)$$

appear, and in some cases also have luminosities higher than the rotational power of the neutron star, namely,  $L_X > |\dot{E}_{\text{rot}}^f|$ .

Due to these theoretically inferred properties, the possibility that this family of pulsars can be the missing link has been

**Table 1**

Properties of the High-magnetic Field Pulsars Obtained Assuming Fiducial Neutron Star Parameters,  $R = 10$  km and  $I = 10^{45}$  g cm<sup>2</sup>, Respectively, and Using Equation (5) with Inclination Angle  $\chi = \pi/2$  and Equation (4)

Pulsar	$B_f/B_c$	$L_X$ ( $10^{33}$ erg s <sup>-1</sup> )	$L_X/ \dot{E}_{\text{rot}}^f $	$P$ (s)	$\dot{P}$ ( $10^{-12}$ )
J1846–0258	1.11	25–28 <sup>a</sup> , 120–170 <sup>b</sup>	0.0031–0.0035 <sup>a</sup> , 0.015–0.021 <sup>b</sup>	0.326	7.083
J1819–1458 <sup>c</sup>	1.13	1.8–2.4	6.21–8.28	4.263	0.575
J1734–3333	1.18	0.1–3.4	0.0018–0.0607	1.169	2.279
J1814–1744	1.24	<43	<91.5	1.169	2.279
J1718–3718	1.67	0.14–2.6	0.0875–1.625	3.378	1.598
J1847–0130	2.13	<34	<200	6.707	1.275

**Notes.** See Zhu et al. (2011); Ng & Kaspi (2011) for additional details of these pulsars.

<sup>a</sup> In 2000, prior to the 2006 outburst.

<sup>b</sup> During the outburst in 2006.

<sup>c</sup> Classified as a rotating radio transient (RRAT).

suggested, i.e., transition objects between rotation-powered pulsars and the so-called magnetars: neutron stars powered by the decay of overcritical magnetic fields. In principle, this would lead to a large unseen population of magnetars in a quiescence state, which could be disguised as radio pulsars (see, e.g., Zhu et al. 2011).

However, as we shall show in this work, these conclusions might be premature since the surface magnetic fields inferred by fiducial neutron star parameters, namely by Equation (5), are generally overestimated. Indeed, much lower values of the magnetic field are obtained when realistic structure parameters are applied and when general relativistic corrections are introduced to the traditional Newtonian Equation (3); see Section 3. The need to use more realistic neutron star configurations is the result of the knowledge of more complex nuclear equation of state (EOS), structure, and stability conditions of both static and rotating neutron stars, which were acquired in the intervening years from the seminal work of Oppenheimer & Volkoff (1939).

We show the results for neutron stars in two cases of interest: (1) configurations obtained under the traditional constraint of local charge neutrality and (2) configurations subjected to the constraint of global charge neutrality, in which the Coulomb interactions are introduced. For the latter configurations, we use our recent formulation of the neutron star theory for both static and uniform rotations, following our previous works (Belvedere et al. 2012, 2014). These new set of equations, which we called Einstein–Maxwell–Thomas–Fermi (EMTF) equations, accounts for the weak, strong, gravitational, and electromagnetic interactions within the framework of general relativity and relativistic nuclear mean-field theory.

We shall show that, independently, on the theoretical model, different structure parameters as functions of the central density and/or rotation frequency of the star give rise to quite different quantitative estimates of the astrophysical observables with respect to the use of fiducial parameters.

This work is organized as follows. In Section 2, we briefly summarize the equations of equilibrium and resulting structure from their integration of both static and uniformly rotating neutron stars. We analyze, in Section 3, the estimates of the magnetic field and radiation efficiency of the high-magnetic field pulsars class. We summarize our conclusions in Section 4.

We use cgs units throughout the article unless otherwise specified.

## 2. NEUTRON STAR STRUCTURE

We have recently shown (Rotondo et al. 2011b; Rueda et al. 2011; Belvedere et al. 2012) that, in the case of both static

and rotating neutron stars, the Tolman–Oppenheimer–Volkoff (TOV) system of equations (Oppenheimer & Volkoff 1939; Tolman 1939) is superseded by the Einstein–Maxwell system of equations coupled with the general relativistic Thomas–Fermi equations of equilibrium, giving rise to the what we have called the EMTF equations. These new equations account for the weak, strong, gravitational, and electromagnetic interactions within the framework of general relativity and relativistic nuclear mean field theory.

In the TOV-like approach, the condition of local charge neutrality is applied to each point of the configuration, while in the EMTF equations the condition of global charge neutrality, is imposed. It was shown in (Rotondo et al. 2011b; Rueda et al. 2011) that the approach based on local charge neutrality is inconsistent with the equations of motion of the particles in the system. Consequently, the general relativistic thermodynamic equilibrium of the star, first introduced by Klein (1949) in the case of a self-gravitating one-component system of uncharged particles, is not satisfied when local charge neutrality is applied to a multi-component system with charged constituents. The equilibrium is ensured by the constancy, along the whole configuration, of the generalized electro-chemical particle potentials for all of the species, what we denominated as the conservation of “Klein potentials.” When finite temperatures are considered, the constancy of the gravitationally redshifted temperature (Tolman 1930) has to be also imposed (Rueda et al. 2011).

The weak interactions are introduced via the condition of  $\beta$ -equilibrium. For the strong interactions, we follow the  $\sigma$ - $\omega$ - $\rho$  nuclear model within the relativistic mean field theory á la Boguta & Bodmer (1977). The nuclear model is fixed by the coupling constants and the masses of the three mesons. Here we adopt the NL3 parameter set (Lalazissis et al. 1997):  $m_\sigma = 508.194$  MeV,  $m_\omega = 782.501$  MeV,  $m_\rho = 763.000$  MeV,  $g_\sigma = 10.2170$ ,  $g_\omega = 12.8680$ ,  $g_\rho = 4.4740$ , plus two constants that give the strength of the self-scalar interactions,  $g_2 = -10.4310$  fm<sup>-1</sup> and  $g_3 = -28.8850$ .

The structure of the neutron star solution of the EMTF equations of equilibrium leads to a new structure of the neutron stars, which is markedly different from the traditional configurations obtained through the TOV equations (see Figure 4 in Belvedere et al. 2012): from the supranuclear central density up to the nuclear density  $\rho_{\text{nuc}} \approx 2.7 \times 10^{14}$  g cm<sup>-3</sup>, we find the neutron star core, which is composed of a degenerate gas of neutrons, protons, and electrons in  $\beta$ -equilibrium, and is positively charged. The core is surrounded by an electron layer that is a few hundreds of Fermi thick, which fully screens its charge. In this core-crust transition layer, the

electric field reaches values as large as  $E \sim (m_\pi/m_e)^2 E_c$ , where  $E_c = m_e^2 c^3 / (e\hbar) \approx 1.3 \times 10^{16}$  Volt  $\text{cm}^{-1}$  is the critical field for vacuum polarization. The  $e^+e^-$  pair creation is, however, inhibited by Pauli blocking (Ruffini et al. 2010). In this layer, the particle densities decrease until the point where global charge neutrality is reached and the crust is found. Consequently, the core is matched to the crust via this interface at a density of  $\rho_{\text{crust}} \leq \rho_{\text{nuc}}$ . In the limit  $\rho_{\text{crust}} \rightarrow \rho_{\text{nuc}}$ , the thickness of the transition layer, as well as the electric field inside of it, vanishes and the solution approaches the one given by local charge neutrality (see Figures 3 and 5 in Belvedere et al. 2012). The crust in its outer region  $\rho \leq \rho_{\text{drip}} \approx 4.3 \times 10^{11}$  g  $\text{cm}^{-3}$  is composed of white dwarf-like material (ions and electrons), following, for instance, the BPS EOS (Baym et al. 1971b). In its inner region, at densities of  $\rho > \rho_{\text{drip}}$ , free neutrons are present and the EOS follows the BBP description (Baym et al. 1971a). Configurations with  $\rho_{\text{crust}} > \rho_{\text{drip}}$  possess both inner and outer crusts, while in the cases with  $\rho_{\text{crust}} \leq \rho_{\text{drip}}$  the neutron stars have only an outer crust. As shown by Belvedere et al. (2012), all of the above new features lead to a new mass–radius relation of static neutron stars.

The extension of the above formulation to the case of uniform rotation has recently been achieved in (Belvedere et al. 2014) within the Hartle formalism (Hartle 1967). It is worth noting that the influence of the induced magnetic field owing to the rotation of the charged core of the neutron star in the globally neutral case is negligible as we will show in sub Section 2.1. From the integration of the equations of equilibrium, we computed in Belvedere et al. (2014), for different central densities  $\rho_c$  and circular angular velocities  $\Omega$ , the mass  $M$ , polar  $R_p$  and equatorial  $R_{\text{eq}}$  radii, angular momentum  $J$ , eccentricity  $\epsilon$ , moment of inertia  $I$ , as well as quadrupole moment  $Q$  of the configurations.

The angular momentum  $J$  of the star is given by

$$J = \frac{1}{6} \frac{c^2}{G} R^4 \left( \frac{d\bar{\omega}}{dr} \right)_{r=R}, \quad (7)$$

which is related to the angular velocity  $\Omega$  by

$$\Omega = \bar{\omega}(R) + \frac{2G^2}{c^5} \frac{J}{R^3}, \quad (8)$$

where  $R$  is the total radius of the non-rotating star and  $\bar{\omega}(r) = \Omega - \omega(r)$  is the angular velocity of the fluid relative to the local inertial frame, with  $\omega$  as the fluid angular velocity in the local inertial frame.

The total mass of the configuration is

$$M = M_0 + \delta M, \quad \delta M = m_0(R) + \frac{G^2}{c^7} \frac{J^2}{R^3}, \quad (9)$$

where  $M_0$  is the mass of the non-rotating star and  $\delta M$  is the contribution to the mass due to the rotation, while  $m_0$  is a second order contribution to the mass related to the pressure perturbation.

The moment of inertia can be computed from the relation

$$I = \frac{J}{\Omega}, \quad (10)$$

which does not account for deviations from spherical symmetry since within the Hartle formalism  $J$  is a first order function of  $\Omega$ . This is a good approximation since, owing to the high density

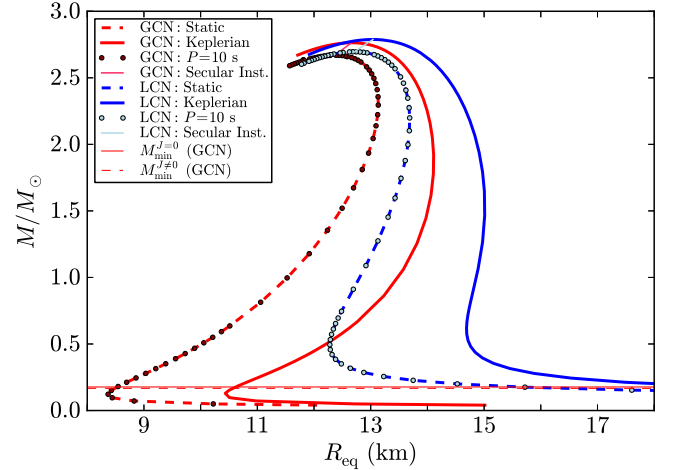


**Figure 1.** Total mass vs. total equatorial radius for the global (red) and local (blue) charge neutrality cases. The dashed curves represent the static configurations, while the solid lines are the uniformly rotating neutron stars. The light red and light blue colored lines define the secular instability boundary for the globally and locally neutral cases, respectively. The horizontal thin red lines define the minimum mass in the globally neutral case. The dots refer to the sequence of the constant period  $P = 10$  s.

of neutron stars, most of the observed pulsars are accurately described by a perturbed spherical geometry. This can be seen, for instance, from the sequence of configurations with periods of  $P = 10$  s, shown in Figure 1, which practically overlap the non-rotating mass–radius relation. The accuracy of the approximation increases for stiffer EOS (see Benhar et al. 2005, for details), as the ones given by  $\sigma$ - $\omega$ - $\rho$  relativistic nuclear mean field models.

In Figure 1, we show the mass–radius relation that results from the integration of the EMTF equations for the equilibrium configurations of static and rotating neutron stars. The dashed lines represent the non-rotating, ( $J = 0$ ), sequences, while the solid lines represent the corresponding maximally rotating (Keplerian) sequences. The pink-red and light blue lines represent the secular instability boundaries for the global and local charge neutrality cases, respectively. The horizontal thin red lines give the minimum masses for the static (solid line) and rotating (dashed line) sequences for the global charge neutrality case. These minimum mass limits are the configurations for which the gravitational binding energy vanishes, namely, below this mass the neutron star is unbound. In the case of the local charge neutrality case, no minimum mass was found (see Belvedere et al. 2014 for further details).

### 2.1. Influence of the Rotationally Induced Magnetic Field

The interior electric field generates a magnetic field inside the neutron star once it is put into rotation. For the sake of clarity and without losing generality, we now give an estimate of such an interior magnetic field by solving the Maxwell equations in the flat Minkowski background. The charge distribution in the core and in the core–crust transition layer, therefore, rotates with constant angular velocity  $\Omega$  around the axis of symmetry. The magnetic field can be first written in terms of the electromagnetic potential  $\mathbf{A}$  as usual, i.e.,  $\mathbf{B}(\mathbf{r}) = \nabla \times \mathbf{A}(\mathbf{r})$ . The electromagnetic potential can then be rewritten in terms of a new potential  $\mathbf{F}(\mathbf{r})$  by  $\mathbf{A}(\mathbf{r}) = \Omega/c^2 \times \mathbf{F}(\mathbf{r})$ , with  $\mathbf{F}(\mathbf{r}) = (4\pi\epsilon_0)^{-1} \int (\mathbf{r}' \rho_{\text{ch}}(\mathbf{r}') / (\mathbf{r}'\mathbf{r} - \mathbf{r}')) d^3\mathbf{r}'$ . For a spherically symmetric charge distribution  $\rho_{\text{ch}}(r)$ , the potential  $\mathbf{F}$  can be taken as radial, i.e.,  $\mathbf{F}(\mathbf{r}) = e_r F(r)$ , being  $e_r$  the unit

radial vector (Marsh 1982). The magnetic field is thus given by

$$\mathbf{B}(\mathbf{r}) = B_r \mathbf{e}_r + B_\theta \mathbf{e}_\theta, \quad (11)$$

where

$$B_r = \frac{2\Omega F}{c^2 r} \cos \theta, \quad B_\theta = -\frac{2\Omega}{c^2} \left[ \frac{F}{r} + \frac{r}{2} \frac{d}{dr} \left( \frac{F}{r} \right) \right] \sin \theta, \quad (12)$$

are, respectively, the radial and the angular component of the magnetic field as  $\theta$ , the angle between the  $r$  and  $z$  axes, and  $\mathbf{e}_\theta$  as the unit vector along  $\theta$ .

Equations (11)–(12) can now be used to calculate the induced magnetic field both in the core and the core–crust interface shell surrounding it. Following Boshkayev et al. (2012), in order to estimate the rotationally induced magnetic field, we describe the core and the core–crust interface using a simplified model based on previous works by Rotondo et al. (2011c, 2011a). The distribution of  $N_p$  protons,  $n_p$ , is assumed to be constant within the core radius  $R_c = \Delta \hbar / (m_\pi c) N_p^{1/3}$ , where  $\Delta$  is a parameter such that  $\Delta \approx 1$  ( $\Delta < 1$ ) corresponds to nuclear (supranuclear) densities when applied to ordinary nuclei, i.e., for  $N_p/A \approx 1/2$ ,  $A = N_p + N_n$ , the total nucleon number, and  $N_n$ , the total number of neutrons. The distribution of  $N_e = N_p$  degenerate electrons,  $n_e$ , subjected to the equilibrium condition determined by the constancy of their Fermi energy,  $E_e^F = \mu_e - m_e c^2 - eV = \text{constant}$ , where  $\mu_e = \sqrt{(cP_e^F)^2 + m_e^2 c^4}$  and  $V$  are the chemical and Coulomb potentials, is computed self-consistently from the electrostatic Poisson equation,  $\nabla^2 V(r) = -4\pi e(n_p - n_e)$ , with boundary conditions of global neutrality. The electron number density is then given by  $n_e = (P_e^F)^3 / (3\pi^2 \hbar^3) = (e^2 V^2 + 2m_e c^2 eV)^{3/2} / (3\pi^2 \hbar^3)$ . The distribution of neutrons is hence obtained from the constraint of the  $\beta$  equilibrium. From the proton and electron densities, we obtain the charge density distribution  $\rho_{\text{ch}} = e(n_p - n_e)$ , which allows us to compute the potential  $F$ , and finally the magnetic field from Equations (11)–(12).

For a neutron star rotating with a period of  $P \approx 10$  s, we obtain

$$\text{Core} : \begin{cases} B_r \sim |B_\theta| \sim 3 \times 10^{-19} B_c, \\ B_{\text{core}} = \sqrt{B_r^2 + B_\theta^2} \approx 10^{-19} B_c; \end{cases} \quad (13)$$

$$\text{Shell} : \begin{cases} B_r \sim 3 \times 10^{-19} B_c, \quad |B_\theta| \sim 10^{-1} B_c, \\ B_{\text{shell}} = \sqrt{B_r^2 + B_\theta^2} \approx 10^{-1} B_c. \end{cases} \quad (14)$$

We can conclude from the above estimates that the magnetic field in the core is small enough to safely neglect its effect on the structure of the neutron star. We can also check the possible effects on the shell's structure. The magnetic, Coulomb, rotational, and gravitational energy of the shell can be estimated, respectively, as

$$\mathcal{E}_{\text{mag}} \approx 0.446 \frac{\pi \hbar^2}{\alpha^{1/2} m_\pi c^2} \frac{N_p^{4/3}}{P^2}, \quad (15)$$

$$\mathcal{E}_{\text{el}} \approx 0.195 \frac{\pi^{1/2} m_\pi c^2}{\alpha^{1/2}} N_p^{2/3}, \quad (16)$$

$$\mathcal{E}_{\text{rot}} \approx 2 \frac{m_n \pi \hbar^2}{\alpha^{1/2} m_\pi^2 c^2} \frac{N_p^{4/3}}{P^2}, \quad (17)$$

$$\mathcal{E}_g \approx -3 \frac{G m_\pi m_n^2 c}{\alpha^{1/2} \hbar} N_p^{1/3} A, \quad (18)$$

where we have used  $\delta R_c \approx \hbar / (\sqrt{\alpha} m_\pi c)$  as the thickness of the shell,  $m_p$ ,  $m_n$ , and  $m_\pi$  are the neutron, proton, and pion masses, respectively, and  $\alpha$  is the fine structure constant. We, therefore, obtain

$$\frac{\mathcal{E}_{\text{mag}}}{|\mathcal{E}_g|} \approx 0.15\pi \left( \frac{m_{\text{Pl}}}{m_n} \right)^2 \left( \frac{\hbar}{m_\pi c} \right)^2 \frac{N_p/A}{(cP)^2} \approx 3.8 \times 10^{-13}, \quad (19)$$

$$\frac{\mathcal{E}_{\text{el}}}{|\mathcal{E}_g|} \approx 0.06\pi^{1/2} \left( \frac{m_{\text{Pl}}}{m_n} \right)^2 \frac{N_p^{1/3}}{A} \approx 0.05, \quad (20)$$

$$\frac{\mathcal{E}_{\text{rot}}}{|\mathcal{E}_g|} \approx \frac{2\pi}{3} \left( \frac{m_n}{m_\pi} \right) \left( \frac{m_{\text{Pl}}}{m_n} \right)^2 \left( \frac{\hbar}{m_\pi c} \right)^2 \frac{N_p/A}{(cP)^2} \approx 1.2 \times 10^{-11}, \quad (21)$$

where  $m_{\text{Pl}} = (\hbar c / G)^{1/2}$  is the Planck's mass, and we have used a rotation period of  $P = 10$  s,  $N_p/A \approx 1/50$  and  $A = 10^{57}$  for the numerical estimates.

We can see that both the rotational and magnetic energies are negligible corrections to the shell's energy for a rotation period of  $P = 10$  s, and are the main contributions owing to the gravitational and the electrostatic energy.

It is clear that the above induced magnetic field in globally neutral neutron stars cannot be an explanation in regards to the observed surface magnetic fields in pulsars because the induced magnetic field only exists in the interior up to the crust's edge where global neutrality is reached. Therefore, it does not emerge up to the neutron star surface. The nature of the magnetic field observed in pulsars represents a major issue in astrophysics and it is not the objective of the present work to try to answer such a question. The interior magnetic field in the neutron star can be larger than the one observed in its surface; however, it is known that the effects of the magnetic field on the properties of nuclear matter at high supranuclear densities present in the cores of neutron stars are expected to be appreciable only for extremely, and likely unrealizable, huge values  $B \gtrsim 10^{18}$  G (see, e.g., Strickland et al. 2012; Isayev & Yang 2012; Dong et al. 2013; de Lima et al. 2013, and references therein). This implies that magnetic fields lower than these values do not have appreciable effects either on the nuclear EOS or on the structure parameters of the neutron star (Bocquet et al. 1995; Broderick et al. 2000). It becomes clear that the effect of the low value of the magnetic field induced by electric field rotation in rotating globally neutral neutron stars, and of the possible interior magnetic field, which may be present in the star's interior, can be safely neglected in the computation of the structure parameters, validating the treatment applied in this work. More importantly, as we show in the following section, are the undeniable general relativistic effects that affect the radiation field near the surface of a rotating magnetic-dipole, i.e., the neutron star, which can drastically modify the estimate of the surface magnetic field.

### 3. INFERENCE OF A PULSAR'S PROPERTIES

We now turn to an analysis of the consequences of using realistic general relativistic structure parameters on the inference

of the magnetic field and the efficiency of a pulsar when converting rotational energy into electromagnetic radiation. We focus here on the high-magnetic field pulsar class (see Ng & Kaspi 2011), but our general qualitative results apply to all pulsars.

As we have already stressed, the simplified picture of a point-like magnetic dipole has traditionally been applied as a model for pulsars of any rotation period, assuming fiducial values for the neutron star structure parameters. It is possible identify four major corrections that might be introduced to the model: (1) the existence of a plasma magnetosphere instead of an electrovacuum; (2) the dependence on the properties of the interior (EOS) by neutron star structure parameters such as mass, radius, and moment of inertia, with respect to the oversimplification lead by the use of fiducial values; (3) the effects due to the relativistic fast rotation, as measured by the fastness parameter,  $\Omega R/c$ ; (4) the corrections measured by the compactness parameter  $GM/(c^2 R)$ , introduced by the finiteness of the mass and size of the star. We now discuss each of these points.

The first correction depends upon the specific model of the pulsar's magnetosphere, which determines the electric potential developed above the neutron star surface and is responsible for the acceleration of particles, which form a wind that exerts a torque on the pulsar. However, starting from the classic work of Goldreich & Julian (1969), many competing models of the pulsar's magnetosphere have been proposed and they are still a matter of debate in the literature. Therefore, we will not consider this issue in the present work.

Concerning the second point, we have shown in Section 2 how the structure parameters depend on both the neutron star theory and the EOS. Nuclear fermion interactions strongly influence the mass–radius relation (Lattimer & Prakash 2007, see, e.g.), and hence all of the derived pulsar parameters. Therefore, different inferences of the magnetic field value can be obtained as functions of the neutron star mass and nuclear EOS.

The generalization of Deutsch's results in the case of relativistic rotation ( $\Omega \sim c/R$ ) was obtained by Belinsky & Ruffini (1992). The radiation power in this case was expressed via a cumbersome integral that has to be solved numerically. The only exception is represented by the analytic expressions in the non-relativistic approximation, which leads to Deutsch's solution, and in the ultra-relativistic approximation when  $\Omega$  approaches  $c/R$ . The Maxwell equations are still solved there in flat Minkowski spacetime. This specific correction is expected to be important for millisecond pulsars. However, for the pulsar class discussed in this work, with rotation periods  $P \sim 10$  s (hence,  $\Omega R/c = 2\pi R/(cP) \sim 10^{-5}$ ), such a correction is negligible and the solution in the slow rotation regime is sufficiently accurate.

We now focus on the fourth correction. The exact solution of the exterior electromagnetic fields of a (slowly) rotating magnetic dipole aligned with the rotation axis in general relativity was first found by Ginzburg & Ozernoi (1964, 1965), see, also, Anderson & Cohen (1970). They solved the Einstein–Maxwell equations in the Schwarzschild background. The generalization to a general electromagnetic multipolar structure in a Schwarzschild metric was found by Anderson & Cohen (1970). The generalization of the Deutsch's solution to the general relativistic case in the slow rotation regime, and for a general misaligned dipole, was obtained in analytic form in the *near zone* ( $r \ll c/\Omega = 1/k = \lambda/2\pi$ ) by Rezzolla et al. (2001, 2003) and, for the wave zone by Rezzolla & Ahmedov (2004). In the

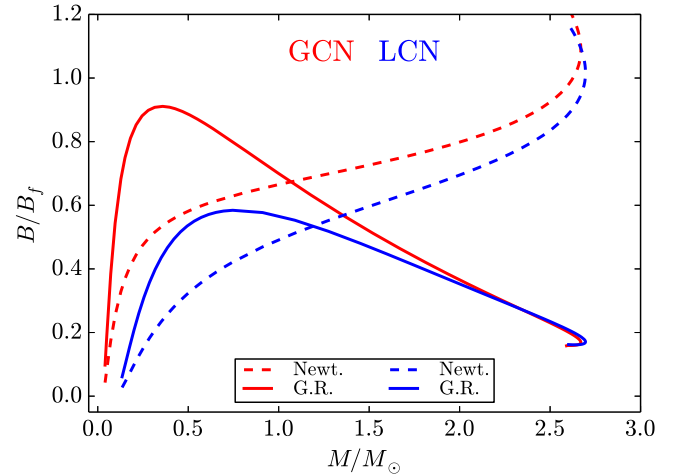


**Figure 2.** Ratio of the magnetic field given by the Newtonian formula (3) and the general relativistic ratio (25) to the fiducial value given by Equation (5). Here we have used the realistic mass–radius relations of globally and locally neutral static neutron stars of this work and an inclination angle  $\chi = \pi/2$ .

latter, the radiation power of the dipole was computed as

$$P_{\text{dip}}^{\text{G.R.}} = -\frac{2}{3} \frac{\mu_{\perp}^2 \Omega^4}{c^3} \left( \frac{f}{N^2} \right)^2, \quad (22)$$

where  $f$  and  $N$  are the general relativistic corrections

$$f = -\frac{3}{8} \left( \frac{R}{M_0} \right)^3 \left[ \ln(N^2) + \frac{2M_0}{R} \left( 1 + \frac{M_0}{R} \right) \right], \quad (23)$$

$$N = \sqrt{1 - \frac{2M_0}{R}}, \quad (24)$$

where  $M_0$  is the mass of the non-rotating configurations. Now, by equating the rotational energy loss to the above electromagnetic radiation power, it is possible to obtain the formula of the surface magnetic field analogous to Equation (3), but with general relativistic corrections:

$$B \sin \chi = \frac{N^2}{f} \left( \frac{3c^3}{8\pi^2} \frac{I}{R^6} P \dot{P} \right)^{1/2}. \quad (25)$$

In Figure 2, we have plotted the ratio of the magnetic field obtained via the Newtonian formula (3) and the general relativistic formula (25) to the fiducial value obtained with (5), for the realistic mass–radius relations of globally and locally neutral neutron stars used in this work.

We can see from this figure that, in the Newtonian case, the inferred magnetic field increases with increasing neutron star mass. Therefore, in such a case, the configurations of maximum and minimum masses give us, respectively, upper and lower limits to the magnetic field. It is worth noting how the general relativistic formula gives us a magnetic field lower than the Newtonian counterpart, for  $M/M_{\odot} \gtrsim 1.1$  and  $M/M_{\odot} \gtrsim 1.2$  for the globally and locally neutral configurations, respectively. In addition, we find a markedly different and interesting behavior. First, the magnetic field is extremely close, at very low masses, with the Newtonian value, as expected; then, it deviates and reaches a maximum value for some value of the mass, and then decreases for increasing masses. The magnetic field inferred from globally and locally neutral configurations coincides for

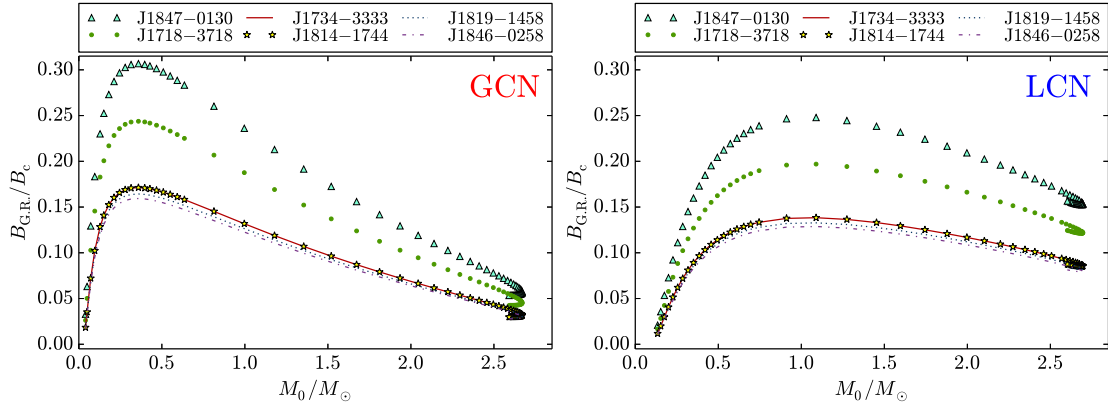


**Figure 3.** Magnetic field  $B_{G,R}$ , obtained from the general relativistic magneto–dipole formula (25), in units of critical magnetic field  $B_c$ , as a function of the mass (in solar masses) for static neutron stars in the global (left panel) and local (right panel) charge neutrality cases.

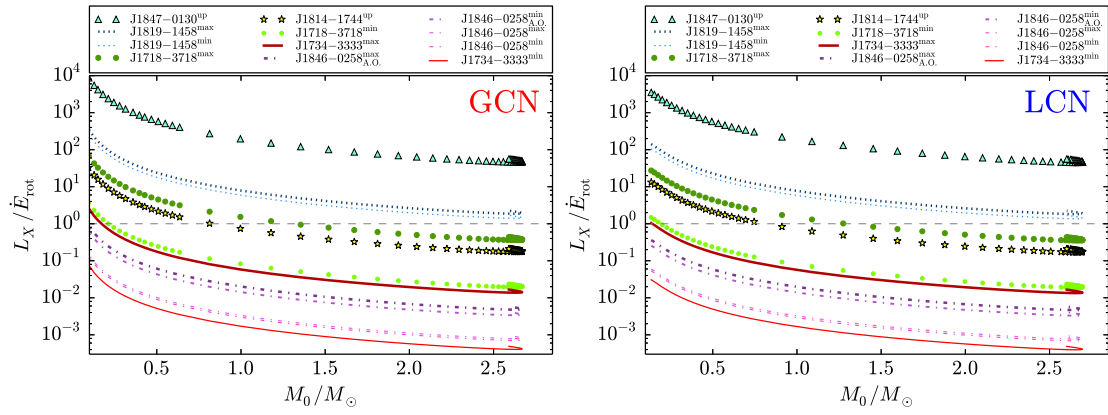


**Figure 4.** Ratio between the observed X-ray luminosity  $L_X$  and the loss of rotational energy  $\dot{E}_{\text{rot}}$  vs. the total mass of the rotating neutron star, in units of  $M_\odot$ . We use the high-B pulsar from the work by Ng & Kaspi (2011) for which a magnetic field higher than the critical field  $B_c$  is inferred, once the fiducial value for the moment of inertia  $I = 10^{45}$  g cm<sup>2</sup> is taken into account (see Table 1). Pulsars with luminosity  $L_X$  defined by an upper limit are labeled with “up,” for pulsars whose luminosity  $L_X$  is not well established we have assumed the existent lower limits (label “min”) and upper limits (label “max”). The values for the pulsar PSR J1846-0258 are divided as prior to the 2006 outburst and after the 2006 outburst (label “A.O.”). Left plot: global charge neutrality. Right plot: local charge neutrality. The magnetic fields shown are referred to the high-magnetic field pulsars of Table 1.

large masses close to the critical mass value, as should be expected since in those massive configurations the structure parameters are dominated by the neutron star core, with a very small role from the crust. Here we are using the parameters of the static configurations. This is a good approximation for this family of pulsars since their rotation periods are far from the millisecond region, where deviations from spherical symmetry are expected. This can be seen in Figure 1, where the sequence of the constant rotation period  $P = 10$  s essentially overlaps the static mass–radius relation.

In Figure 3, we plotted our theoretical prediction for magnetic fields of the pulsars of Table 1 as a function of the neutron star mass, using the general relativistic formula (25).

We find that, both in global and local neutrality case, the assumed high-B pulsars have inferred magnetic fields lower than the critical value for the entire range of neutron star masses.

Concerning the efficiency of pulsars in converting rotational energy into electromagnetic radiation, we show in Figure 4 the X-ray luminosity to rotation energy loss ratio,  $L_X/\dot{E}_{\text{rot}}$ , as a function of the neutron star mass, for both global and local charge neutrality. For the sake of comparison, we also present in Table 1 the ratio  $L_X/\dot{E}_{\text{rot}}^f$ , where  $\dot{E}_{\text{rot}}^f$  is the rotational energy loss as obtained from fiducial neutron star parameters given by Equation (4).

We find that for both globally and locally neutral neutron stars, we have  $L_X < \dot{E}_{\text{rot}}$ : 1) in PSR J1718–3718 for  $M_0 \gtrsim 1.25 M_\odot$

and for the entire range of masses adopting, respectively, the observational upper or lower limits on  $L_X$ ; 2) in PSR J1814–1744 for  $M_0 \gtrsim 0.8 M_\odot$  using the upper limit on  $L_X$ ; 3) for the rest of the objects in the entire range of stable masses.

The only exceptions to the above result are PSR J1847–0130 and PSR J1819–1458, for which no range of masses with  $L_X < \dot{E}_{\text{rot}}$  were obtained. However, for PSR J1847–0130, we have only an upper limit for  $L_X$ , so there is still room for solutions with  $L_X < \dot{E}_{\text{rot}}$  if future observations lead to an observed value lower than the present upper limit. In this line, the only object with  $L_X > \dot{E}_{\text{rot}}$  for any mass is PSR J1819–1458. For this particular object, there is still the possibility of being a rotation powered neutron star since the currently used value of the distance to the source, 3.6 kpc, inferred from its dispersion measure, is poorly accurate with a considerable uncertainty of at least 25% (see McLaughlin et al. 2007, for details). Indeed, a distance to the source 25% shorter than the above value would imply  $L_X < \dot{E}_{\text{rot}}$  for this object in the mass range  $M_0 \gtrsim 0.6 M_\odot$ .

We notice that the efficiency obtained via fiducial parameters,  $L_X/\dot{E}_{\text{rot}}^f$ , is larger than the actual value obtained with the realistic neutron star structure in the entire range of stable masses; see Table 1 and Figure 4.

It is also worth mentioning that the rotation energy loss (1) depends on the neutron star structure only through the moment of inertia, whose quantitative value can be different for different nuclear EOS and/or owing to an improved value accounting for

deviations from the spherical geometry, for instance, considering a third-order series expansion in  $\Omega$ . However, the latter effect is negligible for this specific case ( $P \approx 4.3$  s), see, for instance, Figure 5 in Benhar et al. (2005), where no deviations of  $I$  from its spherical value appear for such long rotation periods.

#### 4. CONCLUDING REMARKS

We explored the consequences of a realistic model for neutron stars on the inference of the astrophysical observables of pulsars. We showed in particular the following.

1. The magnetic field is overestimated when fiducial parameters are adopted independently of the use of either the Newtonian or the general relativistic radiation formula of the rotating magnetic dipole; see Figure 2.
2. The use of the Newtonian formula (3) can overestimate the surface magnetic field of up to one order of magnitude with respect to the general relativistic one given by Equation (25). We applied these considerations to the specific case of the high-magnetic field pulsar class, for which overcritical magnetic fields have been obtained in the literature with the use of fiducial neutron star parameters within the Newtonian rotating magnetic dipole model, i.e., estimating the magnetic field through Equation (5). We found that, instead, the magnetic field inferred for these pulsars turned out to be undercritical for any values of the neutron star mass; see Figure 3.
3. The nontrivial dependence of the inferred magnetic field on the neutron star mass, in addition to the dependence on  $P$  and  $\dot{P}$ , namely  $B = B(I(M_0), R(M_0), P, \dot{P})$ , leads to the impossibility of accommodating the pulsars in a typical  $\dot{P} - P$  diagram together with a priori fixed values of the magnetic field; see Figure 3.
4. We computed the range of neutron star masses for which the X-ray luminosity of these pulsars can be well explained via the loss of rotational energy of the neutron star and, therefore, fall into the family of ordinary rotation-powered pulsars. The only possible exceptions were found to be PSR J1847–0130 and PSR J1819–1458, which, as we argued, still present observational uncertainties in the determination of their distances and/or luminosities that leave room for a possible explanation in terms of spindown power. We also showed that the efficiency of the pulsar,  $L_X/\dot{E}_{\text{rot}}$ , is overestimated if computed with neutron star fiducial parameters.
5. We discussed the possible effects of different nuclear models as well as the improved values of the moment of inertia given by further expansion orders of the slow rotation approximation or full numerical integration of the equilibrium equations in the rotating case. However, the former effect appears to be negligible for long rotation periods,  $P \sim 10$  s, of the high-magnetic field pulsars (see, e.g., Figure 5 in Benhar et al. 2005). We have also given estimates of the magnetic field induced by rotation of the interior charge distribution in neutron stars satisfying the condition of global, but not local, charge neutrality. We have shown that, for the case of these long rotational periods, the effects of the magnetic field both in the core and in the core-crust transition surface of these configurations are, in first approximation, negligible.

It is worth noting that the validity of the results of this work also very likely apply to different nuclear EOS, consistent with the current observational constraints, as suggested by the

high value of the recently measured mass of PSR J0348+0432,  $M = 2.01 \pm 0.04 M_\odot$  (Antoniadis et al. 2013). Such a high value favors stiff nuclear EOS, as the one used here based on relativistic nuclear mean field theory á la Boguta & Bodmer (1977), which lead to a critical mass of the neutron star higher than the above value.

It is a pleasure to thank K. Boshkayev for helpful discussions on the simplified model to estimate the rotationally induced magnetic field in the core and in the core–crust interface of the neutron star. We thank the referee for very constructive comments, which led to an improvement on the presentation of our results. R.B. and J.A.R. acknowledge the support by the International Cooperation Program CAPES-ICRANet financed by CAPES–Brazilian Federal Agency for Support and Evaluation of Graduate Education within the Ministry of Education of Brazil.

#### REFERENCES

- Anderson, J. L., & Cohen, J. M. 1970, *Ap&SS*, **9**, 146  
 Antoniadis, J., Freire, P. C. C., Wex, N., et al. 2013, *Sci*, **340**, 448  
 Baym, G., Bethe, H. A., & Pethick, C. J. 1971a, *NuPhA*, **175**, 225  
 Baym, G., Pethick, C., & Sutherland, P. 1971b, *ApJ*, **170**, 299  
 Belinsky, V., & Ruffini, R. 1992, *ApJL*, **401**, L27  
 Belvedere, R., Boshkayev, K., Rueda, J. A., & Ruffini, R. 2014, *NuPhA*, **921**, 33  
 Belvedere, R., Pugliese, D., Rueda, J. A., Ruffini, R., & Xue, S.-S. 2012, *NuPhA*, **883**, 1  
 Benhar, O., Ferrari, V., Gualtieri, L., & Marassi, S. 2005, *PhRvD*, **72**, 044028  
 Bocquet, M., Bonazzola, S., Gourgoulhon, E., & Novak, J. 1995, *A&A*, **301**, 757  
 Boguta, J., & Bodmer, A. R. 1977, *NuPhA*, **292**, 413  
 Boshkayev, K., Rotondo, M., & Ruffini, R. 2012, in *IJMP Conf. Ser. 12, 2nd Galileo-XuGuangqi Meeting (GX2)*, ed. R. Ruffini (Singapore: World Scientific), 58  
 Broderick, A., Prakash, M., & Lattimer, J. M. 2000, *ApJ*, **537**, 351  
 Caraveo, P. A. 2014, *ARA&A*, **52**, 211  
 de Lima, R. C. R., Avancini, S. S., & Providência, C. 2013, *PhRvC*, **88**, 035804  
 Deutsch, A. J. 1955, *AnAp*, **18**, 1  
 Dong, J., Lombardo, U., Zuo, W., & Zhang, H. 2013, *NuPhA*, **898**, 32  
 Ferrari, A., & Ruffini, R. 1969, *ApJL*, **158**, L71  
 Ginzburg, V. L., & Ozernoi, L. M. 1964, *ZhETF*, **47**, 1030  
 Ginzburg, V. L., & Ozernoi, L. M. 1965, *Sov. Phys. JETP*, **20**, 689  
 Gold, T. 1968, *Natur*, **218**, 731  
 Goldreich, P., & Julian, W. H. 1969, *ApJ*, **157**, 869  
 Gunn, J. E., & Ostriker, J. P. 1969, *Natur*, **221**, 454  
 Hartle, J. B. 1967, *ApJ*, **150**, 1005  
 Isayev, A. A., & Yang, J. 2012, *PhLB*, **707**, 163  
 Klein, O. 1949, *RvMP*, **21**, 531  
 Lalazisis, G. A., König, J., & Ring, P. 1997, *PhRvC*, **55**, 540  
 Lattimer, J. M., & Prakash, M. 2007, *PhR*, **442**, 109  
 Marsh, J. S. 1982, *AmJPh*, **50**, 51  
 McLaughlin, M. A., Rea, N., Gaensler, B. M., et al. 2007, *ApJ*, **670**, 1307  
 Ng, C.-Y., & Kaspi, V. M. 2011, in *AIP Conf. Ser. 1379, Astrophysics of Neutron Stars 2010*, ed. E. Göğüş, T. Belloni, & Ü. Ertan (Melville, NY: AIP), 60  
 Oppenheimer, J. R., & Volkoff, G. M. 1939, *PhRv*, **55**, 374  
 Ostriker, J. P., & Gunn, J. E. 1969, *ApJ*, **157**, 1395  
 Pacini, F. 1968, *Natur*, **219**, 145  
 Rezzolla, L., & Ahmedov, B. J. 2004, *MNRAS*, **352**, 1161  
 Rezzolla, L., Ahmedov, B. J., & Miller, J. C. 2001, *MNRAS*, **322**, 723  
 Rezzolla, L., Ahmedov, B. J., & Miller, J. C. 2003, *MNRAS*, **338**, 816  
 Rotondo, M., Rueda, J. A., Ruffini, R., & Xue, S.-S. 2011a, *PhRvC*, **83**, 045805  
 Rotondo, M., Rueda, J. A., Ruffini, R., & Xue, S.-S. 2011b, *PhLB*, **701**, 667  
 Rotondo, M., Ruffini, R., Xue, S.-S., & Popov, V. 2011c, *IJMPD*, **20**, 1995  
 Rueda, J. A., Ruffini, R., & Xue, S.-S. 2011, *NuPhA*, **872**, 286  
 Ruffini, R., Vereshchagin, G., & Xue, S.-S. 2010, *PhR*, **487**, 1  
 Strickland, M., Dexheimer, V., & Menezes, D. P. 2012, *PhRvD*, **86**, 125032  
 Tolman, R. C. 1930, *PhRv*, **35**, 904  
 Tolman, R. C. 1939, *PhRv*, **55**, 364  
 Zhu, W. W., Kaspi, V. M., McLaughlin, M. A., et al. 2011, *ApJ*, **734**, 44

# Extracting Multipole Moments of Neutron Stars from Quasi-Periodic Oscillations in Low Mass X-Ray Binaries\*

Kuantay Boshkayev<sup>1\*\*</sup>, Jorge Rueda<sup>2\*\*\*</sup>, and Marco Muccino<sup>2\*\*\*\*</sup>

<sup>1</sup>*Physical and Technical Faculty of al-Farabi Kazakh National University,  
al-Farabi ave. 71, 050040 Almaty, Kazakhstan*

<sup>2</sup>*ICRANet, Piazza della Repubblica 10, I-65122 Pescara, Italy  
Dipartimento di Fisica and ICRA, Sapienza Università di Roma,  
Piazzale Aldo Moro 5, I-00185 Roma, Italy*

Received January 26, 2015

**Abstract**—We consider the kilohertz quasi-periodic oscillations of low-mass X-ray binaries within the Hartle–Thorne spacetime. We show that the interpretation of the epicyclic frequencies of this spacetime with the observed kilohertz quasi-periodic oscillations, within the Relativistic Precession Model, allows us to extract the total mass  $M$ , angular momentum  $J$ , and quadrupole moment  $Q$  of the compact object in a low-mass X-ray binary. We exemplify this fact by analyzing the data of the Z-source GX 5-1. We show that the extracted multipole structure of the compact component of this source deviates from the one expected from a Kerr black hole and instead it points to a neutron star explanation.

DOI: 10.1134/S1063772915060050

## 1. INTRODUCTION

It is believed that the quasi-periodic oscillations (QPOs) data of the X-ray flux from low mass X-ray binaries (LMXBs) may be used to test general relativity (GR) in the strong field regime [1–4]. QPOs appear in variabilities of several LMXBs including those which contain a neutron star. A certain kind of these oscillations, the so-called kilohertz (kHz) (or high-frequency) QPOs, come often in pairs of frequencies (traditionally called twin-peak QPOs),  $f_L$  (lower) and  $f_U$  (upper), typically in the range  $\sim 50$ – $1300$  Hz. This is of the same order as the range of frequencies characteristic for orbital motion close to a compact object. Accordingly, most kHz QPO models involve orbital motion in the inner regions of an accretion disk (see [5, 6]).

In order to explain the QPOs, various models have been proposed. These are: (i) the Beat-frequency

models, where one assumes that there is some beating of an orbital frequency by the spin frequency of the central object, (ii) the relativistic precession models, where the QPOs are associated with the orbital motion and the periastron or nodal precession of a particular orbit, (iii) the relativistic resonance models, where a type of resonance between the orbital and the epicyclic frequencies is assumed wherever they have simple integer ratios, and finally (iv) the preferred radii models, where some mechanism chooses a particular radius. These models generally assume the geodesic or almost geodesic orbits of the fluid elements in the accretion disc to be the source of the observed frequencies (see, e.g., [5]), while there are also models in which the frequencies are produced from oscillatory modes of the entire disc (see, e.g., [7]). In one way or another all of these models use the properties of the orbits around the compact object onto which the accretion takes place. In our discussion we will refer to the models that assume that the QPOs are caused by the frequencies associated with the orbital motion of the material in the accretion disc such as the relativistic precession models (RPM) (see [2, 8]).

The RPM has been proposed in a series of papers [1, 2, 4]. It explains the kHz QPOs as a direct manifestation of modes of relativistic epicyclic motion of blobs arising at various radii  $r$  in the inner parts of the accretion disk. The model identifies the lower,  $f_L$ , and upper,  $f_U$ , kHz QPOs with the periastron precession  $f_{per}$  and Keplerian  $f_K$  frequency.

\*The text was submitted by the authors in English.

\*\*E-mail: kuantay@icra.it

\*\*\*E-mail: jorge.rueda@icra.it

\*\*\*\*E-mail: marco.muccino@icra.it

Paper presented at the international conference in honor of Ya.B. Zeldovich 100th Anniversary “Subatomic Particles, Nucleons, Atoms, Universe: Processes and Structure” held in Minsk, Belarus in March 10-14, 2014. Published by the recommendation of the special editors: S.Ya. Kilin, R. Ruffini, and G.V. Vereshchagin.

In the past years, the RPM has been considered among the candidates for explaining the twin-peak QPOs in several LMXBs and related constraints on the sources have been discussed (see, e.g., [6, 9–13]). While some of the early works discuss these constraints in terms of both neutron star mass and spin and include also the neutron star oblateness [3, 14], most of the published implications for individual sources focus on the neutron star mass and neglect its rotation and deformation.

In this work, we consider rotating spacetimes that comprehend the effects of frame-dragging and quadrupole moment of the source and fit directly the correlation between the twin-peak QPO frequencies. Since the angular momentum of the source is in a non-trivial way related to its quadrupole moment, they should be considered together. We shall show below that, indeed, a statistically preferred fit is obtained for the case of three parameters: mass ( $M$ ), angular momentum ( $J$ ) and quadrupole moment ( $Q$ ) with respect to an analysis using only  $M$  and  $J$  [16].

The importance of the quadrupole moment has been emphasized in several works [8, 17–21]. It is known that the quadrupole moment of realistic neutron stars deviates from the Kerr quadrupole moment (see, e.g., [22], and more recently [23]). This fact allows one to distinguish black holes from neutron stars. We shall extract the multipole moments ( $M$ ,  $J$ ,  $Q$ ) of the Z-source GX 5-1 and show that its quadrupole deformation parameter  $Q$  deviates from the value expected from a Kerr black hole. Indeed, we will show that the values ( $M$ ,  $J$ ,  $Q$ ) point to a neutron star nature of the compact component of this LMXB.

## 2. THE HARTLE–THORNE METRIC

The Hartle–Thorne metric [18, 25] describing the exterior field of a slowly rotating slightly deformed object is given by

$$\begin{aligned}
 ds^2 = & - \left(1 - \frac{2M}{r}\right) \left[1 + 2k_1 P_2(\cos \theta)\right] \\
 & + 2 \left(1 - \frac{2M}{r}\right)^{-1} \frac{J^2}{r^4} (2 \cos^2 \theta - 1) dt^2 \\
 & + \left(1 - \frac{2M}{r}\right)^{-1} \left[1 - 2k_2 P_2(\cos \theta)\right. \\
 & \left. - 2 \left(1 - \frac{2M}{r}\right)^{-1} \frac{J^2}{r^4}\right] dr^2 \\
 & + r^2 [1 - 2k_3 P_2(\cos \theta)] \\
 & \times (d\theta^2 + \sin^2 \theta d\phi^2) - 4 \frac{J}{r} \sin^2 \theta dt d\phi,
 \end{aligned} \quad (1)$$

where functions  $k_1$ ,  $k_2$ , and  $k_3$  are defined as follows

$$\begin{aligned}
 k_1 &= \frac{J^2}{Mr^3} \left(1 + \frac{M}{r}\right) \\
 & - \frac{5Q - J^2/M}{8M^3} Q_2^2 \left(\frac{r}{M} - 1\right), \\
 k_2 &= k_1 - \frac{6J^2}{r^4}, \\
 k_3 &= k_1 + \frac{J^2}{r^4} - \frac{5Q - J^2/M}{4M^2 r} \\
 & \times \left(1 - \frac{2M}{r}\right)^{-1/2} Q_2^1 \left(\frac{r}{M} - 1\right),
 \end{aligned}$$

and polynomials are given by

$$\begin{aligned}
 P_2(x) &= \frac{1}{2}(3x^2 - 1), \\
 Q_2^1(x) &= (x^2 - 1)^{1/2} \left[ \frac{3x}{2} \ln \frac{x+1}{x-1} - \frac{3x^2 - 2}{x^2 - 1} \right], \\
 Q_2^2(x) &= (x^2 - 1) \left[ \frac{3}{2} \ln \frac{x+1}{x-1} - \frac{3x^3 - 5x}{(x^2 - 1)^2} \right].
 \end{aligned}$$

Here,  $P_2(x)$  is Legendre polynomials of the first kind,  $Q_l^m$  are the associated Legendre polynomials of the second kind and constants  $M$ ,  $J$ , and  $Q$  are the total mass, angular momentum and quadrupole parameter of a rotating star respectively. The Hartle–Thorne metric is an approximate solution of vacuum Einstein field equations that describes the exterior of any slowly and rigidly rotating, stationary and axially symmetric body. The metric is given with accuracy up to the second order terms in the body's angular momentum, and first order in its quadrupole moment. The approximate Kerr metric [24] in the Boyer–Lindquist coordinates ( $t$ ,  $R$ ,  $\Theta$ ,  $\phi$ ) up to second order terms in the rotation parameter  $a$  can be obtained from (1) by setting<sup>1</sup>

$$J = -Ma, \quad Q = J^2/M, \quad (2)$$

and making a coordinate transformation given by

$$\begin{aligned}
 r &= R + \frac{a^2}{2R} \left[ \left(1 + \frac{2M}{R}\right) \left(1 - \frac{M}{R}\right) \right. \\
 & \left. - \cos^2 \Theta \left(1 - \frac{2M}{R}\right) \left(1 + \frac{3M}{R}\right) \right], \\
 \theta &= \Theta + \frac{a^2}{2R^2} \left(1 + \frac{2M}{R}\right) \sin \Theta \cos \Theta.
 \end{aligned} \quad (3)$$

<sup>1</sup> We note here that the quadrupole moment  $Q$  in this work is related to the mass quadrupole moment defined by Hartle and Thorne [25] through  $Q = 2J^2/M - Q_{HT}$ .

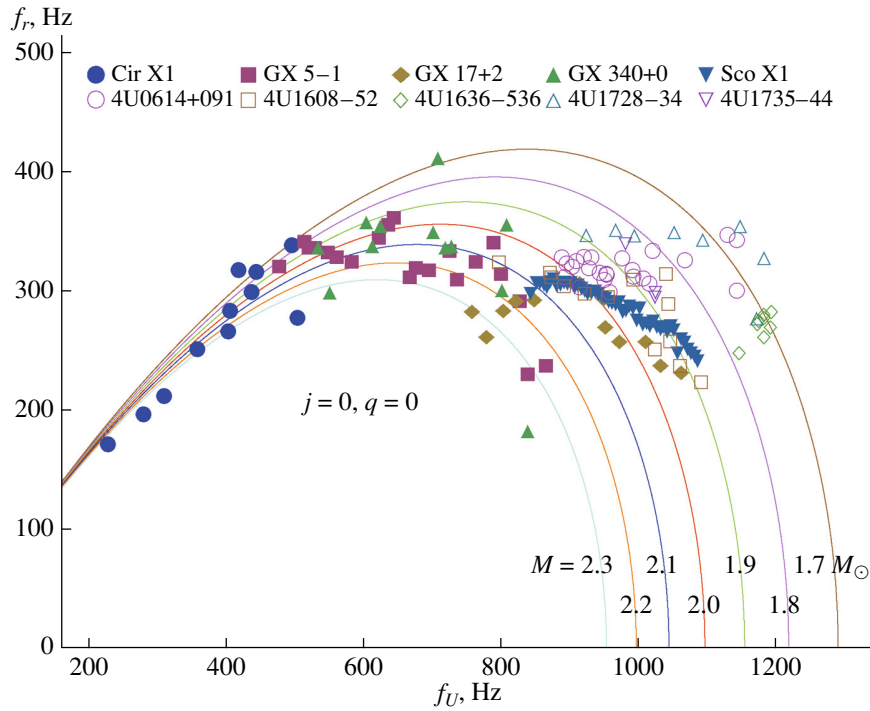


**Fig. 1.** The radial frequency  $f_r$  is plotted versus the upper frequency  $f_U$  for the Schwarzschild spacetime ( $j = 0, q = 0$ ). From top to bottom  $M = [1.7, 1.8, 1.9, 2.0, 2.1, 2.2, 2.3, 2.4]M_\odot$ .

### 3. DETERMINATION OF THE MASS, ANGULAR MOMENTUM AND QUADRUPOLE MOMENT

Spacetimes around rotating neutron stars can be with a high precision approximated by the three parametric Hartle–Thorne (HT) solution of Einstein field equations ([25]; see [26]). The solution considers the mass  $M$ , angular momentum  $J$  and quadrupole moment  $Q$  (supposed to reflect the rotationally induced oblateness of the star). It is known that in most situations modeled with the present neutron star equations of state (EoS) the neutron star external geometry is very different from the Kerr geometry (representing the limit of HT geometry for  $\tilde{q} \equiv QM/J^2 \rightarrow 1$ ). However, the situation changes when the neutron star mass approaches maximum for a given EoS. For high masses the quadrupole moment does not induce large differences from the Kerr geometry since  $\tilde{q}$  takes values close to unity. Nevertheless this does not mean that one can easily neglect the quadrupole moment. For this reason in this work we extend the analyses of [2] involving the Hartle–Thorne solution.

Usually in the literature the QPOs data are given by the following frequencies

$$\begin{aligned} f_\phi &= \omega_K/(2\pi), & f_r &= \omega_r/(2\pi), \\ f_\theta &= \omega_\theta/(2\pi), \end{aligned} \quad (4)$$

where  $f_\phi = f_K = f_U$  is the azimuthal (Keplerian, upper) frequency,  $f_r$  is the radial frequency, and  $f_\theta$  is the polar (vertical) frequency. In Fig. 1 the radial frequency  $f_r$  is plotted versus the upper (Keplerian) frequency  $f_U$  in the Schwarzschild spacetime, where  $j = J/M^2$  and  $q = Q/M^3$  are the dimensionless angular momentum and quadrupole parameter. The smaller mass the higher radial frequency  $f_r$ . Note for ( $j = 0, q = 0$ ), the Keplerian frequency  $f_K$  coincides with the vertical frequency  $f_\theta$  [27]. The Keplerian frequency  $f_\phi$  versus the periastron frequency  $f_{per} = f_\phi - f_r$  is shown in Fig. 2. The observational data-points in the Figs. 1, 2 belong to Atoll (4U0614+091, 4U1608-52, 4U1636-536, 4U1728-34, 4U1735-44) and Z (GX 5-1, GX 17+2, GX 340+0, Sco X-1, Cir X-1) sources. For the sake of clarity the error bars have been omitted. The QPOs data have been taken from [28–31] and references therein. The results for different frequencies with various combinations of mass, angular momentum and quadrupole moment are given in [27].

In this work we used the minimum set of parameters such as the total mass  $M$ , dimensionless angular momentum  $j$  and quadrupole parameter  $q$  of the source. Unfortunately, from the observations it is hard to obtain precise values of the masses of the LMXBs. Different references show contradicting

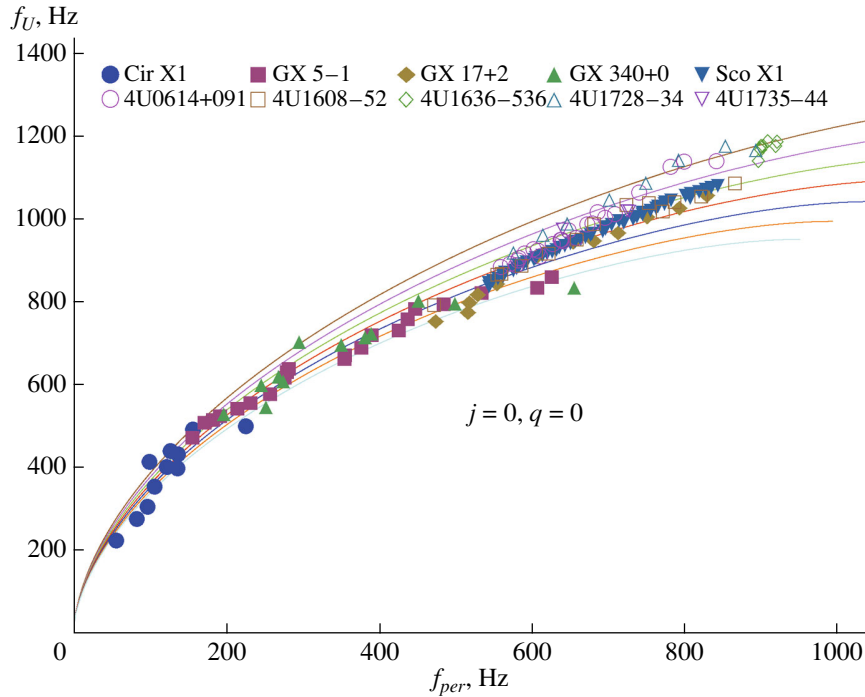


**Fig. 2.** The upper frequency  $f_U$  is plotted versus the periastron frequency  $f_{per} = f_\phi - f_r$  for the Schwarzschild spacetime ( $j = 0, q = 0$ ). From top to bottom the mass  $M = [1.7, 1.8, 1.9, 2.0, 2.1, 2.2, 2.3, 24]M_\odot$ .

numbers. For example, Sco X-1 is a well-known X-ray binary system classified as a low-mass X-ray binary; the neutron star is roughly  $1.4 M_\odot$ , while the donor star is only  $0.42 M_\odot$  [32]. However, references [2, 33] and [34] present various values for the neutron star mass.

In Fig. 3 we show best fits for the upper frequency versus the lower frequency for the Z source GX 5-1. Here we see that the fit with all three parameters is better than the fit with the only one parameter, the mass  $M$ . Statistical test  $\chi^2 = 0.998$  for the three parameter fit and  $\chi^2 = 0.993$  for the one parameter fit.

The Keplerian angular velocity (angular frequency)  $\omega_K$  for co-rotating geodesics at the equatorial plane in the Hartle–Thorne spacetime [35] is given by

$$\omega_K^2(u) = \omega_{K0}^2(u) \quad (5)$$

$$\times [1 - jF_1(u) + j^2F_2(u) + qF_3(u)],$$

where  $u = M/r$ . The rest functions are defined as follows

$$\omega_{K0}^2(u) = u^3/M^2, \quad F_1(u) = 2u^{3/2},$$

$$F_2(u) = \frac{48u^7 - 80u^6 + 12u^5 + 26u^4 - 40u^3 - 10u^2 - 15u + 15}{8u^2(1 - 2u)} - F(u),$$

$$F_3(u) = -\frac{5(6u^4 - 8u^3 - 2u^2 - 3u + 3)}{8u^2(1 - 2u)} + F(u),$$

$$F(u) = \frac{15(1 - 2u^3)}{16u^3} \ln\left(\frac{1}{1 - 2u}\right).$$

In terms of the Keplerian angular velocity we can estimate for GX 5-1 the internal and external radii of the accretion disk. We consider co-rotating orbits. The highest value of the upper frequency determines the internal and the lowest value determines the external radii for a given set of parameters  $M = 1.98 M_\odot$ ,  $j = 0.55$ , and  $q = -2.04$ . As a result  $f_U =$

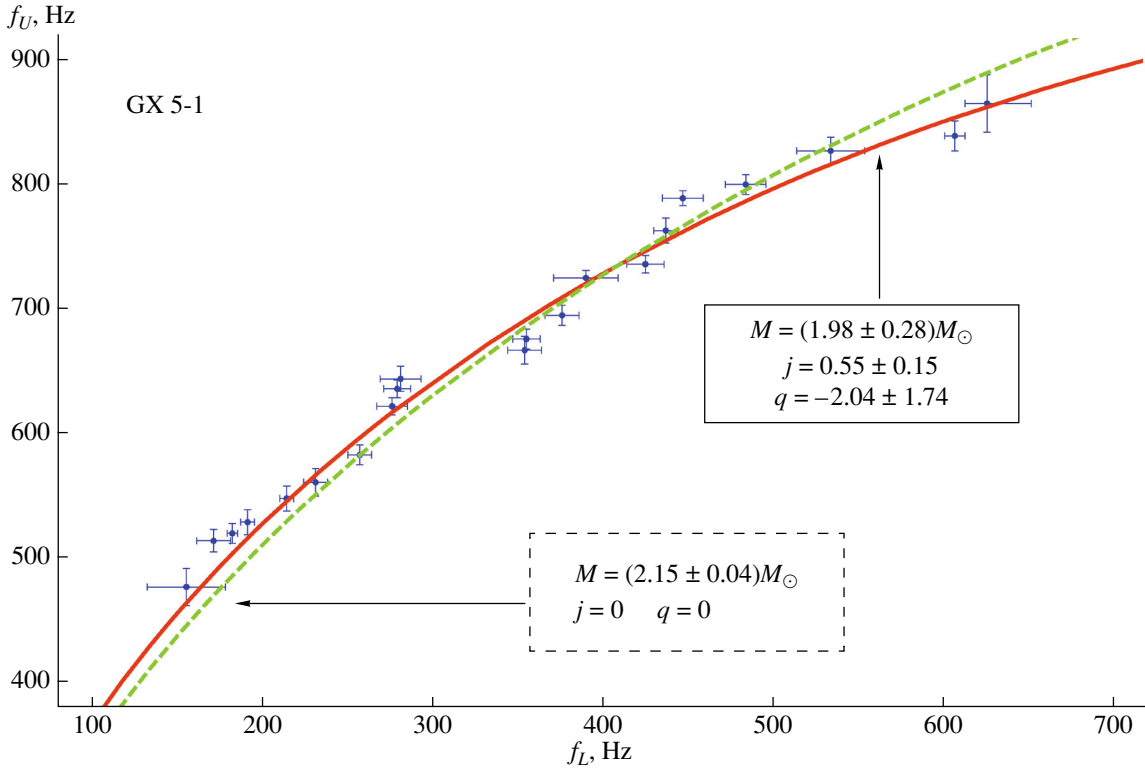


**Fig. 3.** The upper frequency  $f_U$  is plotted versus the lower frequency  $f_L$  for the Z source GX 5-1. The dashed green line corresponds to the static case and the solid red line corresponds to the rotating case.

866 Hz yields  $r \approx 21$  km, and  $f_U = 478$  Hz, yields  $r \approx 31$  km.

The radius determining the marginally stable circular geodesic  $r_{\text{ms}}$  at equatorial plane is given by

$$r_{\text{ms}} = 6M \left[ 1 - \frac{2}{3} \sqrt{\frac{2}{3}} j - \left( \frac{251903}{2592} - 240 \ln \frac{3}{2} \right) j^2 + \left( \frac{9325}{96} - 240 \ln \frac{3}{2} \right) q \right].$$

It is clear that the presence of both the rotation and quadrupole parameters can increase or decrease the values for  $r_{\text{ms}}$  [21]. For our parameters  $M = 1.98 M_{\odot}$ ,  $j = 0.55$ , and  $q = -2.04$  the radius of the marginally stable orbits equals  $r_{\text{ms}} = 19.3$  km which is very near to the inner part of the accretion disk.

#### 4. CONCLUSION

In this work with the help of the epicyclic frequencies of test particles in the Hartle–Thorne spacetime and the relativistic precession model we have interpreted the quasi-periodic oscillations of the low-mass

X-ray binaries. We have constructed the dependence of the higher frequencies with respect to the lower frequencies varying the main parameters of the central compact object such as the mass, angular momentum and quadrupole moment. Eventually for Z source GX 5-1 we have performed the fitting analyses and found the best fit to estimate the mass, angular momentum and quadrupole moment. We have shown that the three parameter fit is better than one-two parameter fit. We have also estimated for GX 5-1 the internal and external radii of the accretion disk around the compact object. The fact that  $q \neq j^2$  allows us to state that GX 5-1 is a neutron star rather than a black hole. Moreover we calculated the radius of the marginally stable co-rotating orbits at the equatorial plane. For better analyses one needs to consider more sources with refined data. It would be interesting to perform further calculations assigning the neutron star equation of state and construct mass-radius, mass-angular momentum, and angular velocity-quadrupole moment relations in order to compare and contrast the theory with observations. This will be the issue of future investigations.

#### ACKNOWLEDGMENTS

The authors thank ICRANet for support. One of them (K.B.) thanks Mariano Méndez for providing

observational data and for stimulating discussions, and Ivan Siutsou for technical assistance.

#### REFERENCES

1. L. Stella and M. Vietri, in *Proceedings of the 19th Texas Symposium on Relativistic Astrophysics and Cosmology*, Ed. by J. Paul, T. Montmerle, and E. Aubourg (CEA Saclay, 1998).
2. L. Stella and M. Vietri, *Phys. Rev. Lett.* **82**, 17 (1999).
3. L. Stella, M. Vietri, and S. M. Morsink, *Astrophys. J.* **524**, L63 (1999).
4. L. Stella and M. Vietri, in *Proceedings of the 9th Marcel Grossmann Meeting on General Relativity: MGIXMM Meeting, La Sapienza Univ., Rome, July 2–8, 2000*, Ed. by V. G. Gurzadyan, R. T. Jantzen, and R. Ruffini (World Scientific Publ., 2002).
5. M. van der Klis, in *Compact Stellar X-Ray Sources*, Ed. by W. H. G. Lewin and M. van der Klis (Cambridge Univ. Press, Cambridge, 2006), p. 39.
6. F. K. Lamb and S. Boutloukos, in *Short-Period Binary Stars: Observations, Analyses, and Results*, Ed. by E. F. Milone, D. A. Leahy, and D. Hobill (Springer, Dordrecht, 2007).
7. L. Rezzolla, S. Yoshida, and O. Zanotti, *Mon. Not. R. Astron. Soc.* **344**, 978 (2003).
8. G. Pappas, *Mon. Not. R. Astron. Soc.* **422**, 2581 (2012).
9. V. Karas, *Astrophys. J.* **526**, 953 (1999).
10. C. M. Zhang, H. X. Yin, Y. H. Zhao, F. Zhang, and L. M. Song, *Mon. Not. R. Astron. Soc.* **366**, 1373 (2006).
11. T. Belloni, M. Méndez, and J. Homan, *Mon. Not. R. Astron. Soc.* **376**, 1133 (2007).
12. C. M. Yan, Y. Zhang, H. X. Yin, and Y. H. Zhao, *Astron. Nachr.* **330**, 398 (2009).
13. D. Barret and M. Boutelier, *Mon. Not. R. Astron. Soc.* **384**, 1519 (2008).
14. S. M. Morsink and L. Stella, *Astrophys. J.* **513**, 827 (1999).
15. S. Boutloukos, M. van der Klis, D. Altamirano, M. Klein-Wolt, R. Wijnands, P. G. Jonker, and R. P. Fender, *Astrophys. J.* **653**, 1435 (2006).
16. G. Török, P. Bakala, E. Šrámková, Z. Stuchlík, and M. Urbanec, *Astrophys. J.* **714**, 748 (2010).
17. H. Quevedo and L. Parkes, *Gen. Relativ. Gravit.* **21**, 1047 (1989).
18. D. Bini, A. Geralico, O. Luongo, and H. Quevedo, *Class. Quantum Grav.* **26**, 225006 (2009).
19. D. Bini, K. Boshkayev, and A. Geralico, *Class. Quantum Grav.* **29**, 145003 (2012).
20. L. A. Pachón, J. A. Rueda, and C. A. Valenzuela-Toledo, *Astrophys. J.* **756**, 82 (2012).
21. D. Bini, K. Boshkayev, R. Ruffini, and I. Siutsou, *Nuovo Cimento* **36C**, 1 (2013). doi:10.1393/ncc/i2013-11483-8
22. W. G. Laarakkers and E. Poisson, *Astrophys. J.* **512**, 282 (1999).
23. G. Pappas and T. A. Apostolatos, *Phys. Rev. Lett.* **108**, 231104 (2012).
24. R. P. Kerr, *Phys. Rev. Lett.* **11**, 237 (1963).
25. J. B. Hartle and K. S. Thorne, *Astrophys. J.* **153**, 807 (1968).
26. E. Berti, F. White, A. Maniopoulou, and M. Bruni, *Mon. Not. R. Astron. Soc.* **358**, 923 (2005).
27. K. Boshkayev, J. A. Rueda, D. Bini, A. Geralico, M. Muccino, and I. Siutsou, *Grav. Cosmol.* **20** (4), 233-239 (2014).
28. M. Méndez, M. van der Klis, R. Wijnands, E. C. Ford, J. van Paradijs, and B. A. Vaughan, *Astrophys. J.* **505**, L23 (1998).
29. M. Méndez and M. van der Klis, *Astrophys. J.* **517**, L51 (1999).
30. M. Méndez and M. van der Klis, *Mon. Not. R. Astron. Soc.* **318**, 938 (2000).
31. M. Méndez and T. Belloni, *Mon. Not. R. Astron. Soc.* **381**, 790 (2007).
32. D. Steeghs and J. Casares, *Astrophys. J.* **568**, 273 (2002).
33. C. Zhang and A. Dolgov, *Int. J. Mod. Phys. D* **10**, 625 (2001).
34. B. Mukhopadhyay, *Astrophys. J.* **694**, 387 (2009).
35. G. Török, P. Bakala, Z. Stuchlík, and P. Cech, *Acta Astron.* **58**, 1 (2008).

# An effective field theory for neutron stars with many-body forces, strong $\Sigma^-$ repulsion, and $K^-$ and $\bar{K}^0$ condensation

A. Mesquita<sup>1</sup>, M. Razeira<sup>2</sup>, R. Ruffini<sup>3,4,5</sup>, J. A. Rueda<sup>3,4,5</sup>, D. Hadjimichef<sup>6</sup>, R. O. Gomes<sup>6</sup>, and C. A. Zen Vasconcellos<sup>4,6,\*</sup>

<sup>1</sup> Universidade de Caxias do Sul (UCS), Campus Sede, Rua Francisco Getúlio Vargas, 1130, CEP 95070-560, Caxias do Sul, RS, Brazil

<sup>2</sup> Universidade Federal do Pampa (UNIPAMPA), Campus Caçapava do Sul, Av. Pedro Anunciação, s/n<sup>o</sup>, Vila Batista, CEP 96570-000, Caçapava do Sul, RS, Brazil

<sup>3</sup> Sapienza Università di Roma, Piazzale Aldo Moro 5, 00185 Rome, Italy

<sup>4</sup> ICRANet, P.zza della Repubblica 10, 65122 Pescara, Italy

<sup>5</sup> ICRANet-Rio, Centro Brasileiro de Pesquisas Físicas, Rua Dr. Xavier Sigaud 150, Rio de Janeiro, RJ, 22290-180, Brazil

<sup>6</sup> Instituto de Física, Universidade Federal do Rio Grande do Sul, Av. Bento Gonçalves 9500, CEP 91501-970, Porto Alegre, RS, Brazil

Received 2015 Sep 21, accepted 2015 Sep 26

Published online 2015 Nov 20

**Key words** dense matter – elementary particles – equation of state – stars: neutron

The role of many-body correlations (many-body forces) and  $K^-$ - $\bar{K}^0$  condensation in  $\beta$ -equilibrated hyperonic matter is investigated in order to shed some light in the hyperonization puzzle, ie that neutron star mass of  $2M_\odot$  cannot be obtained in the presence of exotic degree of freedoms. In this investigation, we use an effective relativistic QHD-model with parameterized couplings which represents an extended compilation of other effective models found in the literature. Our theoretical approach exhausts the whole fundamental baryon octet ( $n$ ,  $p$ ,  $\Sigma^-$ ,  $\Sigma^0$ ,  $\Sigma^+$ ,  $\Lambda$ ,  $\Xi^-$ ,  $\Xi^0$ ) and simulates n-order corrections to the minimal Yukawa couplings by considering many-body nonlinear self-couplings and meson-meson interaction terms involving scalar-isoscalar ( $\sigma$ ,  $\sigma^*$ ), vector-isoscalar ( $\omega$ ,  $\phi$ ), vector-isovector ( $\rho$ ), and scalar-isovector ( $\delta$ ) sectors. Following recent experimental results, we consider in our calculations the extreme case where the  $\Sigma^-$  experiences such a strong repulsion that its influence in the nuclear structure of a neutron star is excluded at all. We study the effects of this exclusion on the phase transition of *conventional exotic* hadronic matter to hadronic matter containing a condensate of kaons and anti-kaons. As a novelty in the treatment of kaon and anti-kaon condensation in high density nuclear matter, we consider a Lagrangian formulation which describes, in addition to the interaction involving baryons and mesons and the contribution of kaons and anti-kaons in free propagation, the presence of many-body forces involving kaon, anti-kaon and meson fields. To implement the corresponding phase transition we considered the Gibbs conditions combined with the mean-field approximation, giving rise to a mixed phase of coexistence between baryon matter and the condensed of kaons and anti-kaons. Our investigation show that even with kaon condensation, the nuclear equation of state satisfies both the maximum mass and the allowed ranges of mass and radius of neutron stars.

© 2015 WILEY-VCH Verlag GmbH & Co. KGaA, Weinheim

## 1 Introduction

In effective nuclear field theory, neutron stars are treated as macroscopic portions of asymmetric and *infinite* nuclear matter, an idealized conception of many interacting baryon systems (containing about  $10^{58}$  baryons). It is assumed that neutron stars are composed of nucleons and possibly hyperon and lepton fields, moving in a condensate of mesons, photons and neutrinos (and their antiparticles). Maybe present in this context are more complex phenomena such as superfluidity, kaon and pion condensation, and a phase transition from hadronic matter to a quark-gluon plasma (QGP) (Glendenning 1997). The study of nuclear

matter at densities higher than those found in ordinary nuclear matter has various interests, in especial regarding to the possibility of allowing a better understanding of the different properties of a neutron star.

Matter density in the core of a neutron star can exceed tens of times the density of nuclear matter under normal conditions. However, our knowledge of the properties of dense nuclear matter is very much determined by the knowledge we have of these properties at a single point in the phase space diagram covered by the entire range of nuclear densities experimentally determined, ie the saturation density, which represents the density point of nuclear matter under normal conditions that nucleons in a nucleus senses approximately a constant number of neighbors.

\* Corresponding author: cesarzen@cesarzen.com

Indeed, all empirical values of the various bulk properties of symmetric nuclear matter, essential inputs for the effective understanding of the structure and evolution of neutron stars, ie, the binding energy, the mass and radius, the surface and volume energy, the bulk symmetry energy, and the compressibility module are only experimentally determined at this density point. Models in turn, starting from the knowledge of these properties at the saturation density of nuclear matter allow a *controlled* extrapolation of those properties to the regime of high densities and highly asymmetric nuclear matter.

Since the seminal work of W. Baade and F. Zwicky (1934) proposing for the first time the existence of neutron stars, and suggesting that these stars are formed in a supernova explosion which results from the gravitational collapse of an ordinary star, the standard theoretical procedure to find the macroscopic properties of a neutron star is by determining the equation of state of nuclear matter, a type of parametric equation that relates the internal energy density of the star with its internal pressure. It has been reported in the last years in the literature a wide spectrum of different equations of state of nuclear matter at different densities with applications to astrophysical problems. The knowledge of the equation of state (EoS) of nuclear matter at high densities in particular, such as those found in neutron stars and pulsars, is still an open problem that combines the understanding of the role of underlying physical principles and experimental and observational verifications<sup>1</sup> placing this way strong constraints on the interior composition of neutron stars<sup>2</sup>.

The understanding of some basic aspects of the structure of the core of a neutron star, at the regime densities of the order of  $10^{14}$  g cm<sup>-3</sup>, – the starting point for the theoretical treatment adopted in this work –, demands going back to the original perception of Baade & Zwicky (1934) that a neutron star would be an uniform assembly of extremely closed packed neutrons. A more accurate understanding of the significance of this perception can be obtained by analyzing, in the non-relativistic regime, the Bethe-Weizsäcker

semi-empirical formula<sup>3</sup>

$$B(Z, N) = a_V A - a_S A^{2/3} - a_C Z(Z-1)A^{-1/3} - a_A (Z-N)^2 A^{-1} - \delta(Z, N), \quad (1)$$

From this expression it results that nuclear states with equal number of neutrons and protons  $N = Z$ , ie with total i-spin equal to zero ( $\sum_{k=1}^A T_k^{i\text{-spin}} = 0$ ), have a higher stability than states with  $N \neq Z$  ( $\sum_{k=1}^A T_k^{i\text{-spin}} \neq 0$ ) since they maximize the nuclear binding energy<sup>4</sup>, ie unequal numbers of neutrons and protons imply filling higher energy levels for one type of particle, while leaving lower energy levels vacant for the other type. According to this formula, the bulk symmetry energy is defined as the difference between the energy per particle for pure neutron matter ( $Z \rightarrow 0; A \rightarrow N$ ) and that of symmetric nuclear matter ( $N = Z$ ) at normal nuclear density. Its empirical value lies in the range 30–40 MeV (Lattimer & Prakash 2001).

An important aspect of the phenomenology of nuclear physics is that the core density is approximately constant within a nucleus. Thus, the core volume increases with the increasing of the number of nucleons in such a way as to maintain a constant density, behaving this way similarly to an incompressible fluid of constant density. On the other hand, the approximate constancy of nuclear density implies that no physical state within a nucleus is energetically more favorable than another<sup>5</sup>. In the limit  $A \rightarrow \infty$ , the bulk symmetry energy *controls* the Fermi momenta of baryons, as well as particle fractions and the equation of state of dense matter.

## 2 The hyperonization puzzle in neutron star models

A few steps further this simple description, in the realm of more realistic models for the strong interaction at high densities and according to experimental data (see, for instance, Nagae 2010), the appearance of exotic particles, ie hyperons and/or a condensed of kaons and anti-kaons, may occur at densities  $(5\text{--}8) \times 10^{14}$  g cm<sup>-3</sup>. However, the so called

<sup>1</sup> We mean, experiments mainly aimed to the understanding of the dynamics of heavy ion collisions and to shed some light on the equation of state of nuclear matter at low density and high temperature and to the structure of nuclei far from stability. Observations related to neutron stars are performed mainly by the X-ray telescopes *Chandra*, ESA's *XMM-Newton*, and NASA's *Rossi* X-ray Timing Explorer (RXTE) providing the most reliable determinations yet of the relation between the radius of a neutron star and its mass. See for instance [www.nasa.gov](http://www.nasa.gov).

<sup>2</sup> Given an EoS that describes the structure of a neutron star, A, with higher internal pressure than another, B, endowed with a higher internal pressure, the star A can withstand a greater gravitational compression than star B and so the first must have a greater mass than the second, since the intensity of the gravitational force is directly related to the stellar mass, although in general relativity pressure is also a mass supply. The EoS of A is said to be more rigid or stiffer than the EoS of B and, conversely, the EoS of B is said to be softer than the EoS of A. Observations of the magnitudes of the stellar mass and radius (mass-radius relation), establish this way strong restrictions on the various possible equations of state existing in the literature. If the radius-mass ratio of a neutron star is determined accurately enough, one can bi-univocally determine the equation of state of that star.

<sup>3</sup> This formula, based partly on the theory of the liquid drop model proposed by George Gamow (1928), and partly on empirical measurements, describes in an approximated way the nuclear binding energy  $B(Z, N)$  of a nucleus with  $N$  neutrons,  $Z$  protons and nuclear number  $A = N + Z$ . The free parameters in the formula, to be determined phenomenologically are:  $a_V$ , volume term;  $a_S$ , surface term;  $a_C$ , Coulombian term;  $a_A$ , asymmetry term and  $\delta$ , pairing term. This expression represents the original theoretical formulation for the definition of nuclear matter in the limit  $A \rightarrow \infty$ .

<sup>4</sup> Roughly speaking in terms only of the nuclear force which is independent of electric charge. In a neutron star it is assumed the presence of leptons and mesons with negative electric charge to assure a electrically neutral system.

<sup>5</sup> Consequently, the nuclear potential should be approximately constant within the core. This result justifies as a primarily approximation for the description of a nuclear system, the use of the Fermi gas model of *free particles*. The term *free* here should be taken carefully since baryons are subject to the Pauli exclusion principle which manifests itself by the presence of a quantum degeneracy pressure. Assuming an uniform static spherical neutron star, the neutron degeneracy pressure may be of the order  $P \sim 3 \times 10^{33}$  Pa

hyperonization process softens the EoS of neutron stars<sup>6</sup> and the maximal allowable mass should be reduced considerably as pointed out (Glendenning & Moszkowski 1991; Glendenning & Schaffner-Bielich 1998; Vidana et al. 2000; Schaffner-Bielich 2008; Schulze & Rijken 2011), affecting this way the theoretical achievement of neutron star masses of the order or larger than  $2 M_{\odot}$  (see Demorest et al. 2010; Antoniadis et al. 2013). These results give rise to the so called *hyperonization puzzle*: how to reproduce the observed masses of neutron stars while taking into account in the equation of state of nuclear matter the presence of hyperons and kaon and anti-kaon condensation?<sup>7</sup>

### 3 On the maximum mass of neutron stars

In 2010, Paul Demorest and colleagues (Demorest et al. 2010), using Shapiro delay measurements, found for the mass of the millisecond pulsar PSR J16142230 the value  $1.97 \pm 0.04 M_{\odot}$ , substantially higher than any previously measured neutron star mass. More recently, in 2013, John Antoniadis and colleagues (Antoniadis et al. 2013) measured the mass of the millisecond pulsar PSR J0348+0432 to be  $2.01 \pm 0.04 M_{\odot}$ , through spectroscopy observations. In addition, there has been historically a recurring discussion about the upper bound limits of neutron star masses, as for instance Rhoades & Ruffini (1974) who found  $M_{\max} \leq 3.2 M_{\odot}$ , Kalogera & Baym (1996) who found  $M_{\max} \leq 2.9 M_{\odot}$ , and more recently Lawrence et al. (2015) who found the limit  $M_{\max} \leq 2.2 M_{\odot}$ . Regardless the uncertainties on those predictions, the *hyperonization puzzle* is still a very current topic.

In the search for a relativistic formulation, consistent with these observations, recently we have shown, using a theoretical framework which simulates n-order corrections to the minimal Yukawa couplings, that many-body correlations may shield the attractive and the repulsive parts of the strong interaction and may increase the effective mass of baryons in nuclear matter<sup>8</sup> (Vasconcellos et al. 2015).

There is another important effect to be considered in our formulation, the presence of hyperons. Our predictions for the particle population show that the threshold equation for a given species (Glendenning 1996) is also affected by the presence of many-body correlations. Moreover, following

<sup>6</sup> The Pauli exclusion principle does not manifest between nucleons and hyperons thus causing a decrease in the internal quantum degeneracy pressure in neutron stars. And thereby making it more difficult for nuclear models containing hyperons to describe stars with masses of the order of  $2 M_{\odot}$  as recently observed (Demorest et al. 2010; Antoniadis et al. 2013).

<sup>7</sup> Theoretical studies (Kaplan & Nelson 1986) indicate the presence of optical repulsive potentials for the SU(2) doublet ( $K^+$ ,  $K^0$ ) (strangeness +1). Therefore in this study we only consider in the star the presence of condensates of the doublet ( $K^-$ ,  $\bar{K}^0$ ) (strangeness -1).

<sup>8</sup> When many-body correlations shield the attractive part of the strong interaction, they intensify the corresponding repulsive part, favoring in this way the stiffening of the EoS. On the other hand, when the effective masses of baryons increase as the shielding of the attractive part of the strong interaction increases, this effect also favors the growth of the internal pressure of the system and the stiffening of the EoS.

experimental results (Bednarek, Keska & Manka 2003), we have considered in our previous calculations the extreme case where the  $\Sigma^-$  experiences such a strong repulsion that it does not appear at all in nuclear matter for densities as those found in neutron stars causing however, due to many-body correlations the increase on the population of the remaining hyperons beyond the  $\Sigma^-$ . The first hyperon species that appears is the  $\Lambda$ : free of isospin-dependent forces, as the density increases, the  $\Lambda$  hyperon continues to accumulate until short-range repulsion forces cause them to saturate. Other hyperon species follow at higher densities.

Our model originates moreover an anti-correlation between the amount of hyperons: for certain values of the parameters, an anti-correlation associated with the predominance of the scalar part occurs. This means that hyperon degrees of freedom become more numerous to the extent that the attractive sector is favored in comparison with the repulsive part, thus favoring smaller neutron star masses. However, the absence of the  $\Sigma^-$  hyperon reduces this effect.

When considering simultaneously both shielding effects involving the attractive and repulsive contributions of the strong interaction, our results indicate that the combination of these effects previously reported favors the stiffening of the EoS. In other words, the shielding of the attractive part of the strong interaction combined with the increase of the effective mass of baryons and the absence of the  $\Sigma^-$  hyperon, are dominant when compared with those effects favoring the softening of the EoS, i.e., the shielding of the repulsive part of the strong interaction and the increase on the population of the remaining hyperons beyond the  $\Sigma^-$ .

The hypothesis of our present work is that the effects aforementioned may therefore be the key argument to allow the nuclear equation of state to satisfy both the maximum mass and the allowed ranges of mass and radius of neutron stars even in the presence of exotic degrees of freedom, i.e. hyperons as well as kaon and anti-kaon condensation.

**Table 1** Properties of the fields considered in the formulation (3). In what follows, we use the abbreviations: ISS: isoscalar-scalar; IVS: isovector-scalar; ISV: isoscalar-vector; IVV: isovector-vector, and  $\Phi = \sigma, \sigma^*, \omega, \varrho, \delta, \phi$ .

Fields	Classification	Particles	Coupling Constants	Mass (MeV)
$\psi_B$	Baryons	N, $\Lambda$ , $\Sigma$ , $\Xi$	N/A	939, 1116 1193, 1318
$\psi_l$	Leptons	$e^-$ , $\mu^-$	N/A	0.5, 106
$\sigma$	ISS-meson	$\sigma$	$g_{\sigma B}^*$	550
$\delta$	IVS-meson	$a_0$	$g_{\delta B}^*$	980
$\omega_\mu$	ISV-meson	$\omega$	$g_{\omega B}^*$	782
$\varrho_\mu$	IVV-meson	$\rho$	$g_{\varrho B}^*$	770
$\sigma^*$	ISS-meson	$f_0$	$g_{\sigma^* B}^*$	975
$\phi_\mu$	ISV-meson	$\phi$	$g_{\phi B}^*$	1020
$\psi_{K^-}$	Kaon	$K^-$	$g_{\phi K^-}^*$	494
$\psi_{\bar{K}^0}$	Anti-kaon	$\bar{K}^0$	$g_{\phi \bar{K}^0}^*$	498

## 4 Lagrangian density and Gibbs phase transition

### 4.1 Baryon phase

The Lagrangian density for the baryon phase in the mean field approximation,  $\mathcal{L}_{\xi\zeta\kappa\eta}$  (see Vasconcellos et al. 2015) reads

$$\begin{aligned} \mathcal{L}_{\xi\zeta\kappa\eta} = & \frac{1}{2}m_\sigma^2\sigma_0^2 + \frac{1}{2}m_{\sigma^*}^2\sigma_0^{*2} + \frac{1}{2}m_\omega^2\omega_0^2 + \frac{1}{2}m_\phi^2\phi_0^2 \\ & + \frac{1}{2}m_\rho^2\varrho_{03}^2 + \frac{1}{2}m_\delta^2\delta_3^2 + \sum_l \bar{\psi}_l (i\gamma_\mu\partial^\mu - m_l)\psi_l \\ & + \sum_B \bar{\psi}_B (i\gamma_\mu\partial^\mu - g_{\omega B}m_{B\xi}^*\gamma_0\omega_0 - M_{B\zeta}^*)\psi_B \\ & - \sum_B \bar{\psi}_B \left( \frac{1}{2}g_{\rho B}m_{B\kappa}^*\gamma_0\tau^{(3)}\varrho_{03} + g_{\phi B}m_{B\eta}^*\gamma_0\phi_0 \right) \psi_B. \end{aligned} \quad (2)$$

In this expression, the effective parameterized baryon-meson coupling constants are defined as  $g_{\omega B\xi}^* = g_{\omega B}m_{B\xi}^*$ ;  $g_{\rho B\kappa}^* = g_{\rho B}m_{B\kappa}^*$ ; and  $g_{\phi B\eta}^* = g_{\phi B}m_{B\eta}^*$ , with

$$m_{B\alpha}^* \equiv \left( 1 + \frac{g_{\sigma B}\sigma_0 + g_{\sigma^* B}\sigma_0^{*2} + \frac{1}{2}g_{\delta B}\tau \cdot \delta}{\alpha M_B} \right)^{-\alpha}; \quad (3)$$

( $\alpha = \xi, \kappa, \eta, \zeta$ ) (Vasconcellos et al. 2015), the effective baryon mass is defined in turn as  $M_{B\zeta}^* = M_B m_{B\zeta}^*$ . Properties of the fields considered in our formulation are presented in Table 1. For certain values of the parameters of the model ( $\xi, \kappa, \eta, \zeta$ ), the treatment adopted in this work reproduces the same predictions for global properties of neutron stars as most of the models based on Yukawa-type couplings involving the  $\sigma$ ,  $\omega$ , and  $\varrho$  mesons. For other choices of the space of parameters, dictated by basic physical principles and the phenomenology, our approach allows the description of the effects of many-body forces and self-correlations of higher orders involving the extended Yukawa sector of the strong interaction. In this case a new physics for neutron star may become feasible. This is basically the motto of our investigation.

### 4.2 Mixed phase - $B\bar{K}^0 K^-$

In the mixed phase, we consider a theoretical approach which combines the previous effective relativistic Lagrangian density QHD-model for the baryon phase (3) with, as a novelty in the treatment of kaon and anti-kaon condensation in high density nuclear matter, a Lagrangian density  $\mathcal{L}_K$  which describes the free propagation of kaons and many-body interaction forces involving kaons, anti-kaons and meson fields. The Lagrangian density for the free propagation of kaons and anti-kaons and with self-energy insertions reads

$$\begin{aligned} \mathcal{L}_K = & \sum_K \left( \partial_\mu \bar{\psi}_K \partial^\mu \psi_K - \bar{\psi}_K M_K^2 \Sigma_{K\iota}^s(\sigma, \sigma^*, \delta) \psi_K \right) \\ & + \sum_K \bar{\psi}_K \left( \gamma_\mu \Sigma_{K\zeta}^\mu(\sigma, \sigma^*, \delta, \omega) \gamma^\mu \Sigma_{\mu K\zeta}(\sigma, \sigma^*, \delta, \omega) \right. \\ & + \gamma_\mu \tau_K \cdot \Sigma_{K\nu}^\mu(\sigma, \sigma^*, \delta, \varrho) \gamma^\mu \tau_K \cdot \Sigma_{\mu K\nu}(\sigma, \sigma^*, \delta, \varrho) \\ & \left. + \gamma_\mu \Sigma_{K\beta}^\mu(\sigma, \sigma^*, \delta, \phi) \gamma^\mu \Sigma_{\mu K\beta}(\sigma, \sigma^*, \delta, \phi) \right) \psi_K. \end{aligned} \quad (4)$$

From this expression, we can identify the following self-energy insertions:

$$\begin{aligned} \Sigma_{K\zeta}^\mu(\sigma, \sigma^*, \delta, \omega) &= g_{\omega K\zeta}^* \omega^\mu; \quad \Sigma_{K\nu}^\mu(\sigma, \sigma^*, \delta, \varrho) = \frac{1}{2} g_{\varrho K\nu}^* \varrho^\mu, \\ \Sigma_{K\beta}^\mu(\sigma, \sigma^*, \delta, \phi) &= g_{\phi K\beta}^* \phi^\mu; \quad \Sigma_{K\iota}^s(\sigma, \sigma^*, \delta) = M_K \Sigma_{K\iota}^s, \end{aligned} \quad (5)$$

with the mass of kaons and anti-kaons defined as

$$\begin{aligned} M_K \Sigma_{K\iota}^s &= M_{K\iota}^* \\ &= M_K \left( 1 + \frac{g_{\sigma K}\sigma_0 + g_{\sigma^* K}\sigma_0^{*2} + g_{\delta K}\tau_K \cdot \delta}{\iota M_K} \right)^{-\iota}. \end{aligned} \quad (6)$$

In the mean field approximation the complete Lagrangian density for the mixed Phase -  $B\bar{K}^0 K^-$  is

$$\begin{aligned} \mathcal{L}_{\xi\zeta\kappa\eta\iota\nu\beta} = & \frac{1}{2}m_\sigma^2\sigma_0^2 + \frac{1}{2}m_{\sigma^*}^2\sigma_0^{*2} + \frac{1}{2}m_\omega^2\omega_0^2 + \frac{1}{2}m_\phi^2\phi_0^2 \\ & + \frac{1}{2}m_\rho^2\varrho_{03}^2 + \frac{1}{2}m_\delta^2\delta_3^2 + \sum_l \bar{\psi}_l (i\gamma_\mu\partial^\mu - m_l)\psi_l \\ & + \sum_B \bar{\psi}_B (i\gamma_\mu\partial^\mu - g_{\omega B}m_{B\xi}^*\gamma_0\omega_0 - M_{B\zeta}^*) \\ & - \frac{1}{2}g_{\rho B}m_{B\kappa}^*\gamma_0\tau^{(3)}\varrho_{03} + g_{\phi B}m_{B\eta}^*\gamma_0\phi_0 \Big) \psi_B \\ & + \sum_K \left( \partial_\mu \bar{\psi}_K \partial^\mu \psi_K - \bar{\psi}_K \left\{ M_{K\iota}^{*2} + g_{\phi K}m_{K\iota}^*\phi_0^2 \right\} \right) \psi_K \\ & + \sum_K \bar{\psi}_K \left( g_{\omega K}^2 m_{K\zeta}^{*2} \omega_0^2 + g_{\varrho K}^2 m_{K\nu}^{*2} \varrho_{03}^2 \right) \psi_K, \end{aligned}$$

with

$$m_{\Psi\chi}^* = M_\Psi \left( 1 + \frac{g_{\sigma K}\sigma_0 + g_{\sigma^* K}\sigma_0^{*2} + g_{\delta K}\tau_{K3}\delta_3}{\chi M_\Psi} \right)^{-\chi}; \quad (7)$$

in this expression  $\Psi = (B, K)$  and  $\chi = (\xi, \kappa, \eta, \zeta, \iota, \zeta, \nu)$ .

### 4.3 Coupling constants

In the following, the values of the sets of parameters ( $\xi, \kappa, \eta, \zeta, \iota, \zeta, \nu$ ) have been chosen to allow the model to reproduce nuclear properties at saturation, like for example the compressibility modulus of nuclear matter smaller than 300 MeV. We assume for the saturation density of nuclear matter  $\rho_0 = 0.17 \text{ fm}^{-3}$  and for the binding energy of nuclear matter  $\epsilon_B = -16.0 \text{ MeV}$ . The isovector coupling constant  $g_\varrho$  is constrained to the symmetry energy coefficient  $a_{\text{asym}} = 32.5 \text{ MeV}$  (Haensel et al. 2007). The values of the coupling constants are shown in Table 2.

**Table 2** Coupling constants in our model. The coupling constants involving nucleons and  $\delta$  meson are  $g_{\delta N} = 3.1$  and  $g_{\sigma K} = 3.325$ .

Model	$g_{\sigma N}$	$g_{\omega N}$	$g_{\rho N}$
$\zeta = 0.044$	9.893	10.719	8.657
$\zeta = 0.05$	9.782	10.477	8.721
$\zeta = 0.06$	9.600	10.103	8.813

**Table 3** Equilibrium properties for nuclear matter:  $\rho_c$  is the baryon density in the star center,  $K$  is the compressibility modulus and  $M_{\star\text{max}}$  is the maximum neutron star mass.

Model	$M_N^*/M_N$	$K$ (MeV)	$M_{\star\text{max}}$ ( $M_\odot$ )	$R_\star$ (km)	$\rho_c/\rho_0$
$\zeta = 0.044$	0.66	297	2.43	11.67	4.21
$\zeta = 0.05$	0.68	281	2.38	11.50	4.36
$\zeta = 0.06$	0.70	262	2.31	11.16	4.68

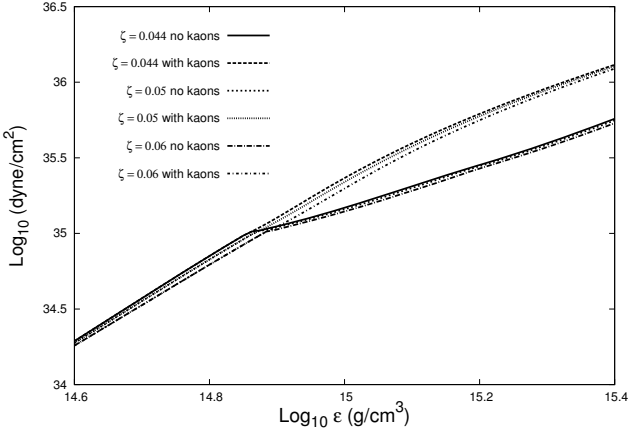


**Fig. 1** Equation of state of nuclear matter.

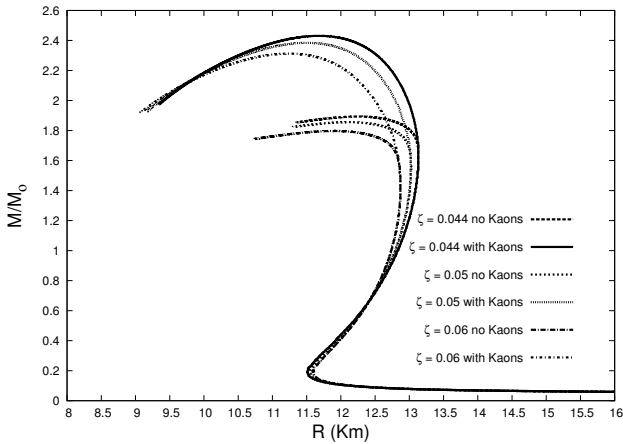


**Fig. 2** Mass-radius relation and maximum mass limits for neutron stars.

## 5 Conclusions

The results of our study confirm the hypothesis assumed in the present work, ie, that shielding effects involving attractive and repulsive contributions of many-body forces in nuclear matter, combined with the increase of the effective mass of baryons, – due to many-body scalar field correlations –, and the absence of the  $\Sigma^-$  hyperon, are dominant and favour the stiffening of the EoS of nuclear matter when compared with those effects favoring the softening of the EoS, i.e., the shielding of the repulsive part of the strong interaction and the increase on the population of the remaining hyperons beyond the  $\Sigma^-$  even in the presence of

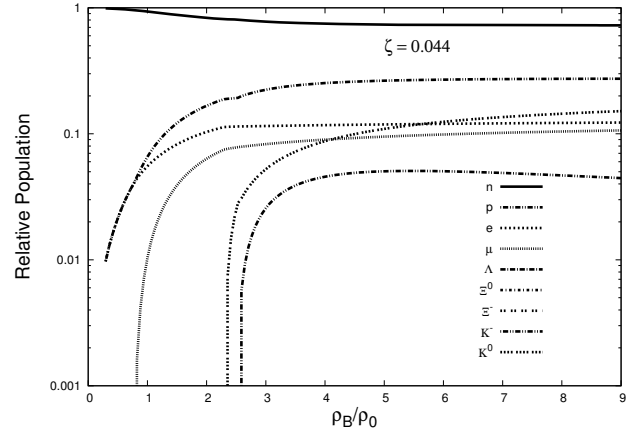


**Fig. 3** Relative population for particle constituents of neutron stars.

exotic degrees of freedom, ie hyperons as well as kaon and anti-kaon condensation. Those effects aforementioned may therefore be the key argument to allow the nuclear equation of state to satisfy both the maximum mass and the allowed ranges of mass and radius of neutron stars as well as to go beyond those known maximum mass limits.

## References

- Antoniadis, J., Freire, P.C.C., Wex, N., et al. 2013, *Science*, 340, 6131, 448
- Astashenok, A.V., Capozziello, S., & Odintsov, S.D. 2014, *Phys. Rev. D*, 89, 103509
- Baade, W. & Zwicky, F. 1934, *Phys. Rev. D*, 46, 76
- Bednarek, I., Keska, M. & Manka, R. 2003, *Phys. Rev. C*, 68, 035805
- Bethe, H.A. & Bacher, R.F. 1936, *Rev. Mod. Phys.*, 8, 82
- Chandrasekhar, S. 1931, *ApJ*, 74, 81
- Demorest, P., Pennucci, T., Ransom, S., Roberts, M., & Hessels, J. 2010, *Nature*, 467, 1081
- Gamov, G. 1928, *Z. Phys.*, 51, 204
- Glendenning, N.K., & Moszkowski, S.A. 1991, *Phys. Rev. Lett.*, 67, 2414
- Glendenning, N.K. 1997, *Compact Stars*, (Springer-Verlag, New York)
- Glendenning, N.K. & Schaffner-Bielich, J. 1998, *Phys. Rev. Lett.*, 81, 4564
- Kaplan, D.B., & Nelson, A.E. 1986, *Phys. Lett. B*, 175, 57
- Lattimer, J.M. & Prakash, M. 2001, *ApJ*, 550, 426
- Nagae, T. 2010, *Prog. Theor. Phys. Suppl.*, 185, 299
- Schaffner-Bielich, J. 2008, *Nucl. Phys. A*, 804, 309
- Schulze, H.-J. & Rijken, T. 2011, *Phys. Rev. C*, 84, 035801
- Vidana, I., Polls, A., Ramos, A., Engvik, L., & Hjorth-Jensen, M. 2000 *Phys. Rev. C*, 62, 035801
- Yakovlev, D.G., Haensel, P., Baym, G., & Pethick, C.J. 2013, *Physics Uspekhi*, 56, 289; 2012, arXiv:1210.0682.
- Weizsaecker, C. F. 1935, *Z. Phys.*, 96, 431